



HAL
open science

Understanding and modelling the thermal runaway of Li-ion batteries

Thi Thu Dieu Nguyen

► **To cite this version:**

Thi Thu Dieu Nguyen. Understanding and modelling the thermal runaway of Li-ion batteries. Material chemistry. Université de Picardie Jules Verne, 2021. English. NNT : 2021AMIE0006 . tel-03617656

HAL Id: tel-03617656

<https://theses.hal.science/tel-03617656>

Submitted on 23 Mar 2022

HAL is a multi-disciplinary open access archive for the deposit and dissemination of scientific research documents, whether they are published or not. The documents may come from teaching and research institutions in France or abroad, or from public or private research centers.

L'archive ouverte pluridisciplinaire **HAL**, est destinée au dépôt et à la diffusion de documents scientifiques de niveau recherche, publiés ou non, émanant des établissements d'enseignement et de recherche français ou étrangers, des laboratoires publics ou privés.



Thèse de Doctorat

Mention Chimie

Spécialité Génie Electrochimique

présentée à l'*Ecole Doctorale en Sciences Technologie et Santé (ED 585)*

de l'Université de Picardie Jules Verne

par

Thi Thu Dieu NGUYEN

pour obtenir le grade de Docteur de l'Université de Picardie Jules Verne

Understanding and modelling the Thermal runaway of Li-ion batteries

Soutenue le 04/02/2021, après avis des rapporteurs, devant le jury d'examen :

M. Serge Péliissier, Directeur de Recherche, UGE

M. Guillermo Rein, Professeur, Imperial College London

M^{me} Sylvie Grugeon, ingénieur de recherche, LRCS

M. Guy Marlair, ingénieur de recherche, INERIS

M. Julien Bernard, ingénieur de recherche, IFPEN

M. Stéphane Laruelle, Professeur, UPJV

M^{me} Amandine Lecocq, ingénieur de recherche, INERIS

M. Martin Petit, ingénieur de recherche, IFPEN

Président, Rapporteur

Rapporteur

Examineur

Examineur

Examineur

Directeur de thèse

Invité

Invité



Acknowledgement

This thesis represents not only my research work in the last three years, but it is also one of the milestones in the long-term collaboration between IFPEN/INERIS/LRCS on the R&D of Li-ion batteries and specifically their safety aspects.

The project started on October 1st, 2017. I had such a wonderful working experience ever since. My first and third year was at IFPEN (Solaize) and my second year was at INERIS (Verneuil-en-Halatte), I have felt at home at both places thanks to the warm welcome of the people there. Teamwork is crucial for research and innovation. It is important to emphasize that this thesis represents the lessons learned and the achievements of the whole research team. Thanks to the continuous support and guidance of my remarkable mentors as well as the technicians in both institutes, this thesis is achieved as the result of overcoming the unexpected challenges we have encountered together throughout the whole project.

First and foremost, I wish to thank my thesis director, Prof. Stéphane Laruelle. Even from far distance, he has always supported me, not only by providing a research mentorship, but also academically and administratively through the rough road to finish my thesis.

Secondly, I wish to thank my thesis committee. Thank you to Guy Marlair, Julien Bernard, Sylvie Grugeon, Martin Petit and Amandine Lecocq for being my direct supervisors. You have guided me throughout the whole project, especially through the most difficult times in the final year when writing this thesis, you gave me not only the academic guidance but also the moral support and the freedom I needed to carry on. Now looking back, I remember not only the lessons you taught me in our many discussions but also your smiles.

Also thank you to Prof. Serge Pélissier and Prof. Guillermo Rein for being part of my thesis committee as manuscript reporter and thesis defence jury. I also appreciate very much your interests in our work and your suggestions.

My special acknowledgement goes to the technicians who work on this project: Elisa Calas, Dominique, Emmanuelle Braco, ... (IFPEN) and Jérôme Engler, Aurélien Zantman, Alexandra

Sosniak, Pierre-Alexandre Le Lore, ... (INERIS). You have supported me through many challenging experiments. Moreover, thank you all so much for making me felt happy and at home in the labs.

Specially, I would like to express my gratitude to the coordinators of this thesis project, Valérie Sauvant-Moynot (IFPEN) and Thierry Delbaere (INERIS). More than welcoming me to the labs, you have helped and taught me immensely. You also have been a source of positive energy, understanding and moral support ever since I know both of you. To me, you are always inspiration in so many ways.

I also wish to thank my office mates over the last three years: Venkat, Sayda, Simon, Medhi, Edoardo, Lois, Francois, David, ... You are all amazing people who have made our office time very rememberable with full of supports and joys.

A special thanks to my dear friend and colleague: Evelyne. You are so kind and talented in so many things. Your vision in life and your experiences always inspire me to be better and to live happier. I am so thankful for knowing you and for all the souvenirs we have with Elodie and our dear friends: Stéphanie, Nathalie, Laurent, ...

A special thanks to Guy and his family. Your hard-working and professional attitude and warm welcoming gesture meant greatly to me. Thank you so much for helping me finding the accommodation and riding with me to work from time to time. I enjoyed very much the time with Liziane and the discussions we had throughout dinners.

I also wish to thank the colleagues in IFPEN and in INERIS that I have a chance to work with. I will remember the coffee-break every morning that we shared so much laughter together. Also, a special thanks to Jérôme Lesage for your supportive discussions and your positive energy. I have learnt many things from you.

I also took part of many activities organized by IFPEN Doctoral College, with countless people teaching and helping me every step. A special thanks to the organizers and the PhD students participated in the study trips in Norway (2018) and in Scotland (2019) as well as the trainings, the Christmas dinners and the Doc's Day event every year. These experiences were irreplaceable.

I was also involved in activities outside work where I met amazing people. A great thank to my house mates at Vernaison: Christophe, Dadravi, Franck, Yan, Matthieu, Cecile, Adrian, Sophie,

Pierre, ... who have shared with me so many dear memories that I will always keep near my heart. I am so grateful for the time we had together. You all have taught me so much.

A special thanks to my Vietnamese friends and colleagues in IFPEN, INERIS and LRCS: Phuong, chi Ngoc, anh Tuan, anh Nam, em Son, Thoi, chi Anh, anh Thuy, be Nga, chi Cuc, anh Trung, anh Duy. Your friendship and unconditional support have been essential to me. I appreciate a lot the time we spent together. Thank you for giving me encouragement to carry on till the end of the thesis.

I wish to acknowledge the friendships that began at elementary school, BK, BKDEC, at l'X, at Schneider Electric and became ripe throughout years until now: thay Thi, co Huy, co Thuan, thay Thang, anh Dat, chi Hai, chi Van, Tuong, sep Hoang, Son, Nam, Huan, Xuan, Farhana, Jessi, Aissatou, chi Nguyen, chi Yen, chi Huong, anh Tuan, Trung, Binh, Bao, Tuan, Uyen, Nguyen, anh Huy, Sylvain, Javier, Laurent, ... Thank you for being my teachers, my friends and always encouraging me to follow my dream. I cannot become who I am today without you.

I am so grateful to my love and his family. You have given me love and emotional support throughout the whole journey. I felt like I have a 2nd home with you. Thank you so much for welcoming me to the family, for supporting me and giving me warm hugs every Christmas. Thanks to you, I also know more about France and about its beautiful/ complicated language.

Finally, I want to end where the dearest place can be: family. I have a wonderful and unique family. We have been through so many tough times together. Thanks to my parents, I think I have the most beautiful childhood in the world. Thank you so much for believing in me, for your sacrifices and unconditional love. You have been and always will be close to me wherever I go.

“Con cảm ơn ba mẹ đã sinh ra và nuôi con khôn lớn. Con xin lỗi vì không ở bên cạnh chăm sóc ba mẹ hàng ngày. Con mong ba mẹ và gia đình mình luôn hạnh phúc. Nhờ tình yêu với gia đình mà con đủ nghị lực để đi đến giấc mơ của mình. Đây cũng là món quà con muốn dành cho ông nội, ông bà ngoại và dì Út. Con yêu cả nhà.”

February 2021,

Thị Thu Diệu NGUYỄN

Table of contents

Table of contents	v
Abbreviations	ii
List of symbols and subscripts	xi
List of figures	xii
List of tables	xviii
General Introduction	1
1.1 <i>Context</i>	1
1.2 <i>Research strategy and scientific approach</i>	4
Chapter 1. Literature review on LIB general safety and aging-driven safety aspects	6
1.1 <i>Li-ion Batteries</i>	7
1.1.1 Working principle	7
1.1.2 Cell technology.....	9
1.1.3 Cell type	9
1.1.4 Cell and module assembly	10
1.1.5 Cell components.....	11
1.1.5.1 Negative electrode	12
1.1.5.2 Positive electrode.....	14
1.1.5.3 Electrolytes	17
1.1.5.4 Separator	20
1.1.6 Cell formation – SEI formation	21
1.1.7 Novel generation of Li-ion battery with a focus on Ni-rich Li-ion technologies	23
1.1.7.1 Selected technologies of positive electrodes: Ni-rich high energy technologies	24
1.1.7.2 Selected technologies of negative electrodes: Graphite-SiO _x composites (+ amorphous carbon).....	26
1.2 <i>Aging of Li-ion Batteries</i>	27
1.2.1 Definitions and overview of mechanisms	27
1.2.2 SEI growth.....	29
1.2.2.1 Calendar aging	29
1.2.2.2 Cycling aging	31
1.2.3 Li Deposition/Plating	34

1.2.3.1	Mechanisms during charging	34
1.2.3.2	Mechanisms during discharging.....	36
1.2.3.3	Morphologies of Li deposition and gradients in Li-ion cells.....	37
1.2.3.4	Degradation effects caused by Li deposition	39
1.2.4	Methods of detection and analysis of aging	40
1.2.4.1	SEI growth.....	40
1.2.4.2	Li Plating	41
1.3	<i>Thermal runaway of Li-ion Batteries</i>	48
1.3.1	Overview and definitions.....	48
1.3.1.1	Cell failures	48
1.3.1.2	Reported incidents involving Thermal runaway of Li-ion Batteries.....	49
1.3.1.3	Abuse conditions, triggering events and thermal runaway detecting methods	50
1.3.2	Thermal runaway mechanisms	52
1.3.2.1	Overview of the chain reactions during Thermal runaway.....	52
1.3.2.2	Exothermic decomposition reactions related to Negative electrode.....	53
1.3.2.3	Exothermic decomposition reactions related to Positive electrode	54
1.3.2.4	Exothermic decomposition and combustion of electrolytes	57
1.3.2.5	Melting of separator.....	58
1.3.2.6	Additional reactions relating to Li Plating.....	59
1.3.2.7	Other reactions	60
1.3.3	The risk of fire and explosion from vent gas and particles	60
1.3.4	The impact of SOC on the Thermal runaway	63
1.3.5	The role of Safety features in cylindrical cells.....	66
1.3.6	Impact of aging on Thermal runaway	71
1.3.6.1	Impact of SEI-driven aging	71
1.3.6.2	Impact of Li deposition/plating aging	74
1.4	<i>Modelling the Thermal runaway of Li-ion Batteries</i>	75
1.4.1	General strategy for Thermal runaway modelling.....	75
1.4.1.1	Modelling approach	76
1.4.1.2	Model calibration and validation for LFP/Gr (A123).....	77
1.4.2	Recent Thermal runaway model developments	79
1.4.2.1	Adding the venting into thermal runaway model	79
1.4.2.2	Adding the venting and short-circuit into thermal runaway model in IFPEN/Siemens Digital Industries Software project and DEMOBASE project.....	80
1.4.2.3	Early detection of Thermal runaway based on gas sensing modelling.....	82
1.5	<i>Conclusions</i>	82

Chapter 2. Experimental study targeting further understanding of the Thermal Runaway of LIBs at Pristine and Aged States 84

2.1	Introduction.....	85
2.2	Technology selection rationale.....	88
2.3	Multi-scale cell analysis	89
2.3.1	Physico-chemical characterization of the selected batteries.....	91
2.3.1.1	Cell electrodes.....	93
2.3.1.2	Cell separators	99
2.3.1.3	Cell electrolytes.....	102
2.3.2	Electrical characterization.....	104
2.3.2.1	Full cells	104
2.3.2.2	Half cells.....	108
2.3.3	Thermal analysis.....	110
2.4	Cell aging behaviour study.....	111
2.4.1	Check-ups and cell storage	113
2.4.1.1	Check-ups:	113
2.4.1.2	Cell storage condition:.....	114
2.4.2	SEI-driven aging.....	115
2.4.2.1	SEI-driven calendar aging.....	115
2.4.2.2	SEI-driven cycling aging	119
2.4.3	Experimental evaluation of cell aging due to Li plating	126
2.4.3.1	Preliminary tests	126
2.4.3.2	Defined protocols.....	127
2.5	Thermal safety tests	128
2.5.1	Thermal safety test in pseudo-adiabatic condition of ARC.....	129
2.5.1.1	Test setup	131
2.5.1.2	HWS test results.....	132
2.5.1.3	Main findings about the thermal runaway of Ni-rich LIBs	150
2.5.2	Thermal safety test in Oven (Oven test)	151
2.5.2.1	Test setup	152
2.5.2.2	Test protocol.....	153
2.5.2.3	Cell characteristics before and after oven test	153
2.5.2.4	Oven test result analysis.....	154
2.5.2.5	Oven test results of Panasonic NCR GA at pristine state	155
2.5.2.6	Oven test results of LG HG2 at pristine state.....	157
2.5.2.7	Influence of calendar aging and cycling aging on the thermal runaway.....	159

2.6	<i>Conclusions</i>	162
Chapter 3.	Model construction, calibration and validation	164
3.1	<i>Introduction</i>	165
3.2	<i>Model construction</i>	167
3.2.1	Electrical-thermal sub-model.....	167
3.2.2	Thermal runaway process sub-model.....	168
3.2.2.1	Solid electrolyte interface decomposition reaction	170
3.2.2.2	Decomposition reaction between the intercalated lithium and electrolyte solvent at the negative electrode	171
3.2.2.3	Reactions at the positive electrode.....	172
3.2.2.4	Electrolyte combustion reaction	173
3.2.2.5	Hard internal short circuit.....	174
3.2.2.6	Venting	175
3.2.3	Energy balance sub-model.....	178
3.2.3.1	0D energy balance model	178
3.2.3.2	3D energy balance model	179
3.2.4	Thermal exchange sub-model.....	181
3.2.4.1	Thermal exchange sub-model accounting the non-ideal adiabatic condition during HWS test in BTC	182
3.2.4.2	Thermal exchange sub-model simulating the oven test.....	184
3.2.5	Integration of SEI-driven Aging	186
3.3	<i>Model calibration</i>	187
3.3.1	Electrical-thermal sub-model calibration.....	188
3.3.2	Cell thermal properties characterization	191
3.3.2.1	Heat capacity of the selected technologies	191
3.3.2.2	Thermal conductivity.....	194
3.3.3	Thermal exchange sub-model calibration.....	194
3.3.3.1	Calibration of the thermal exchange sub-model accounting the non-ideal adiabatic condition during HWS test in BTC.....	194
3.3.3.2	Calibration of the thermal exchange sub-model simulating the oven test.....	195
3.3.4	Thermal runaway process sub-model calibration	196
3.3.4.1	Chemical degradation reactions.....	201
3.3.4.2	Hard ISC calibration	205
3.3.4.3	Venting calibration	206
3.4	<i>Model validation</i>	208
3.4.1	Model validation results of Panasonic NCR GA Pristine cell 100%SOC.....	209

3.4.1	Model validation results of LG HG2 Pristine cell 100%SOC.....	214
3.4.2	Model limitation.....	221
3.5	<i>Conclusion</i>	222
Chapter 4.	SOC and SOH parametric study	224
4.1	<i>Introduction</i>	225
4.2	<i>Impact of SOC on the thermal runaway overall phenomenology</i>	226
4.3	<i>Impact of SEI thickness growth by calendar aging on the thermal runaway</i>	230
4.4	<i>Impact of SEI growth influenced by calendar aging and cycling aging</i>	235
4.4.1	Thermal runaway of cycling aged cell _ Scenario (I).....	236
4.4.2	Thermal runaway of cycling aged cell _ Scenario (II).....	237
4.4.3	Comparison between the simulation results with the experimental data	238
4.5	<i>Simulation conclusions and perspectives</i>	245
	Conclusions and Perspectives	246
	Résumé de thèse en français	246
	References	265

Abbreviations

2RC-ECM	<i>Second-order resistor-capacitor equivalent circuit model</i>	IFPEN	<i>Institut Français du Pétrol Energies Nouvelles</i>
ARC	<i>Accelerated Rate Calorimetry</i>	INERIS	<i>Institut National de l'EnviRonnement Industriel et des risques</i>
BMI	<i>Bismaleimide</i>	IR	<i>Infrared reflection</i>
BMS	<i>Battery management system</i>	ISC	<i>Internal short circuit</i>
BTC	<i>Battery Testing Calorimeter</i>	LAM	<i>Loss of active electrode material</i>
CE	<i>Coulombic efficiency</i>	LAMneg	<i>Loss of negative active material</i>
CID	<i>Current interrupting device</i>	LAMpos	<i>Loss of positive active material</i>
CL	<i>Loss of conductivity</i>	LiPF6	<i>Li hexafluorophosphate</i>
CMC	<i>Carboxymethyl cellulosis</i>	LLI	<i>Loss of Li inventory</i>
CNTs	<i>Carbon nanotubes</i>	LRCS	<i>Laboratoire de Réactivité et Chimie des Solides</i>
DEC	<i>Diethyl Carbonate</i>	OCV	<i>Open circuit voltage</i>
DEMOBASE	<i>DEsign and MOdelling for improved BAttery Safety and Efficiency project</i>	PAA	<i>Polyacrylate</i>
DMC	<i>Dimethyl Carbonate</i>	PC	<i>Propylene carbonate</i>
DMMP	<i>Dimethyl methyl phosphonate</i>	PE	<i>Polyethylene</i>
DSC	<i>Differential scanning calorimetry</i>	PM	<i>Post-Mortem analysis</i>
DTV	<i>Differential Thermal Voltammety</i>	PP	<i>Polyethylene</i>
DV	<i>Differential Voltage</i>	PPC	<i>Pulse power characterization</i>
EC	<i>Ethylene Carbonate</i>	PTC	<i>Positive temperature coefficient</i>
EDS	<i>Energy Dispersive Spectrometry</i>	PVdF	<i>Polyvinylidene fluoride</i>
EDX	<i>Energy Dispersive X-Ray Analysis</i>	SBR	<i>Styrene butadiene rubber</i>
EIS	<i>Electrochemical Impedance Spectroscopy</i>	SEI	<i>Solid electrolyte interphase</i>
EMC	<i>Ethyl methyl carbonate</i>	SEM	<i>Scanning Electron Microscopy</i>
FAA	<i>Federal Aviation Administration</i>	SHR	<i>Self-heating rate</i>
FEC	<i>Fluorinated ethylene carbonate</i>	SOC	<i>State of charge</i>
GC – MS	<i>Gas chromatography mass spectrometry</i>	SOH	<i>State of health</i>
GD-OES	<i>Glow discharge optical emission spectroscopy</i>	THC	<i>Total Hydrocarbon Content</i>
GEIS	<i>Galvanostatic electrochemical impedance spectroscopy</i>	TMP	<i>Trimethyl phosphate</i>
GITT	<i>Galvanostatic intermittent titration technique</i>	TPP	<i>Triphenyl phosphate</i>
HWS	<i>Heat-wait-search or seek</i>	VC	<i>Vinylene carbonate</i>
IC	<i>Incremental Capacity</i>	VEC	<i>Vinyl ethylene carbonate</i>
		VGCFs	<i>Vapour-grown carbon fibres</i>
		XRD	<i>X-Ray Diffractometry</i>

List of symbols and subscripts

Symbols

T	Temperature
P	Pressure
V	Volume
U	Voltage
I	Current
R	Resistance
Q	Capacity
C	Capacitance
ϕ	Heat flow
h	Specific enthalpy
R	Reaction rate
A_i	Frequency of reaction i
m	Reaction order
E_a	Reaction activation energy
Vg_i	Amount of gas produced by reaction i relative to its mass of reactant
M	Molar mass
C_p	Heat capacity
k_r	thermal conductivities in the radial direction of the cylindrical cell
k_z	thermal conductivities in the vertical directions of the cylindrical cell
w	Mass of active material
t	Time
t_{SEI}	Average thickness of SEI layer
α	Conversion degree of the positive electrode active material
ρ	Density
σ	Stefan-Boltzmann's constant
ε	emissivity of the cell surface
A	Surface

Subscript

amb	Ambient	avg	Average	TR	Thermal runaway
ex	Exchange	$skin$	Cell skin	ref	Reference value
i	Reaction i	ch	Charge	dch	Discharge
h	Cell headspace	res	Residual	$vent$	Venting
pe	Positive electrode	ne	Negative electrode	e	Electrolyte
max	Maximum	eq	Equivalent	lim	Limit

List of figures

Figure 1: Project strategy: Combined experimental (left) and modelling (right) studies.	4
Figure 2: Schematic representation of the rocking chair model of a Li-ion cell [4].....	8
Figure 3: Li ion technology overview (inspired by [23]).....	9
Figure 4: Cross section of cell, assembly into a module and into a battery pack [24].	10
Figure 5: Cap assembly cross section of an 18650 cell with sealing gasket indicated [4].....	11
Figure 6: Safety problems with Li metal negative electrode. Li deposition during charge (left) and Li dissolution during discharge (right) [26].....	12
Figure 7: Crystal structures of (a) lithiated graphite, (b) Li titanate (LTO), and (c) silicon during lithiation and (d) charge–discharge profiles against Li metal foil at low charge/discharge rates, showing specific capacity and voltage hysteresis [30].....	13
Figure 8: Crystal structure of (a) layered (LiCoO_2), (b) spinel (LiMn_2O_4), (c) olivine (LiFePO_4), and (d) tavorite (LiFeSO_4F) and (e) typical discharge profiles of some positive electrode materials [30].	15
Figure 9: (Left) Comparison of the performance of NMC89 vs NCA89 and NMC90 positive electrodes; (Right) DSC profiles for the NCA89, NCM90, and NCMA89 measured in their second charged state (Li0.3MO_2) in the presence of 1.2 M LiPF_6 EC:EMC = 3:7 [37].....	16
Figure 10: Lithium-ion batteries’ world market value from 1992 to 2020. [62].....	23
Figure 11: Short and long term R&D strategies. The roadmap of the LIBs for pure electric vehicle: the demand of longer range and the potential of less thermal stable materials [3].....	23
Figure 12: Comparison of electrochemical properties, operation constraints (top) and thermal stability vs Capacity retention of different layered delithiated NMCs [13, 66], adapted by [63].	25
Figure 13: The most commonly studied aging mechanisms on cell level [69].....	28
Figure 14: SEI evolution and Li Plating interconnected degradation mechanisms and the factors that affect them [61].	28
Figure 15: Calendar aging after 9–10 months of storage at various SOCs and different temperatures: (a-b) capacity fade; (d-e) rise of internal resistances [70].....	30
Figure 16: Degradation analysis of the cell based on dV/dQ analysis. (a) dV/dQ analysis of discharge voltage curves for the fresh cell; (b) evolution of the dV/dQ of discharge voltage curves during the aging process. [75].....	33
Figure 17: a) Atomic model for Li intercalation and deposition, b) involved energy barriers [10].....	34
Figure 18: Li striping and formation of “dead Li” under different C-rates [80].....	37
Figure 19: Electrode surface morphologies of Li deposition often observed in Li-ion cells. [10].....	37
Figure 20: Aging mechanisms related to Li deposition in Li-ion cells. The arrows next to R_i , Q , E , CE , and η indicate if these values are decreased or increased [10].....	39
Figure 21: Identification of degradation mode using IC-DV analysis [88].....	41

Figure 22: Typical curve shapes for the capacity fade of commercial Li-ion cells when Li deposition is involved. a) linear, b) decelerated, c) accelerated decrease [10]	43
Figure 23: Evolution of C/25 discharges voltage vs. capacity curves with cycling Li plating aging. The inset panel shows a magnification of peak 0 [91].	45
Figure 24 : a) Oct 2013 - A Tesla Model S electric car on fire after a piece of debris hit the battery pack while the car was on the highway causing cells to short circuit and go into thermal runaway; b) Jan 2016 – A Tesla Model S burns to the ground while fast-charging at the Sundebru supercharger in Gjerstad, Norway; c) Remains of the UPS Boeing 747 cargo plane that crashed in 2010 [Photo credit: EPA].....	50
Figure 25: Incidents related with Li ion battery failure, and correlated abuse conditions.[3].....	51
Figure 26: Thermal runaway chain exothermic reactions of Ni-rich lithium-ion batteries [106].....	52
Figure 27: Normalized rate temperature of different technologies (left) and the peak temperatures of the first exothermic reaction and temperature of gas formation [13] (right).....	54
Figure 28: Oxygen formation (top) and phase transition (bottom) of different NMCs [13].	56
Figure 29: Mechanisms related to Li deposition and thermal runaway of Li-ion cells [10].....	59
Figure 30: Battery vent gas species compositions from literature [123].....	61
Figure 31: Vent particles (5kx) from the thermal runaway of 3 different NMCs technologies [110].....	62
Figure 32: The temperature versus time of the thermal runaway of the same capacity (3Ah) of 18650 NCA/Gr and 26650 LFP/Gr batteries at different SOCs (0, 50 and 100%). [126]	63
Figure 33: (Top) The heating rate as a function of temperature based on ARC results from 18650 Panasonic NCA/Graphite cells at 0%, 50%, 75% and 100% SOC. [124]; (Bottom) Thermal runaway temperature and heating rate curves of 18650 NMC523/Graphite cells at different SOC. R _i means the i th repetition. [127].....	64
Figure 34: Measured O ₂ , CO and CO ₂ concentrations as functions of time during the thermal runaway for batteries at different SOCs. [130]	65
Figure 35: Some common safety features in the cap assemblies of cylindrical cells [4].	66
Figure 36: Ejection of windings from a cylindrical cell subject to a thermal runaway reaction (left to right): (a) cross section of a cell without a stiff centre tube; (b) during thermal runaway windings expand and collapse into cell core; (c) cell vent, (d) electrodes ejection and (e) the role of stiff centre tube [4]	68
Figure 37: X-ray tomography results of No Mandrel cell (Left) and mandrel cell (Right), taken before (as received) and after 0 °C cycling.....	69
Figure 38: (Top) Discharge capacity delivered per cycle. (Bottom) Investigation and comparison of profiles changes over cycling in the Mandrel cell at ambient (solid lines) and 0 °C (dashed lines) conditions. [131]	70
Figure 39: A Heat-wait-search temperature over time profile of representative cells. B Trends of thermal runaway onset temperature, venting temperature and peak temperature for each cell type. C-E Photographs of representative failures after ARC thermal runaway testing. [131].....	71
Figure 40: Comparison of the 3 stages of thermal runaway between fresh cell (1 st Bar) and calendar aged cells (10 % (2 nd Bar) and 30 % (3 rd Bar) discharge capacity loss) [16].....	72

Figure 41: The volume of released gas and the heat release of thermal runaway of (a) pristine cells, (b) cells aged by cycling aging (20 % discharge capacity loss) and (c) cells aged by storage at 60 °C (20 % discharge capacity loss) during venting (left) and thermal runaway (right) [132].....	73
Figure 42: The ARC test data profiles of 18650 NMC532/Graphite aged cells at 100% SOCs: (a) cell surface temperature; (b) ARC's internal pressure. [95]	74
Figure 43: Thermal runaway coupled multiphysics model [16].....	76
Figure 44: Comparison of the simulated average surface temperature of a fresh A123 cell with the experimental data [16].....	78
Figure 45: The different processes that were taken into account in [139, 140]	79
Figure 46: Comparison between experimental and simulation results [141].....	80
Figure 47: (Left) Voltage and temperature evolution versus time: comparison between model prediction and experiment measurements. (Right) Gas release during HWS test [138].....	81
Figure 48: Project experimental study.....	86
Figure 49: Process of the complete multi-scale analysis of Li-ion battery cell	91
Figure 50: Global view from axial direction and longitudinal direction of the selected technologies (performed by IFPEN).....	92
Figure 51: Cell header design of cell P1453 - Panasonic NCR GA and cell L1452 - LG HG2 (analysed by IFPEN) revealing included safety devices from tomography imaging.....	93
Figure 52: SEM analysis of the geometry of pristine cell's electrodes (performed by IFPEN).....	95
Figure 53: EDX results of chemical mapping of the positive electrodes (performed by IFPEN).	96
Figure 54: EDX results of chemical mapping of Si and O of the negative electrodes (performed by IFPEN).	97
Figure 55: The selected technologies.....	98
Figure 56: SEM and EDS analysis results of the selected technologies' double-layer separators (results from the Physical Research and Analysis division of IFPEN, 2018).	101
Figure 57: The actual capacity profiles of the selected technologies at their initial states (6 cells for each technology), Panasonic NCR GA (red curves) and LG HG2 (brown curves) (performed by IFPEN).....	104
Figure 58: Charge at different C-rates (left) and discharge at different C-rates (right) of LG HG2 and Panasonic NCR GA (performed by IFPEN).	106
Figure 59: (a1,b1) OCV (Q) of Panasonic NCR GA and of LG HG2, respectively. (a2,b2) and (a3,b3) Rch(T,SOC) and Rdch (T, SOC) of Panasonic NCR GA and of LG HG2, respectively, with x axis is temperature (T), y axis is SOC and z axis is resistances (Rch or Rdch).	107
Figure 60: x values at the 100%SOC and 0%SOC of Panasonic NCR GA (red: positive electrode, blue: negative electrode).....	108
Figure 61: The melting points of the tested separators.	110
Figure 62: Safety-focus aging campaign.....	112
Figure 63: Check-up setup in 25 °C chamber (left) and Check-up protocol (right).....	114
Figure 64: SEI-driven calendar aging of Panasonic 18650 GA (6 cells for each check-up): Discharge capacity loss (top), discharge profiles and cell impedance at the pristine and aged states (bottom).....	117

Figure 65: SEI-driven calendar aging of LG 18650 HG2 (6 cells for each check-up): Discharge capacity loss (top), discharge profiles and cell impedance at the pristine and aged states (bottom).....	118
Figure 66: Test setup of cycling aging	120
Figure 67: Discharge profiles (top) and cell impedances (bottom) comparison between SEI-driven calendar and cycling aging of Panasonic NCR GA	122
Figure 68: The differential voltage and discharge profiles vs capacity of pristine cell (A,B respectively) and of its electrode half-cells (C,D respectively) on Clément's tool interface.....	123
Figure 69: The differential voltage and discharge profiles vs capacity of calendar aged cell (A,B respectively) and of its electrode half-cells (C,D respectively) on Clément's tool interface.....	125
Figure 70: The Li plating of Panasonic NCR 18650 GA: The hints of Li deposition of aged cells (P1, P2) compared with reference cell (P4).....	127
Figure 71: a) The heat-wait-seek or heat-wait-search (HWS) method, b) Example of cell surface temperature curve during HWS experiment in an ARC. [144]	129
Figure 72: The applied HWS test protocol in quasi-adiabatic conditions.....	130
Figure 73: ARC and its vessel (Top). ARC test sensors (thermocouples) and heater setup on 18650 cells (Bottom).	131
Figure 74: (a,b) The 5 stages in the evolution of cell temperatures obtained from the heat–wait–search (HWS) test of LG HG2 at 100% SOC and of Panasonic NCR GA at 100% SOC, respectively; (c,d) the initial observations of the endothermic reaction of separator melting of the LG HG2 at 100% SOC and Panasonic NCR GA at 100% SOC, respectively; (e,f) the final venting and hard ISC after the ceramic separator layer collapse occurs at T3 for both the LG HG2 at 100% SOC and Panasonic NCR GA at 100% SOC. [106].....	134
Figure 75: Temperature rates and test time versus temperature during the thermal runaway of the LG HG2 pristine cells at 100% SOC.....	139
Figure 76: Temperature rates and test time versus temperature during the thermal runaway of the Panasonic NCR GA pristine cells at 100% SOC.....	140
Figure 77: Comparison of the final stages of the thermal runaway of the selected Ni-rich technologies versus the “safest technology”, LiFePO ₄ (LFP)/graphite.	142
Figure 78: The C (–) temperature rate and cell voltage of LG HG2 and Panasonic NCR GA (at 100% SOC) versus C (–) temperature.....	143
Figure 79: Temperature rate of C (+) and vessel pressure rate of LG HG2 and Panasonic NCR GA (at 100% SOC) versus C (+) temperature.....	144
Figure 80: The C (–) temperature rate and voltage of LG HG2 at 50% and 100% SOC versus C (–) temperature.	146
Figure 81: (a) Temperature profiles versus test time and (b) temperature rate versus temperature of the 50% and 100% SOC LG HG2 and Panasonic NCR GA cells. (c) Duration of the reversible self-heating region (stage ② + ③) and duration of the irreversible self-heating region (stage ④) during thermal runaway of the presented cells.	147
Figure 82: Cell mass before and after thermal runaway.....	148
Figure 83: Cell voltage and vessel pressure (bar) versus temperature for LG HG2 100% SOC and 50% SOC.	149
Figure 84: The experimental set up of Oven test (top) and the thermocouples (TCs) distribution on the cell skin and in the ambient air.	152

Figure 85: Oven test protocol.....	153
Figure 86: Example of the thermocouple temperatures rough data of 2 different oven tests (Pristine Panasonic NCR GA), plotting with test time (left) and Δ Time (right).	155
Figure 87: Temperature evolution of the TCs distributed on the skin of pristine Panasonic NCR GA tested cells.	156
Figure 88: Temperature evolution and voltage of pristine Panasonic NCR GA tested cells.	157
Figure 89: Temperature evolution of the TCs distributed on the skin of pristine LG HG2 and Panasonic NCR GA tested cells.....	158
Figure 90: Temperature evolution and voltage behaviours of pristine LG HG2 cells compared to that of pristine Panasonic NCR GA cells.	159
Figure 91: The venting of the Panasonic NCR GA pristine and aged tested cells.....	160
Figure 92: Temperature evolution of the TCs distributed on the skin of pristine, calendar aging and cycling aging Panasonic NCR GA tested cells.	161
Figure 93: Thermal runaway coupled multi-physics model.....	166
Figure 94: Second-order resistor-capacitor equivalent circuit model (2RC-ECM) of LIB, inspired by [156].	168
Figure 95: Rotationally symmetric 2D approach for 3D thermal model.	181
Figure 96: The positions of the heater winding around the cell modelled with the rotationally symmetric 2D approach.	183
Figure 97: The 3D oven test simulation tool to validate the developed thermal runaway model.	184
Figure 98: The thermocouples set up in the oven test (A) and their models distributed over the cell skin (red points in (C) and (D)). (B) The 2D symmetrical mesh used in the model.	185
Figure 99: Current $I(t)$ applied in the 2RC-ECM electrical-thermal model of LG HG2.....	188
Figure 100: 2RC-ECM model cell voltage calibration result of LG HG2.	189
Figure 101: Cell voltage comparison between 2RC-ECM model result and experimental data of LG HG2 pristine cell and Panasonic NCR GA cell.....	190
Figure 102: The estimated C_p of the selected technologies.....	193
Figure 103: The comparison between the thermal runaway model with and without heat exchange.	195
Figure 104: Comparison of the measured and simulated (by use of oven test sub-model) cell skin temperature TC4 in the oven test according to different heat transfer coefficient $h [W.K^{-1}. m^{-2}]$ for oven test sub-model calibration purposes.	196
Figure 105: Thermal runaway reaction model calibration process.	198
Figure 106: The TC position in the 3D calibration model (red point).	198
Figure 107: Calibration results of Panasonic NCR GA (top) and LG HG2 (bottom).....	199
Figure 108: The temperature overshoot at the TC position in the 3D model.	200
Figure 109: The cell temperature during Heat step in 3D calibration model.	201
Figure 110: Chemical degradation reaction calibration results of Panasonic NCR GA (top) and LG HG2 (bottom).	204
Figure 111: Hard ISC calibration results of Panasonic NCR GA (top) and LG HG2 (bottom).....	205
Figure 112: Venting calibration results of Panasonic NCR GA (top) and LG HG2 (bottom).....	208
Figure 113: The hollow cylinder-shaped reaction zone before the accelerated thermal runaway process.....	209

<i>Figure 114: The skin temperature evolution of the TC1,TC2 (top) and TC3,TC4 (bottom) in the oven test vs simulation results.</i>	<i>210</i>
<i>Figure 115: The average skin temperature evolution of the oven test in the oven vs simulation results.</i>	<i>212</i>
<i>Figure 116: Simulation results of the evolution of the chemical species concentration c_{SEI}, c_{ne}, ce and the conversion degree α of the pristine Panasonic NCR GA cell 100%SOC.</i>	<i>213</i>
<i>Figure 117: The hard ISC simulation result vs the cell voltage measured in oven test.....</i>	<i>213</i>
<i>Figure 118: The average skin temperature evolution of the oven test data vs simulation results of pristine 100%SOC Panasonic NCR GA and LG HG2 cells.</i>	<i>214</i>
<i>Figure 119: Heat flows contributing to the accelerated thermal runaway.</i>	<i>217</i>
<i>Figure 120: The venting simulated by 3D model of Panasonic NCR GA and LG HG2 pristine cells 100%SOC.....</i>	<i>218</i>
<i>Figure 121: Evolution of c_{SEI}, c_{ne}, α, ce vs time / vs average skin temperature of pristine cells.....</i>	<i>220</i>
<i>Figure 122: Simulation results of the average skin temperature evolution of pristine cells at different SOC levels.</i>	<i>226</i>
<i>Figure 123: Evolution of c_{SEI}, c_{ne}, α, ce vs time / vs average skin temperature of pristine cells.....</i>	<i>229</i>
<i>Figure 124: The average skin temperature of pristine cell and calendar aging cell of the simulation results vs oven test data.....</i>	<i>232</i>
<i>Figure 125: The evolution of the average c_{ne} vs time / vs average skin temperature of pristine and calendar aged cells.</i>	<i>233</i>
<i>Figure 126: Cell internal pressure and average skin temperature of the pristine and calendar aged Panasonic NCR GA cells.....</i>	<i>234</i>
<i>Figure 127: The average skin temperature of pristine cell 100%SOC, calendar aging cell 100%SOC and cycling aging cell 100%SOC of the simulation results vs oven test data.....</i>	<i>239</i>
<i>Figure 128: Evolution of c_{SEI}, c_{ne}, α, ce vs time / vs average skin temperature of pristine cell (green curves), calendar aged cell (red curves) and cycling aged cell scenario I (blue curves), cycling aging scenario II (yellow curves).</i>	<i>243</i>
<i>Figure 129: Illustration de la stratégie de recherche : Approches expérimentales (à gauche) combinées à des travaux de modélisation (à droite).....</i>	<i>253</i>

List of tables

Table 1: Properties of some commonly used negative electrode active materials [30, 31]	13
Table 2: Measured flash points, auto-ignition temperatures, and heats of combustion of some typical Li-ion cell organic electrolyte components [4].....	18
Table 3: Known chemical compounds formed on the carbon/graphite SEI layers surface [56–60]	22
Table 4: Methods which give hints on Li deposition. [10]	42
Table 5: Advantages and disadvantages of different methods for monitoring and detecting thermal runaway. [62]	51
Table 6: The enthalpies (ΔH) of the exothermic reactions of different NMCs [3]	56
Table 7: EDS results of vent particles for cells with different NCM cathodes after TR. [110].....	62
Table 8: Summary of gases released by the thermally abused Sanyo UR18650ZL2 NMC111/Graphite LIBs identified using GC-MS chromatograms. [125]	66
Table 9: The experimental databases required for the calibration of the thermal runaway model. (*) The relating equations used in modelling work in chapter 3.....	86
Table 10: Selected Ni-rich commercial batteries (from datasheets). (*) Verified by IFPEN.	89
Table 11: Cell mass and extracted electrolyte mass of the tested cells	93
Table 12: Physical measurements for the negative and positive electrodes and separator of Panasonic NCR GA. (*) Average values.....	94
Table 13: Physical measurements for the negative and positive electrodes and separator of LG HG2. (*) Average values	94
Table 14: The oxyde stoichiometry of the active grains of positive electrodes (performed by IFPEN).....	97
Table 15: Data on the composition of the solvents and additives in the Panasonic NCR GA's electrolyte from performed chemical analyses.....	102
Table 16: Data on the composition of the solvents and additives in the LG HG2's electrolyte from performed chemical analyses.	103
Table 17: Charge and discharge capacity of the selected technologies.....	105
Table 18: x values estimation at 100%SOC and 0%SOC of Panasonic NCR GA.	109
Table 19: x values estimation at 100%SOC and 0%SOC of LG HG2.	109
Table 20: Estimation of the quantity of the active materials of the selected technologies.	109
Table 21: CU planning of SEI-driven calendar aging for Panasonic NCR 18650 GA.....	116
Table 22: The results of LLI, LAMpos, LAMneg of pristine, calendar aged and cycling aged cells.	126
Table 23: The impact of safety features and SOC on venting and component ejection mechanisms, as seen through the pictures of LG HG2 and Panasonic NCR GA (50% and 100% SOC) after thermal runaway.	150
Table 24: Cell characteristic before and after the oven test.	154
Table 25: Occurrence times and critical temperature of Panasonic NCR GA tested cells.	160
Table 26: The calibrated parameters for the electrical-thermal sub-model.	189

<i>Table 27: Average heat capacity of the selected cells</i>	<i>193</i>
<i>Table 28: Thermal conductivity of the selected cells</i>	<i>194</i>
<i>Table 29: Thermal exchange sub-model parameters</i>	<i>195</i>
<i>Table 30: Model parameters of the negative materials reaction.....</i>	<i>202</i>
<i>Table 31: Model parameters of the positive materials reaction</i>	<i>203</i>
<i>Table 32: Model parameters of the electrolyte reaction</i>	<i>203</i>
<i>Table 33: The fitting parameters of the hard ISC of LG HG2 and Panasonic NCR GA model.....</i>	<i>206</i>
<i>Table 34: Calibration results and comparison between the amount of ejected gas modelled and the call mass loss from experiment. ^(a) adjusted values.....</i>	<i>207</i>
<i>Table 35: The critical temperature T₃, the maximum temperature reached T_{max} and times to these temperatures identified from the oven test vs simulation results of Panasonic NCR GA pristine cell 100%SOC.....</i>	<i>211</i>
<i>Table 36: The temperature range and occurrence time of the exothermic chemical reactions of pristine cell 100%SOC and the related bibliography sections.</i>	<i>212</i>
<i>Table 37: The critical temperature T₃, the maximum temperature reached T_{max} and times to these temperatures identified from the oven test vs simulation results of pristine Panasonic NCR GA and LG HG2 cells.....</i>	<i>215</i>
<i>Table 38: The temperature range and occurrence time of the exothermic chemical reactions occurred during the thermal runaway of pristine and calendar aged cells.....</i>	<i>216</i>
<i>Table 39: The amount of ejected gas (simulation results vs test measurements).</i>	<i>219</i>
<i>Table 40: Parameters set for SOC levels.</i>	<i>226</i>
<i>Table 41: The critical temperature T₃, the maximum temperature reached T_{max} and times to these temperatures identified from the oven test vs simulation results.....</i>	<i>227</i>
<i>Table 42: The temperature range and occurrence time of the exothermal chemical reactions.....</i>	<i>228</i>
<i>Table 43: Estimation of the SEI thickness growth through calendar aging.....</i>	<i>230</i>
<i>Table 44: The critical temperature T₃, the maximum temperature reached T_{max} and times to these temperatures identified from the oven test vs simulation results of pristine cell and calendar aging cell.....</i>	<i>231</i>
<i>Table 45: The temperature range and occurrence time of the exothermic chemical reactions occurred during the thermal runaway of pristine and calendar aged cells.....</i>	<i>233</i>
<i>Table 46: Comparison between the amount of ejected gas modelled and the cell mass loss from experiment.</i>	<i>234</i>
<i>Table 47: Analysis of capacity loss due to LLI, LAMpos and LAMneg for pristine, calendar aging and cycling aging Panasonic NCR GA cells.</i>	<i>235</i>
<i>Table 48: The different parameters for scenario I of cycling aged cell vs pristine cell.....</i>	<i>237</i>
<i>Table 49: Estimation of the SEI thickness growth through cycling aging.....</i>	<i>238</i>
<i>Table 50: The different parameters for scenario II of cycling aged cell vs pristine cell.</i>	<i>238</i>
<i>Table 51: The critical temperature T₃, the maximum temperature reached T_{max} and times to these temperatures identified from the oven test vs simulation results of pristine cell, calendar aged cell and cycling aged cell.</i>	<i>240</i>
<i>Table 52: The temperature range and occurrence time of the exothermic chemical reactions occurred during the thermal runaway of pristine, calendar aged and cycling aged cells.....</i>	<i>242</i>
<i>Table 53: Comparison between the amount of ejected gas modelled and the cell mass loss from experiment.</i>	<i>244</i>

Table 54: Occurrence times and critical temperature of Panasonic NCR GA tested cells.259

General introduction

1.1 Context

Lithium-ion battery (LIB) is one of the most important energy storage technologies available today, thanks to their high specific energy densities and stable cycling performance [1, 2]. The challenging requirements for LIB technology are (i) the targeting of lower cost systems, (ii) achieving higher performance with a longer lifetime (>10 years for automotive applications), (iii) allowing fast-charging (<20 min for 80% state of charge (SOC)), and (iv) providing low temperature cycling. At the same time, these expected improvements should not compromise safety performance, which must remain excellent in all situations (i.e., over the whole lifetime, including in all weather and abuse conditions) [3].

However, LIBs contain flammable electrolytes, and thus not only do they store electrical energy in the form of chemical potential energy, they also store chemical energy (especially compared to cells with water-based electrolytes) in the form of combustible materials [4]. Therefore, when LIBs are operated improperly, either outside of the specifications of its manufacturer or due to cell defects, electrical and chemical energies inside the cells can be unintentionally released and lead to gassing, fires, or even explosions. During these incidents, the most energetic catastrophic failure of a LIB system is a cascading thermal runaway event. This is characterized by a deficit of energy evacuation versus energy accumulation in the cells, leading to uncontrollable overheating of the battery system. In general, this energetic failure occurs when an exothermic reaction gets out of control. As the temperature of the battery rises to a certain threshold, the exothermic chemical reaction rate inside the battery increases and further heats up the cell. The continuously rising temperatures may trigger cascading chain reactions [3, 5] and result in uncontrolled flammable and toxic gassing, fires, and explosions, which are especially critical for large battery packs. This complex event involves multi-scale phenomena ranging from internal physico-chemical to battery components reactions (electrodes, electrolytes and separator) and further to the thermal propagation of cell core and safety features (CID, PTC disk, Pressure disk, Button vent, steel can). This is considered the key to battery safety concerns. Therefore, understanding the causes and processes of thermal runaway is especially important to guide the design of functional materials and improve the safety and reliability of LIBs.

Since the commercialization of LIBs by Sony Inc. in 1991 until today, recurrent incidents involving LIBs undergoing thermal runaway have been reported worldwide in electronics devices such as cell phones, laptops, and electric vehicles, and even auxiliary power units powering commercial aircrafts [6, 7]. Although these incidents are highly unlikely, they are reminders that safety is a prerequisite for batteries, whatever the level of innovation, and that understanding the causes and processes of thermal runaway of high-energy LIBs before their applications is essential to guiding the design of functional materials and improving the safety and reliability of LIBs.

Battery safety is becoming even more critical with the emergence of highly reactive Ni-rich LIBs in the market. These batteries are commercialized to meet novel energy- or power-demanding applications and are expected to dominate the market in the coming years, likely until the occurrence of a new technological breakthrough. This novel battery generation of such high energy density and more intrinsically reactive materials could possibly lead to more catastrophic events involving thermal runaway. Future safe and sustainable use of such innovative chemistry batteries requires at an early stage a comprehensive characterization of the properties impacting their safety profile.

According to recent literature [8–13], aging of LIBs has a notable impact on the abusive behaviour of thermal runaway. Aging is an inevitable degradation process which leads to capacity loss and internal impedance increase, thereby, loss of rate capability and cell performance during the whole lifetime of Li-ion batteries. It links closely to the inherent safety issues inside Li-ion batteries. Several studies confirmed that SEI Growth aging seems to play a critical role in thermal runaway. In the context of emerging higher capacity Li-ion batteries including Ni-rich high energy technologies, Li Plating also seems to have a notable impact on the behaviour of Li-ion cells in thermal abuse conditions through increased risk of short circuit, and hence higher sensitivity to thermal runaway [9–11, 14, 15]. Therefore, two main safety-focused aging mechanisms in LIBs are SEI growth and Li deposition/plating.

In this context, there is a clear need to better understand the underlying specific electrochemical and thermal behaviours of these cells in both normal and abuse conditions across their lifetime.

Former IFPEN/INERIS/LISE thesis of Sara ABADA [16, 17] on the thermal runaway of Li-ion batteries has focused on the previous generation of Li-ion batteries (essentially LFP/Graphite) [16] which

has shown that thermal runaway is triggered through a series of exothermic reactions which occur in cascade at higher or lower temperatures. The work led to the development of a methodology to model the thermal runaway at cell scale and subsequently to the prediction of the battery state of health. They confirmed that SEI Growth driven calendar aging seems to play a critical role in thermal runaway. However, the impact of SEI driven cycling aging was not covered and some initial choices (such as the study of low-reactive Li-ion technologies) and constraints have limited the scope of this work.

Accordingly, and inspired by the works of Abada *et al.* [13, 16, 17], and other researchers [18, 19], this thesis, within the framework of IFPEN/INERIS/LRCS collaboration, aims to go deeper into the understanding and modelling of this complex multi-physics phenomenon, featuring the thermal runaway process at cell scale, taking into account the intertwined impact of the novel highly reactive Ni-rich technologies (NMC811 or NCA positive electrodes in combination with graphite-SiOx composite negative electrodes) and the influence of aging with 2 target degradation mechanisms: SEI evolution and Li Plating, in order to understand what are the keys to inherently safer highly reactive Li-ion batteries during usage. It is a matter of establishing the link between the materials used (electrodes, separator, electrolytes) in high energy density and intrinsically reactive Li-ion battery technologies, the degradation products during cell aging (mainly SEI evolution during cell lifetime and Li deposition during cold recharges) and thermal runaway kinetics. The role of aging on thermal runaway is extendedly studied by adding the impact of SEI-focused cycling aging and Li deposition/plating phenomenon occurring during cold recharges. In addition, the cells are analysed at all stages (new, after aging and after runaway). This is a prerequisite for adapting experimental, analytical, and modelling tools, as developed in previously performed studies, which are essentially validated for more mature and less reactive positive and negative chemistry combinations [20–22] in order to expand their applicability to innovative energetic chemistries.

The model developed can be implemented to understand the electrical or thermal initiation of the phenomenon of thermal runaway. This is critical step for future projects on avoiding this undesirable phenomenon and its propagation within battery cell and further battery pack regarding its design.

1.2 Research strategy and scientific approach

The methodology for investigating the thermal runaway through combined experimental and modelling studies is presented within 3 main work packages (WP) in the thesis:

- The first WP deals with the study of the effect of high energy density technologies on safety: Ni-rich positive electrode materials with a novel negative electrode technology: SiOx-Graphite Composites;
- The second WP aims at understanding underpinning mechanisms and relationship between calendar and cycling aging and safety focusing on 2 target degradation mechanisms: SEI evolution as a function of temperature and Li Plating (under low temperature conditions);
- The final WP deals with the development of a consolidated thermal runaway 3D model and the implementation of test protocols for model calibration and validation.

This three step research strategy relies on the achievements of several previous works [13, 16, 17] [18, 19] and on the combination and synergisms offered by combined experimental and modelling studies (Figure 1).

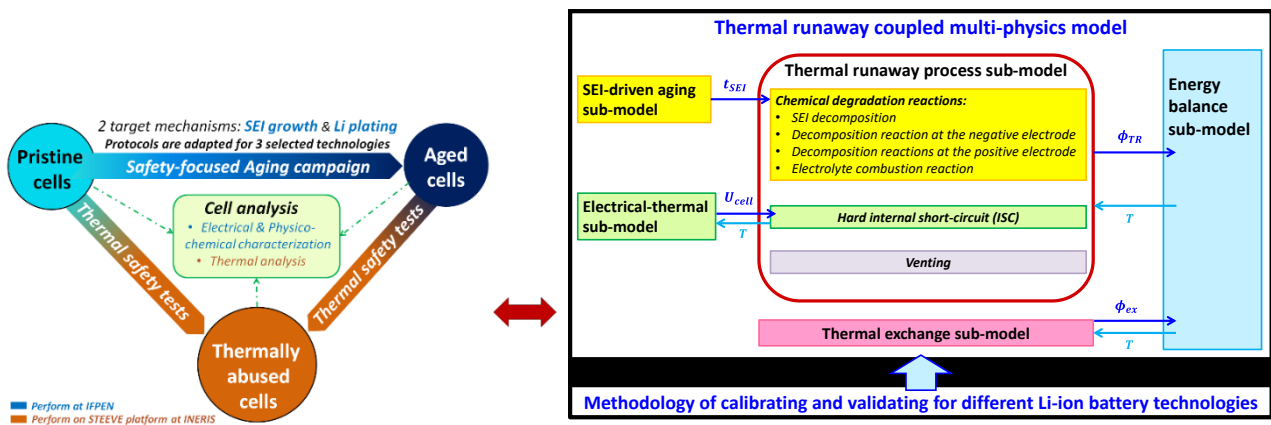


Figure 1: Project strategy: Combined experimental (left) and modelling (right) studies.

The modelling study is included in the final WP of the project which leads to the development of a 3D extended thermal runaway model to predict the behaviours of different Li-ion batteries nearby and during thermal runaway. The main goals of the experimental study were to perform the thermal runaway on LIBs at different state of charge (SOC) and different aging states to provide

sufficient databases for predictive model calibration and validation considering different factors impacting the battery safety at cell level.

The thesis works will be presented in this manuscript which consists of 4 chapters:

The first chapter presents the bibliography study carried out during the thesis which consists of the state-of-the-art literatures on the development of Li-ion batteries, their aging and safety aspects. Especially, the thermal runaway process of Li-ion batteries, its activation and consequences, will be discussed. At the end, the state-of-the-art developments of thermal runaway modelling will be exposed.

The second chapter is devoted to the results of the experimental works associated with the requirements of the calibration and validation of the extended thermal runaway model. The experimental results of cell analysis as well as their aging campaign will be firstly presented. Then the results of thermal abuse tests dedicated to the calibration and validation of the thermal runaway model will be discussed.

The third chapter is dedicated to the development, calibration and validation of the extended multi-physics thermal runaway 3D model at cell scale on COMSOL Multi-physics software. This model is obtained via the coupling of 5 sub-models as illustrated in Figure 1. The imperfections and limitations as well as the advantages of the model were also highlighted in this chapter.

Using the developed model, the fourth chapter carried out the parametric simulation study which investigates the influence of different impact parameters on the phenomenon of thermal runaway.

Finally, the conclusions extracted from the key points of this thesis work are presented at the end of this manuscript, with the emphasis on the perspectives for future research.

Chapter 1. Literature review on LIB general safety and aging-driven safety aspects

“Life can only be understood backwards, but it must be lived forwards.”

- Soren Kierkegaard

Contents

1.1	<i>Li-ion Batteries</i>	7
1.1.1	Working principle	7
1.1.2	Cell technology	9
1.1.3	Cell type	9
1.1.4	Cell and module assembly	10
1.1.5	Cell components	11
1.1.6	Cell formation – SEI formation	21
1.1.7	Novel generation of Li-ion battery with a focus on Ni-rich Li-ion technologies	23
1.2	<i>Aging of Li-ion Batteries</i>	27
1.2.1	Definitions and overview of mechanisms	27
1.2.2	SEI growth	29
1.2.3	Li Deposition/Plating	34
1.2.4	Methods of detection and analysis of aging	40
1.3	<i>Thermal runaway of Li-ion Batteries</i>	48
1.3.1	Overview and definitions	48
1.3.2	Thermal runaway mechanisms	52
1.3.3	The risk of fire and explosion from vent gas and particles	60
1.3.4	The impact of SOC on the Thermal runaway	63
1.3.5	The role of Safety features in cylindrical cells	66
1.3.6	Impact of aging on Thermal runaway	71
1.4	<i>Modelling the Thermal runaway of Li-ion Batteries</i>	75
1.4.1	General strategy for Thermal runaway modelling	75
1.4.2	Recent Thermal runaway model developments	79
1.5	<i>Conclusions</i>	82

1.1 Li-ion batteries

1.1.1 Working principle

The cell consists of 4 major components [4]:

1. The negative electrode or anode -the reducing electrode- that gives up electrons to the external circuit during discharging and is oxidized during the electrochemical reaction. Negative electrodes of LIBs are commonly made from carbon/graphite-containing polymer slurry coated onto a Cu current collector.
2. The positive electrode or cathode -the oxidizing electrode- that accepts electrons from the external circuit during discharge and is therefore reduced during the redox process. Positive electrodes of LIBs are mainly made of metal oxide active materials coated onto an Al current collector.
3. The electrolyte -the ionic conductor- that provides the medium for transfer of charge, as ions, inside the cell between the negative and positive electrodes. The electrolyte is typically a liquid solvent, with dissolved salts, to impart ionic conductivity. Some batteries use solid electrolytes, which are ionic conductors at the operating temperature of the cell.
4. The polymeric separator acts as a barrier between the two electrodes. It prevents physical contact between the positive and negative electrode, while facilitating ion transport in the cell.

Li ion batteries are able to be charged and discharged many cycles; which are referred to as secondary or rechargeable batteries. The functioning of a Li-ion electrochemical cell can be briefly summarized in Figure 2.

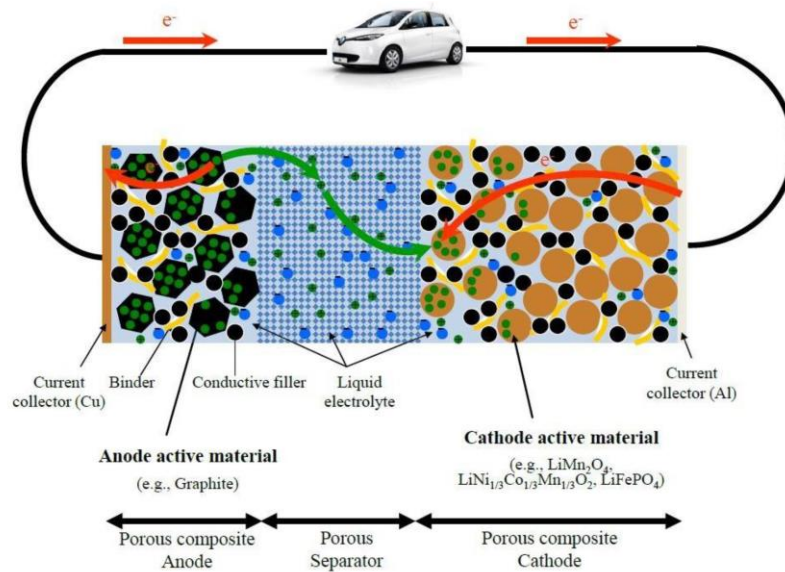
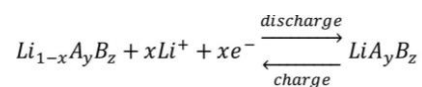


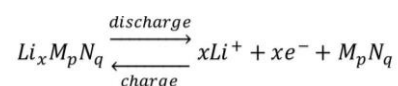
Figure 2: Schematic representation of the rocking chair model of a Li-ion cell [4].

The Li^+ ions will be transported between the positive and the negative electrodes during cycling. While the Li^+ ions travel through the electrolyte (green arrow), the electrons shuttle between the electrodes through an external circuit (red arrow), connected to the cell via their respective current collectors, in the presence of a load, in the same direction as the ions. During charge, at the positive electrode, the insertion compounds ionize giving out Li^+ ions and electrons that move to the negative electrode through the electrolyte and current collector, respectively, where they recombine at their respective insertion compound. The vice versa occurs during discharge. This is illustrated in the equations below:

At positive electrodes:



At negative electrode:



Li^+ ions intercalate (or insert) and de-intercalate (or de-insert) into/from the complex compounds of electrodes. The Li atoms diffuse through the material to either occupy the

vacant space present in the structures or proceed to the outer surface of the material to oxidize.

1.1.2 Cell technology

While the term battery is often used, the basic battery unit is referred to a battery cell. The battery cells are classified mainly based on their technology of cell negative and positive electrode active materials because they directly correspond to the amount of energy stored in the cell and also indicate the cell performance. Since the commercialization of LIBs in 1991 by Sony Inc., the technology of LIBs has been growing diversely and expected to further growing in the future. The most common cell technologies are illustrated in Figure 3.

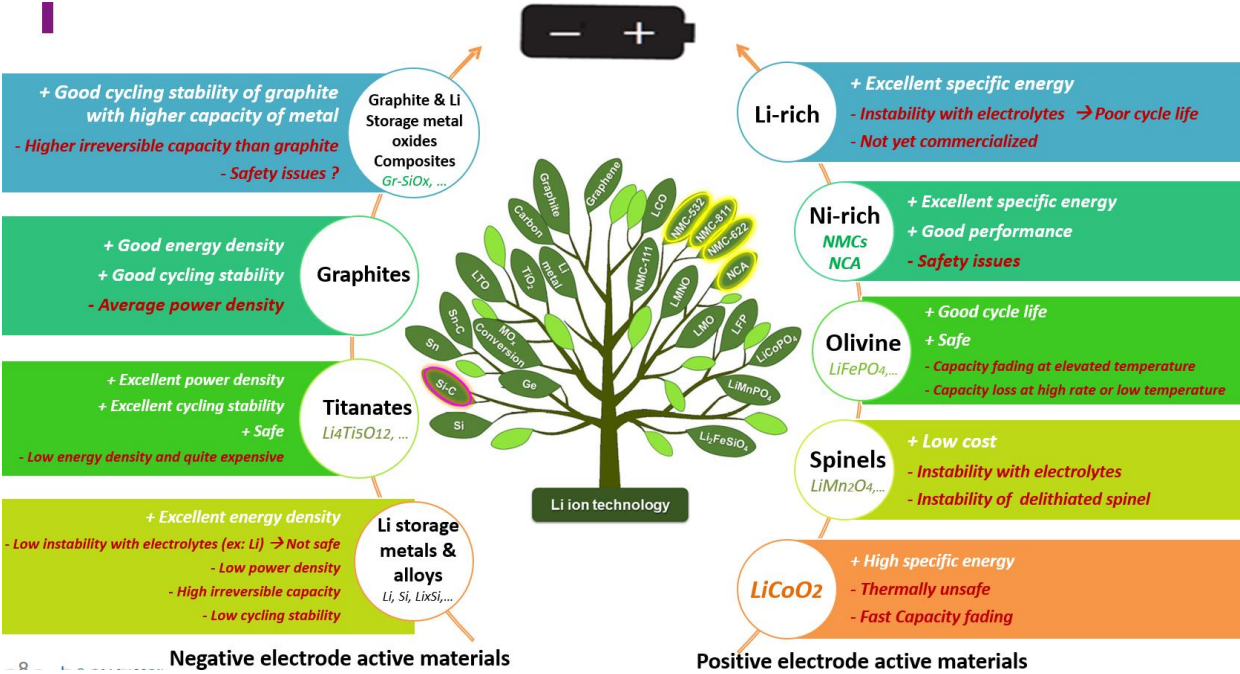


Figure 3: Li ion technology overview (inspired by [23]).

1.1.3 Cell type

Batteries can also be grouped based on their specific energy (power) or energy (power) density. Specific energy (power) is defined as the energy (power) per unit mass and is given by Wh/kg (W/kg). In addition to this, energy (power) density is defined as the energy (power) per unit volume and is given by Wh/L (W/L). In the context of Li-ion batteries, there are generally 3 cell types: High energy cells for high energy applications, High power cells for high power applications and Balanced cells for balanced energy and power applications.

High energy cells would require thicker electrodes in order to have the capability to store more active material. The rate of supply of Li^+ ions, that directly corresponds to the power capability of a cell, could be achieved by the use of thinner electrodes (because thinner electrodes correspond to lower resistance to the transport of Li^+ ions) which is contrary to obtaining high energy. This is a trade-off one must deal with, when designing batteries but the choice is primarily driven by the type of application.

1.1.4 Cell and module assembly

When battery cells are connected in series or parallel, or both, they can give the desired output voltage and capacity. Therefore, module assembly strongly depends on the required energy/power of the application.

The important design factors considered are the form and the nature of cell case. There are 3 cell formats available today which are Cylindrical, Pouch and Prismatic cells (Figure 4):

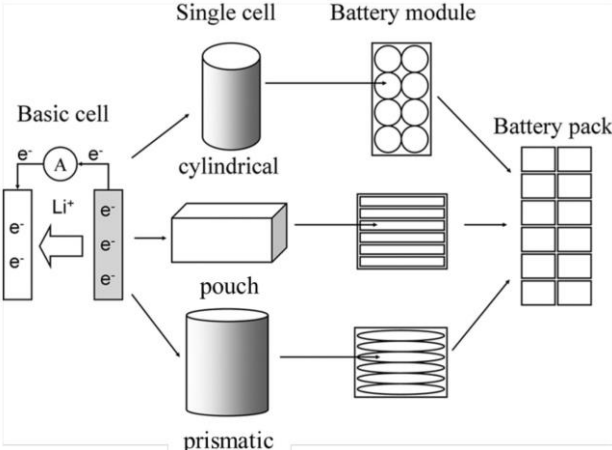


Figure 4: Battery module and battery pack assembly [24].

Cylindrical cells

Name code for this cell designation usually is “*abcde*”: the first two digits *ab* define cell diameter in millimetres and the next three digits *cde* define cell length in tenths of millimetres. Therefore, the 18650 indicates a cylindrical cell with a diameter of 18 mm, and a length of 65.0 mm. Nowadays, the 18650 is one of the most common cylindrical cell size. Ex: The Tesla Roadster battery pack is composed of approximately 6800 18650 cells [4].

This cell format is constructed by winding long strips of electrodes into a “jelly roll” configuration. Electrode rolls can be inserted into hard case which is usually a “deep drawn” can that only require formation of a seal at one end cap to minimize the possibility of cell leakage [4]. The end cap closure is accomplished with gaskets (typical of 18650 cells) (Figure 5).

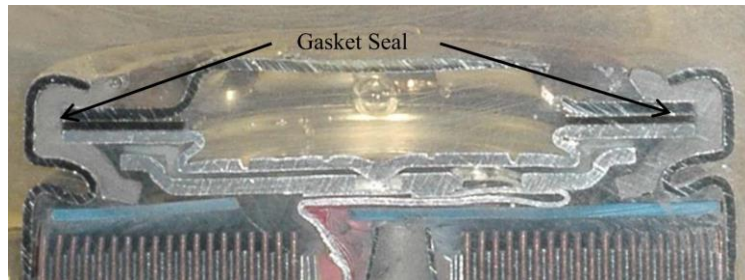


Figure 5: Cap assembly cross section of an 18650 cell with sealing gasket indicated [4]

The gasket acts as an enclosure of the hard case which is composed of metal: usually nickel-coated steel. Since the hard case and enclosure are negative, they are at least partially covered with shrink-wrap to provide electrical isolation [4].

Prismatic cells

This cell format is constructed often by winding and flattening electrodes into a pseudo-prismatic jelly roll (typical for high-rate capability prismatic cells). Electrode stacks can be inserted into hard cases that are usually laser-welded [4].

Pouch cells

Soft-pouch cells (also known as Li-ion polymer, soft-pack polymer, Li polymer, or Li-Po cells) have an enclosure of polymer-coated aluminium foil. This enclosure allows production of light and slender cell designs that are not possible to make in a hard case format. A soft-pouch cell may be embedded in a device and the device case itself may provide mechanical protection to prevent the incident of thermal runaway [4, 25].

1.1.5 Cell components

This section focuses on the major components of Li-ion cells.

1.1.5.1 Negative electrode

Negative electrode includes active materials which are responsible for energy (Li^+) storage and inactive components that are required for the operation of active materials.

Active materials

The oxidation of Li to Li^+ ion has the lowest electrochemical potential, thus, Li metal foil would be an ideal choice for a negative electrode in a Li-ion cell. However, they are known to exhibit severe safety issues, arising from growth of Li metal dendrites causing short circuits when it comes in contact with the positive electrode. Dendrites are formed due to Li Plating on the Li foil electrode when the negative electrode potential reaches the Li^0/Li^+ couple potential (Figure 6):

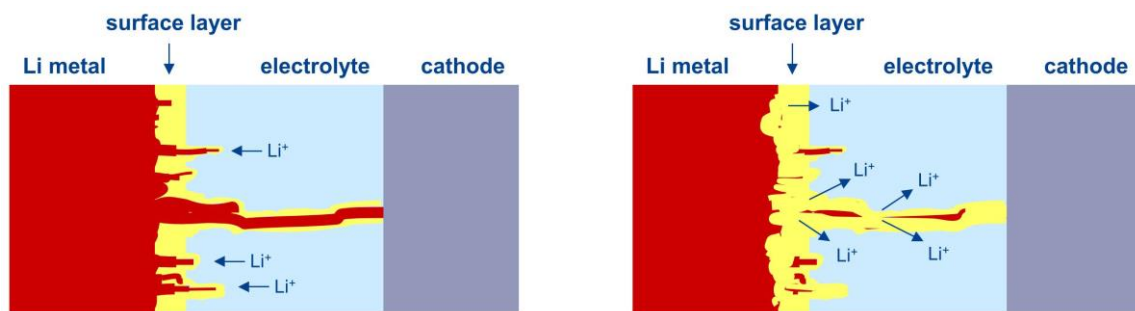


Figure 6: Safety problems with Li metal negative electrode. Li deposition during charge (left) and Li dissolution during discharge (right) [26]

This led to the searching and discovery of alternate electrodes which are Li insertion-based compounds with a similar operating potential range as that of the Li metal.

The most widely used commercially viable negative electrode is graphite because of its abundance on the earth and low cost, good electrochemical properties and also good theoretical capacity of 372 mAh/g. The electrolyte has a stable potential domain, however, unfortunately the potential of the lithiated graphite is outside of this domain. Therefore, mixtures of lithiated graphite (or Li metal) and organic electrolyte are not thermodynamically stable. As a consequence, the reactions between them will occur and produce a passivation layer on the negative electrode which is commonly referred to as the solid electrolyte interphase (SEI). SEI is essential for the cycling ability of this technology and will be explained in the forthcoming paragraph.

Li titanium oxide ($Li_4Ti_5O_{12}$ (LTO)) is an interesting alternate electrode thanks to its good power density and cycling stability. However, the combustion of large scale LTO battery is still concerned, especially at high SOC level [27]. Moreover, its energy density and its nominal reduction potential are far off when compared to Li. There are also newer negative electrode materials such as alloying materials (such as silicon (Si) [28], tin (Sn) [29]).

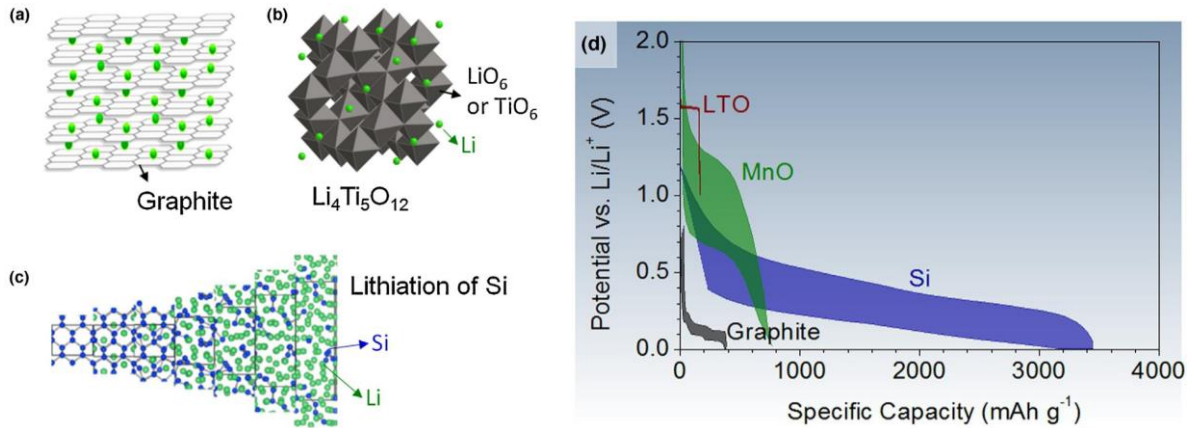


Figure 7: Crystal structures of (a) lithiated graphite, (b) Li titanate (LTO), and (c) silicon during lithiation and (d) charge–discharge profiles against Li metal foil at low charge/discharge rates, showing specific capacity and voltage hysteresis [30]

Crystal structures, performance and properties of these positive electrode active materials are illustrated on Figure 7 and Table 1.

Table 1: Properties of some commonly used negative electrode active materials [30, 31]

Material	Lithiation potential (V)	Delithiation potential (V)	D ($cm^2 s^{-1}$)	Volume change
Graphite	0.07, 0.10, 0.19	0.1, 0.14, 0.23	10^{-11} – 10^{-7}	10%
LTO	1.55	1.58	10^{-12} – 10^{-11}	0.20%
Si	0.05, 0.21	0.31, 0.47	10^{-13} – 10^{-11}	270%
Ge	0.2, 0.3, 0.5	0.5, 0.62	10^{-12} – 10^{-10}	240%
Sn	0.4, 0.57, 0.69	0.58, 0.7, 0.78	10^{-16} – 10^{-13}	255%
Li ₂ O (amorphous)	N/A	N/A	5×10^{-12} – 5×10^{-10}	N/A

Among all alloying materials, Si has received the most attention due to its relatively low average delithiation potential, extremely high gravimetric and volumetric capacity, abundance, low cost, chemical stability and especially non-toxicity [30]. Therefore, with the main objective of combining the cycling stability of graphite with the high capacity of Si, the blending of Si or SiOx with graphite got the market interests. This novel negative electrode technology will be further studied in this scoping thesis.

Inactive components

There are inactive components in the negative electrode side such as: binder, conductive additives and current collector. Binder is responsible for holding the particles of the active material particles together. Some commonly used binders are PVdF (Polyvinylidene fluoride), CMC (Carboxymethyl cellulosis) [32], SBR (styrene butadiene rubber) [33], PAA (polyacrylate) [34]. Conductive additives provide a path of good percolation for electrons in the solid matrix. The most well-known conductive additive is carbon blacks with specialties such as VGCFs (vapour-grown carbon fibres), CNTs (carbon nanotubes) [35]. Cu current collector at the negative electrode can include some reagents (carbon coatings for example) to improve adhesion / electrical contact with electrode material [35].

1.1.5.2 Positive electrode

Active materials

There are 4 types of insertion-based positive electrodes: 2D layered, 3D spinel, olivine and tavorite. Tavorite cells are not yet commercialized.

3D spinel of $LiMn_2O_4$ (LMO) technology enjoyed great success and was the major topic of research for several years, however, this technology has constraints of low specific capacity and low stability with electrolyte.

Olivine type crystal structure of the form $LiMPO_4$, such as LFP ($LiFePO_4$) has been investigated in the recent years because of its low cost, high-rate capability, high specific capacity and also low toxicity. $LiFePO_4$ cells are widely manufactured across the world for portable electronics, power tools and automotive applications.

2D layered oxide of the general form $LiMO_2$ (M is a transition metal such as Ni, Co or Mn) has a structure of two-dimensional layered sheets. The first known battery used for electronic devices is $LiCoO_2$ (LCO).

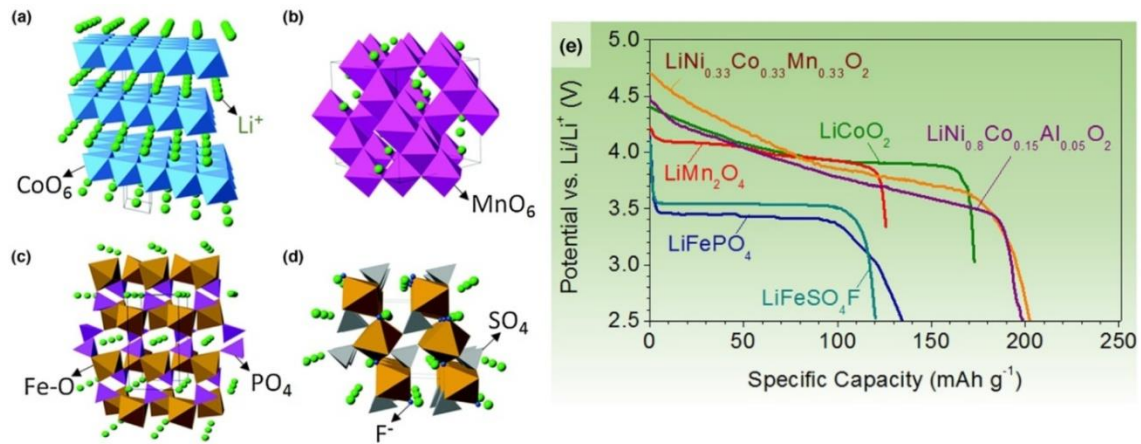


Figure 8: Crystal structure of (a) layered (LiCoO_2), (b) spinel (LiMn_2O_4), (c) olivine (LiFePO_4), and (d) tavorite (LiFeSO_4F) and (e) typical discharge profiles of some positive electrode materials [30].

However since Co is expensive and due to safety issues, it was partially substituted by other elements such as Ni, Al and Mn. As a result, there are other technologies with layered structure namely NCA ($\text{LiNi}_{0.8}\text{Co}_{0.15}\text{Al}_{0.05}\text{O}_2$) and the NMCs family ($\text{LiNi}_x\text{Mn}_y\text{Co}_z\text{O}_2$). Crystal structures, performance and properties of these technologies are summarized and illustrated on Figure 8 and Table 2.

Table 1: Characteristics of representative intercalation positive electrode compounds; crystal structure, theoretical/experimental/commercial gravimetric and volumetric capacities, and level of development [30].

Crystal structure	Compound	Specific capacity (mAh g^{-1}) (theoretical/experimental/typical in commercial cells)	Volumetric capacity (mAh cm^{-3}) (theoretical/ typical in commercial cells)	Level of development
Layered	LiTiS_2	225/210	697	Commercialized
	LiCoO_2	274/148	1363/550	Commercialized
	LiNiO_2	275/150	1280	Research
	LiMnO_2	285/140	1148	Research
	$\text{LiNi}_{0.33}\text{Mn}_{0.33}\text{Co}_{0.33}\text{O}_2$	280/160	1333/600	Commercialized
	$\text{LiNi}_{0.8}\text{Co}_{0.15}\text{Al}_{0.05}\text{O}_2$	279/199	1284/700	Commercialized
	Li_2MnO_3	458/180	1708	Research
Spinel	LiMn_2O_4	148/120	596	Commercialized
	LiCo_2O_4	142/84	704	Research
Olivine	LiFePO_4	170/165	589	Commercialized
	LiMnPO_4	171/168	567	Research
	LiCoPO_4	167/125	510	Research
Tavorite	LiFeSO_4F	151/120	487	Research
	LiVPO_4F	156/129	484	Research

Among all the commercialized technologies mentioned above, 2D layered structure namely NCA and the NMCs family can reach the capacities of 200 mAh/g or more, depending on the Ni content. NMC111 shows the highest thermal stability while Ni-rich NMCs shows low thermal stability. Focus shifted towards Ni-rich high energy layered oxides recently due to the needs of increasing energy density applications. These novel positive electrode technologies will be further studied in this scoping thesis.

Recently, an interesting hybrid technology, namely NCMA, was presented in the works of Kim *et al.* [36, 37]. The concept is to combine the NCA and NMC technologies within a single particle resulting in microstructural attributes that improved its cycling stability and also thermal stability. Their first hybrid positive electrode NCMA89 ($Li[Ni_{0.886}Co_{0.049}Mn_{0.05}Al_{0.015}]O_2$), consisting of a core of NCA89 (89% of Ni content) encapsulated by NMC90 (90% of Ni content), provides an exceptionally high discharge capacity of 225 mAh/g at 4.3 V and 236 mAh/g at 4.5 V. As seen in Figure 9, it is capable of outperforming both NCA89 and NCM90 with similar Ni contents in terms of cycling and thermal stabilities.

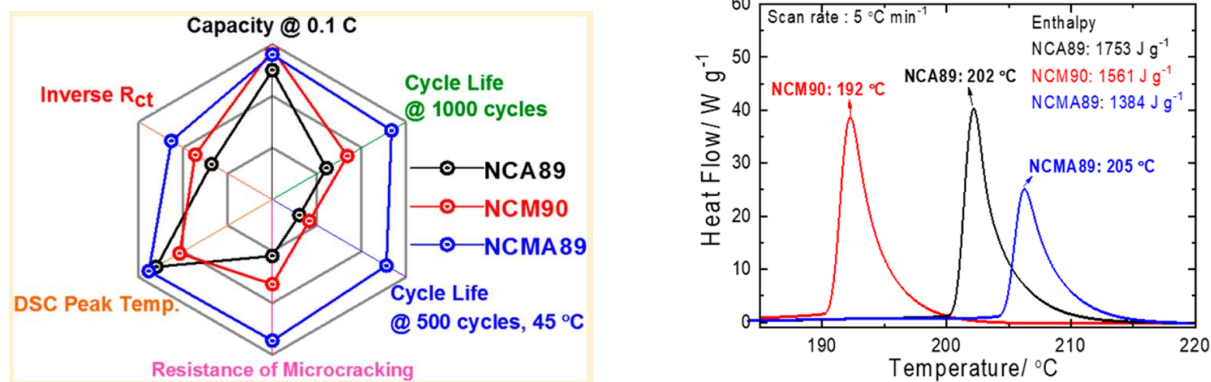


Figure 9: (Left) Comparison of the performance of NMCA89 vs NCA89 and NCM90 positive electrodes; (Right) DSC profiles for the NCA89, NCM90, and NCMA89 measured in their second charged state ($Li_{0.3}MO_2$) in the presence of 1.2 M $LiPF_6$ EC:EMC = 3:7 [37].

By in situ XRD analysis, they explained that thanks to the slight volume contraction/expansion during the phase transition of this hybrid technology and together with the enhanced intrinsic mechanical strength of its active single-particles, this is sufficient to

suppress micro-crack which was the key to ensure its long-term cycling stability and also higher thermal stability [36, 37]

Inactive components

Inactive components in the positive electrode side also compose binders, conductive additives and current collector. Some well-known binders nowadays are PVDF, SBR [38]. The current collector metal is aluminium.

1.1.5.3 Electrolytes

Electrolyte provides the medium for transfer of charge, Li ions, inside the cell between the electrodes. The use of a solid electrolyte has been the focus of the battery narrative lately, but it is still at the material selection phase of development. In the scope of this research, we focus only on the liquid electrolytes of LIBs. Liquid electrolytes for LIBs should have high ionic conductivity and be insulator for electrons, low viscosity, aprotic, liquid over a broad temperature range, high stability, nontoxicity, low flammability, and most importantly good solid electrolyte interphase (SEI) forming properties (SEI will be explained in section [1.1.6](#)).

The organic liquid electrolyte inside commercialized LIBs is critical to the safety because they compose the intrinsically flammable organic solvents [39, 40], therefore, researchers keep seeking a more stable electrolyte system to improve the intrinsic safety of Li ion batteries [41]. They are also developing innovative and optimized electrolyte systems based on room-temperature molten salts (i.e., ionic-liquids), polymers, a combination of solid and liquid electrolyte, or ceramics. The improvement of the thermal stability must consider the trade-off of safety, longevity, and specific capacity. Many trials were inapplicable in commercial use because of their poor performances in the longevity or the specific capacity [3].

Commonly used electrolytes (commercialized)

The most commonly used electrolyte solutions contain solvated Li-ions, which are provided by Li hexafluorophosphate (LiPF_6), dissolved in Alkyl Carbonate solvents such as: Ethylene Carbonate (EC), Dimethyl Carbonate (DMC), Diethyl Carbonate (DEC), Ethyl methyl carbonate (EMC) and propylene carbonate (PC) [42]. The mixture ratios vary depending upon the desired cell properties.

Table 2 shows the measured flash points, auto-ignition temperatures, and heats of combustion of some typical Li-ion cell organic electrolyte components:

Table 2: Measured flash points, auto-ignition temperatures, and heats of combustion of some typical Li-ion cell organic electrolyte components [4]

Electrolyte Component	Molecular Formula	Melting Point	Boiling Point	Vapor pressure (torr)	Flash Point	Auto-Ignition Temperature	Heat of Combustion
Propylene Carbonate (PC)	C ₄ H ₆ O ₃	-49°C	242°C	0.13 at 20°C	135°C	455°C	-20.1 kJ/ml -4.8 kcal/ml
Ethylene Carbonate (EC)	C ₃ H ₄ O ₃	36°C	248°C	0.02 at 36°C	145°C	465°C	-17.2 kJ/ml -4.1 kcal/ml
Di-Methyl Carbonate (DMC)	C ₃ H ₆ O ₃	2°C	91°C	18 at 21°C	18°C	458°C	-15.9 kJ/ml -3.8 kcal/ml
Diethyl Carbonate (DEC)	C ₅ H ₁₀ O ₃	-43°C	126°C	10 at 24°C	25°C	445°C	-20.9 kJ/ml -5.0 kcal/ml
Ethyl methyl carbonate (EMC)	C ₄ H ₈ O ₃	-14°C	107°C	27 at 25°C	25°C	440°C	None available

In case of graphite negative electrode, EC is commonly used. However, pure EC solvent has a relatively high melting point with high viscosity at ambient temperature. Thus, linear aliphatic carbonates, mainly dimethyl and/or diethyl carbonate (DMC and/or DEC), are mixed with EC to obtain suitable electrolyte-solvent systems, forming good conducting media for Li-ion [3]. However, for high voltage operation (beyond about 4.3-4.4 V), it becomes critical for the stability of carbonates and therefore leads to a big challenge for high potential positive technologies: finding an electrolyte that holds at higher potentials. Furthermore, these organic solvents also have high volatility and are intrinsically highly flammable. The safety improvements in these carbonate electrolytes rely on the additives or salt substitution [43].

Additives can improve the performance characteristics of Li-ion cell by enhancing the electrolyte bulk properties such as: conductivity, temperature range, film formation, chemical stability, cycle stability, overcharge protector, wettability, and most importantly non-flammability. They are the secret sauces of the battery world. However, commercialized additives are often developed without understanding the true electrochemical characteristics of the battery. Cell manufacturers typically include low concentrations of a

variety of additives to maintain the electrochemical performance of the cell, this amount should not exceed 10 %, either by weight or by volume, of the total electrolyte [3].

The alternative salts for safer electrolytes were reported. However, the practical application of the substitute salts was still rare. The studies on solvents for a safer battery also show interesting results but are still mainly under development [43, 44].

Safety additives

In the scope of this research, we are only focusing on the common electrolyte additives that mainly use for a safer carbonate electrolyte including:

- *the solvent substitute additives (the partial substitution of the flammable and volatile solvent):*

Fluorinated carbonates are promising to provide enhanced safety features considering their reduced flammability and increased thermal stability due to the presence of the strong carbon-fluorine bond [45, 46]. Ex: the fluorinated ethylene carbonate (FEC).

- *the SEI supporting additives:*

Its main objective is to improve the thermal stability of the SEI in order to mitigate and/or tackle the SEI decomposition and consequent thermal hazard. Several SEI supporting additives have been developed such as vinylene carbonate (VC) or vinyl ethylene carbonate (VEC) [47].

- *the flame-retardant additives:*

Its main objective is to reduce/suppress the fire potential during Thermal runaway. The working principle is:

- The catalytic removal of highly reactive, free radical species released during thermal runaway reactions ($H\cdot$ or $\cdot OH$);
- Forming a condensed state as a thermal insulating barrier to block the self-propagating fire.

The phosphorous and/or halogen containing materials are the most commonly used flame-retardant additives. Ex: Phosphates and alkyl phosphonates: trimethyl phosphate (TMP), triphenyl phosphate (TPP), dimethyl methyl phosphonate (DMMP) [48].

- *the thermal shutdown additives:*

It can prompt the solidification of liquid electrolyte at high temperature which effectively blocks the ion transport between electrodes, thereby shuts down the battery at high temperature [3].

Xia *et al.* [49] reported a thermally polymerizable monomer bismaleimide (BMI) that could cause a solidification of electrolyte at ~110 °C.

- *the overcharge protection additives:*

The overcharge protection additives can be classified as redox shuttle additives and shutdown additives. The former protects the cell from overcharge reversibly, while the latter terminates cell operation permanently.

The shutdown overcharge additives can electrochemically polymerize at high potentials or release gas at high potentials to activate a current interrupter device. The working potentials of these additives depend on their specific chemical structure. Typical shutdown overcharge additives for high voltage range are biphenyl, xylene, cyclohexylbenzene [3].

During long term operation of the cell, the irreversible oxidation of the additive compounds can have negative impacts on cell performance.

1.1.5.4 Separator

The polymeric separator acts as a barrier between the two electrodes avoiding direct contact between them. It also plays an important role in determining the occurrence of internal short circuit during Thermal runaway [4]. More details can be found in section 1.3.2.5.

Therefore, one of the challenging goals for the development of separators are reducing the thermal shrinkage and postponing the collapse to a higher temperature. There are 3 well-known milestones in developing separator technologies:

- Traditional separators include single layer of PE or PP [50];
- In order to form a time gap between the electrical shutdown and the thermal shrinkage, trilayer PP/PE/PP separator was developed by Celgard LLC. However, the

collapse temperature of the trilayer PP/PE/PP separator is similar to that of the single layer PP separator;

- Coating with ceramics is an effective way to reduce the thermal shrinkage and increase the collapse temperature of separator [51]. For these technologies, binder is essential to bind the ceramic onto the PE or PP base [52]. The most commonly used binder is PVDF. It can be substituted by curable copolyester or polydopamine, which contribute to lower thermal shrinkage [3]. Nowadays, the separator with ceramic coating has been accepted by the market.

Separator thickness, porosity, permeability, toughness, and resistance to penetration can considerably vary depending on desired cell properties. For example, one way to increase the capacity and rate capability of a cell design, is to select a thinner separator thus including more electrode material in a given, fixed, cell case. However, this strategy can also lead to cell failures, as thinner separators can be more susceptible to damage. For commercial cells, separators are typically around 20 μm thick, although thinner (approximately 10 μm) and thicker separators can also be found (even > 40 μm) [4].

1.1.6 Cell formation – SEI formation

At typical cell voltages, mixtures of lithiated graphite (or Li metal) and organic electrolyte are not thermodynamically stable. The reactions between them will occur at their interphase and produce a passivation layer on the negative electrode which is commonly referred to as the solid electrolyte interphase (SEI) and some gases that result from breakdown of the electrolyte (short chain hydrocarbons,...) [53].

Therefore, during cell manufacturing after cell assembly, the cell is slowly charged (and possibly repeatedly cycled and aged) at particular conditions of temperature. This process is called “cell formation” [54]. This formation process is designed to produce a uniform and stable effective SEI layer on the cell negative electrode [4].

The SEI layer covers the graphite surfaces and shields Li^+ from the electrolyte solution, which prevents further electrolyte decomposition. During charging, the solvated Li^+ ions arrive at the negative electrode. At the solid electrolyte interphase (SEI) they strip off their solvation shell, travel through the SEI, and intercalate into graphite or they deposit on the surface.

This shielding property of SEI enables reversible capacity during extended charge / discharge cycling. SEI formation mainly depends on:

- Electrolyte mixture (salt, solvent, additives) and electrode technologies (surface chemistry, structure, morphology);
- Conditions of cell formation process.

SEI compositions and morphologies are complicated and differ depending on graphite surface properties, electrolyte, and formation conditions [55, 56]. According to the importance of the SEI, the identification of the compounds of SEI formed on the surface of carbon/graphite were the topic of numerous dedicated studies and reviews: a compilation of known compounds to date, adapted from [56–60] is presented in Table 3.

Table 3: Known chemical compounds formed on the carbon/graphite SEI layers surface [56–60].

Component	Present	Not present	Notes
(CH ₂ OCO ₂ Li) ₂ ROCO ₂ Li			Being a two electron reduction product of EC; it is found mostly in the SEI formed in EC based electrolytes. They are present in the outer layer of the SEI. They occur in most PC containing electrolytes, especially when the concentration of PC in the electrolyte is high.
Li ₂ CO ₃			It may also appear as a reaction product of semicarbonates with HF, water, or CO ₂ .
ROLi			Most commonly found in the SEI formed in ether electrolytes like tetrahydrofuran (THF), but may also appear as DMC or ethyl methyl carbonate (EMC) reduction product. It is soluble and may undergo further reactions.
LiF			Mostly found in electrolytes comprising of fluorinated salts like LiAsF ₆ , LiPF ₆ , LiBF ₄ . It is a major salt reduction product. HF contaminant also reacts with semicarbonates to give LiF byproduct. Amount of LiF increases during storage.
Li ₂ O			It may be a degradation product of Li ₂ CO ₃ during Ar ⁺ sputtering in the XPS experiment.
Polycarbonate LiOH Li ₂ C ₂ O ₄			Present in the outermost layer of the SEI, close to the electrolyte phase. This part imparts flexibility to the SEI. It is mainly formed due to water contamination. It may also result from reaction of Li ₂ O with water or with aging. It is found to be present in 18,650 cells assembled in Argonne National Laboratory containing 1.2 M LiPF ₆ in EC:EMC (3:7) electrolyte. Li carboxylate and Li methoxide were also found in their SEI.
HF			It is formed from decomposition LiPF ₆ and the water in the solvents. It is highly toxic and can attack components of the cell.

As a consequence, cell capacity is reduced with SEI layer formation [53, 61] because SEI formation is an exothermic process that consumes Li atoms. This results in first-cycle irreversible capacity and Li inventory losses. An effective SEI is formed when graphite can be cycled in a stable manner by preventing solvent reduction during cycling, solvent co-intercalation and graphite exfoliation. Therefore, effective SEI layer is required to be:

- Electronically insulating,
- Conducting (permeable) for Li⁺,
- Impermeable for solvated Li⁺.

1.1.7 Novel generation of Li-ion battery with a focus on Ni-rich Li-ion technologies

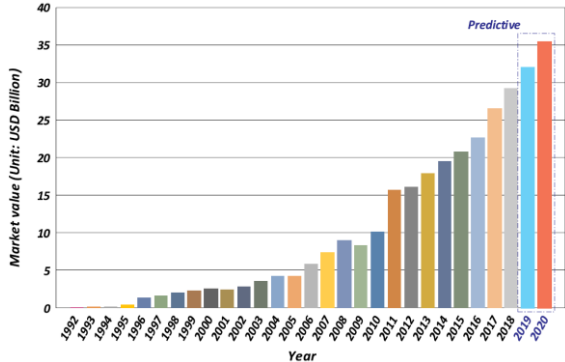


Figure 10: Lithium-ion batteries’ world market value from 1992 to 2020. [62]

With the development and promotion of clean, renewable, and distributed energy technologies, the worldwide market value of the lithium-ion battery is growing rapidly every year [62], with statistics from 1992 to 2020 demonstrated in Figure 10.

To meet the rapidly increased demand of LIBs for wide range of applications, the market is focusing on Ni-rich technologies. In this section, we are talking about Ni-rich chemistries for large scale applications such as in automotive industry, in stationary energy storage systems. It should be noted that even though a battery chemistry may work in electronic devices (cell phones, laptops), it does not mean they can always be scaled up for use in larger applications as proven in the Figure 11.

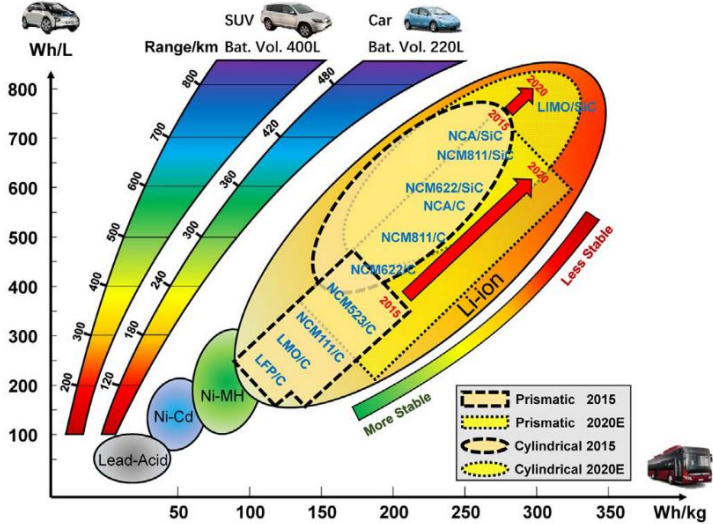


Figure 11: Short and long term R&D strategies. The roadmap of the LIBs for pure electric vehicle: the demand of longer range and the potential of less thermal stable materials [3]

1.1.7.1 Selected technologies of positive electrodes: Ni-rich high energy technologies

For decades, NMC111 was the most widely used positive electrode material for large scale applications [13]. However, NMC111 shows a capacity of 160-170 mAh/g (depending on the cell voltage) which cannot fulfil the requirements for future applications that require higher energy density and correspondingly higher capacity. Moreover, researchers also make efforts in engineering less Co in the active materials. To achieve this, the so-called Ni-rich high energy Li-ion battery technologies, with higher proportion of Ni in the active materials of positive electrodes, e.g., NCA, Ni-rich NMC family ($\text{LiNi}_x\text{Co}_y\text{Mn}_z\text{O}_2$), are regarded as the solution [13]. However, as Ni content increases, safety and longevity decreases in case of Ni-rich NMCs family and also NCA.

Ni-rich NMCs family

Mixing Ni (higher capacity), Co (better rate capability) and Mn (good thermal stability) is beneficial [63]. Ni ions contribute to the majority of capacity through the $\text{Ni}^{2+}/\text{Ni}^{3+}$ and $\text{Ni}^{3+}/\text{Ni}^{4+}$ redox couples, Co ions suppress Ni/Li cationic mixing in the synthesis and cycling while increasing rate capability, and Mn ions stabilize the structure and enhance thermal stability by remaining at Mn^{4+} valence to act as a structural stabilizer [64, 65].

However, the optimal mix is still debatable and scientists need to overcome some major technological problems to optimize the combined characteristics that make these technologies attractive while mitigating the negative properties. As illustrated in the Figure 12, the magnitude of these combined problems is difficult to overcome, making the scale-up process from NMC532→NMC811 risky.

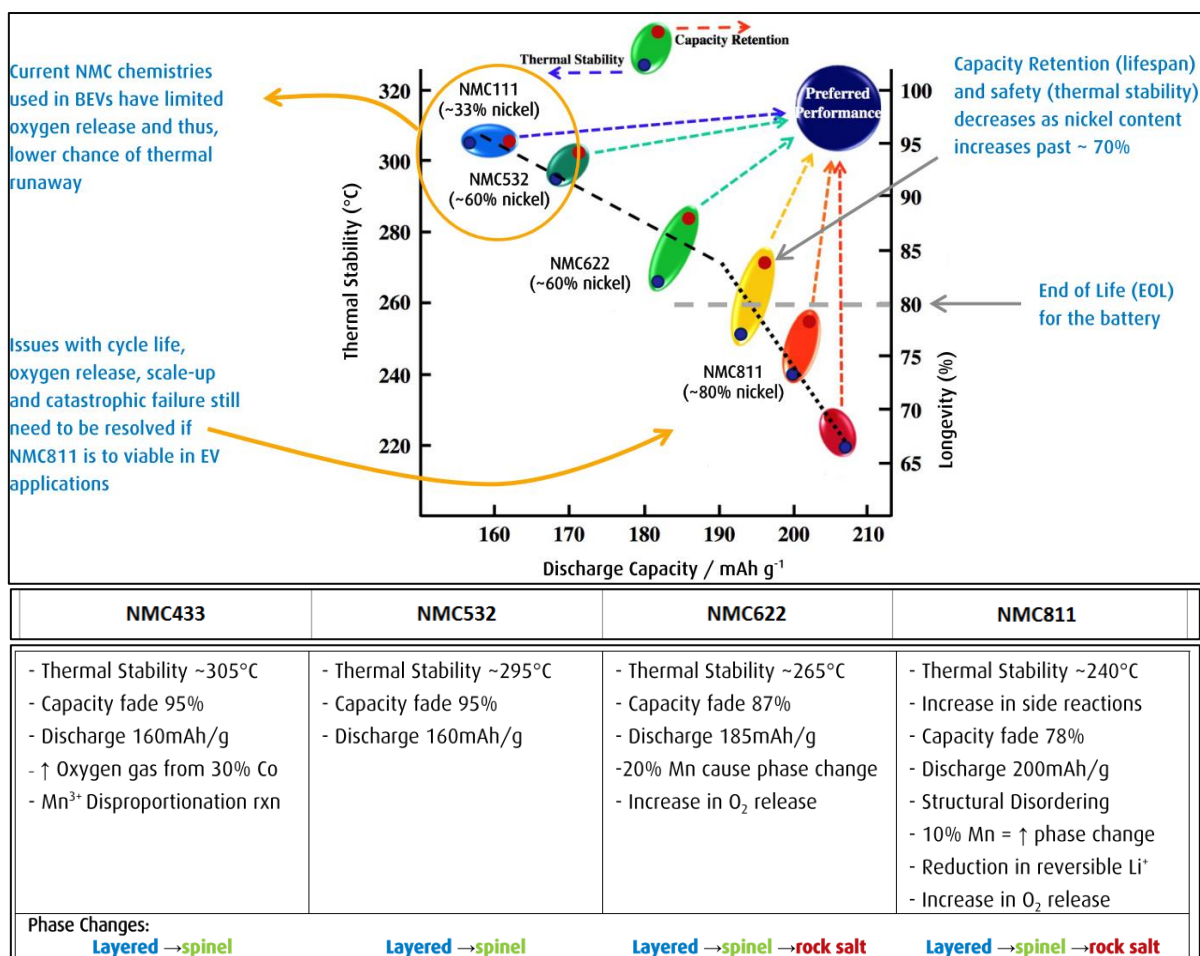


Figure 12: Comparison of electrochemical properties, operation constraints (top) and thermal stability vs Capacity retention of different layered delithiated NMCs [13, 66], adapted by [63].

Apart from inferior cycling stability [64] and gas generation [67] (more details in 2.2.2.3), as we can see that Ni-rich NMCs also shows very low thermal stability [13, 66], NMC811 ($\text{LiNi}_{0.8}\text{Mn}_{0.1}\text{Co}_{0.1}\text{O}_2$) was surprisingly absent from many of the discussions and presentations and there was a scientific consensus that NMC 532/622 may be possibly the limit for this technology. However, NMC811 technologies were recently commercialized on the market which is sooner than we expected. With very high content of Ni, safety is critically the major technological problems of NMC811.

NCA

Among the various Ni-based layered oxide systems in the form of $\text{Li}[\text{Ni}_x\text{Co}_y\text{Al}_z]\text{O}_2$, the compositions with $x \geq 0.8$, $y = 0.1 - 0.15$, and $z = 0.05$ are the most successful and

commercialized positive electrodes used in EVs, e.g., the battery cell in Tesla Model S [3]. Adding Al makes this technology much more stable for fast charging but does not stop the phase change that occurs in Ni-rich chemistries because the phase change issue is managed or eliminated by Mn and the amount of O₂ gas generation is still a problem in NCA chemistry.

However, Al-doping (~5 %) is also responsible for the increased capacity retention because it stabilizes the crystal structure meaning that vehicle range is increased. Al also improves cyclability by decreasing the Co dissolution at high voltage enabling the use of a supercharger if the depth of discharge is controlled around 10 – 70 % (in reality, that range may be tighter) as micro-cracks form and the phase change to the NiO-type rock salt is accelerated if the battery pack was fully charged/discharged.

1.1.7.2 Selected technologies of negative electrodes: Graphite-SiO_x composites (+ amorphous carbon)

This novel technology was found in the commercialized studied cells by our analysis for both NCA and Ni-rich NMCs positive electrode technologies. The main advantages of graphite-SiO_x composites are:

- To combine the cycling stability of graphite with the high capacity of Si [30];
- To increase the average potential of the negative electrode → The electrode potential characteristics are a superposition of the Si and graphite materials [68];
- Higher capacity than graphite;
- Better cycling stability than pure Si.

Of course these composites also have constraints and limitations:

- The addition of silicon also introduces a large potential hysteresis between the charge and discharge cycles. It leads to a large difference in measured impedance at a given voltage between charge and discharge. However, it is also important to note that the impedance rise on cycling mainly arises at the positive electrode. The contribution of the C or SiO_x-C negative electrode to the impedance rise is small [68];
- Usually leads to higher irreversible capacity loss than graphite.

In conclusion, this technology makes it possible for 18650 Ni-rich cells to reach > 3 Ah capacity. Some first composites with few % of Si (or SiO_x) are commercialized: Samsung SDI INR18650-35E (3.5 Ah), Panasonic NCR18650GA (3.45 Ah), LG Chem INR18650MJ1 (3.5Ah).

1.2 Aging of Li-ion batteries

Aging and their impact on Thermal runaway will be explored in this section. This is considered as the inherent safety issues inside Li-ion cell.

1.2.1 Definitions and overview of mechanisms

All secondary batteries degrade inevitably over time and with usage. This degradation is manifested as a loss of available capacity, energy and an increase in impedance, thereby, reduction of power (rate capability) and efficiency. These symptoms are intertwined in a reciprocal relationship.

Due to their comparably high cost, the degradation of Li-ion batteries has been extensively studied over the past two decades.

Many physical and chemical processes contribute to battery degradation. Although the aging mechanisms undoubtedly are complex and with rates strongly related to operating conditions [3, 6, 15], they can be divided into a few categories:

- Loss of active and accessible electrode material (LAM),
- Loss of Li inventory (LLI),
- Loss of conductivity (CL) in electrodes or electrolyte,

An example of the overview of the most commonly studied aging mechanisms on cell level shown on Figure 13.

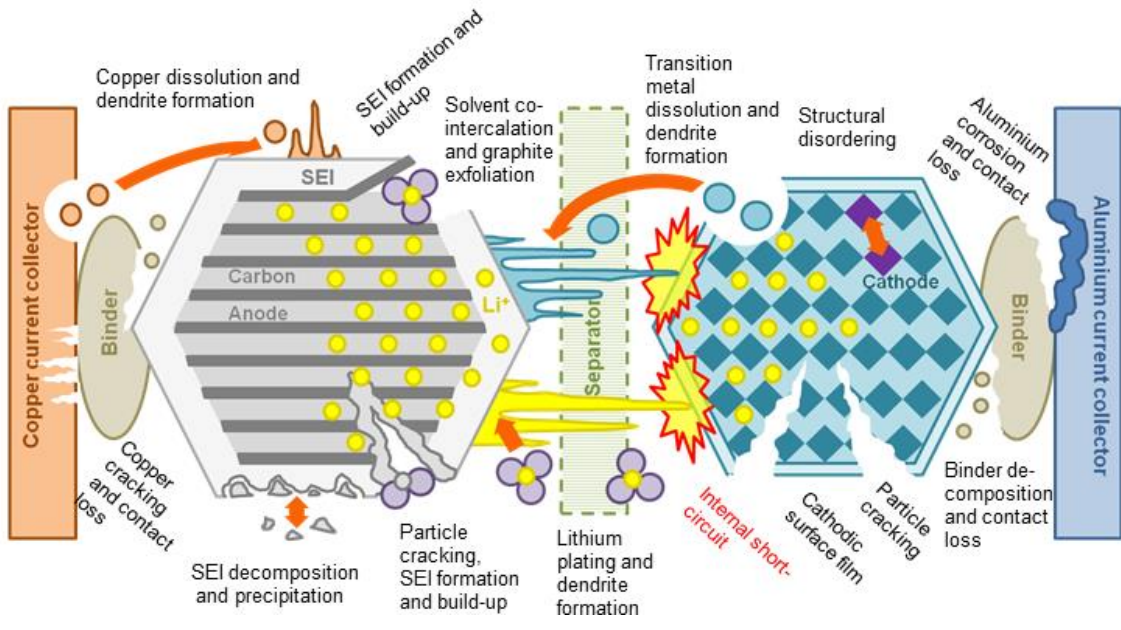


Figure 13: The most commonly studied aging mechanisms on cell level [69].

Depending on the combinations of operating conditions one or a few aging mechanisms may dominate the overall degradation (Figure 14). In the scope of this research, SEI evolution and Li plating are 2 main mechanisms studied.

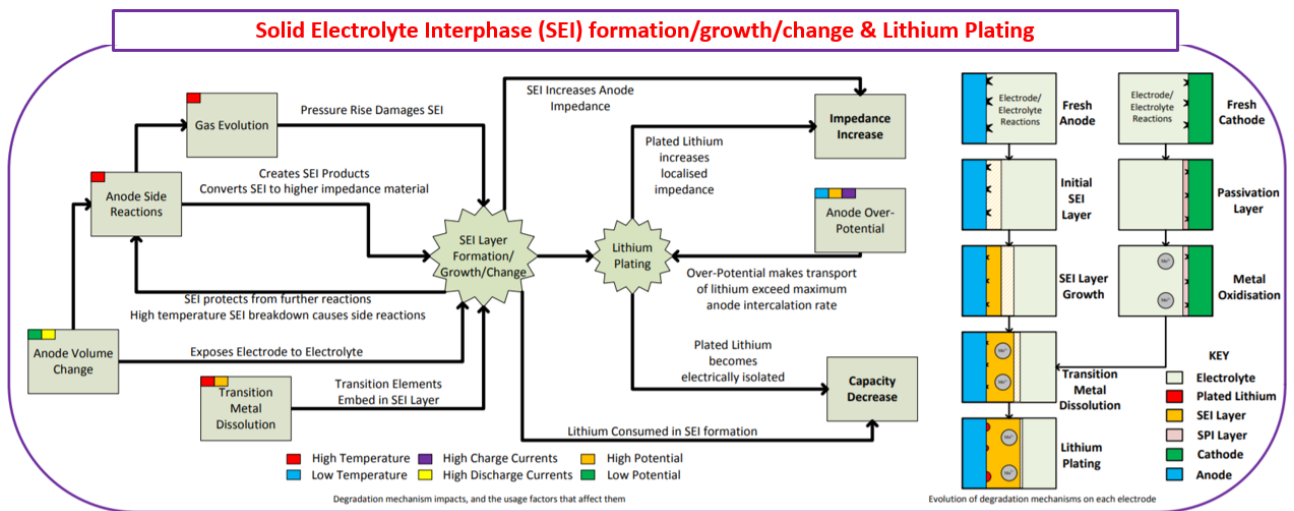


Figure 14: SEI evolution and Li Plating interconnected degradation mechanisms and the factors that affect them [61].

1.2.2 SEI growth

During cell aging, capacity is further reduced with SEI layer growth [61] because SEI formation is an exothermic process that consumes Li stored within active materials. While the presence of the effective SEI is vital, as seen in previous section, it is difficult to control its growth, as it depends on several factors during usage. An ineffective SEI usually forms during cell aging, especially cycling, with poor conductivity or being rapidly growing. The ineffective SEI growth increases impedance of electrode and limits rate capability, thereby has a strong negative effect on cell and can accelerate aging.

Following Arrhenius behaviour, as temperature increases, the reaction rates between the electrolyte and lithiated carbon exponentially increase. It is also important to note that the gases produced of SEI evolution are usually flammable. Gas generation from these reactions are similar to those responsible for SEI-formation [4]. Therefore, with increased ambient temperatures, cell capacity fading and internal impedance growth accelerates due to the growth of SEI layer.

1.2.2.1 Calendar aging

Calendar aging is an important factor in many applications of Li-ion batteries where the operation periods are substantially shorter than the idle intervals, such as in electric vehicles [70]. Including all aging processes that lead to a degradation of a battery cell independent of charge-discharge cycling, it is found to decrease cell capacity linearly with time and shows a faster decrease at higher storage temperatures [71]. The predominant mechanism of calendar aging is the growth of passivation layers which all consume cyclable Li as a result of electrolyte decomposition, i.e., reduction at the negative electrode interphase (SEI growth) and oxidation at the positive electrode interface.

For Li-ion cells with graphite negative electrodes and transition-metal-layered positive electrodes, the growth of SEI at the negative electrode interphase can be additionally catalysed by dissolved transition-metal ions from the positive electrode, such as Mn_{2+} in case of LMO, which can reduce to metals at the negative electrode [70]. As these are the main drivers of calendar aging, SEI growth is generally responsible for the Li loss and impedance rising is associated to the passivation layer at the positive electrode [72]. The

reconstruction of the differential voltage spectra of aged cells with the half-cell profiles of negative electrode and positive electrode has indicated that there is very minor positive electrode degradation. Thus, the loss of cyclable Li due to SEI growth can be confirmed as the major cause of capacity fade due to calendar aging [70]. SEI growth in this case depends solely on the graphite potential and not on the thickness of the graphite electrode [70]. Thus, the accelerated capacity fade above the central graphite peak is attributed to the lower negative electrode potential, which aggravates electrolyte reduction and, thus, promotes SEI growth [70] [53] [73].

Researchers commonly assumed that continuously accelerated calendar aging is correlated with an increase of the storage SOC and temperature. Keil *et al.* [70] has investigated more deeply about this correlation as shown in Figure 15 for NMC and NCA technologies:

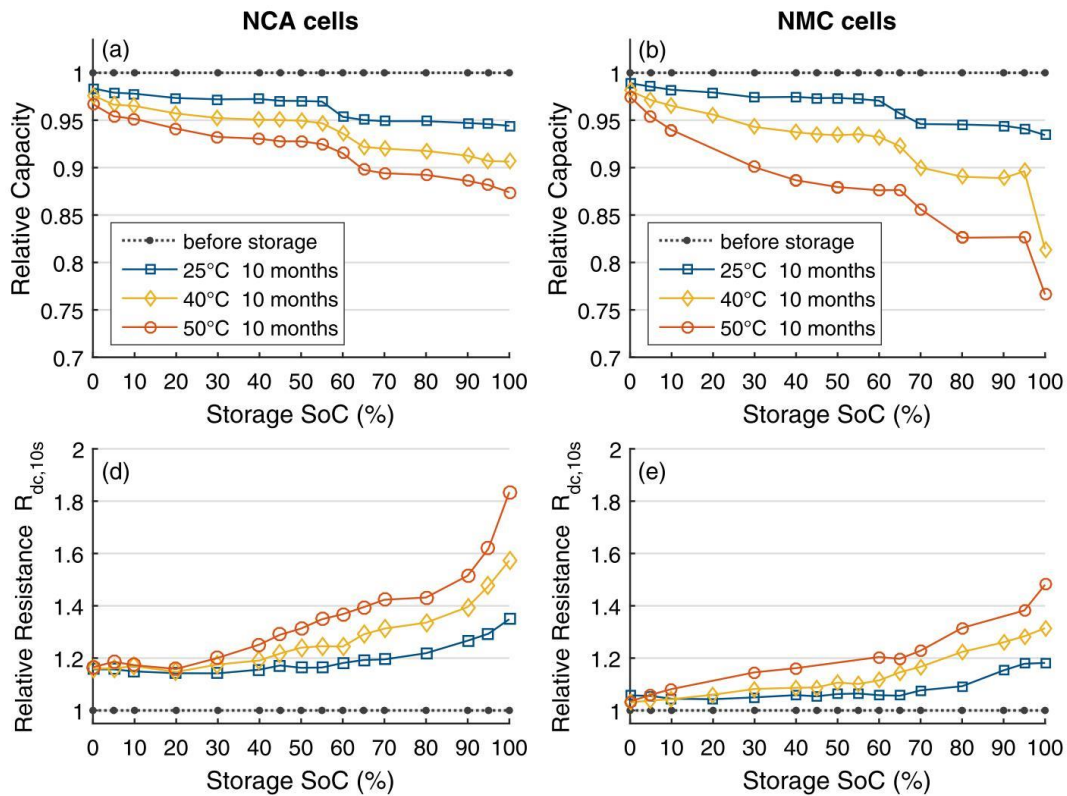


Figure 15: Calendar aging after 9–10 months of storage at various SOC and different temperatures: (a-b) capacity fade; (d-e) rise of internal resistances [70]

All the tested cells exhibit an increased calendar aging with higher storage temperature. For the NCA and NMC cells, resistances generally increase with higher storage SOC. For the NCA

cells, the capacity fade increases notably and the resistance increase accelerates substantially above 90 % SOC, where the capacity fade only slightly increases. Overall, the rate of capacity decrease is significantly higher for cells stored at 100 % SOC [70][71].

The degradation owing to calendar aging can also be predominant in cycle aging studies, especially when cycle depths and current rates are low [70].

1.2.2.2 Cycling aging

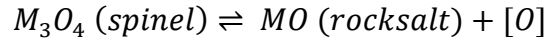
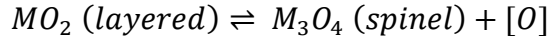
Graphite exhibits volume expansion /contraction during lithiation / delithiation of 5 % – 10 %. Several researchers have suggested that SEI cracks and SEI reformation due to these volume changes of the graphite negative electrode during cycling operations are the major cause of Li consumption. Graphite negative electrodes exhibit a largely linear expansion from 0 % to 25 % lithiation SOC, only minor volume changes between 25 % and 50 % lithiation SOC, and another linear expansion above 50 % lithiation SOC, where the LiC_6 phase formation begins.

To avoid cracking of SEI layers due to stress from the volume changes mentioned above, the SEI layer should be physically strong or flexible enough to accommodate the volume change of the negative electrode during the cycling process [56]. Osswald *et al.* found that higher temperatures and higher currents lead to stronger SOC inhomogeneities inside the cell [10] and also higher self-heating, especially during charging.

Most Li-ion cells are not designed to be cycled or stored above approximately 60 °C. It is also important to note that at the same C-rate, the heat release during the charging process is always greater than that during discharging process. [74]

Cycling aging of Ni-rich NMC / Graphite-SiOx technologies

As mentioned in 1.1.5.2, Ni-rich NMCs such as NMC622 and NMC811 show higher capacity yet with the trade-off of decreasing cycling stability (capacity fade and impedance increase) [75, 76]. As the concentration of Ni increases, more Ni ions at higher oxidation states (Ni^{3+} and Ni^{4+}) are unstable and tend to react with the electrolyte, leading to oxygen release and phase transition [75]. In the thermodynamic view, the oxygen evolution caused by the oxidation of lattice oxygen can be understood by these chemical equilibriums [64]:



Note that M represents Ni, Mn, Co and [O] represents active oxygen intermediates.

The [O] may combine into the oxygen molecules (O_2 formation) or simultaneously reacts with the electrolyte solvents, resulting in gas generation (O_2, CO_2, CO, \dots) and an increase in cell's impedance [64]. Furthermore, due to the similarity in ionic radius between the Ni^{2+} (0.69 Å) and Li^+ (0.76 Å), the Ni^{2+} have the strongest tendency to migrate into the Li^+ layer and occupy the position of Li^+ , thereby, reduce the capacity and the mobility of Li^+ . This Ni/Li mixing occurs over the whole life of the battery, however, its degree increases with the Ni content, SOC and temperature, especially during the Thermal runaway. As a consequence, this loss of O and Li leads to the irreversible layered-spinel-rocksalt phase transition [77], lowers the average valence of transition metal ions and NMC active particles cracking, resulting in a decrease of operating voltage and specific capacity of Ni-rich NMC positive electrodes. It is noteworthy that this might occur similarly for NCA technology.

To understand the cell capacity fading and electrodes aging behaviour during cycling conditions, Li *et al.* [75] have investigated the cycling aging of LG MJ1 18650 battery (NMC811/ Graphite-SiOx) by using the dV/dQ analysis (as shown in Figure 16). The dV/dQ curve of the full cell exhibits 3 peaks, the authors claimed that the first 2 peaks reveal the signatures from the Ni-rich NMC positive electrode while the last peak is contributed from the Graphite-SiOx negative electrode. Therefore, the distance between the first two peaks (Q_{AB}) can be used to quantify the change of positive electrode capacity, while the change of negative electrode capacity can be estimated from the evolution of the width of the third peak (Q_{CD}). The loss of Li^+ inventory in the cell can be generally represented by the voltage offset between the 2 electrode potential curves.

For example, as observed in Figure 16, Q_{AB} and Q_{CD} both degraded as the cell aged, indicating that the loss of active material happened to both electrodes. After 250 cycles, the positive electrode showed 7.5% capacity loss, as Q_{AB} decreased to 92.5% of its original value, while the capacity retention of the negative electrode was 86.0%. Q_{BC} decreased to 88.1%,

demonstrating 11.9% Li^+ inventory loss. Therefore, the capacity loss contributed from the positive active material loss is slightly smaller than that of the negative active material and Li^+ loss. [75]

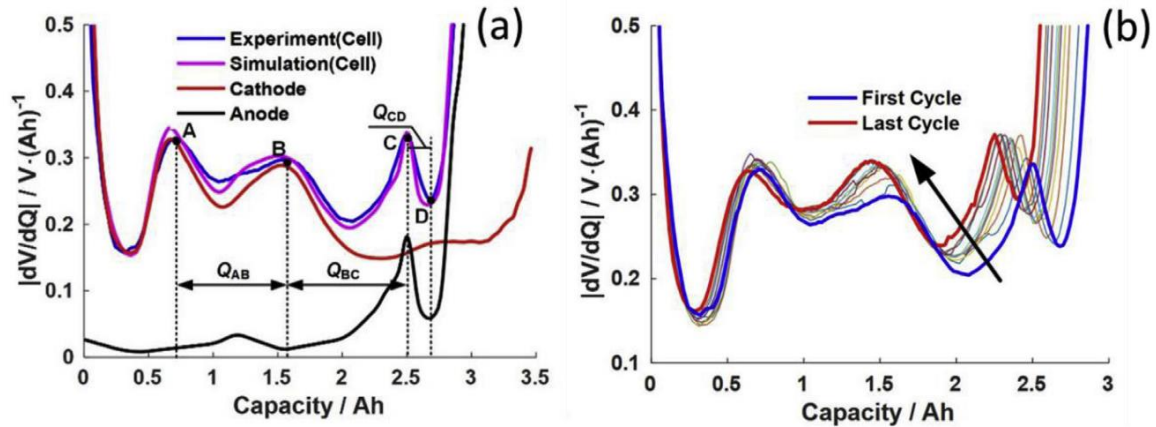


Figure 16: Degradation analysis of the cell based on dV/dQ analysis. (a) dV/dQ analysis of discharge voltage curves for the fresh cell; (b) evolution of the dV/dQ of discharge voltage curves during the aging process. [75]

After cycling, using Post-Mortem analysis (PM), the authors found that the morphology of both electrodes changed:

On the negative electrode, cracks appeared across the whole electrode. They confirmed that this is mainly caused by the Si volume fluctuation during repeated lithiation/ delithiation cycles. Cracks started from and extended to where Si particles aggregate [75]. This eventually led to the thickening of SEI and reduces contact among active material particles, the current collector, and the electrolyte. Moreover, the average fluorine ratio, indicator of SEI destruction/growth and loss of Li^+ inventory, was more than doubled after cycling. [69, 75] This increase cell impedance and decrease cell capacity. The impact of Si is well observed here. Even a small amount of Si (~5% by mass) in the graphite can accelerate capacity fading because the huge volume fluctuation of Si particles. [75]

On the positive electrode, micro-cracks appeared on cycled positive electrode which would result in higher porosity, higher active surface area and leading to more side reactions on the positive electrode [75, 78], resulting in the increase of voltage hysteresis after cycling, suggesting that the electrode impedance increased. However, they observed no new

plateaus in the voltage profiles of half-cell positive electrode occurred after cycling. Interestingly, they found that the positive electrode resistance growth dominates that of the negative electrode [75].

1.2.3 Li deposition/plating

This topic was investigated by literature research on different Li-ion technologies, including commercial state-of-the-art cells. It is a complex topic which is connected to many factors like cycle stability, safety, fast charging capability, and in-homogeneities inside Li-ion cells.

1.2.3.1 Mechanisms during charging

During charging of Li-ion cells, Li^+ ions are de-intercalated from the positive electrode and transferred through the electrolyte to the negative electrode. On the negative electrode side, intercalation of Li^+ ions into the graphite particles is the preferred reaction path. However, charging can also lead to an additional reaction of Li deposition on the negative electrode side.

On the atomic scale:

The kinetic cause for Li deposition is diffusion over-potential. This can be explained by the balance of negative electrode kinetics (barriers for charge transfer and solid diffusion) and the arriving amount of Li^+ ions (charging current) on the negative electrode surface (Figure 17).

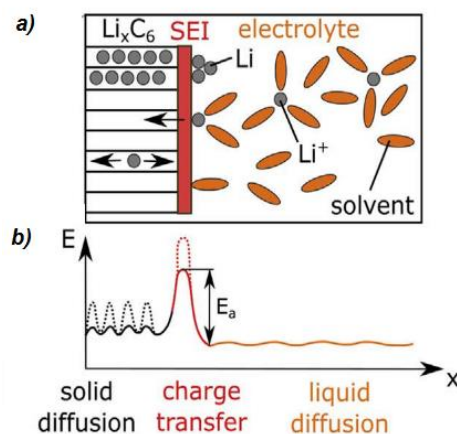


Figure 17: a) Atomic model for Li intercalation and deposition, b) involved energy barriers

[10]

The liquid diffusion is usually low in the liquid phase. However, the charge transfer barrier E_a between liquid and solid phase for de-solvation and moving Li into the graphite lattice is usually much higher and in the range of 0.3–0.7eV for the edge plane and ~ 10 eV for basal plane (transport through the SEI and electron transfer included) [10].

The solid diffusion of inserted Li between the graphene planes of graphite is limited by energy barriers in the range of 0.22–0.36eV [10]. Persson *et al.* [79] found that the intercalation kinetics are slowed down with higher SOC because this solid diffusion barrier is increased by x in Li_xC_6 . This is consistent with macroscopic measurements that show lower negative electrode potentials vs Li/Li⁺ for higher SOC levels [10].

→ The negative electrode potential is decreased during charging with increasing SOC.

Even though the energy barrier itself is not changed by the temperature, the probability to overcome the barrier gets lower with decreasing temperature according to the Arrhenius law. Therefore, lower temperatures slow down the charge transfer probability and the solid diffusion of Li on graphite. In this case, Li deposition on the negative electrode surface is more favoured compared with intercalation of Li into the graphite. It is important to note that lower temperatures also slow down the reaction of deposited Li with electrolyte. The experiments on macroscopic scale and simulations on the microscopic scale also showed that the negative electrode potential gets lower with decreasing temperature [10].

→ The negative electrode potential gets lower with decreasing temperature.

The diffusion of intercalated Li from the surface of a graphite particle to its inside is driven by concentration gradients. Therefore, in the cases of higher charging C-rates (higher charging current densities) on the macroscopic scale, the ion flux of Li per negative electrode area on the atomic scale is eventually higher. This can lead to Li deposition, especially when the diffusion is slow (at low temperatures, high SOC, or in materials with high energy barriers).

→ The negative electrode potential decreases with higher charging C-rate and consequently leads to Li deposition above a certain threshold value [10]. Higher charging rates were found to lead to the formation of small Li dendrites. In contrast, smaller charging rates provoke the forming of less dendritic but larger deposited Li [80].

On the microscopic scale:

This aging mechanism concerns the transport of Li^+ ions in the pores of the negative electrode and the transport of electrons from the particles involved in an intercalation to the current collector. Therefore, Li deposition is affected by the porosity and tortuosity properties of the negative electrode active material [10].

On the macroscopic scale:

The insertion potential of Li into graphite is in the range of 200 to 65 mV vs Li/Li^+ while the potential for Li deposition on the graphite negative electrodes is below 0 V vs Li/Li^+ , therefore, thermodynamically, Li deposition is not a competitive reaction to Li insertion. However, it is difficult to separate these over-potentials experimentally. In simulations, it is usually assumed that the kinetic condition for Li deposition is when the sum of the equilibrium potential and the over-potential get negative vs Li/Li^+ [10].

In conclusion, Li deposition is more likely with decreasing temperature, increasing SOC and increasing charging C-rate. The interplay of these main operating parameters decides if Li deposition happens or not. For example:

- Low temperatures do not lead to Li deposition in all cases, however, if certain limits of SOC and/or charging C-rate are exceeded. At low temperatures, the Li deposition might be suppressed/minimized by low charging currents or by self-heating of batteries;
- A cell might be charged by high currents at low SOC and later by lower currents without Li deposition.

1.2.3.2 Mechanisms during discharging

Discharging leads to de-intercalation and stripping of deposited Li [10].

Stripping process of Li: during the stripping process a part of the deposited Li can lose electrical contact to the negative electrode, which is then called 'dead Li' as illustrated in Figure 18:

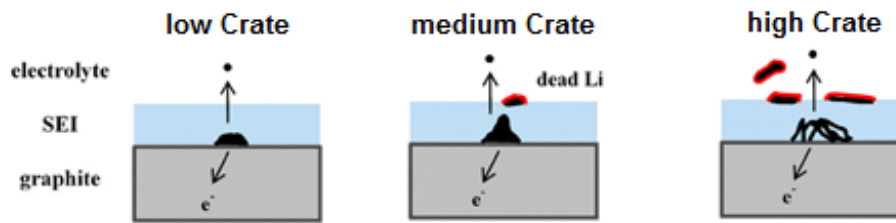


Figure 18: Li stripping and formation of “dead Li” under different C-rates [80]

Formation of dead Li strongly depends on the C-rate discharge. Dead Li in combination with Li that has reacted with electrolyte are often the main sources for capacity loss when Li deposition is involved in the aging mechanism [10].

1.2.3.3 Morphologies of Li deposition and gradients in Li-ion cells

The term ‘Li plating’ stands for a homogeneous film covering a surface and is often used in literature on Li-ion cells for Li deposition without knowing if the deposited Li film is homogeneous or not. However, recent studies have revealed that Li metal can be deposited in different macroscopic morphologies (Figure 19):

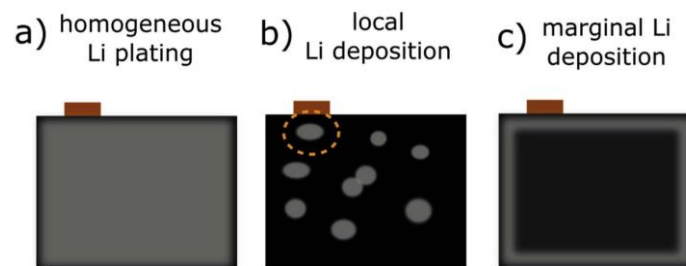


Figure 19: Electrode surface morphologies of Li deposition often observed in Li-ion cells.

[10]

Since Li deposition depends on temperature, SOC, and the charging current, it will get inhomogeneous if gradients of these parameters develop in a cell during each charging and during aging. Lower local temperatures, higher local SOC levels, and higher local current densities are likely to lead to local Li deposition [10]. This explains why on the cell scale, it is experimentally observed that Li deposition can happen as a reaction in parallel to intercalation. Such effects can lead to a variety of macroscopic morphologies for Li deposition, including:

+ Homogeneous Li deposition (Li plating)

The majority of Li plating is located on the negative electrode surface, i.e. between negative electrode and separator. However, Li deposition can partly spread ($\sim 10 \mu\text{m}$) into the bulk of negative electrodes and therefore partly adds up to thickness of the negative electrodes.

For all cell types, the more homogeneous utilization of a cell during charging at low temperatures contributes to the more homogeneous appearance of Li plating [10, 81].

+ Local Li deposition

The Li is located at different random positions on the negative electrode and in the separator (near the current collector). This type of aging usually leads to the formation of a thick SEI layer by electrolyte decomposition, drying of the cell, and possibly to gas formation.

Furthermore, local Li deposition leads to a local thickness increase of the negative electrode and thus increases the inhomogeneity in Li-ion cells. Local inhomogeneities are likely to lead to further Li deposition effects due to locally negative electrode potentials. This type of morphology was observed by different groups [82–85] and with different cell types after cycling at high temperatures ($> 45 \text{ }^\circ\text{C}$) and high charging C-rates due to local formation of gas bubbles or SEI growth and clogging of pores at high temperatures.

For 18650 cells, Bach *et al.* [86] found that local Li deposition starts in unevenly compressed areas of the “jelly roll”.

+ Marginal Li deposition

The Li deposits around the edge area of the negative electrode because the current density at the edge of electrodes can be significantly increased. This effect can be reduced by extending the area of the negative electrode compared to the positive electrode (‘negative electrode overhang’). Additional reasons could be lower temperatures at the edges of the cell or a different coating thickness at the edge of the negative electrode.

Temperature inhomogeneity is well-known in case of cylindrical cells: The temperature inside the core is typically higher than on the cell housing during charging and discharging. The main reason is most likely the low heat conductivity in the radial direction of cylindrical cells since the heat has to be conducted through many layers of negative electrodes, positive

electrodes, and separators. In contrast, the temperature gradients on the cell surface of cylindrical cells are much weaker, due to the high thermal conductivity of the electrode collectors housing materials (steel, Al). The different temperatures in the core of the jelly roll and on the cell housing most likely result in differences in the negative electrode potential in maximum temperature during long-term cycling and lead to the observed difference in Li plating thickness [10].

Osswald *et al.* [87] reported that lower ambient temperatures lead to a stronger radial temperature gradient. This effect is counteracting the effect of SOC and favours stronger inhomogeneities and thicker Li plating on the outer windings of the jelly roll in cylindrical cells [10]. Other inhomogeneities in the Li-ion cells can also lead to similar localized Li deposition [10].

1.2.3.4 Degradation effects caused by Li deposition

On the cell scale, Li deposition leads to capacity fade (Q), Coulombic efficiency decrease, energy fade (E), energy efficiency fade (η), and resistance increase (R_i) by 3 main mechanisms shown in Figure 20.

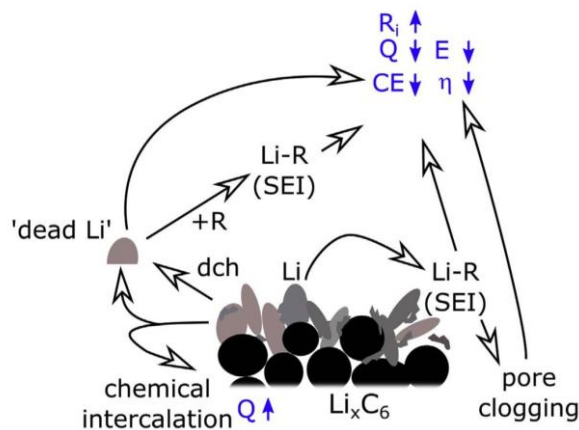


Figure 20: Aging mechanisms related to Li deposition in Li-ion cells. The arrows next to R_i , Q, E, CE, and η indicate if these values are decreased or increased [10]

- 1) Li metal can react with electrolyte (R) forming SEI (R-Li). This can lead to pore clogging, which lowers the negative electrode kinetics and therefore increases the probability of Li deposition.

2) Chemical intercalation of Li into graphite and Li stripping can promote the formation of electrically disconnected 'dead Li' which directly leads to the macroscopic degradation effects listed above.

3) Additionally, SEI can also form on the surface of dead Li, leading to the same results.

Even though chemical intercalation can lead to a partial recovery of the capacity during a rest time, it is clear that actions have to be taken to suppress or even avoid the occurrence of Li deposition on negative electrodes of Li-ion cells. This is possible by choosing the right combination of operating conditions, as well as further development of optimized cell designs and new negative electrode material with improved kinetics [10].

1.2.4 Methods of detection and analysis of aging

Several techniques are commonly applied and reported within the literature to identify and analyse the effects of aging. These are often classified into in-situ and ex-situ electrochemical techniques. Examples of in-situ methods are Incremental Capacity (IC) and Differential Voltage (DV), electrochemical Impedance Spectroscopy (EIS) and Differential Thermal Voltammetry (DTV).

Ex-situ methods consist of applying physicochemical and electrochemical invasive techniques to study the cells internally, mostly by post-mortem analysis such as Scanning Electron Microscopy (SEM), Energy Dispersive Spectrometry (EDS) or X-Ray Diffractometry (XRD). It is beyond the scope of this thesis to discuss deeply about these techniques. Therefore, in the following, we are only focusing on the most commonly used techniques for both the 2 target aging mechanisms studied.

1.2.4.1 SEI growth

Beside post-mortem analysis, in-situ methods such as Incremental Capacity (IC) - Differential Voltage (DV) and electrochemical Impedance Spectroscopy (EIS) are considered the most convenient and effective techniques.

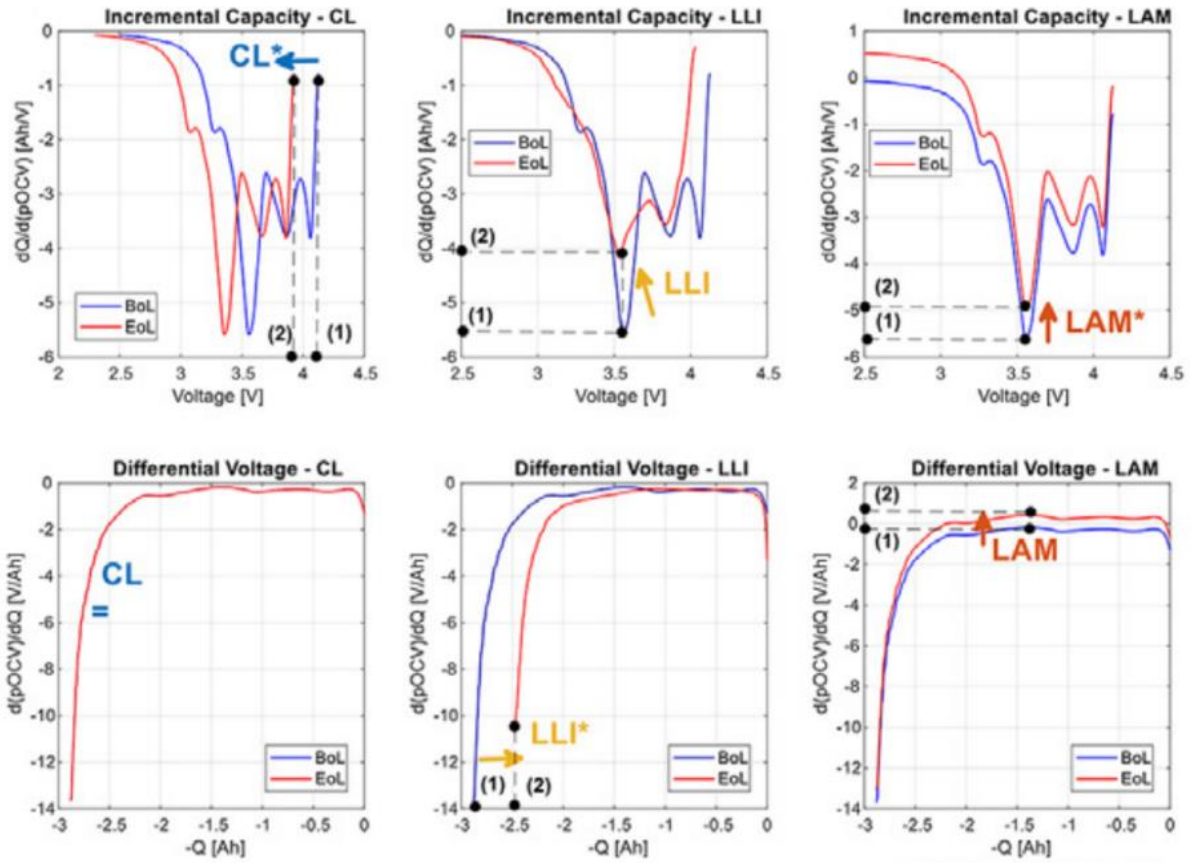


Figure 21: Identification of degradation mode using IC-DV analysis [88]

The use of these methods helps to identify the different aging mechanisms, including Conductivity Loss (CL), Loss of Lithium Inventory (LLI) and Loss of Active Materials (LAM) (Figure 21).

However, this can be misleading to some inaccuracy. Therefore, it is recommended to quantify such inaccuracy and validate the results obtained by the combination of in-situ diagnosis techniques and ex-situ post-mortem analysis such as SEM, EDS or XRD.

1.2.4.2 Li Plating

As shown in Table 4, there are many methods which give hints on Li deposition but only few to prove it indirectly or even directly.

Direct evidence of Li deposition can be proven by ^7Li NMR, XPS, semi-quantitative GD-OES depth profiling after Post-Mortem analysis of cells.

Indirect evidence of Li deposition can be proven by in-operando measurements on Li deposition carried out by Neutron scattering (by measurement of LiC_6 and LiC_{12} signals) and measurements of negative electrode potentials in full cells with a Li reference electrode, additionally to negative electrode and positive electrode.

Table 4: Methods which give hints on Li deposition. [10]

Method/principle	Limitation	Scale
Low CE	High precision devices needed	Macroscopic, cell level
Analysis of capacity fade/change of slope in Arrhenius plot	Massive Li deposition	Macroscopic, cell level
Capacity recovery	Only if Li deposition partly reversible	Macroscopic, cell level
Voltage plateau during discharge	Low T, area of Li deposition must be large enough	Macroscopic, cell level
Voltage curve shape during rest after charging	Low T, area of Li deposition must be large enough	Macroscopic, cell level
Dilation, measurement of cell thickness	Limited to pouch cells, low T, superposition with gassing possible, massive Li deposition	Macroscopic, cell level
Early exothermic reactions in ARC tests	Massive Li deposition	Macroscopic, cell level
Fire during reaction with H ₂ O	Reactivity of Li depends on its microscopic morphology and passivation	Macroscopic, electrode level
Melting point of Li, DSC	Melting point might be influenced by alloying	Macroscopic, electrode level
Dendritic structure	Microscopic morphology of Li depends on pressure in cell	Microscopic, electrode level
Neutron diffraction, LiC_6 and LiC_{12} intensities	Indirect evidence	Macroscopic, cell level
⁷ Li-NMR	Direct evidence	Microscopic, electrode level
GD-OES	Semi-quantitative evidence	Macroscopic, electrode level
XPS	Direct evidence, limited to surface particles	Microscopic, electrode level

It is clearly advised to use a reasonable combination of methods (e.g. an evidence and a hint together) to be sure about the presence or absence of Li deposition. In the scope of this research, we do not have access to the methods above. Therefore, we can only focus on the evidences from Post-Mortem analysis and the various non-destructive and destructive existing methods which are based on aging behaviour, analysis of electrochemical data, cells, electrodes. Even though most of these methods only provide hints of Li deposition, their reasonable combination can be useful for the interpretation of our results.

Non-destructive detection methods of Li deposition

The detection methods discussed below are non-destructive and give hints on Li deposition.

Hints from aging behaviour

Li deposition often leads to a comparably fast capacity, energy, and energy efficiency fade. This is generally hard to quantify in absolute numbers, however, regarding the specific cell types, the clear trend can be found that the aging rate is usually higher if Li deposition is involved. In contrast, slower aging can also be a hint for the absence of Li deposition [10].

+ Hints from Capacity fade curves:

The main mechanism of capacity loss originates from Li which cannot be extracted from the negative electrode, Li which is bound in the SEI, and Li which has been deposited on the negative electrode. For long-term cycling at different temperatures capacity fade curves can be analyzed via an Arrhenius-plot. In this type of plot, the change of the aging mechanism becomes visible because Li deposition results in faster aging with decreasing temperatures. In contrast, without Li plating aging becomes usually faster with increasing temperatures.

Under defined cycling aging conditions at low temperatures, there are 3 typical curve shapes of capacity fade (Figure 22).

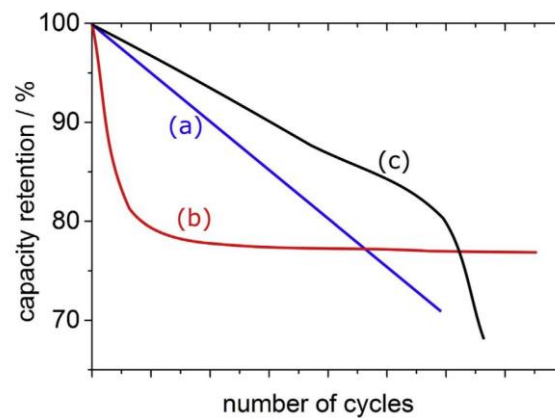


Figure 22: Typical curve shapes for the capacity fade of commercial Li-ion cells when Li deposition is involved. a) linear, b) decelerated, c) accelerated decrease [10]

- Linear capacity fade means that in each cycle, the same amount of Li is irreversibly consumed. However, it cannot indicate if Li deposition is involved or not;
- Decelerated capacity fade means that capacity fade curves getting more flat with cycling, usually at low temperature. In these cases, the main source for capacity loss is the loss of cyclable Li and that the last intercalation stage is not reached anymore. This means that less (or even no) Li is deposited in later cycles and therefore the capacity fade is decelerated;
- Accelerated capacity fade starts after a certain number of cycles, often when the capacity has reached < 80% of its initial value. The sudden capacity drop may be observed for different operating conditions. It was suggested that the drop is linked to

the occurrence of Li deposition when Li deposition starts to get irreversible and that the reasons for the mechanism change might be reduced kinetics of the graphite negative electrode as a result of SEI growth and loss of graphite active material. In this case, local Li deposition starts at unevenly compressed areas and then spreads over the whole negative electrode of the cell. Li deposition is also induced by reduced negative electrode porosity which is induced by SEI growth during aging.

The latter two cases are coupled to a change of the aging mechanism. While decelerated capacity fade with cycles indicates a change from Li deposition to no or less Li deposition, accelerated capacity fade indicates the propagation of Li deposition from small areas into the whole cell.

Under calendar aging, the Arrhenius plot usually does not show a change of the aging mechanism because no charging is involved [10].

+ Hints from the Coulombic efficiency (CE)

If more capacity is charged into than discharged from a cell, the charge difference is involved in reactions apart from Li intercalation and de-intercalation [10]. High precision CE analysis is practical for the identification of side reactions in early stages of a cell, Downie *et al.* reported that CE-values in the range of 0.997–0.999 for conditions without Li deposition [89] and significantly lower CE values (0.97–0.98) were found in case of Li deposition [89]. However, one has to consider that low CE-values can of course originate also from other side reactions such as SEI growth, loss of electrical contact of active material and pore clogging.

+ Hints from the observation of capacity recovery

After cycling aging cells under Li plating conditions at low temperature, some authors observed a partly recovery of capacity during cycling [90] or rest time [9] at room temperature. This reversible effect is in the range of 8–10 % and is also an indication for previous Li deposition [10].

Hints from analysis of voltage curves

+ Hints from the high discharge voltage plateau during discharge

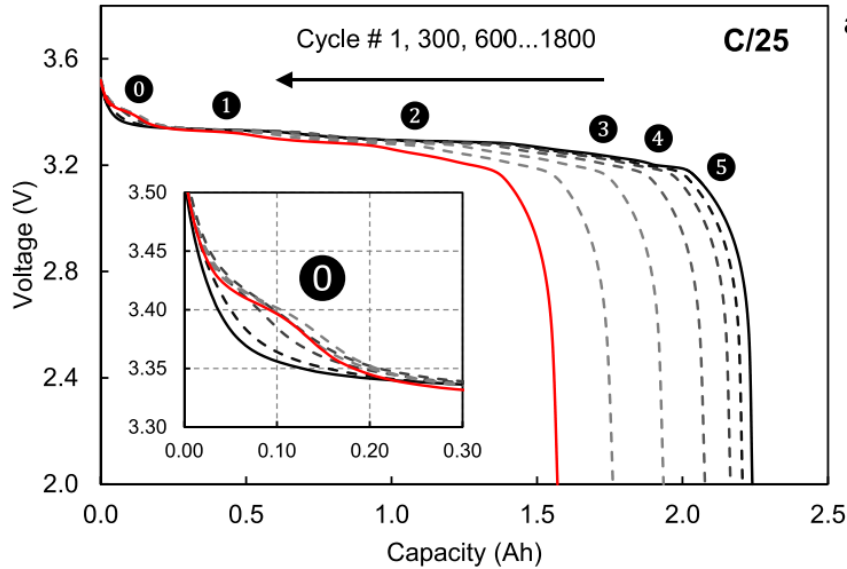


Figure 23: Evolution of C/25 discharges voltage vs. capacity curves with cycling Li plating aging. The inset panel shows a magnification of peak 0 [91].

There is a correlation between Li deposition and the plateau at high level of voltage in the discharge voltage curve after charging at low temperature, as shown in Figure 23 [91]. This plateau is caused by Li stripping and is wider for increased amounts of stripped Li. Furthermore, the amount of stripped Li can be estimated from dQ/dU and dU/dQ plots, while the latter turned out to be more practical [80]. This correlation is proven by glow discharge optical emission spectroscopy (GD-OES) depth profiling [10].

+ Hints from the curve shape of voltage relaxation after charging

Uhlmann *and al.* [81] studied the voltage relaxation after charging in half cells. They found that Li deposition influences the shape of the voltage curve during relaxation due to the mixed potential of Li_xC_6 in contact with Li. Recently, this method was transferred to full cells [92] and Von Lüdgers *et al.* [93] correlated the voltage relaxation to Li deposition by operando neutron diffraction experiments. Recently, by GD-OES depth profiling Waldmann *and al.* have proven that the voltage relaxation behaviour is directly correlated to Li plating [94] [10].

These analyses are usually applied in literature at low temperatures only because the low temperatures slow down the relaxation processes so the reversibility of partly deposited Li can be observed. In contrast, at higher temperatures ($> 25\text{ }^\circ\text{C}$) the reversibility of Li

deposition would be too fast to be observed [10]. Therefore, the features in the voltage curves indicate Li deposition and:

- In case of cells aged at low temperature, their absence might be a hint on the absence of Li deposition;
- For the cells aged at $> 25\text{ }^{\circ}\text{C}$, their absence might not be a hint on the absence of Li deposition.

These electrochemical methods discussed can give hints on Li deposition. However, localized deposition effects are hard to detect in electrochemical tests due to averaging effects. When localized Li deposition or very thin homogeneous Li films represents only small fractions of the negative electrode, it is likely that such effects are below the limit of detection for methods based on voltage curve analysis [10].

Hints from physical analysis of cells

In-operando measurements of pouch cell thickness have been carried out by several groups [10]. The cell thickness is superimposed with the thickness change of the electrodes due to intercalation and/or Li deposition and SEI growth. At high temperatures, gassing may additionally increase the cell thickness and disturb the measurement by superposition with the thickness rise by Li deposition. Therefore, thickness measurements may give useful hints on Li deposition at low temperature, however, its conclusions about Li deposition are limited [10].

Destructive methods

Hints from tests in pseudo-adiabatic condition of accelerating rate calorimetry (ARC)

In these tests, several recent researches [22, 51, 95–97] showed an early onset-of-self-heating (usually defined by a self-heating rate $> 0.02\text{ }^{\circ}\text{C}/\text{min}$) if Li deposition was present [10]. In these tests, the cells were cycled at low temperatures ($-10\text{ }^{\circ}\text{C}$ and at $0\text{ }^{\circ}\text{C}$) and showed an onset-of-self-heating already in the range of $30\text{--}53\text{ }^{\circ}\text{C}$ which is in contrast with cells without Li deposition ($> 80\text{ }^{\circ}\text{C}$).

In case of exothermic reactions of Li metal with electrolyte during Thermal runaway, dendritic growth plays a role due to its high surface area but not due to internal short circuits.

It has to be considered that a rest after cycling can lead to chemical intercalation of plated Li and this can shift the onset-of-self-heating to higher temperatures, although Li metal is still present in the cell [9]. Therefore, low onset temperatures in ARC tests are a further indicator for massive Li deposition if the cells are tested directly after cycling [10].

Evidences from Post-Mortem analysis

+ Dismantling cell:

Cells are often opened in the discharged state (end of discharge voltage, SOC = 0 %) due to safety concerns. However, cells should not be deep discharged to 0 V since this lowers the probability for Li deposition to be observed. Moreover, since Li metal can chemically intercalate into neighbouring graphite particles, the rest time between the end of cycling and the disassembly should be as short as possible [10].

+ Hints from physico-chemical analysis of electrodes

Li deposition on negative electrode has been investigated with differential scanning calorimetry (DSC) and a temperature drop at around 180.5°C which corresponds to the melting point of Li [98]. Negative electrodes with Li deposition can react with H₂O forming H₂ gas. When the Li deposition is mossy, it provides enough surface area that results the reaction in fire. However, this is only an indicator and may not work with more compact Li due to its lower surface area.

Most importantly, negative electrodes with Li deposition from disassembled cells often show dendritic or mossy structures as observed by SEM [99–101] and laser microscopy [102]. Due to the dendritic growth of Li, dendritic structures on graphite negative electrodes are an indicator for Li deposition.

However, as mentioned before, the appearance of deposited Li on graphite negative electrodes of Li-ion cells is sometimes not dendritic due to mechanical compression of Li in

cell types with higher internal pressure. Therefore, the absence of dendritic structures does not indicate the absence of Li deposition [10].

1.3 Thermal runaway of Li-ion batteries

1.3.1 Overview and definitions

1.3.1.1 Cell failures

The failures of Li-ion cell can be non-energetic or energetic and depends on whether these failures involve releasing energy from the battery or not.

Non-energetic failures associating with cell mechanical designs

Some non-energetic failures may happen under abuse conditions depending strongly on the mechanical designs of the Li-ion cell:

- Electrolyte leakage with subsequent cell dry-out
- Cell swelling
- Activation of a disabling mechanism such as current interrupting device (CID), shutdown separator, fuse.

The first two failures rarely happen on 18650 Li-ion cells [4]. The activation of a disabling mechanism will be explored in section 1.3.5.

Energetic failures: Thermal runaway phenomenon

Thermal runaway is the most catastrophic energetic failures of Li-ion battery. It refers to a rapid self-heating process of a Li-ion cell derived from the exothermic chemical reactions that rapidly release the stored energy inside Li-ion cell. Therefore, the more energy a cell has stored, the more energetic the thermal runaway reaction will be. The thermal runaway reactions of Li-ion batteries can be very energetic because these batteries have high energy densities compared to other batteries. The other reason that Li-ion cell thermal runaway reactions can be very energetic is because these cells contain flammable electrolyte, and thus, not only do they store electrical energy in the form of chemical potential energy, they store appreciable chemical energy in the form of combustible materials [4].

The thermal runaway is characterized by a process of energy evacuation leading to an uncontrollable overheating of the system. The severity of a cell thermal runaway will depend on the SOC of the cell (how much electrical energy is stored in the form of chemical potential energy). For any given cell, the most severe thermal runaway reaction will be achieved when that cell is at 100 % SOC, or is overcharged, because the cell will contain maximum electrical energy. They also showed that self-heating onset temperature can be strongly impacted by SOC. Through testing of multiple cell models, Sandia researchers found that thermal runaway onset temperature is reduced for cells at increased SOC [4].

The severity of thermal runaway also depend upon a number of different factors including the ambient environmental temperature, the electrochemical design of the cell (cell chemistry), and the mechanical design of the cell (type (cylindrical, prismatic, pouch), cell size, electrolyte volume, etc.) [4]. More details about the effects of these factors will be discussed in section 1.3.5.

1.3.1.2 Reported incidents involving Thermal runaway of Li-ion Batteries

Usage of Li-ion cell outside of the specification of its manufacturer or defects inside the cells can lead to Thermal runaway. Since January 23, 2006 until January 22, 2020, 268 air/airport incidents involving lithium batteries carried as cargo or baggage that have been recorded [7]. Note that these are recent cargo and baggage incidents that the FAA is aware of. This should not be considered as a complete listing of all such incidents. These events have led to costly product recalls and stricter rules in the past [10]. Some recorded incidents are shown in Figure 24.

It is noteworthy that these catastrophic events are highly unlikely. Lithium-ion batteries have a failure rate that is less than one in a million. The failure rate of a quality Li-ion cell is better than 1 in 10 million [103]. However, the safety risk concerns the entire life cycle of the battery (from manufacturing to recycling) and all battery applications have experienced accidents (including consumer equipment, electric vehicles, stationary storage, etc.). It demonstrates the high importance of safety consideration when integrating the battery into the equipment or application.



Figure 24 : a) Oct 2013 - A Tesla Model S electric car on fire after a piece of debris hit the battery pack while the car was on the highway causing cells to short circuit and go into thermal runaway; b) Jan 2016 – A Tesla Model S burns to the ground while fast-charging at the Sundebru supercharger in Gjerstad, Norway; c) Remains of the UPS Boeing 747 cargo plane that crashed in 2010 [Photo credit: EPA]

1.3.1.3 Abuse conditions, triggering events and thermal runaway detecting methods

Learning from typical incidents, there are a number of abuse conditions that exceed the thermal stability limits of a Li-ion cell and even trigger cell thermal runaway. It may be induced by external forces such as exposure to high temperature originated from fire or internal heating sources as well as exothermic reactions in combination with poor heat transfer to the surroundings or severe mechanical damage, or it may be the result of problems involving cycling/storage during usage such as overcharging, internal or external short circuits, and/or battery protection circuitry design and implementation, or they may be caused by internal cell faults that result from rare and/or subtle manufacturing problems (poor cell electrochemical design, defects,...) [21]. Generally, the abuse conditions during usage of the cell can be classified into mechanical abuse, electrical abuse and thermal abuse [4][3][10][13, 16]. They are linked together as illustrated on Figure 25.

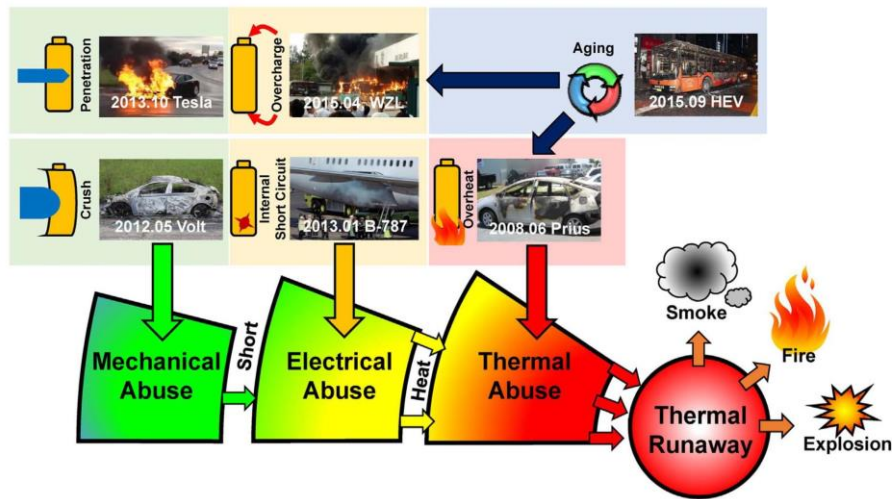


Figure 25: Incidents related with Li ion battery failure, and correlated abuse conditions. [3]

Having their advantages and disadvantages, many feasible solutions for detecting a thermal runaway initiation are based on monitoring certain characteristic fault signals, commonly including the terminal voltage, the surface/ inner temperature and the vented gas as presented in Table 5. [62]

Table 5: Advantages and disadvantages of different methods for monitoring and detecting thermal runaway. [62]

Method	Advantages	Disadvantages
Terminal voltage and surface temperature monitoring method	<ul style="list-style-type: none"> ✓ Monitor the voltage and surface temperature in real-time; ✓ Capable of locating faulty battery; ✓ Predict the state of health, state of charge, etc. of the battery in real-time. 	<ul style="list-style-type: none"> ◆ Low accuracy of thermal runaway prediction; ◆ Complex topology of voltage sensors and high cost.
Embedded optical fiber sensors method	<ul style="list-style-type: none"> ✓ Monitor the internal core temperature of the battery directly; ✓ High accuracy of thermal runaway prediction. 	<ul style="list-style-type: none"> ◆ Higher cost of embedded optical fibers; ◆ Higher requirements for battery packaging.
Electrochemical impedance spectroscopy analysis method	<ul style="list-style-type: none"> ✓ Predict the internal core temperature of the battery without complex hardware; ✓ High accuracy of thermal runaway prediction; ✓ Predict the state of the battery on-line and seamlessly couple with the BMS. 	<ul style="list-style-type: none"> ◆ Fail to monitor large-scale batteries quickly and effectively; ◆ Complex calibration process as different lithium-ion battery systems have different parameters of impedance.
Gas sensor monitoring method	<ul style="list-style-type: none"> ✓ High accuracy and rapid of thermal runaway detection; ✓ Simple, feasible, easy to implement and low cost; ✓ Easy to connect with the BMS interface. 	<ul style="list-style-type: none"> ◆ Fail to predict the state of the battery; ◆ Potential sensor-related faults, including gas cross-interference and gas sensor poisoning.

For the terminal voltage and surface temperature monitoring method, the precision of voltage and temperature sensors needs to be improved in order to enhance the thermal runaway detection accuracy. Similarly, for the internal state prediction method, it is necessary to improve the detection resolution and the high temperature resistance of sensors embedded in the battery. These methods can be coupled with battery management

system (BMS) to establish a more accurate risk assessment model for detecting the thermal runaway of LIBs.

Last but not least, gas sensor monitoring method has been shown as a most feasible and effective method. However, there are still many sensor-related problems such as the low detection accuracy, the complex gas cross-interference, and the gas sensor poisoning. [62]

1.3.2 Thermal runaway mechanisms

The thermal runaway follows a process of chain reactions, during which the decomposition reactions of the battery component materials occurs usually one after another [3].

1.3.2.1 Overview of the chain reactions during Thermal runaway

Based on our experimental work and inspired by the studies on the abuse behaviour of different 18650 cells [3, 10, 12, 13, 16, 17, 55, 104, 104, 105], the thermal runaway chain exothermic reactions of Ni-rich LIBs based on negative graphite electrodes can be summarized in Figure 26.

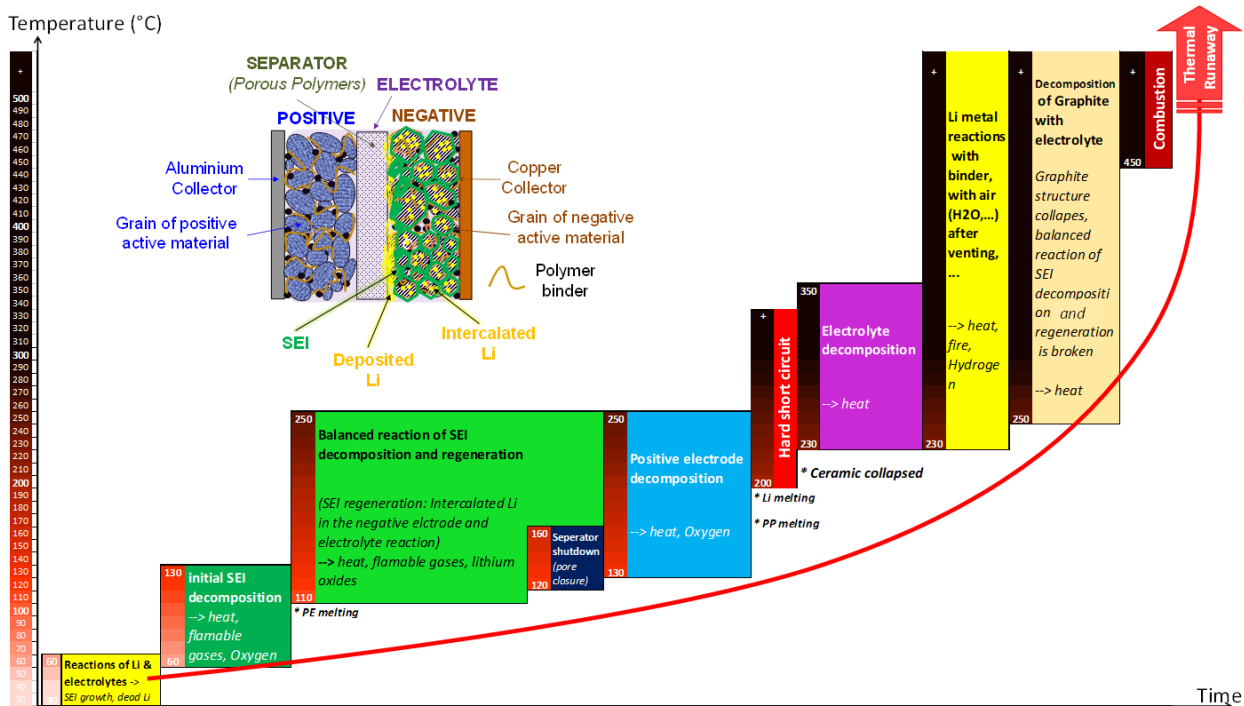


Figure 26: Thermal runaway chain exothermic reactions of Ni-rich lithium-ion batteries

[106].

It should be noted that these reactions do not strictly happen one after another in the given order. They are rather complex and systematic issues. The reactions relating to the deposited Li are for the case of Li deposition (Li plating) occurring in the cell.

More details about these chain reactions are presented in the following.

1.3.2.2 Exothermic decomposition reactions related to Negative electrode

This section focuses on the reaction kinetics for the lithiated graphite/carbon based negative electrode.

First stage: The initial decomposition of SEI

The initial decomposition of SEI occurs around 60 –130 °C [3], with a peak located at approximately 100 °C which is considered as an indicator of the SEI decomposition, exact temperature depends upon cell chemistry and SOC. This is regarded as the first side reaction that occurs during the full thermal runaway process. The SEI decomposition might start from a temperature as low as 57°C. Heat generation rate strongly depends on the surface area of the graphitized samples.

Second stage: The balanced reaction of the SEI decomposition and regeneration.

Once the SEI decomposes, the intercalated Li in the graphite negative electrode has the chance to contact the electrolyte again and the reaction between them eventually occurs, thereby, regenerates SEI. So it would be called the reaction of SEI regeneration.

Within the temperature range of 120 °C–250 °C, the SEI decomposition and regeneration occur simultaneously, with the average thickness of SEI maintaining at a stabilized level. The SEI decomposition will not cease when there is sufficient regenerated SEI, meanwhile the reaction between the intercalated Li and the electrolyte will not boost because the surface of the negative electrode is still covered by certain thickness of SEI layer. This wide and mild exothermic process represents the balanced reaction of SEI decomposition and regeneration.

Third stage: The decomposition of graphite with electrolyte

When the temperature rises to 250 °C or higher, the balanced reaction of SEI decomposition and regeneration will be broken. The reaction between the intercalated Li in the graphite negative electrode and the electrolyte eventually accelerates and dominates. Therefore, the reaction at the negative electrode at the third stage is less complex than the balanced reaction at the second stage. Chen *et al.* [107] confirmed that the reaction peak of the third stage stands for the reaction at the negative electrode, by testing several types of graphite negative electrode.

1.3.2.3 Exothermic decomposition reactions related to Positive electrode

This section reviews the decomposition mechanisms of the selected positive electrode active materials.

Based on thermal stability measurements of the positive electrode materials with electrolyte at full-charge voltage conditions, a number of studies [3, 4, 13, 108] show that positive electrode materials begin to react exothermically with electrolyte at a range of temperatures from approximately 130 to 250 °C and the order of thermal stability of different positive electrode materials for Li ion battery can be LFP > LMO > NCM111 > NCA > LCO, with the LFP as the most stable positive electrode material during thermal runaway process [13]. Some comparisons on the impact of cell technology on the thermal runaway are shown in Figure 27:

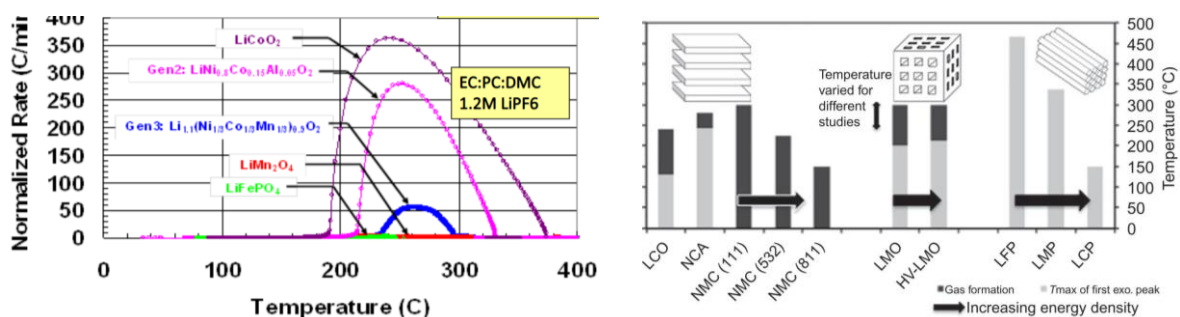


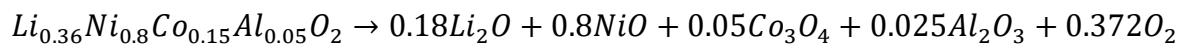
Figure 27: Normalized rate temperature of different technologies (left) and the peak temperatures of the first exothermic reaction and temperature of gas formation [13] (right).

Furthermore, these positive electrode decomposition reactions produce oxygen. This may be a factor that increase the possibility of self-heating due to local faults [4].

The decomposition of selected positive electrode active materials (NCA and Ni-rich NMCs) with electrolyte

The decomposition of NCA ($LiNi_{0.8}Co_{0.15}Al_{0.05}O_2$) with electrolyte

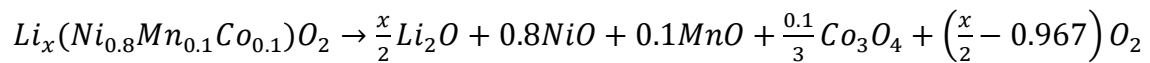
The decomposition of the NCA positive electrode is intensive. It may conform to this main equation [3]:



Several studies summarized that the decomposition characteristics of NCA (charged to 4.2 V with 1 M LiPF₆ EC:DEC electrolyte) has an onset temperature of 160 °C - 170 °C. [3]

The decomposition of NMCs ($LiNi_xMn_yCo_zO_2$) with electrolyte

The thermal decomposition of the NMC positive electrode is less intensive than that of the LCO and NCA. It may conform to this main equation:



The reduction from Ni^{4+} to Ni^{2+} is the main reaction during the NMC decomposition, because Ni^{4+} is more active than Co^{4+} and Mn^{4+} . Therefore, in the Ni-rich NMCs family, the phase degradation is shifted to lower temperatures due to the destabilizing effect of Ni. The temperature range of oxygen formation and phase transition depends on the Ni content as in the Figure 28.

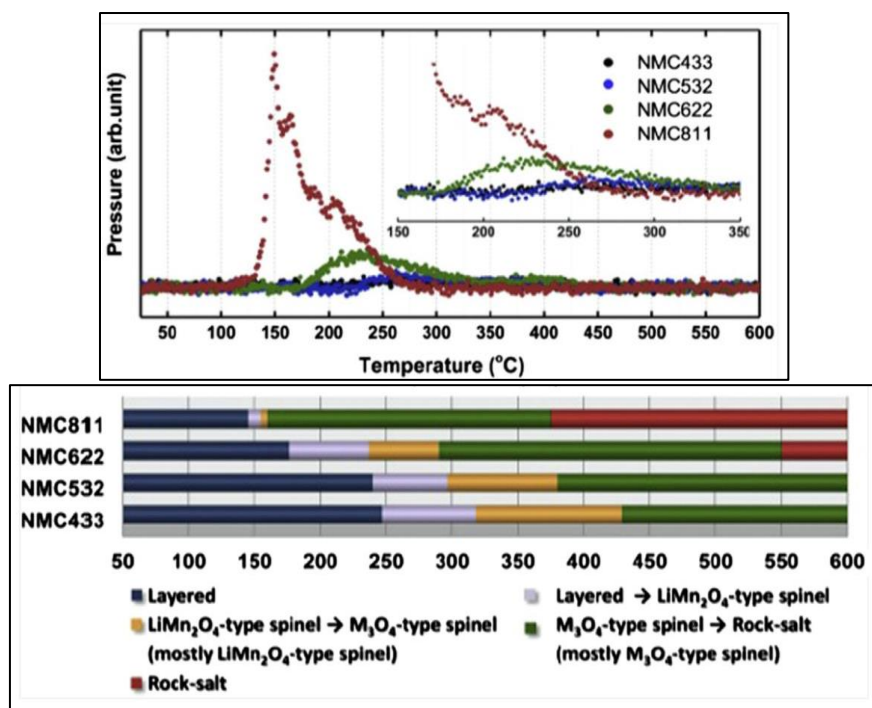


Figure 28: Oxygen formation (top) and phase transition (bottom) of different NMCs [13].

Clearly, higher Ni content in the Ni-rich NMC leads to increased sensitivity to elevated temperatures, releases of more oxygen than their counterparts and larger structural changes. Some studies suggested that the active oxygen intermediates can be dissolved into the liquid electrolyte, diffused into the negative electrode and react with the lithiated graphite [64, 109, 110]. They also proposed that these strong exothermic reactions might trigger the accelerated thermal runaway of Ni-rich technologies without the need of hard internal shorting.

Moreover, according to section 1.1.7 and study from Noh *et al.* [66], Ni-rich NMC releases more heat during decomposition as in Table 6.

Table 6: The enthalpies (ΔH) of the exothermic reactions of different NMCs [3]

Material	$\Delta H, \text{J g}^{-1}$
$\text{Li}_{0.37}[\text{Ni}_{1/3}\text{Co}_{1/3}\text{Mn}_{1/3}]\text{O}_2$	512.5
$\text{Li}_{0.34}[\text{Ni}_{0.5}\text{Co}_{0.2}\text{Mn}_{0.3}]\text{O}_2$	605.7
$\text{Li}_{0.30}[\text{Ni}_{0.6}\text{Co}_{0.2}\text{Mn}_{0.2}]\text{O}_2$	721.4
$\text{Li}_{0.26}[\text{Ni}_{0.7}\text{Co}_{0.15}\text{Mn}_{0.15}]\text{O}_2$	826.3
$\text{Li}_{0.23}[\text{Ni}_{0.8}\text{Co}_{0.1}\text{Mn}_{0.1}]\text{O}_2$	904.8
$\text{Li}_{0.21}[\text{Ni}_{0.85}\text{Co}_{0.075}\text{Mn}_{0.075}]\text{O}_2$	971.5

Several studies about the thermal stability of the NMC positive electrode observed three exothermic peaks at 325 °C, 362°C and 458°C. The first two peaks can be ascribed to the NMC decomposition and the last exothermic peak as the decomposition of the fluorine-based binder [3].

1.3.2.4 Exothermic decomposition and combustion of electrolytes

There are comprehensive reviews of the state-of-art of the contribution of the electrolyte to the safety of the Li ion battery [41, 111–113]. Both the negative electrode and positive electrode materials in the battery react with the electrolyte and the electrolyte itself can also decompose during thermal runaway. The equilibrium equation for the decomposition reaction of the $LiPF_6$ salt is $LiPF_6 \rightleftharpoons LiF + PF_5$. Depending on the thermal stability of the electrolyte with different mixtures, the decomposition product PF_5 will further react with the EC/DMC solvent [3]. These reactions also release heat and therefore accelerate the decomposition of the electrolyte. The measured heat of the 1 M $LiPF_6$ was 375 J/g in 1:1 PC:DMC (or EC:DMC) and 515 J/g in 1:1 PC:DEC (or EC:DEC), respectively. The exothermic peaks located at 230 °C and 280 °C [3].

The mixture ratio and the amount of electrolyte can influence the total heat generation of the full cell during thermal runaway [3]. Furthermore, when thermal runaway occurs, the cell might vents due to the internal pressure rise caused by the vaporization and the gases generated by the electrolyte decomposition with other component materials. Part of the carbonate electrolyte decomposes inside the cell and releases small molecule gases during thermal runaway, whereas the other part of the carbonate electrolyte evaporates and bursts out of the cell. The vent-out substances include aerosol droplets of evaporating electrolyte with partially reacted gases such as $H_2, CO, CO_2, C_2H_4, \dots$. This vent-out mixtures can be ignited into disastrous combustions [39, 114]. These ignitions usually require temperatures well above gas auto-ignition temperatures (Table 3).

The complete combustion energy of any carbonate solvent was much higher than the heat generation of the electrolyte decomposition [3]. Therefore, the electrolyte decomposition and combustion can significantly contribute to the full cell thermal runaway.

1.3.2.5 Melting of separator

As mentioned in the section 1.1.5.4, the commonly used commercial separators are PE (polyethylene) and PP (polypropylene) based separators. These separators will shrink when the temperature reaches their melting points.

The melting points of the PE and PP separators are approximately 130 °C and 170 °C [3], respectively. We found also the multilayer separators mostly designed with a shutdown feature, by which two of the layers have different phase transition temperatures. As the temperature of the cell increases, the lower-melting component melts and fills the pores of the other solid layer and stops ion transport and current flow in the cell. For example, in case of PP/PE/PP three layer separator, it can provide a shutdown behaviour at 130 °C (PE melt) with little shrinkage until 170 °C (PP melt). The gap between 130 °C–170 °C can enhance the safety of the cell to some extent. The shutdown leads to a sharp increase in the cell resistance [115] and help to block the abuse condition that accompanies with high current flow, such as short circuit [116], or overcharge. The separator melting is an endothermic process, and the temperature increase rate will thus slow down. The enthalpy of the PE and PP separator during melting are –90 J/g and –190 J/g, respectively [3][117].

When temperature continues increasing, the shrinkage follows the shutdown and diminishes the separation of the positive electrode and negative electrode. The internal short circuit (ISC) will occur once the positive electrode and negative electrode contact together. The ISC caused by shrinkage can produce massive heat generation that the separator collapses quickly, whereas the ISC can also be mild and the separator may collapse much later. The collapse temperature of the three layer PP/PE/PP separator is similar with that of the PP separator (170 °C). PE-based or PP-based separator with ceramic coating enhance the collapse temperature which can be as high as 200–260 °C [3].

Therefore, the moment of ISC is critical for revealing the thermal runaway mechanisms. If the collapse temperature of the separator is higher than the decomposition temperature of the positive electrode/negative electrode materials, the ISC may not occur during thermal runaway, leading to significantly reduced total heat generation.

1.3.2.6 Additional reactions relating to Li Plating

The microscopic processes involving Li deposition leading to macroscopic safety failures on the cell level has been studied by Waldmann *et al.* [10] (Figure 29).

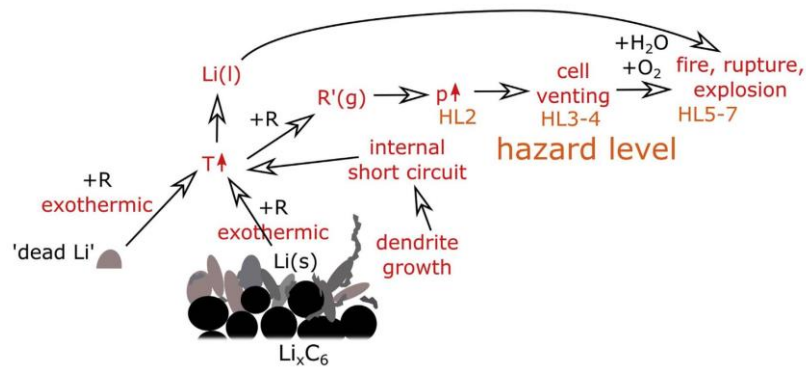


Figure 29: Mechanisms related to Li deposition and thermal runaway of Li-ion cells [10]

Two main safety mechanisms were identified, including:

1) Exothermic reactions of Li with electrolyte

Following is the process of the exothermic reactions of Li metal with electrolyte in an extreme case - the quasi-adiabatic conditions (very high thermal isolation):

- As mentioned above, the onset-of-self-heating of fresh cells is usually link to the initial decomposition of SEI at ~ 100 °C, however, if cell has Li deposition, the exothermic reactions of Li with electrolyte can already start around 30 °C. This low onset-of-self-heating due to these exothermic reactions increases cell temperature and leads to gaseous reactions products ($R(g)$). The produced gas mixture leads to an increase of the pressure inside cells with rigid cell housing and to inflation in case of pouch cells;
- When the cell is irreversibly damaged, both, cylindrical and pouch cells are then vented if the pressure inside the cell is further increased by ongoing reactions. The jelly roll is likely to be ejected from the cell housing;
- When mass of the cells is lost by evaporation of electrolyte after venting, water and oxygen might diffuse into the cell and thus, they are likely to react with the cell components including the deposited Li. Deposited Li react with H_2O with the occurrence of fire;

- Metallic Li will melt at a temperature of $\sim 180.5^{\circ}\text{C}$. In case of alloying of Li with other elements, the melting point might shift to $\sim 200^{\circ}\text{C}$.

From the reported study [10], the destruction level of the 18650 cells are higher in the case of Li deposition.

2) Internal shorts caused by the dendritic growth of Li

Internal short circuits in Li-ion cells caused by Li deposition can be divided into soft and hard shorts:

- Soft shorts often disappear during discharge and thus cells do not fail catastrophically. Soft shorts are usually caused by thin dendrites. A soft short can lead to considerable currents and therefore to a drop in cell voltage and a local temperature rise. The local heating can lead to: exothermic reactions with the electrolyte, melting of Li, and melting of the separator;
- Hard shorts are characterized by a comparably low resistance and therefore by significantly higher short circuit currents between negative electrode and positive electrode. Therefore, hard shorts are more likely to lead to thermal runaway due to stronger local temperature rise [10]. However, there is very low probability of hard shorts due to Li dendrites in Li-ion cells (ppm range) because in most cases, Li deposition was found to be not dendritic or not dendritic enough due to the high pressure inside Li-ion cells.

1.3.2.7 Other reactions

Other reactions do exist but may not have significant influences on the thermal runaway of Li-ion cell. For example, the decomposition of the PVDF binder has been studied by several groups [3, 38], however, the chemical kinetics of the decomposition of the PVDF binder with electrolyte seems to have little influence on the thermal runaway [3].

1.3.3 The risk of fire and explosion from vent gas and particles

The severity of the thermal runaway is highly connected to the explosion hazards of the phenomenon. While several studies mainly focus on SOC and cell chemistries, other important variables such as component compositions [118–120], electrode design [118,

121], form factor, manufacturer, failure mode, cell capacity and experimental setup should also be considered. As far we know, the explosion hazards depend strongly on the flammability of the vented matters, hence, the composition of the vent gas and vent particles [122].



Figure 30: Battery vent gas species compositions from literature [123].

This dedicated to present the literature on the composition of vent gas and particles released from the cells. Several studies have experimentally characterized battery vent gas composition released during thermal runaway. These studies are summarized in Figure 30

[123] (THC is Total Hydrocarbon Content). Therefore, H_2 , CO , CO_2 and TCH are the common vent gases detected during the thermal runaway of LIBs. It is also noteworthy that the LIB from different manufacturers with the same cell chemistry might produce different vent gas composition. This is related to the variation in cell manufacturing or the electrolyte species.

There are fewer studies about the composition of the vent particles. Wang *et al.* have analysed the vent particles of different NMCs battery samples after the abuse tests in EV-ARC as shown in Figure 31. [110]



Figure 31: Vent particles (5kx) from the thermal runaway of 3 different NMCs technologies [110]

Using EDS analysis, the compositions of these vent particles are presented below:

Table 7: EDS results of vent particles for cells with different NCM cathodes after TR. [110]

Element	NCM111(wt%)	NCM523(wt%)	NCM622(wt%)
C	30.55	20.94	46.54
O	13.12	16.45	14.80
F	2.85	2.7	6.95
Al	4.5	27.5	2.23
P	0.29	2.74	0.84
S	/	0.81	/
Cl	0.31	0.38	0.85
Mn	15.48	8.42	8.47
Co	16.98	4.44	4.19
Ni	15.90	15.62	15.14
The total	100.00	100.00	100

However, there is no study to confirm these compositions. There should be further studies to investigate deeper the composition of the vented matters, along with the study of the

exothermic reactions during the thermal runaway, in order to mitigate the hazards and more especially to guide the future battery material designs.

1.3.4 The impact of SOC on the Thermal runaway

The chain exothermic reactions of thermal runaway happen under near adiabatic conditions, where the exact reaction temperature highly depends on the cell chemistry and also SOC level. The thermal runaway at different SOC levels has been studied by several research groups [74, 95, 124–129]. They usually used Heat-Wait-Search test in standard ARC as a powerful technique to analyse and compare the thermal runaway phenomenon of different batteries at different SOC levels. This technique will be described in chapter 2.

The works of [126, 128] confirmed that the safety of the NCA and LFP technologies decreases with increasing SOC levels, as shown in Figure 32.

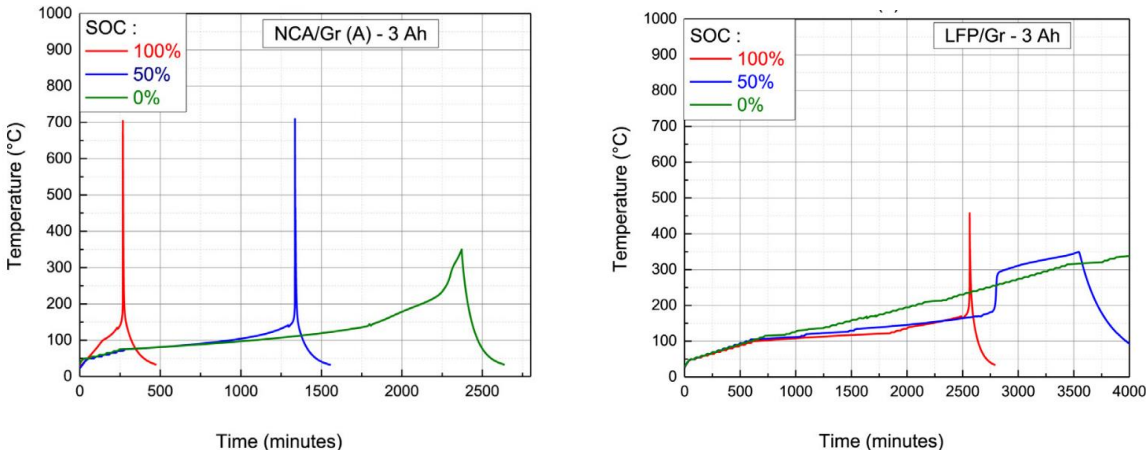


Figure 32: The temperature versus time of the thermal runaway of the same capacity (3Ah) of 18650 NCA/Gr and 26650 LFP/Gr batteries at different SOC levels (0, 50 and 100%). [126]

As a common conclusion, LFP-Graphite was found to be the most thermally stable, mainly, due to the high thermal stability of $LiFePO_4$ compared to relatively thermally unstable NCA layered oxide which generates oxygen upon heating. However, this battery configuration still does not remove all risk of thermal runaway.

The SOC-dependency is observed to be very strong in case of Ni-rich technologies [124, 127]. Figure 33 shows that multiple exothermic peaks are distinguished on the heating rate curves of 0% SOC cells. This is different from the curves of 50%–100% SOC cells which reach very

high temperature rate during the thermal runaway. Mao *et al.* [127] believes that the exothermic chemical reactions are not intense enough for 0% SOC batteries, thereby, they do not overlap each other as in case of increased SOC batteries.

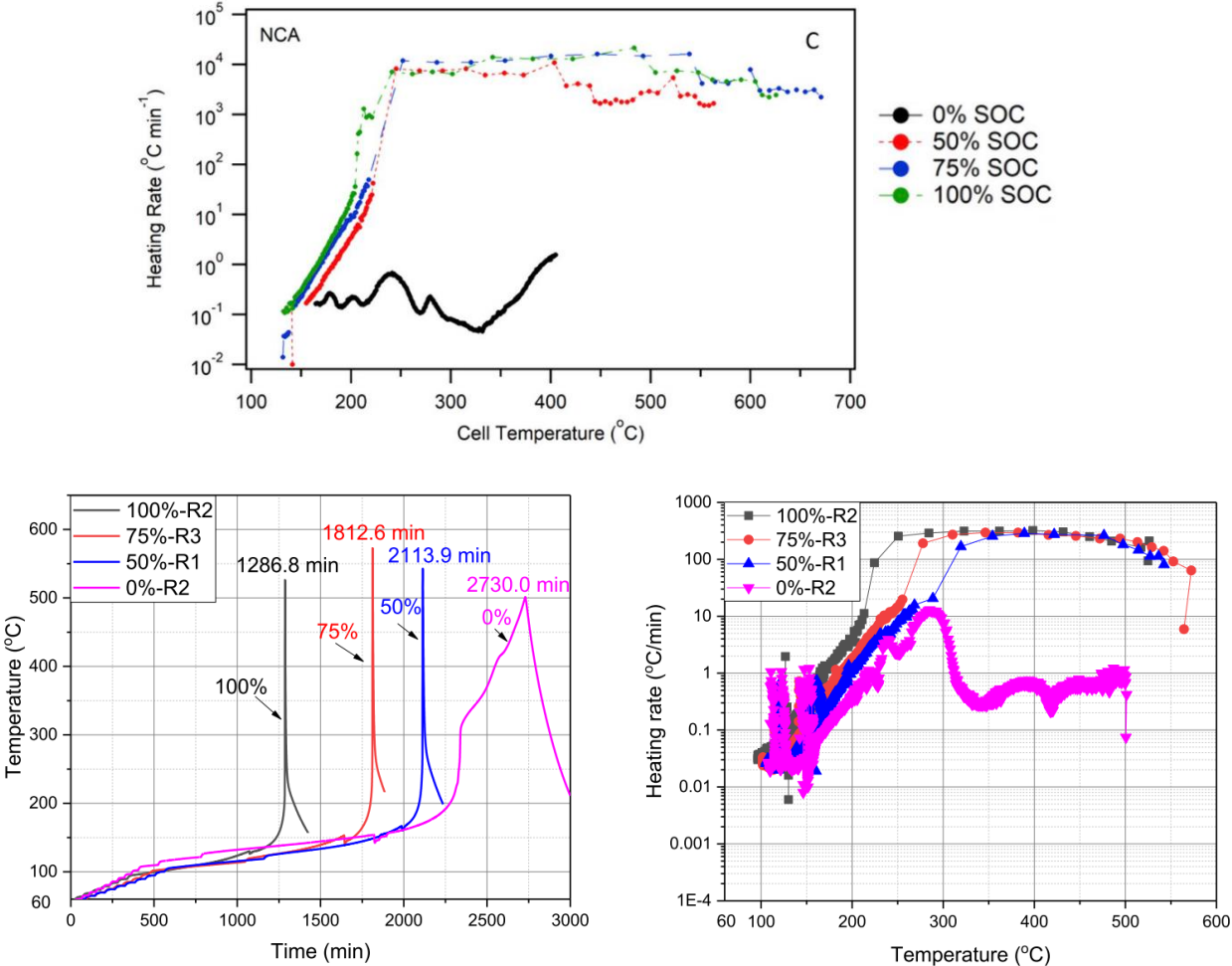


Figure 33: (Top) The heating rate as a function of temperature based on ARC results from 18650 Panasonic NCA/Graphite cells at 0%, 50%, 75% and 100% SOC. [124]; (Bottom) Thermal runaway temperature and heating rate curves of 18650 NMC523/Graphite cells at different SOC. R i means the ith repetition. [127]

Besides the heat released by exothermic chemical reactions, the hard shorting after the collapse of separator also releases a large amount of stored electric energy, which relatively corresponds to the SOC level of the batteries. Therefore, battery with increased SOC can trigger the thermal runaway instantly once the separator collapses, and the exothermic chemical reactions can occur simultaneously and overlap each other. [127]

The combustion characteristics and fire behaviours during the thermal runaway are also affected by SOC. Peng *et al.* [130] have shown in Figure 34 the measured O₂, CO and CO₂ concentrations as functions of time during the thermal runaway for batteries at different SOCs. O₂ concentration is very low which indicates that the thermal abuse tests were conducted under well-ventilated condition. Higher SOCs lead to higher production of CO and CO₂. The CO and CO₂ generation rates present a significant increase when the thermal runaway reactions start and then decrease rapidly as the flame weakens. Compared to 0% and 50% SOC, it is understandable that the 100% SOC has the highest peak of CO concentration caused by the incomplete combustion during the violent fire [130] which is in accordance with the observations of burning behaviours.

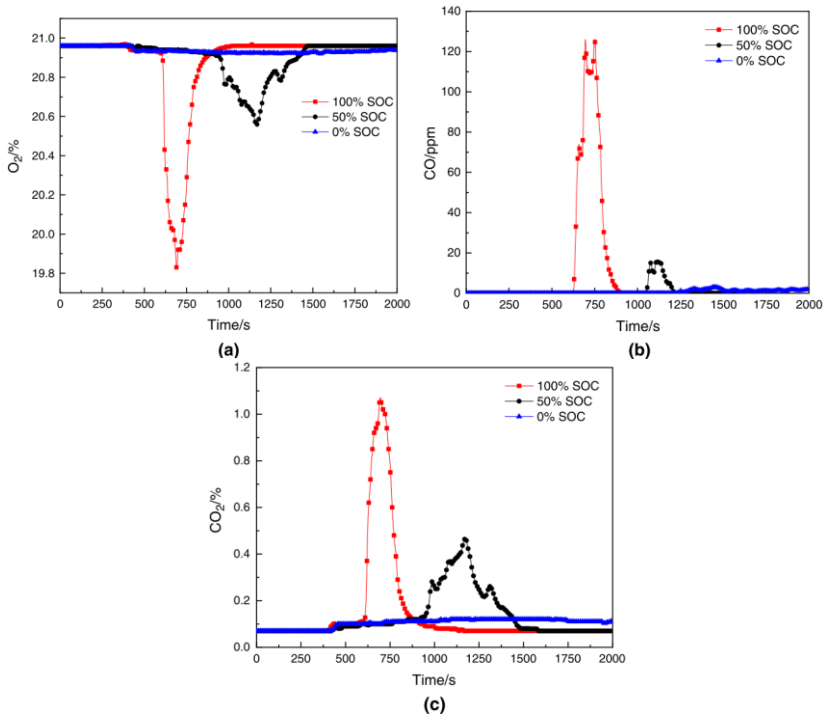


Figure 34: Measured O₂, CO and CO₂ concentrations as functions of time during the thermal runaway for batteries at different SOCs. [130]

Table 8: Summary of gases released by the thermally abused Sanyo UR18650ZL2 NMC111/Graphite LIBs identified using GC-MS chromatograms. [125]

Gases	SOC			
	5%	50%	90%	100%
CO	●	●	●	●
CH ₄	●	●	●	●
C ₂ H ₆	●	●	●	●
CO ₂	●	●	●	●
C ₂ H ₄	●	●	●	●
C ₂ H ₂			●	●
C ₃ H ₈				●
C ₃ H ₆			●	●
1-C ₄ H ₈		●	●	●
1,3-C ₃ H ₄				●
1,3-C ₄ H ₆			●	●
(E)-2-C ₄ H ₈		●		●
g-C ₄ H ₈			●	●
C ₅ H ₁₂				●
1-C ₄ H ₄				●
1-C ₅ H ₁₀			●	●
2-C ₅ H ₁₀				●
g-C ₅ H ₁₀				●
r-1,3-C ₅ H ₆				●
cis-1,3-C ₅ H ₈				●
1-C ₆ H ₁₂			●	●
C ₆ H ₆		●	●	●
CH ₃ OCHO		●	●	●
1-C ₇ H ₁₄				●
CH ₃ OCH ₃	●	●	●	●

Accordingly, at increased SOC, more types of gas will be released due to the presence of more violent electrochemical side reactions as seen in Table 8 [125]. Similarly for the residuals of the battery after the thermal runaway: Liao *et al.* [125] found that the higher the battery SOC, the more severe damage to the battery.

1.3.5 The role of Safety features in cylindrical cells

In commercial Li-ion cells, several safety features are used to lower the risk of thermal runaway [10]. In this thesis, we focus only on the safety features of cylindrical commercial cells which are shown in the Figure 35.

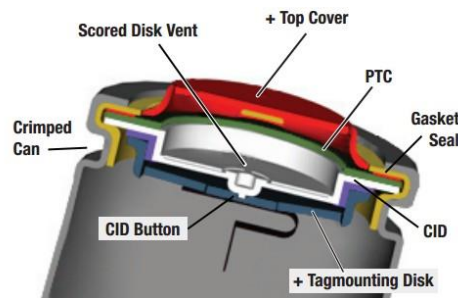


Figure 35: Some common safety features in the cap assemblies of cylindrical cells [4].

The venting mechanisms in these cells can be activated when internal temperature and pressure are high. It functions thanks to the implementation of:

- Positive temperature coefficient resistor (PTC),
- Current Interrupting device (CID),
- Vents,
- Stiff centre tubes.

Their operating mechanisms are described in the following.

Polymeric positive temperature coefficient (PTC) device

These devices include a conductive polymer layer that becomes very resistive above some threshold temperature. They remain conductive within specified current and temperature conditions. When discharge/charge current become excessive, the polymer will heat and become highly resistive, greatly reducing current from/to the cell. When PTC device cools, it again becomes conductive. Therefore, the current is reversibly limited for higher temperatures [4]. Due to this characteristic, PTC devices may not be applicable to high power cells.

Current interrupting device (CID)

In cylindrical cells with a rigid housing the pressure will rise but the volume will stay constant (isochoric conditions). Therefore, cell internal pressure will develop prior to venting. When the pressure inside this cell increases too strongly, the CID will physically break and leads to irreversible interruption of current. At the same time, the cell is often vented and air components such as oxygen and moisture can get into the cell. For reliable operation of CIDs, it must appropriately match to cell chemistry so that overcharge conditions result in sufficient gas generation prior to thermal runaway to activate the CID.

Vents:

Vents are usually formed by including a burst disk in the cell design [4]. In most small commercial cells, CIDs connect to vent assemblies so venting includes 2 stages. First, the CID activates, creating a small hole for venting and a soft pop or click sound. Shortly thereafter, the full vent opens with a loud pop, followed by a rushing sound of venting gas. The gas itself

has been shown to contain toxic compounds or potentially flammable products with relatively low auto-ignition temperatures [13] Depending upon the surrounding environment, the cell vent gases may ignite. The flow of vent gases is somehow restricted due to the configuration of the vent port, flames emanating from 18650 cells will be highly directional and are often described as “torch-like” [4].

Stiff center tubes (mandrel)

Pressure releasing mechanism depends on the presence of the open cell core.

Under high temperature, electrodes expand and collapse into the core of the windings roll, thereby, creating an internal obstruction to gas release at the base of the cell. When the cell vents at the cap, the pressure differential between the cell cap area and cell base can result in a piston-like effect that drives the cell contents out of the cell. Contents ejected can travel significant distances (many meters), spreading heated/toxic materials, and possibly flames [4]. Therefore, the manufacturers implement a stiff metal centre tube in cylindrical cells to maintain an open cell core and allow equalization of pressures within the cell in the event of a thermal runaway as illustrated in Figure 36.

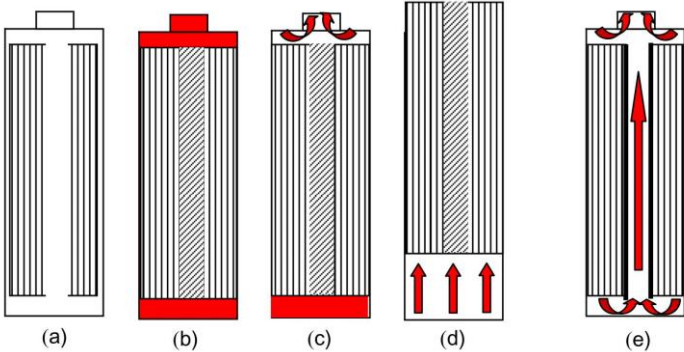


Figure 36: Ejection of windings from a cylindrical cell subject to a thermal runaway reaction (left to right): (a) cross section of a cell without a stiff centre tube; (b) during thermal runaway windings expand and collapse into cell core; (c) cell vent, (d) electrodes ejection and (e) the role of stiff centre tube [4]

The use of mandrel has significantly reduced the likelihood of electrode ejection, however, is not a required design element and not present in all cell designs [4]. However, recent research [131] has confirmed the high importance of this metal tubes during cycling,

especially at low temperature. By comparing between 2 types of cell (“No Mandrel” and “Mandrel” cells with the same energy rating of 2.6 Ah and the same active materials, graphite and NMC), they claimed that:

- In case of Mandrel cells, after 0 °C cycling, slight rotation of the jellyroll and inward movement of the tab is observed which is possibly due to the pressure build up in the electrodes during cycling caused by the undesired side reactions like SEI growth or gas evolution. However, general stability was maintained.
- In case of No Mandrel cells, after 0 °C cycling, the cycling effect is more serious: several layers have collapsed into the core of the cell. Bending and delamination are apparent as observed in Figure 26. The authors also claimed that this mechanical deformation of the cell layers can enhance the side reaction of Li deposition at cold temperature [131].

Consequently, without the presence of a mandrel, the mechanical deformation of the electrodes closest to the empty battery core has accelerated the capacity fade of the battery during cycling aging at cold temperature (Figure 37 and Figure 38), therefore, leading to the earlier thermal runaway process and more violent ejection of cell jellyroll of these cells (Figure 39).

These observations emphasize the importance of a proper pressure compensation in the cell core operated at low temperatures.

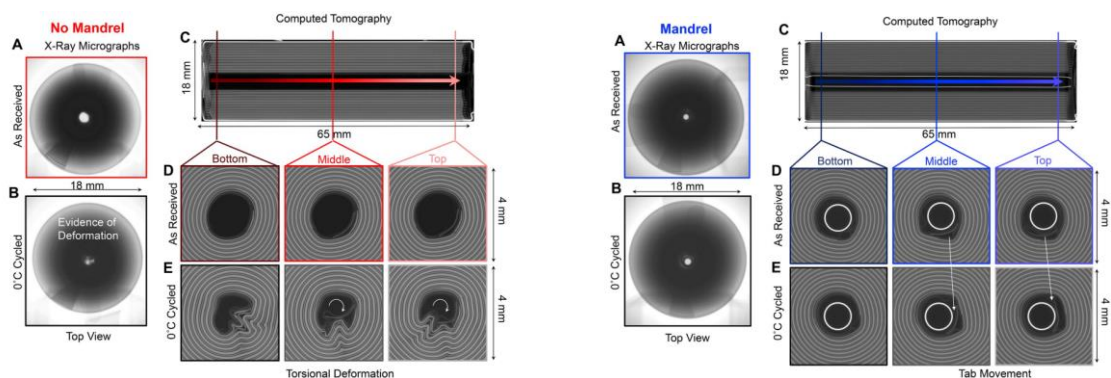


Figure 37: X-ray tomography results of No Mandrel cell (Left) and mandrel cell (Right), taken before (as received) and after 0 °C cycling.

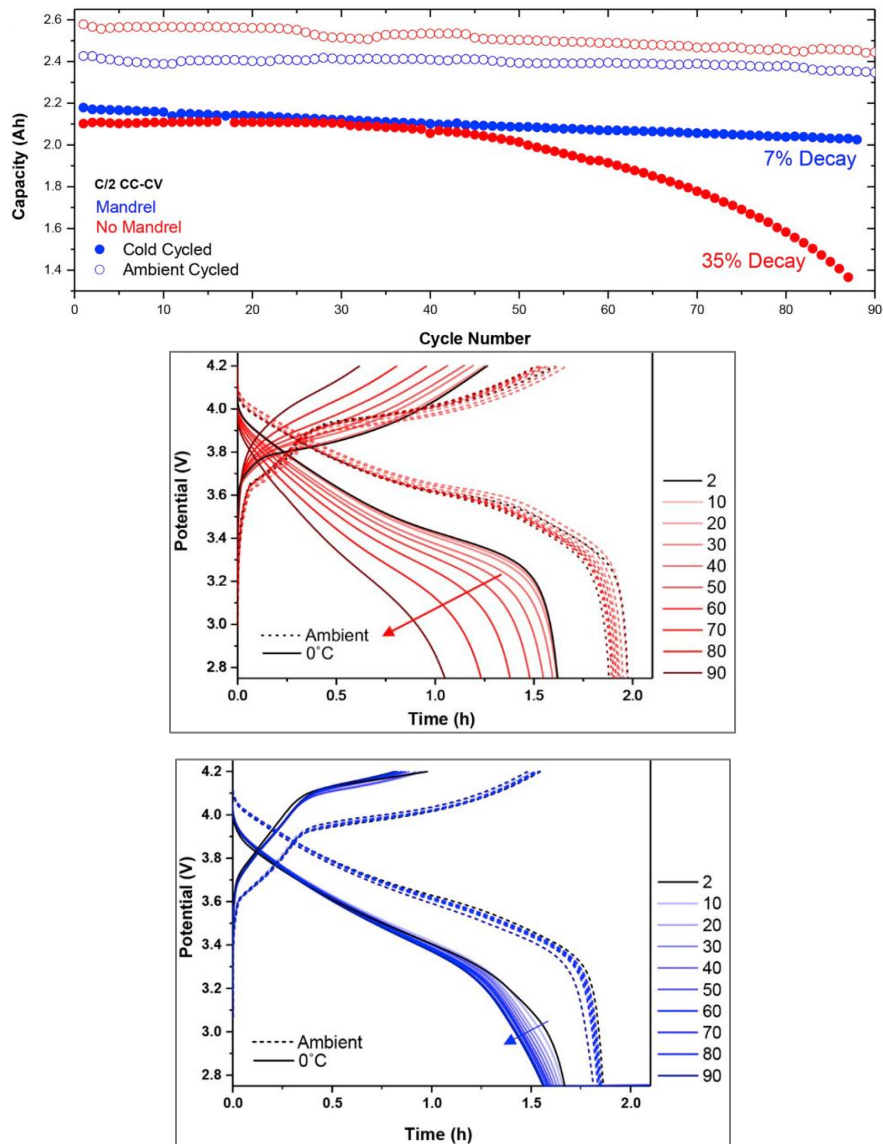


Figure 38: (Top) Discharge capacity delivered per cycle. (Bottom) Investigation and comparison of profiles changes over cycling in the Mandrel cell at ambient (solid lines) and 0 °C (dashed lines) conditions. [131]

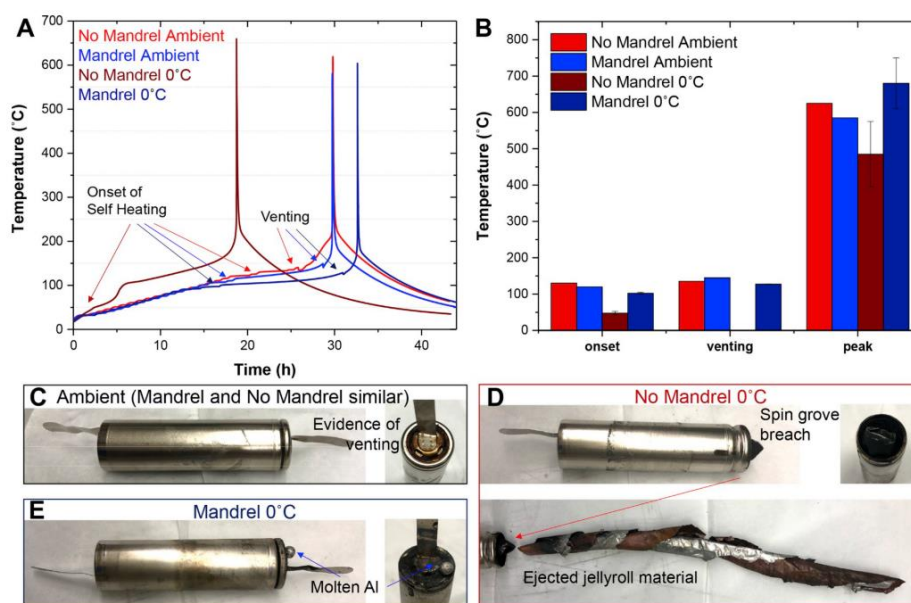


Figure 39: **A** Heat-wait-search temperature over time profile of representative cells. **B** Trends of thermal runaway onset temperature, venting temperature and peak temperature for each cell type. **C-E** Photographs of representative failures after ARC thermal runaway testing. [131]

1.3.6 Impact of aging on Thermal runaway

Several studies on this topic has been published recently [8, 9, 13, 16, 132].

1.3.6.1 Impact of SEI-driven aging

Impact of Calendar aging

The work of Abada *et al.* [16] emphasized the relationship between the diffusional limitations generated by the growth of the SEI layer induced by calendar aging (60 °C/100 % SOC) and the behaviour of accelerated aged cells studied. Thermal abuse tests were performed on LFP/C cylindrical fresh cells and cells aged at 2 levels (10 % and 30 % of capacity loss) The results showed that due to a thicker SEI layer, calendar aging leads to a delayed onset of the cell self-heating temperature with a thermal runaway starting at a lower temperature for aged cells comparing with fresh cells, as shown in Figure 40.

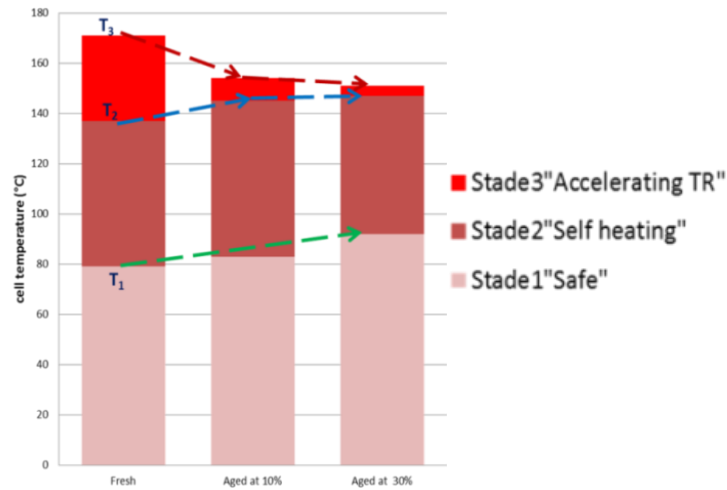


Figure 40: Comparison of the 3 stages of thermal runaway between fresh cell (1st Bar) and calendar aged cells (10 % (2nd Bar) and 30 % (3rd Bar) discharge capacity loss) [16]

Therefore, calendar aged cells appear to be slightly safer due to greater safe zone (T_1 30 % aged cell > T_1 10 % aged cell > T_1 fresh cell) as seen in Figure 40. However, their released temperature increases faster (closer to separator melting: T_3 closer to T_2 for aged cells). The temperature T_3 reaches higher for fresh cells than for that of the aged cells.

Lammer *et al.* [132][133][134] investigated the impact of calendar and cycling aging on the thermal runaway of several 18650 commercial Li-ion cells. According to their works, cells aged by storage at 60 °C, 100 % SOC showed the lowest emission of heat and the largest influence on the reactivity in comparison with cycling aged cells and fresh cells. Specifically, at the same level of aging, cells aged by storage at 60 °C appeared to be less reactive during thermal runaway than cycling aged cells. This is indicated by the lower heat consumption during venting and heat emission during thermal runaway, which is proven by Figure 41.

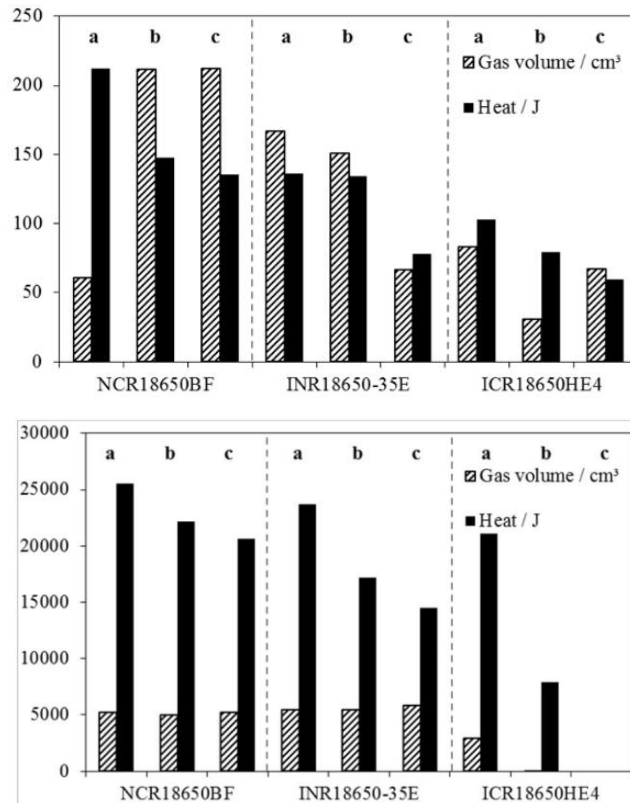


Figure 41: The volume of released gas and the heat release of thermal runaway of (a) pristine cells, (b) cells aged by cycling aging (20 % discharge capacity loss) and (c) cells aged by storage at 60 °C (20 % discharge capacity loss) during venting (left) and thermal runaway (right) [132]

Impact of Cycling aging

The thermal stability of LIBs is affected by cycling aging [135]. Recently, Zhao *et al.* [95] claimed that the thermal runaway hazards of 18650 LIB increase with the increase of cycle numbers. They cycled the cells with 1C at ambient temperature with 100, 200, 300 and 400 times and then finally fully charged the aged cells with 0.5C before thermal abuse tests in ARC. With the same protocol, this type of thermal test accelerates the thermal runaway process (less than 100mins/test).

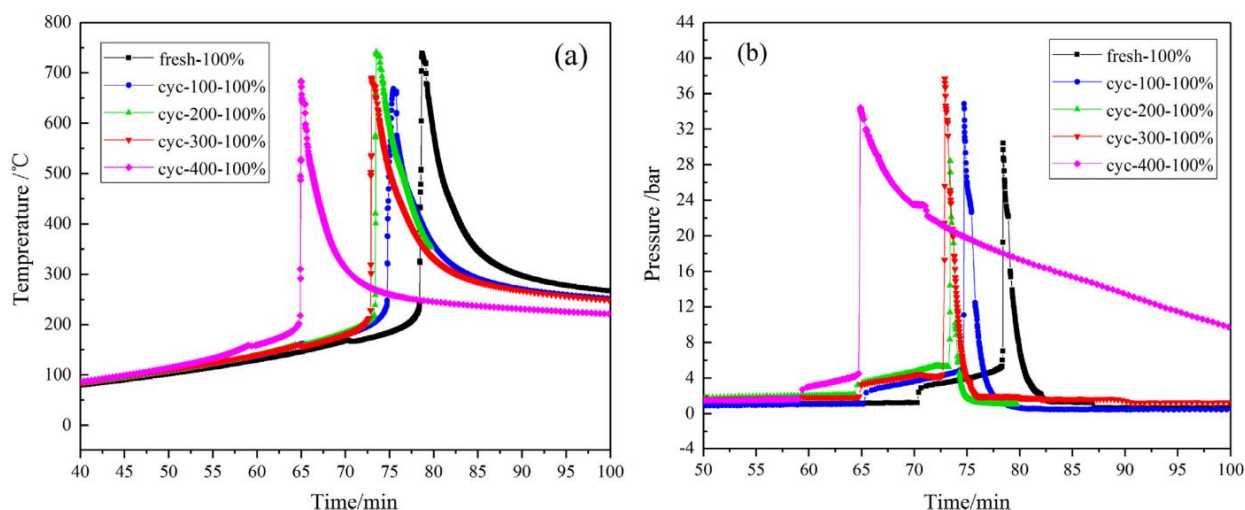


Figure 42: The ARC test data profiles of 18650 NMC532/Graphite aged cells at 100% SOC:

(a) cell surface temperature; (b) ARC's internal pressure. [95]

The results (Figure 42) show that not only higher SOC can enhance the risk of thermal runaway, but also aged cycled batteries can increase the hazard, the thermal stability of these aged batteries has been decreasing with number of cycles [95].

1.3.6.2 Impact of Li deposition/plating aging

The rest time after Li deposition can reduce the amount of deposited Li as explained in section 1.3.2.6. Therefore, studies on this topic have highlighted the effects of rest time after Li deposition on thermal runaway behaviours. Waldmann *et al.* have reported that a rest time after the end of cycling under Li deposition conditions leads to a partial recovery of safety. After cycling at Li deposition conditions, the rest was applied for the aged cells at 25 °C and was in the range of 1.5 h to 8 days. In case of a rest time of 1.5 h, the thermal runaway has higher destruction level compared to that after a rest time of 8 days. Moreover, the onset of self-heating in case of rest time 8 days returns to the value of the fresh cells, probably due to chemical intercalation of Li into graphite and by passivation of Li on its surface by reaction with electrolyte. However, the ejection of the jelly roll was still observed after the rest time of 8 days. It is likely that this is due to exothermic reactions of 'dead Li' with electrolyte [10].

1.4 Modelling the Thermal runaway of Li-ion Batteries

Abada *et al.* [17] has reviewed on the safety-focus modelling of Li-ion batteries, including battery operating models, aging under normal operating conditions, and thermal runaway models potentially occurring in incidental situations. They have been carefully examined in terms of overall methodology taken, consideration with genuine multiphysics associated phenomena, prediction capabilities and relating limitations, as well as development and validation modes.

In the following, the first thermal runaway coupled multiphysics model developed at IFPEN and the recent model developments will be summarized.

1.4.1 General strategy for Thermal runaway modelling

In the mentioned context, a thermal runaway coupled multiphysics model has been developed based on the identified chemical degradation reactions introduced in Hatchard *et al.* [136] which were calibrated / validated for LiCoO₂/Graphite technology in Kim *et al.* [137] and for LFP/Graphite technology in Abada *et al.* [13, 16, 138]. These works focused on the development and validation of a 3D physical model of the Li-ion battery nearby thermal runaway conditions. The works of Abada *et al.* [13, 16, 138] has also taken into account the effect of calendar aging. A combined modelling and experimental investigation has provided a better understanding of the mechanisms leading to thermal runaway of Li-ion cell, taking into account the influence of calendar aging. One of the major outcomes of this work is also the proven fact that calendar aging leads to a delayed onset of the cell self-heating temperature with a thermal runaway starting at a lower temperature. This is supported by computer simulations showing that the thickening of the SEI hinders the diffusion of Li ions, which delays the degradation of the negative electrode and the occurrence of thermal runaway [16].

The core goal of the thermal runaway model is to evaluate the global heat released by the degradation reactions. The modelling approach and calibration, validation results are briefly discussed below.

1.4.1.1 Modelling approach

Electro-thermal modelling of Li-ion batteries relies on the coupling of an electrochemical modelling describing the transport and electrochemical phenomena occurring in the battery and a thermal modelling that will account for the energy transfers inside and outside the battery. Based on the chemical degradation reactions considered in Kim *et al.*'s model [137] and taken into account the influence of cell calendar aging, Abada *et al.* [16] has proposed the coupled multiphysics thermal runaway model which is structured as an interactive assembly of 3 sub-models as illustrated in Figure 43.

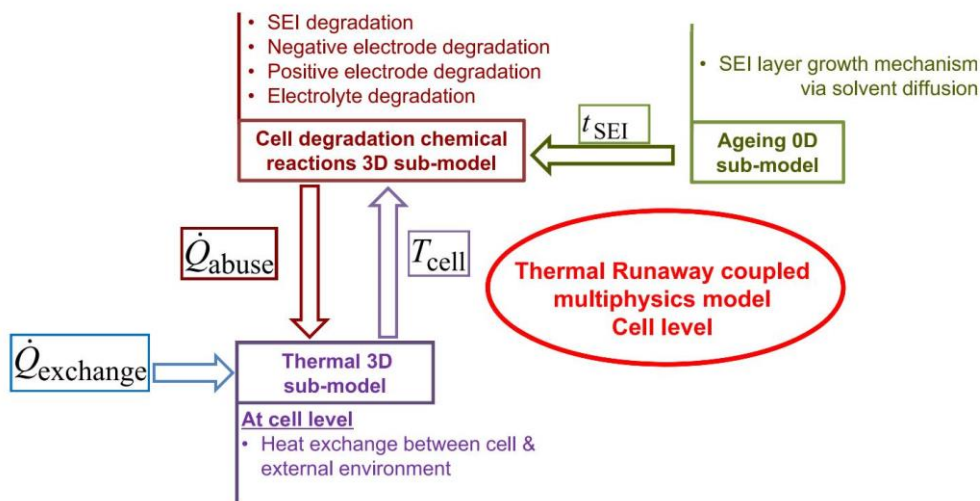


Figure 43: Thermal runaway coupled multiphysics model [16]

Sub-model 1: 3D cell degradation chemical reactions

This sub-model considers the physicochemical mechanisms leading to thermal runaway to predict the chemical heat released by the exothermic reactions related to the degradation of the various cell components in extreme operating conditions. This sub-model takes into account 4 main exothermic reactions:

- SEI degradation: stabilization of unstable elements in the SEI on the negative electrode.
- Negative electrode degradation: solvent reduction at the negative electrode leading to SEI formation
- Positive electrode degradation
- Electrolyte degradation

The degradation reaction kinetics are described by Arrhenius laws and each variable is localized meaning that it depends of its position within the cell and the time. As a consequence, it is a 3D model.

Sub-model 2: 0D calendar aging

The thickness of the SEI layer is assumed uniform inside the cell (0D model) and a static aging approach has been followed to evaluate the thickness of the SEI layer corresponding to a specific cell state of health. Thereby, this approach is based on the assumption that the capacity loss measured was entirely due to the SEI growth and does not take into account the aging conditions of the cell. Moreover, to estimate the increase in SEI thickness, it is assumed that the geometric area of the negative electrode is flat and the radius of the graphite particle representing the negative electrode is larger than the thickness of the formed SEI.

Sub-model 3: 3D-thermal model

This sub-model is based on the energy balance equation involving the different heat sources in the core of the battery cell. The temperature depends on the time and the position within the cell. It is then a 3D model. This 3D thermal model takes into account the anisotropy of thermal conductivity inside the cell and simple boundary conditions relevant for experimental conditions.

These 3 sub-models have been ultimately coupled to achieve a multi-physics predictive model of the thermal runaway of fresh and aged Li-ion cells. It was implemented on Comsol Multiphysics platform with fit-to-purpose experimental calibration and validation procedures for the cell under study, as described in the following section [16]. Further details and discussion surrounding this model development and methodology has been published in [13]. This model will also be explored deeper in the future works of this thesis.

1.4.1.2 Model calibration and validation for LFP/Gr (A123)

Abada *and al.* [16] has focusing on the previous generation of Li-ion technology, which is LFP/Graphite. The selected cell was A123 (2.3 Ah) cylindrical LFP/C cells. All the thermal runaway tests were carried out with fully charged cells (100 % SOC), which is known to be the worst-case scenario. In order to calibrate the thermal sub-model, the thermal properties

of the cell under investigation were estimated by fitting experimental data obtained from thermal characterization tests in a Battery Testing Calorimeter (BTC).

The evolution of the surface temperature of a fresh A123 cell and its voltage during the test in the BTC has been analyzed and there were three critical temperatures identified:

- the initial self-heating temperature, T1, related to the SEI layer decomposition reaction;
- the starting temperature, T2, of the melting process of the battery separator material;
- the thermal runaway trigger temperature, T3 [16].

To save calculation time without losing efficiency, as similar in a comparative study by Kim *et al.* [6], in this thermal runaway lumped model, the variables are considered uniform and only depend on time. It allows the temperature of a LFP/C cell to be simulated in pseudo-adiabatic conditions representative of thermal abuse tests in a BTC [16]. After the model implementation and parameters setting, it has been well validated as shown in Figure 44:

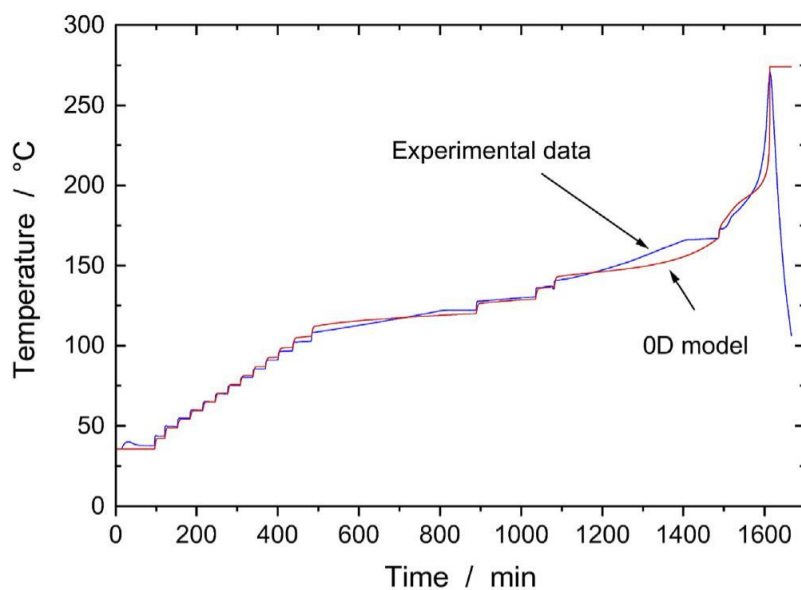


Figure 44: Comparison of the simulated average surface temperature of a fresh A123 cell with the experimental data [16]

1.4.2 Recent Thermal runaway model developments

Recently, there have been new model developments, especially for the integration of venting phenomenon in the works of Coman *et al.* [139, 140] and for further refinement of venting and self-discharge / short-circuit reactions from Petit *et al.* [141] at IFPEN.

1.4.2.1 Adding the venting into thermal runaway model

Coman *et al.* [139, 140] has built a mathematical model for analysing the thermal runaway when venting of the electrolyte and contents of the jelly roll (ejecta) is considered as presented in Figure 45.

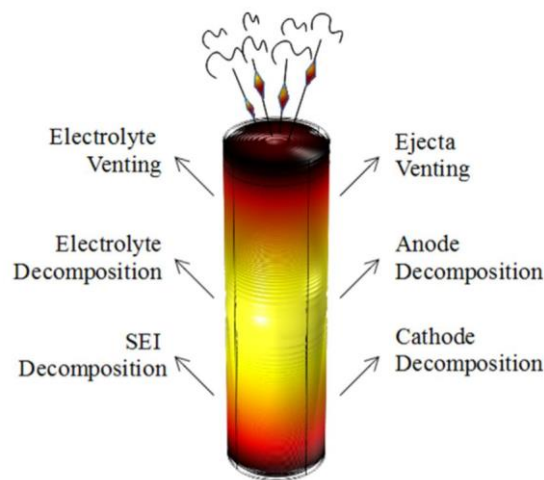


Figure 45: The different processes that were taken into account in [139, 140]

This model aims to predict the temperature-pressure behaviour as well as the gas generation inside 18650 LCO/Graphite cells with a DMC (Dimethyl carbonate) electrolyte. It was found that by modelling only the generation of vapour, while keeping a constant mass of gas inside the cell, the model fails to predict the experimental pressure. However, when adding the mass rate of gas generation due to pre-venting reactions together with the isentropic flow equations, the model predicted the pressure profile inside the battery cell. [140]

1.4.2.2 Adding the venting and short-circuit into thermal runaway model in IFPEN/Siemens Digital Industries Software project and DEMOBASE project

Based on Hatchard *et al.* [136], Kim *et al.* [137] and Abada *et al.* [13, 16, 138], and Coman *et al.* [139, 140], Petit *et al.* [141] have added 2 reactions into the thermal runaway model: short-circuit and venting.

IFPEN/Siemens Digital Industries Software project

They have succeeded to make a demo on High power LFP/C cell as shown in Figure 46.

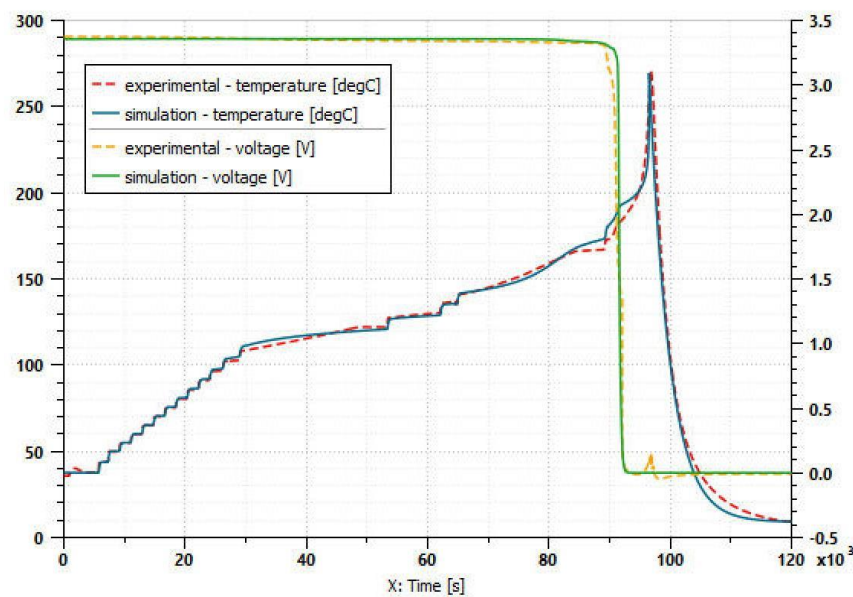


Figure 46: Comparison between experimental and simulation results [141]

When venting and short-circuit is taken into account, it is proven that this model is able to describe correctly both the thermal and the electrical behaviour of the cell thanks to the assessment of the role of different phenomena involved in the thermal runaway process.

This electrothermal model integrating thermal runaway thermophysics has been implemented in the battery cell component of Siemens Digital Industries Software Simcenter Amesim TM.

DEMOBASE project (DEsign and MOdelling for improved BAttery Safety and Efficiency)

This project has integrated the thermal runaway model at cell level to investigate the safety behaviours of the battery module. The pouch cell studied was Saft NMC/Graphite. The

results are shown in Figure 47. As observed in this figure, there is a good agreement between experimental and modelling results regarding voltage and temperature profiles. The model has been able to accurately predict the evolution of temperature during the thermal abuse test with a maximum temperature reached being 415°C for both model and experiment. In the same time, voltage drop due to self-discharge is also well predicted [138]. This model can also calibrate the gas release during the thermal runaway process. This model is a powerful tool which have high potential in many applications relating LIBs.

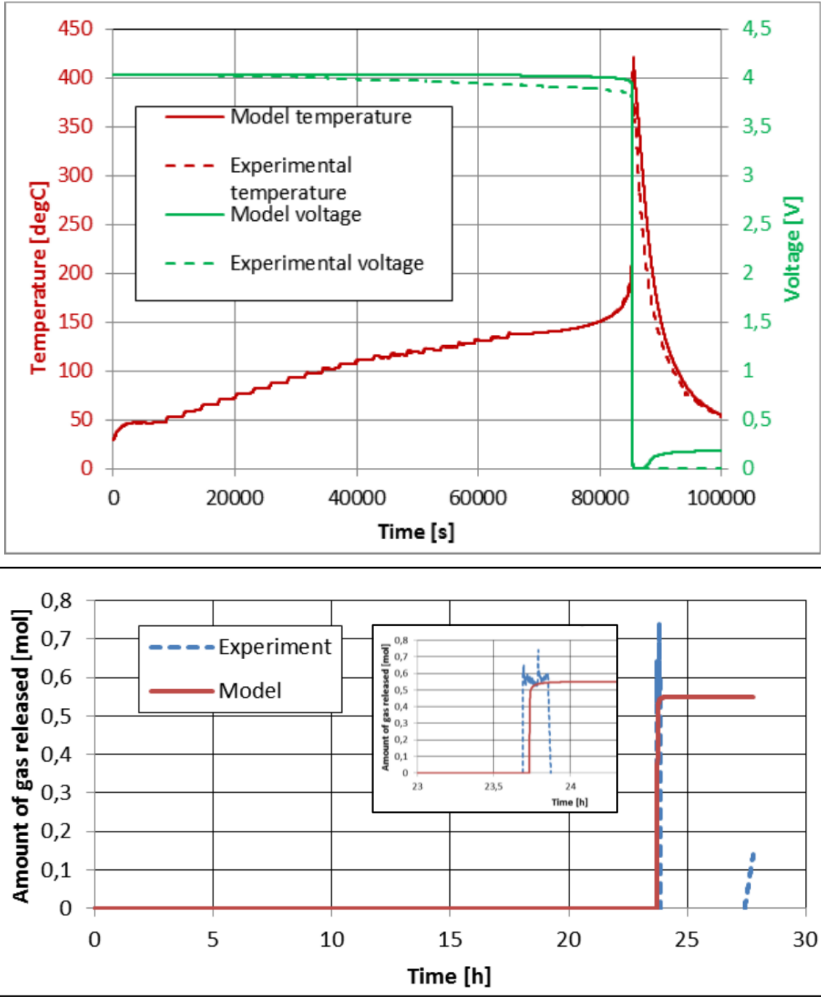


Figure 47: (Left) Voltage and temperature evolution versus time: comparison between model prediction and experiment measurements. (Right) Gas release during HWS test [138]

1.4.2.3 Early detection of Thermal runaway based on gas sensing modelling

Early detection made before propagation critical time is needed to avoid further hazards of thermal runaway. The recent study of Cai *et al.* [142] has shown that surface temperature measurement is too slow for thermal runaway detection while using gas sensing method can enable earlier detection for thermal runaway.

They modelled the initial gas generation coming from SEI decomposition which is used for early detection of a potential thermal runaway event, with the assumption that the quantity of CO₂ generated is equal to the amount of SEI decomposition [142]. The gas flow process is simulated in COMSOL, using the module Transport of Diluted Species in Porous Media.

Their model has successfully predicted the amount of gas release in the initial stage of a thermal runaway. The gas sensor readings for CO₂ concentrations will determine the presence of a thermal runaway event if the CO₂ gas detector exceeds 2000 ppm for more than 10 seconds.

1.5 Conclusions

With an intense bibliography study since the very beginning, we have explored above the state-of-the-art bibliography on almost all aspects relating to the thesis works. This bibliographic study has been updated throughout the whole research. Some main conclusions have been drawn yet, regarding thermal runaway target mechanisms, material choice or modelling approach, as guideline for this thesis.

With very high content of Ni, safety is critically the major technological problems of NMC811. This is therefore one of the target technology studied in this scoping project. Besides, safety concerns of NCA are also one of the target study of this thesis.

Soft internal shorting is often the predominant reason for thermal runaway activation, but they are relatively hard to control, and therefore not included in this study. In the scope of this work, we will study the thermal runaway phenomenon under the thermal abuse only because it is the most direct way to exceed the thermal stability limits of a Li-ion cell and lead to thermal runaway. Moreover, the chain exothermic reactions happen under near adiabatic conditions. It explains our experimental strategy to use Accelerated Rate

Calorimetry (ARC) as a preferable technique to simulate the environment inside the Li-ion cells, which can facilitate the identification of the thermal runaway reaction kinetics.

As safety control of Li-ion battery is very critical and urgent, it is believed that the effort in modelling thermal runaway phenomenon is worth to be emphasized for a long time. The development of multi-physics and multi-scale models is the selected way, to pave the way for future optimization of Li-ion battery safety management system at module or pack levels.

Chapter 2. Experimental study targeting further understanding of the thermal runaway of LIBs at pristine and aged states

“Not everything that can be counted counts, and not everything that counts can be counted.”

- Albert Einstein

Contents

2.1	Introduction	85
2.2	Technology selection rationale	88
2.3	Multi-scale cell analysis	89
2.3.1	Physico-chemical characterization of the selected batteries	91
2.3.2	Electrical characterization	104
2.3.3	Thermal analysis	110
2.4	Cell aging behaviour study	111
2.4.1	Check-ups and cell storage	113
2.4.2	SEI-driven aging	115
2.4.3	Experimental evaluation of cell aging due to Li plating	126
2.5	Thermal safety tests	128
2.5.1	Thermal safety test in pseudo-adiabatic condition of ARC	129
2.5.2	Thermal safety test in Oven (Oven test)	151
2.6	Conclusions	162

2.1 Introduction

Thermal runaway has been identified as a major hazard with LIBs. The investigation on the battery safety as a standalone component or in various contexts of use (consumer products, e-mobility...) has become a hot topic from last decade [97, 143]. As described in Chapter 1, at the cell level, this complex phenomenon depends mainly on the chemistry of the cell components, the safety features of the cell, the level of state of charge and the aging state of the cell.

Most of the studies on the thermal runaway of LIBs have been consisted in experimental approaches based on the safety abuse tests and battery post-mortem analyses [9, 84, 94, 97, 113, 144]. These approaches can access the occurrence of thermal runaway as well as the reactivity of the battery cell. However, due to the complexity of the phenomena, modelling approach and simulation are then needed to predict battery safety performance while taking into account different factors influencing the thermal runaway. Therefore, the combined experimental and modelling approaches are used in this thesis.

The main goals of this experimental study were to perform the thermal runaway on LIBs at different state of charge (SOC) and different aging states to provide sufficient databases for predictive model calibration and validation considering different factors impacting the battery safety at cell level.

Figure 48 presents the interconnected processes included in the experimental study. The complete multi-scale cell analysis investigated the pristine, aged and thermally abused states of LIBs while the safety-focused aging campaign artificially aged the battery samples, focusing on the two target mechanisms of SEI-growth and Li Plating in a controlled and measurable way. And finally, the thermal safety tests on cell level performed the thermal runaway considering the intertwined impact between cell technology, SOC level and aging on the phenomenon.

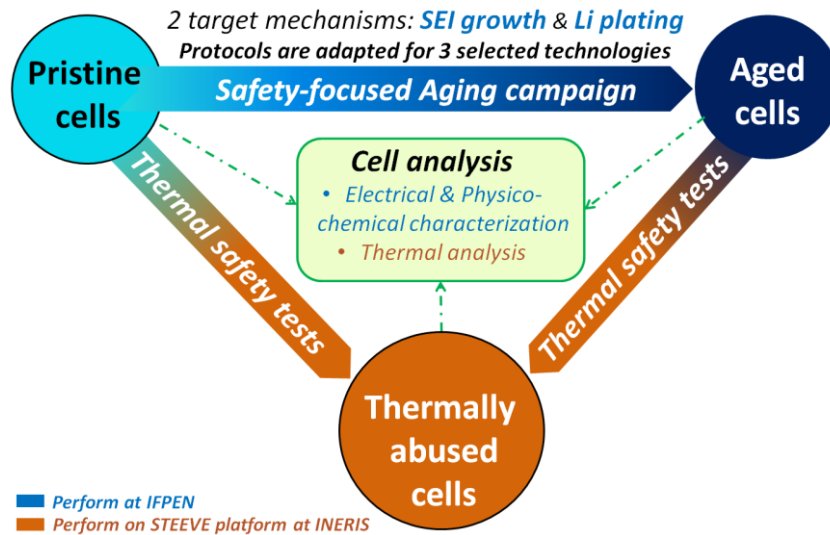


Figure 48: Project experimental study

The required experimental databases for the calibration of the thermal runaway model are summarized in Table 9.

Table 9: The experimental databases required for the calibration of the thermal runaway model. (*) The relating equations used in modelling work in chapter 3.

Experimental tests	Extracted brut data for the model	Unit	Input parameters for the model	Relating equation(*)
Thermal abuse test in pseudo-adiabatic condition in ARC	C_p of the cell from 35°C - 60°C (estimated by developed R application)	$J/(kg \cdot K)$	Average C_p of the cell	45
	Power sent from sample heater P_{heater}	W	P_{heater}	30, 34,35
	Cell skin average temperature during thermal runaway	°C	$T_{experiment}(t)$	-
	Ambient temperature around the tested cell	°C	$T_{amb}(t)$	35,36
	Cell voltage	V	$U_{cell_real}(t)$	-
Physical measurement	Cell weight	g	M_{cell}	30, 34,35
	Cell volume	m^3	V_{cell}	
Galvanostatic test: C/20 at	Cell capacity before the thermal runaway	Ah	Q_{cell}^0	17

25°C				
Post-Mortem analysis on Pristine state	Estimated mass of negative electrode active material	g	w_{ne}	7,9
	Estimated mass of positive electrode active material	g	w_{pe}	11
	Estimated mass of electrolyte	g	w_e	13
	Initial advancement of positive electrode and electrolyte decomposition reaction (Fractional conversion of positive electrode) at 100%SOC	[-]	α_0	12
	Initial concentration of Li intercalated in the negative electrode at 100%SOC	[-]	c_{ne0}	10
Electrochemical tests: GITT at 25 °C	OCV(SOC)	V	OCV(SOC)	2
HPPC at different temperatures and SOC	Cell charge/discharge resistances depending on different temperatures and different SOC	Ω	$R_{ch}(T, SOC), R_{dch}(T, SOC)$	2,3,4
Post-Mortem analysis on aged states	Initial advancement of positive electrode and electrolyte decomposition reaction (Fractional conversion of positive electrode) at 100%SOC at aged state	[-]	α_{0_aged}	12
	Initial concentration of Li intercalated in the negative electrode at aged state	[-]	c_{ne0_aged}	10
	The amount of SEI formed: estimated fraction of Li inside unstable SEI and the normalized thickness of SEI	[-]	c_{SEI0_aged}	8
		[-]	t_{SEI0_aged}	10

2.2 Technology selection rationale

The initial choice of study technologies greatly influences the rest of the work. The high energy density Ni-rich technologies were selected for this research because of the growing interest about these technologies in the context of a quest for better performances (according to the recent literatures mentioned in Chapter 1). The size (in term of capacity) and format of a cell can also have a significant effect on safety behaviour [10]. For this project, we fixed the cell format studied in order to simplify and to avoid introducing another variable in the study. After discussion, we decided to choose cylindrical 18650 cell format according to these reasons:

- The cylindrical format is one of the most common cell formats and the basic phenomenology of the provided battery chemistry is the same, while difficulties may arise from mechanical aspects. This is also one of the formats studied in the recent studies [134, 145, 146] and the previous thesis [16]. The heat generation and diffusion in a cylindrical format is usually lower than in pouch or prismatic formats [147] which allows to assume that if the thermal runaway is well studied in case of cylindrical cell, it could also be estimated in pouch or prismatic cells with an acceptable uncertainty.
- 18650 size: 18650 cells (e.g., from Japanese/Korean manufacturers) have been widely used essentially for consumers products for quite a while, and according to international regulations for transport of dangerous goods (UN TDG model regulations), these are subject to reportable quality control procedures. Therefore, functional and safety performance repeatability could be assumed as representative of best products currently available on the market.
- The detection of a temperature rise could be easier in the case of small cells, since only one or two sensors (thermocouples) might be needed for detection. In contrast, for larger cells, more sensors are needed.

Two 18650 Ni-rich, high-energy batteries from the new Li-ion battery generation were selected, namely a LG 18650 HG2 and a Panasonic NCR 18650 GA. The general electrical characteristics of these selected cells are shown in Table 10.

Table 10: Selected Ni-rich commercial batteries (from datasheets). (*) Verified by IFPEN.

	LG 18650 HG2	Panasonic NCR18650GA
<i>Nominal Capacity</i> (*)	3Ah	3.45 Ah
<i>Charging voltage</i>	4.20V+/-0.05V	4.20 +/-0.03V
<i>Standard charge</i>	1.5 A (C/2)	1.725 A (C/2)
<i>Standard discharge</i>	0.6 A (C/5)	0.69 A (C/5)
<i>Max. charge current</i> (*)	4 A	1.725 A
<i>Max. discharge current</i> (*)	20A	10A
<i>Cut off voltage</i>	2.5V	2.5V
<i>Operating temperature</i> (*)	Charge 0 °C ~ 50 °C Discharge: -20 °C ~ 75°C	Charge: +10 ~ +45 °C Discharge: -20 ~ +60 °C

A complete analysis was performed on pristine cells in order to carefully check the cell chemistry, and thereby to confirm the choice of highly reactive Ni-rich LIBs technologies studied. The LG HG2 and Panasonic NCR GA are based on NMC811 and NCA, respectively, as the positive electrode active materials, and with graphite-SiOx composite technologies as the negative electrode active materials. More details are found in the following.

2.3 Multi-scale cell analysis

The aim of this complete multi-scale cell analysis was to support the interpretation of the multi-scale thermal runaway phenomena, ranging from internal physico-chemical characterization to battery components reactions (electrodes, electrolytes, and separator), and further to the thermal propagation of cell core and safety features (pressure disk, button vent, gasket seal, open center core, etc.) involved in the thermal runaway process. To take into account the aging impact factor, the cells were analysed at different stages (pristine, after certain level of aging and after thermal runaway). Figure 49 presents the multi-scale analysis process of Li-ion cell.

At the cell scale in Figure 49, the electrical analysis was carried out on the selected batteries at 25 °C which provided the information on the cells' state of health (corresponding to the cell actual capacity) by galvanostatic test at C/20, impedance distribution by galvanostatic electrochemical impedance spectroscopy (GEIS) and pulse power characterization (PPC)

tests, OCV of the cell depending on SOC by galvanostatic intermittent titration technique (GITT) technique and cell rate capability by cycling test at different charge/discharge C-rates. The X-ray tomography analysis was made on the selected cells to investigate the internal structure of a battery, especially for cell safety features that directly link to the venting mechanism and for battery types with a central core metallic structure.

At the half-cell scale in Figure 49, the electrical analysis were made to estimate the negative / positive electrode capacities as well as the concentration of Li intercalated in the negative electrode and the fractional conversion of positive electrode. The quantity of SEI formed was also estimated thanks to the half-cell analysis.

At the component scale in Figure 49, scanning electron microscopy (SEM) and Energy Dispersive X-Ray Analysis (EDX) methods have been used to give the knowledge about the morphology and geometry of cell components, especially about the cell electrode active grains and different layers of the separator. Additionally, techniques based on differential scanning calorimetry (DSC) measurements were implemented to study the thermal stability of the separators used in selected LIBs.

At the material scale in Figure 49, Energy Dispersive X-Ray Analysis (EDX) was used to indicate the existing chemistry in the cell electrodes, and to identify the active material stoichiometry in the electrode grains. The electrolyte was analyzed by gas chromatography mass spectrometry (GC – MS) method.

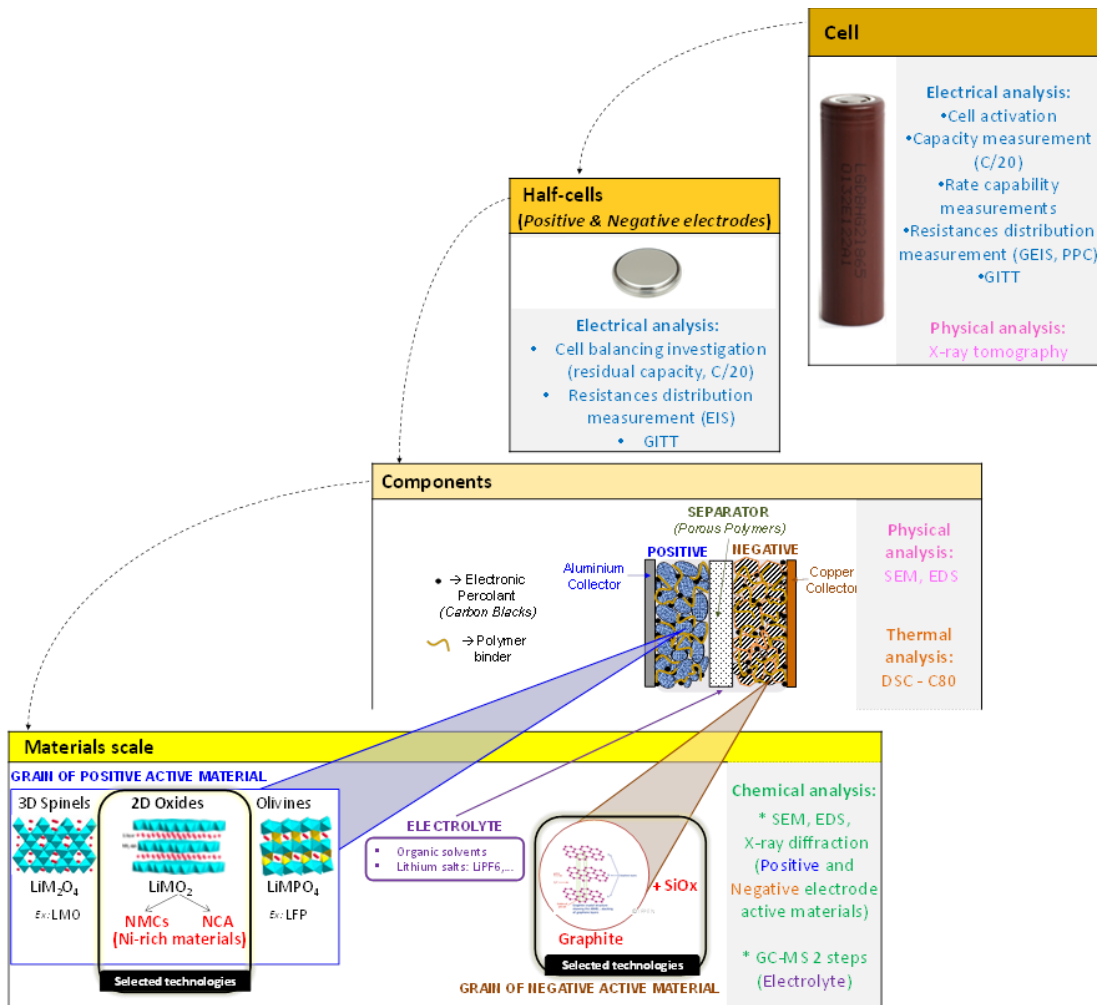


Figure 49: Process of the complete multi-scale analysis of Li-ion battery cell

The results of the multi-scale cell analysis on pristine cells are presented in the following.

2.3.1 Physico-chemical characterization of the selected batteries

These cell physical properties have very small cell-to-cell variation. The cell weights of LG HG2 and Panasonic NCR GA are 44.70 ± 0.30 g and 47.25 ± 0.15 g, respectively.

The internal structure and safety features of these cells were investigated by the X-ray tomography analysis. Figure 50 presents the global view from axial direction (left) and longitudinal direction (right) of 2 selected technologies.

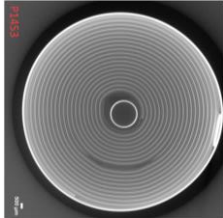

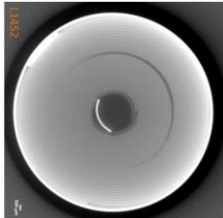
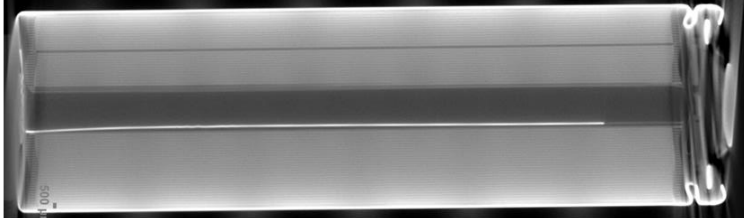
	Global view from axial direction	Global view from longitudinal direction
Panasonic NCR GA		
LG HG2		

Figure 50: Global view from axial direction and longitudinal direction of the selected technologies (performed by IFPEN).

The presence of the stiff metal tube in the centre of Panasonic cells (the open centre core) is clearly observed in Figure 50 (the light line in the global view from longitudinal direction), which allows the pressure equalization and prevents the winding ejection during thermal runaway (explained in chapter 1). In case of LG cells, there is a metal bar instead of a complete stiff metal tube. Other safety features implemented in the selected cells were also revealed by X-ray tomography techniques applied to visualize cell header content, as shown in Figure 51.

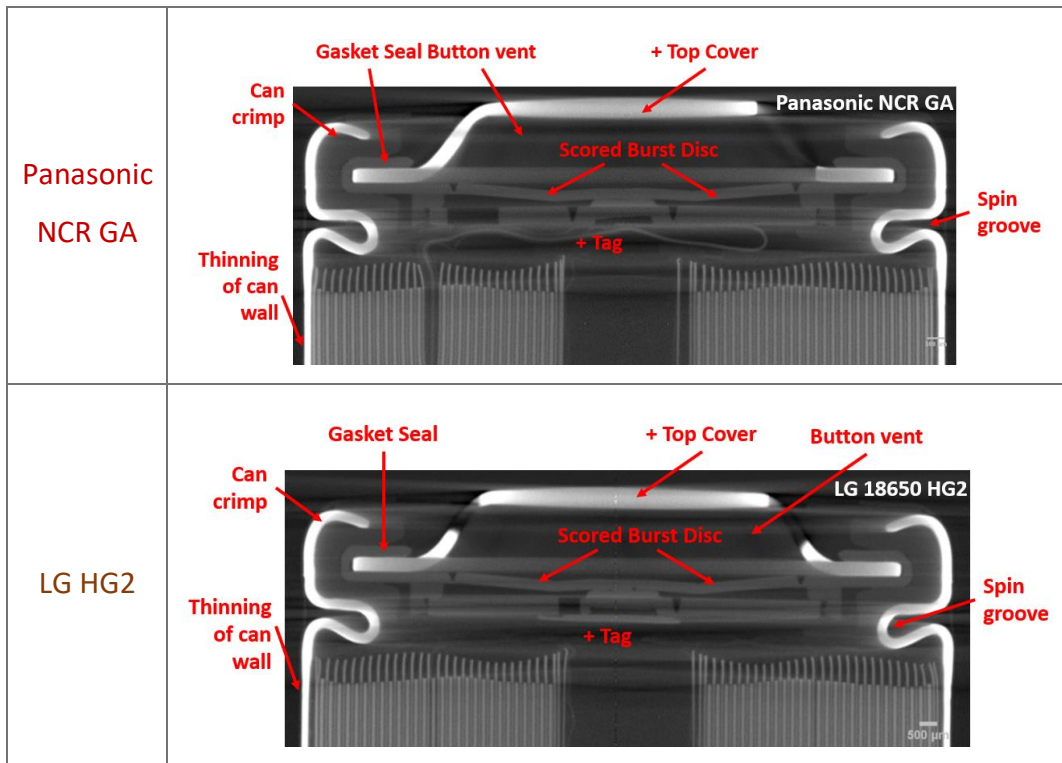


Figure 51: Cell header design of cell P1453 - Panasonic NCR GA and cell L1452 - LG HG2 (analysed by IFPEN) revealing included safety devices from tomography imaging.

2.3.1.1 Cell electrodes

After dismantling, the geometry of cell electrodes was analysed by SEM and EDX analysis. The physical measurements are summarized in Table 11, Table 12 and Table 13.

Table 11: Cell mass and extracted electrolyte mass of the tested cells

Tested cell	Cell mass (g)	Extracted electrolyte mass (g)
Panasonic NCR GA	47.173	2.223
LG HG2	44.57	2.48

Table 12: Physical measurements for the negative and positive electrodes and separator of Panasonic NCR GA. () Average values*

Parameter	Unit	Positive electrode	Negative electrode	Separator
Length	cm	124.8	128.8	138.2
Width	cm	5.8	6	6
Electrode plating area	cm ²	723.84	772.8	-
Electrode plating thickness (*)	μm	69	84	-
Electrode collector area	cm ²	730.8	840	-
Electrode collector thickness (*)	μm	15	12	-
Mass of electrode	g	17.09	13.0956	-
Separator area	cm ²	-	-	1658.4
Mass of separator	g			3.08

Table 13: Physical measurements for the negative and positive electrodes and separator of LG HG2. () Average values*

Parameter	Unit	Positive electrode	Negative electrode	Separator
Length	cm	185.6	213.3	208
Width	cm	5.8	6	6
Electrode plating area	cm ²	1076.48	1279.8	-
Electrode plating thickness (*)	μm	45	50	-
Electrode collector area	cm ²	1083.44	1362	-
Electrode collector thickness (*)	μm	15	14	-
Mass of electrode	g	14.55	9.44	-
Separator area	cm ²	-	-	2496
Mass of separator	g			1.46

The results show that the plating volume of the active materials on the negative electrode is bigger than that on the positive electrode for all 2 technologies, this might be due to the recommended design of cell electrode balancing for a proper and stably cell performance and aging: the negative electrode loading should be higher than the positive electrode loading to prevent the Li deposition during charging.

The positive electrode of Panasonic NCR GA consists of an Al collector of 15 μm average thickness on which is deposited an active layer of 69 μm average thickness. The SEM results show that the active layer is mainly composed of the globally spherical grains whose size varies from a few microns to nearly 20 μm with an average value around 7 μm (Figure 52). These grains are composed of particles with faceted contours whose size varies from less than 200 nm to around 1 μm . The EDX analyses show that these grains are rich in Ni and mainly composed of Ni, Co, Al and O (Figure 53). A phase of the same nature (faceted particles) forms like a binder and agglomerated between the Ni-rich grains. They are rounded carbon particles which are smaller than 70 nm.

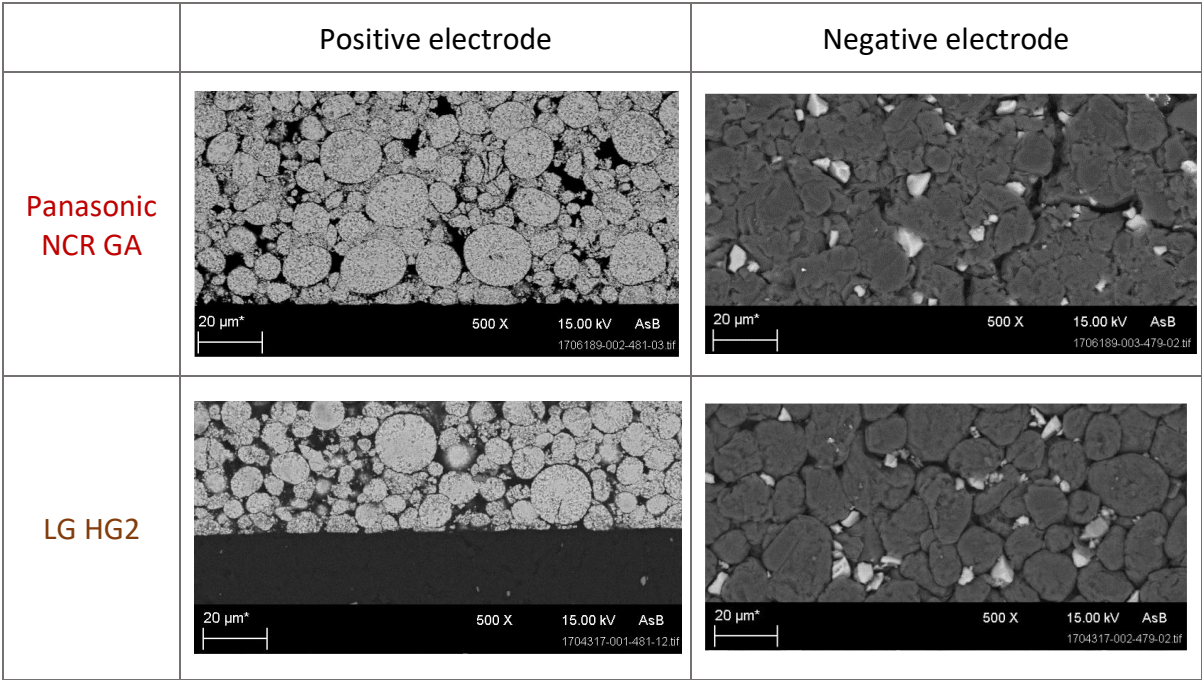


Figure 52: SEM analysis of the geometry of pristine cell's electrodes (performed by IFPEN).

The positive electrode of LG HG2 also consists of an Al collector of 15 μm average thickness on which is deposited an active layer of 45 μm average thickness. The SEM results of LG HG2 show that its positive electrode also mainly composes of spherical grains, the size of which

varies from a few microns to about 30 μm with an average size of around 10 μm (Figure 52). EDX results show that these grains are made up of the faceted particles which are mainly composed of Mn, Co, Ni and O distributed homogeneously (Figure 53). The binder, consisting of rounded particles of about 50nm, are also mainly composed of carbon.

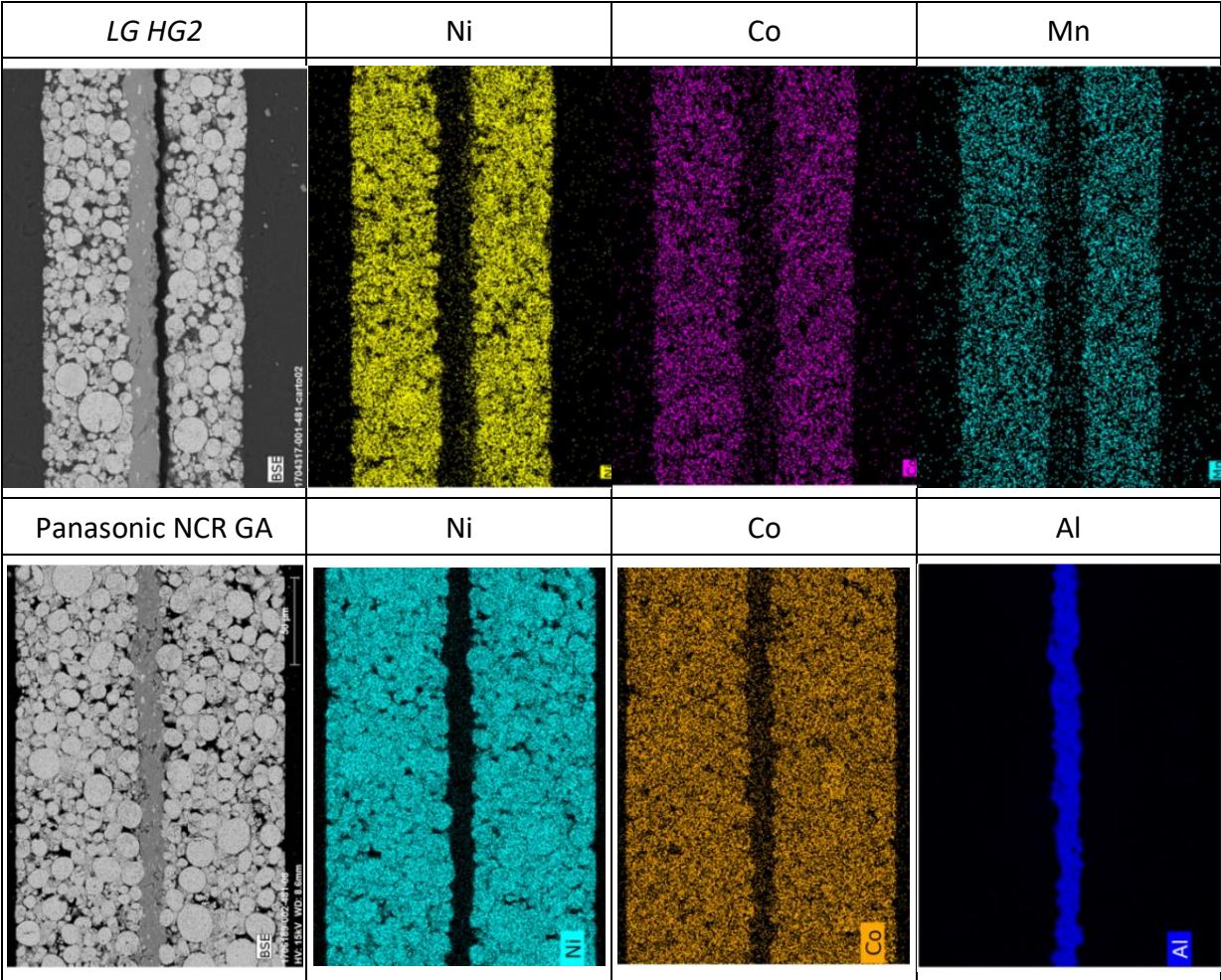


Figure 53: EDX results of chemical mapping of the positive electrodes (performed by IFPEN).

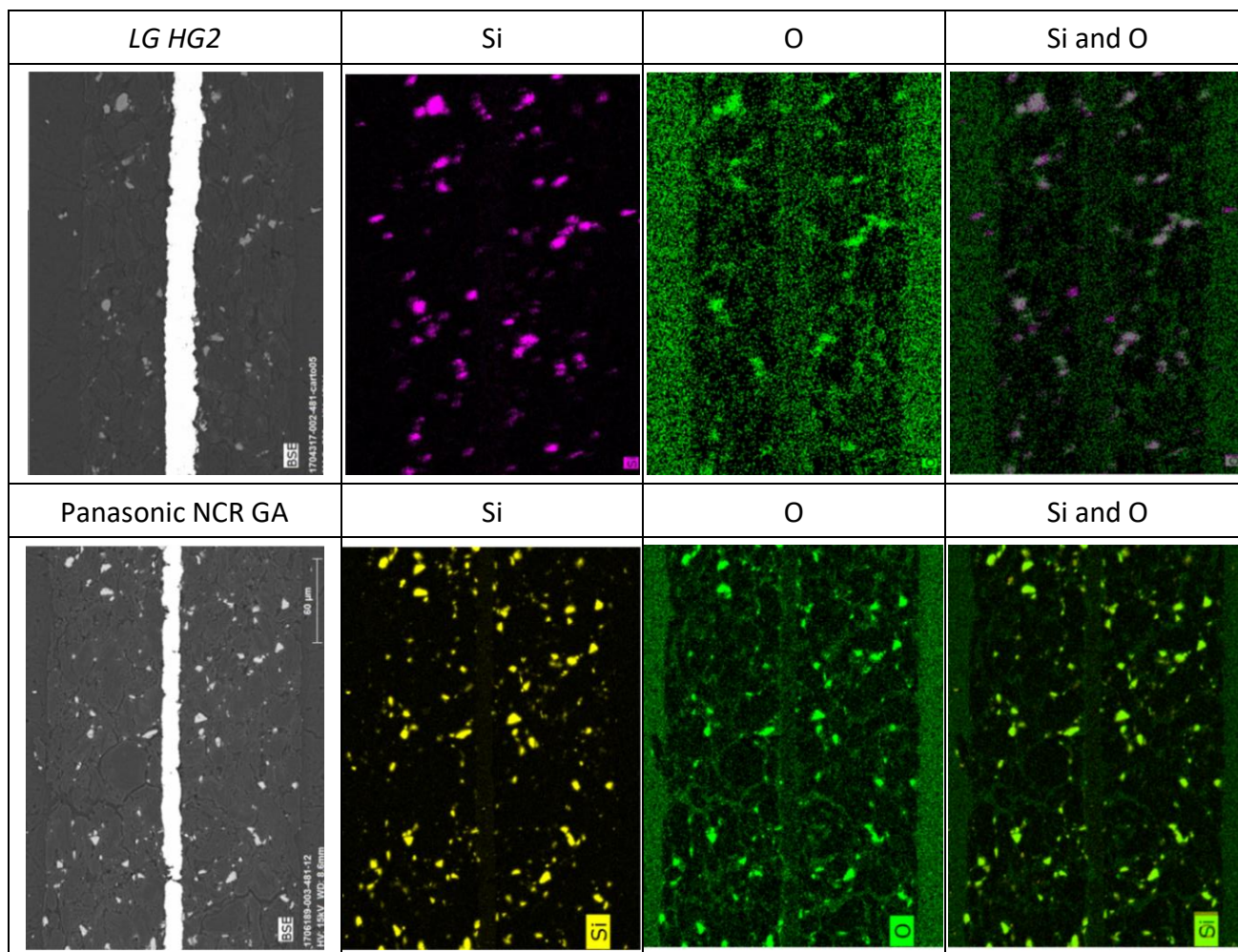


Figure 54: EDX results of chemical mapping of Si and O of the negative electrodes (performed by IFPEN).

The positive electrode composition has been identified by EDX analysis. To identify the oxide stoichiometry of the active grains, SEM-EDX semi-quantitative measurements have been made on 20 points for each technology. The results are shown in Table 14.

Table 14: The oxide stoichiometry of the active grains of positive electrodes (IFPEN).

	Panasonic NCR GA	LG HG2
Ni	0.8630 ± 0.0540	0.8357 ± 0.0105
Mn		0.0560 ± 0.0600
Co	0.0985 ± 0.0284	0.1083 ± 0.0058
Al	0.0384 ± 0.0256	
Oxyde Stoichiometry	$Li(Ni_{0.863}Co_{0.0985}Al_{0.0384})O_2$	$Li(Ni_{0.8357}Mn_{0.0560}Co_{0.1083})O_2$
Closest commercial formular	NCA	NMC811

The negative electrode of Panasonic NCR GA is composed of a 12 μm thick Cu collector on which is deposited an active layer of 84 μm average thickness. The active layer is mainly composed of graphite grains, the size of which varies from a few microns to more than 20 μm (Figure 52). These grains are blended with the smaller grains, appearing in light grey in Figure 52, which do not exceed approximately 10 μm and which are composed of Si and O according to EDX analyses.

The negative electrode of LG HG2 consists of a Cu collector of approximately 14 μm thickness on which is deposited an active layer of around 50 μm average thickness. This active layer consists of graphite grains, the size of which varies from a few microns to more than 30 μm (Figure 52). They are blended with the compact smaller grains (appearing in light gray in Figure 52 in chemical contrast) of variable shapes, rich in Si and O, of an average size being close to about 5 μm . They are evenly distributed and are located between the graphite grains.

The negative electrode compositions identified by EDX for both technologies are mainly composed of graphite grains blended with the compact smaller grains rich in Si and O. Figure 54 shows that the Si and O correspond to the same position. Therefore, we can conclude that these technologies are based on Graphite-SiO_x composite negative electrode technologies.

The analyses results described above confirmed that the selected technologies for the thesis are Ni-rich technologies, as shown in Figure 55, which is coherent with our selection priority.

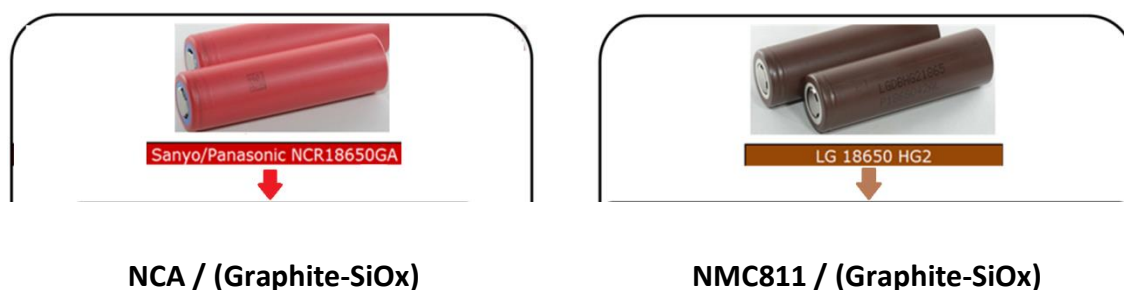


Figure 55: The selected technologies.

2.3.1.2 Cell separators

The cell separators were investigated by SEM and EDX analysis. The results show that both selected technologies' separators have double layers. However, the morphology, porosity and geometry of these separators are not the same.

The Panasonic NCR GA' separator thickness varies between approximately 31 μm and 38 μm . It is composed of 2 layers:

- a main layer, appearing dark in Figure 56 whose thickness varies between 21 and 26 μm , are rich in C. Through direct observations, we see that this layer is composed of intermingled fibers, generating a greater or lesser porosity depending on the areas observed (Figure 56.a2).
- a ceramic layer, appearing light grey in in Figure 56 whose thickness varies between 11 and 12 μm . This layer consists of small spherical grains ranging in size from about 50 nm to about 500 nm and mixed in a phase consisting of entangled carbon fibers (visible in Figure 56). On the surface of this layer, there are small particles of Co, Ni, O, and some grains of SiO_x, which are probably the pollutions come from the electrodes.

The LG HG2' separator thickness varies approximately from 12 to 13 μm , which is surprisingly thinner than that of Panasonic NCR GA. It is also composed of 2 layers:

- a main layer, appearing dark in Figure 56, is rich in C. Through direct observations, we also found that this layer is composed of entangled fibers, resulting in a greater or lesser porosity depending on the areas observed. Compared to the main layer of Panasonic NCR GA's separator, it appears that the porosity of that of LG HG2's separator is more homogeneous. On the surface of this layer, a large number of small particles rich in Al, O are visible. There are also some crystals of NaCl, some grains rich in Ca, O or Si, O and some pieces of C, which are probably the pollutions coming from the negative electrode. Therefore, this main layer is facing the negative electrode side.

- a thin ceramic layer, appearing light grey in Figure 56, whose thickness is about 1 μm . It is composed of the agglomerates of small grains rich in Al, O. These grain sizes are ranging approximately between 200 nm and 800 nm. On the surface of this layer we observed rare particles rich in Co, Ni, O and some pieces of C, which are probably the pollutions come from the positive electrode. Therefore, this main layer is facing the positive electrode side.

In order to identify the composition of these separators, the separator samples were also analysed by infrared reflection (IR) spectroscopy using a ThermoOptek Nicolet spectrometer equipped with a DTGS type detector. The IR single-reflection ATR technique (Golden Gate-type accessory) has been used.

The ATR-IR analysis found that both layers of the LG HG2 separator reported similar contributions related to similar polymer species but in different concentrations. The main layer side mainly consists of an intense contribution linked to polyethylene (PE) and the contributions related to the presence of polypropylene (PP) and ethylene carbonate (EC). The spectrum on the ceramic layer side mainly reports the contributions of EC and probably of the PP.

The 2 sides of Panasonic NCR GA's separator were also investigated by ATR-IR. The main polymer layer side mainly reports the contributions linked to PE. In addition, contributions related to the presence of EC. The ceramic layer side shows an NH function, a CO function and in addition, contributions linked to the presence of EC.

Therefore, the LG HG2' separator technology is double-layer of PP/(PE,PP) with ceramic coating and the Panasonic NCR GA' separator technology is double-layer of PE with ceramic coating.

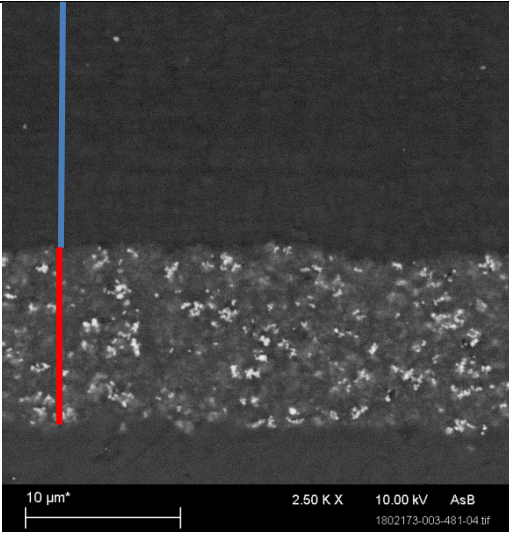
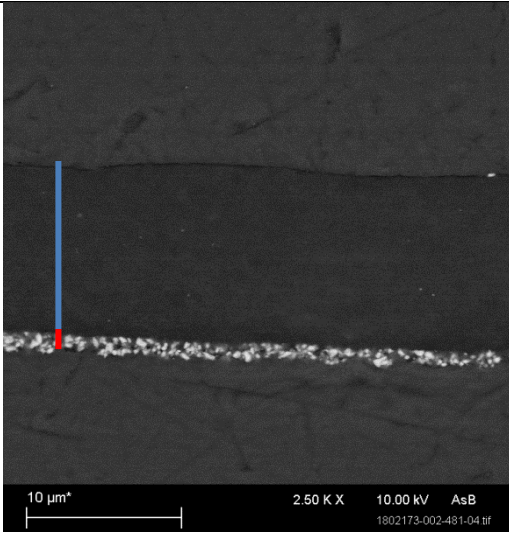
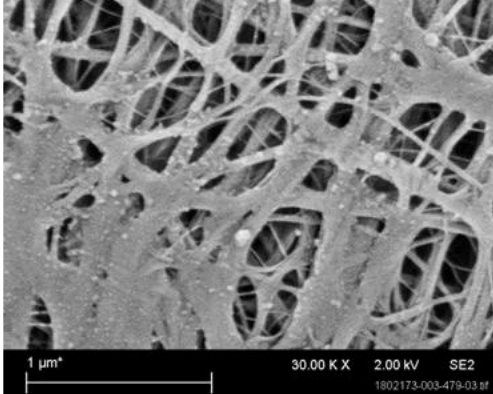
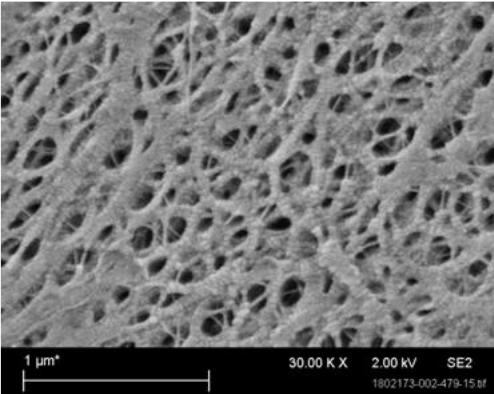
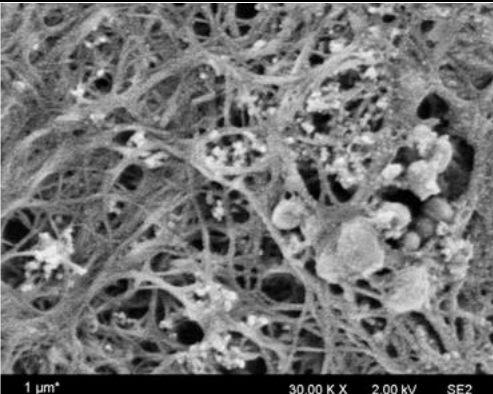
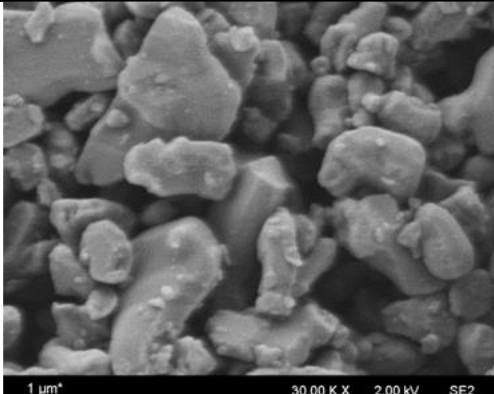
	Panasonic NCR GA	LG HG2
Double-layer separator	 <p>— : main layer, 21 – 26 μm — : ceramic layer, 11 – 12 μm (a1)</p>	 <p>— : main layer, 11 – 12 μm — : ceramic layer, ~1 μm (b1)</p>
Main layer zoom in	 <p>(a2)</p>	 <p>(b2)</p>
Ceramic layer zoom in	 <p>(a3)</p>	 <p>(b3)</p>

Figure 56: SEM and EDS analysis results of the selected technologies' double-layer separators (results from the Physical Research and Analysis division of IFPEN, 2018).

2.3.1.3 Cell electrolytes

The Lithium salt in the electrolyte, according to these cell specifications, is LiPF₆ for all 2 technologies. The composition of the electrolyte solvents and additives was investigated by GC-MS with two different protocols.

- GC-MS 2 steps: first step is the analyse of the electrolyte extracted under vacuum, the second step is the acetonitrile rinsing of the separator recovered from the pristine cell.
- GC-MS 1 step: the separator was recovered from the pristine cell and rinsed with acetonitrile x time. Then the solution was analysed by GC-MS.

The results are shown in Table 15 and Table 16.

Table 15: Data on the composition of the solvents and additives in the Panasonic NCR GA's electrolyte from performed chemical analyses.

Panasonic NCR GA's electrolyte		GC-MS 2 steps		GC-MS 1 step (Acetonitrile rinsing)
		Step 1: Extraction under vacuum	Step 2: Acetonitrile rinsing	
Alkyl Carbonate solvents (%m/m)	DMC	98.5460	0.0166	0.2694
	EMC	0.3347		
	EC	0.5374	1.1422	0.1166
	PC	0.3393	0.2074	
	DEC			0.0253
Additive	MPC			0.0059
Acetonitrile	-	-	98.4569	99.5766
Unknown	-	0.2426	0.1769	0.0062

Table 16: Data on the composition of the solvents and additives in the LG HG2's electrolyte from performed chemical analyses.

LG HG2's electrolyte		GC-MS 2 steps		GC-MS 1 step (Acetonitrile rinsing)
		Step 1: Extraction under vacuum	Step 2: Acetonitrile rinsing	
Alkyl Carbonate solvents (%m/m)	DMC	96.6743	0.0675	0.1977
	EMC	0.0031	0.0182	
	EC	2.3145	1.2486	0.1240
	PC	0.0679		0.0194
	DEC	0.0155		
Additive	MPC	0.7117	0.0565	
	VC	0.0346		
Acetonitrile	-	-	98.5804	99.6559
Unknown	-	0.1784	0.0288	0.0029

The analysis results identified the main solvents mixture existing in the electrolyte of these technologies and reveals the important concentration of the linear carbonates. For Panasonic NCR GA's electrolyte, the solvent are composed of (Dimethyl carbonate (DMC), Ethyl methyl carbonate (EMC), Ethylene carbonate (EC), Propylene carbonate (PC)) with the concentration of mostly DMC and the additive detected is methyl phenyl carbonate (MPC) $C_8H_8O_3$ (flame-retardant additive). For LG HG2's electrolyte, the solvent are composed of (DMC, EMC, EC, PC, Diethyl carbonate (DEC)) with the concentration of mostly also DMC and the additive detected is also MPC (flame-retardant additive) and VC (SEI supporting additive). Even though some additives were detected by our analysis on these commercial Li-ion cells, the presence of additives found were still limited.

It is important to note that there are some limitations of these analysis techniques. The differences in vaporization temperature between the linear (more volatile) and cyclic

carbonates cause the "under vacuum" method to favour the more volatile linear carbonates. Therefore, the technique used with 2 steps (Solvent extraction under vacuum, then acetonitrile rinsing) cannot precisely and thoroughly analyse the electrolyte solvents and additives because it cannot measure an equilibrium between the quantity of linear and cyclic solvents. Probably the cyclic solvent is not volatile and is not trapped during extraction. The technique used with 1 step (acetonitrile rinsing) also cannot identify all the composition of electrolyte.

2.3.2 Electrical characterization

2.3.2.1 Full cells

In this section, we presented the main findings of our electrical characterisation tests, focusing on the actual capacity, the rate capability, open circuit voltage and resistance of these technology at pristine state.

Stored electrical energy is straightforward to measure and usually expressed in mAh for the case of 18650 cells. Throughout cell life, cell capacity fade occurs with usage and storage. Thus, the capacity of a used cell will likely be below nominal capacity. Therefore, firstly, investigating the actual capacity of cell is necessary. In this thesis, the cell actual capacity has been estimated by C/20 _ Low C-rate charge/discharge method, as shown in Figure 57.

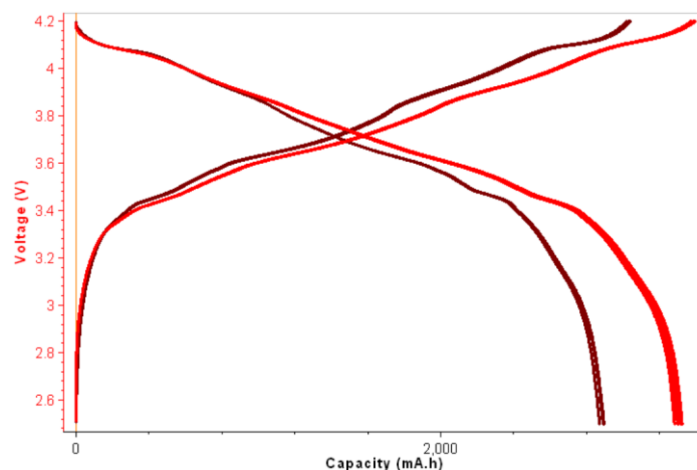


Figure 57: The actual capacity profiles of the selected technologies at their initial states (6 cells for each technology), Panasonic NCR GA (red curves) and LG HG2 (brown curves) (performed by IFPEN).

As shown in Figure 57 and Table 17, these technologies show a very good repeatability, few dispersions in pristine cell behaviours of each technology.

Table 17: Charge and discharge capacity of the selected technologies.

	Charge capacity (mAh)	Dispersion (%)	Discharge capacity (mAh)	Dispersion (%)
Panasonic NCR GA	3387.28 ± 4.93	0.14	3307.23 ± 13.39	0.40
LG HG2	3029 ± 3.30	0.11	2887.63 ± 10.77	0.37

Secondly, in order to verify if we have chosen 2 different types of technologies, we investigate the rate capability of these cells to determine their type (power, balance or energy type). The rate capability test indicate how the cell sustains high-current pulses at fast charge/discharge conditions and diffusion related processes [75]. This information is important for our understanding of the cell design and our interpretation for further results of aging and thermal runaway. Therefore, a proper cycling protocol has been applied, as follow:

- Cycling at 25°C with the same standard discharge C-rate of C/5 and charge at different C-rates (C/20, C/10, C/ 5, C/2, ...) to identify the highest limit of charge rate while maintaining the temperature safety limit of the cell during each cycle.
- Cycling at 25°C with the same standard charge C-rate of C/2 and discharge at different C-rates (C/20, C/10, C/ 5, C/2, C, 2C, ...) to identify the highest limit of charge rate while maintaining the temperature safety limit of the cell during each cycle.

The results are found in Figure 58. As observed, LG HG2 cell reached high charge/discharge rate limits, which means that this technology can provide more power, thereby, proves that this technology is power type. In the other hand, Panasonic NCR GA reached an average charge/discharge rate limits and therefore, this technology is balance type. These results also correspond to the data provided from the manufacturer.

It is also noteworthy that the higher charge/discharge C-rates can lead these cells to higher self-heating.

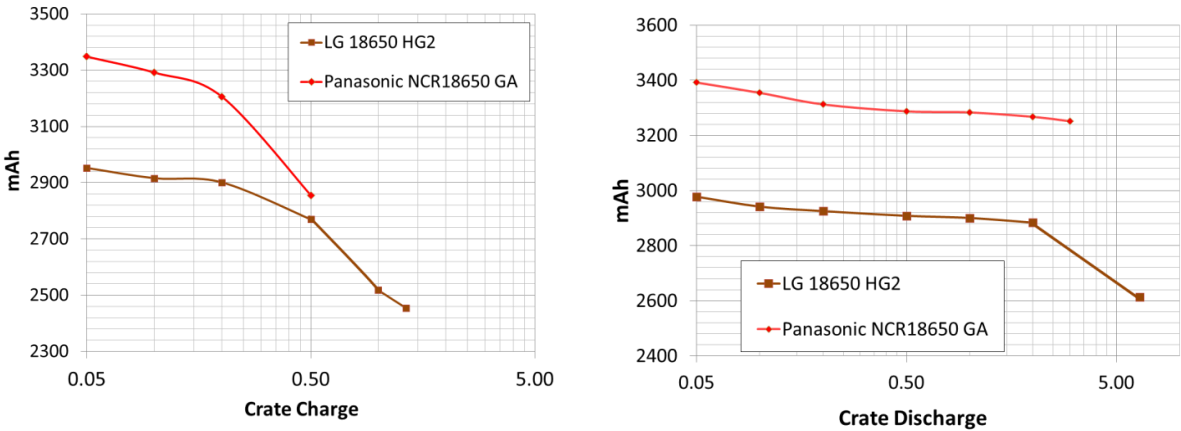


Figure 58: Charge at different C-rates (left) and discharge at different C-rates (right) of LG HG2 and Panasonic NCR GA (performed by IFPEN).

For the electrical model of these battery, the relationship between OCV and capacity, denoted as $OCV(Q)$, has been investigated thanks to GITT test (every 5% capacity increment) at 25°C in order to estimate the SOC-dependency of OCV, denoted as $OCV(SOC)$, of pristine cells. The cell charge/discharge resistances depending on different temperatures and SOC (denoted as $R_{ch}(T,SOC)$ and $R_{dch}(T, SOC)$, respectively) have also been investigated at different levels of temperatures (20°C, 40°C) and different SOCs. The result are presented in Figure 59.

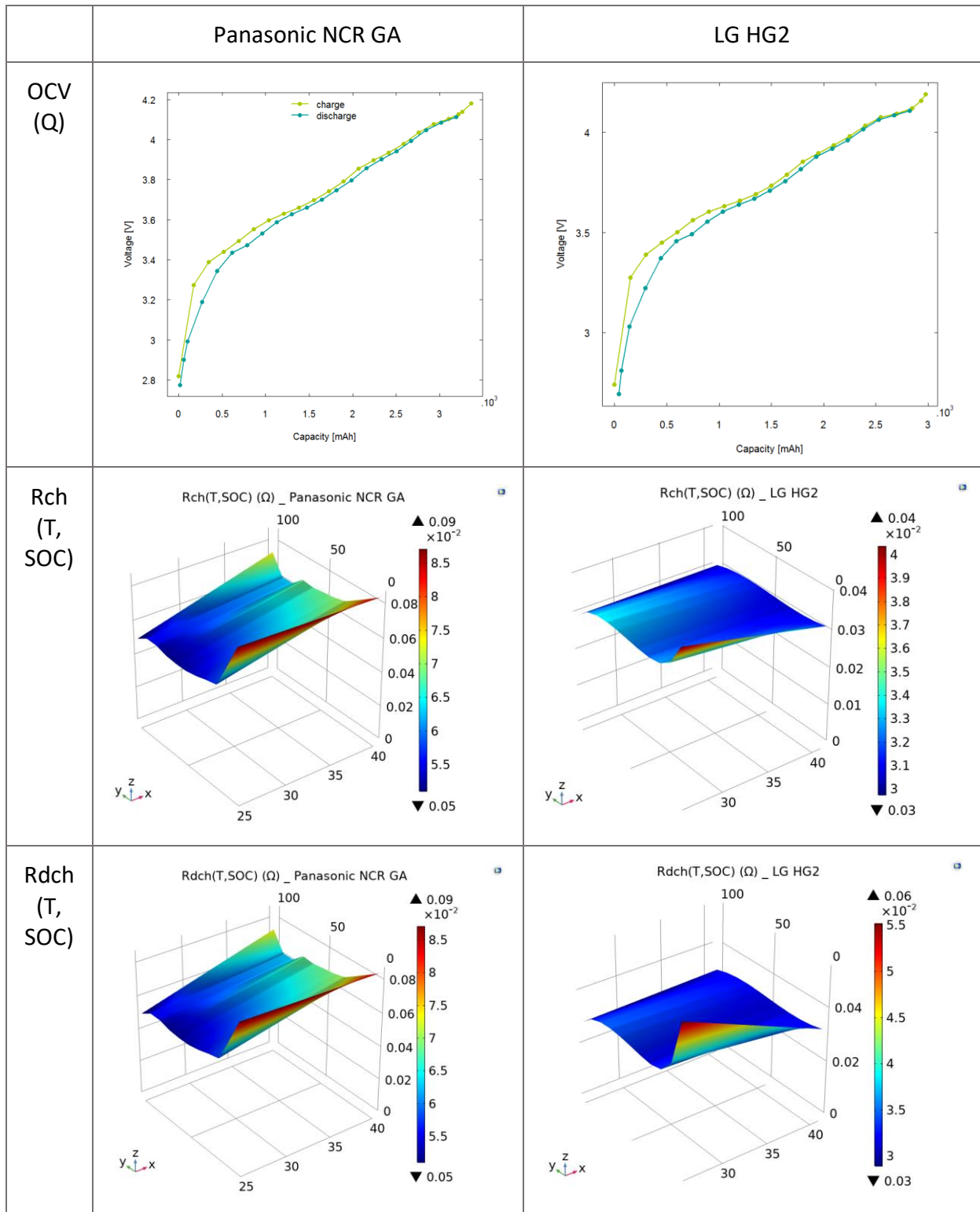


Figure 59: (OCV (Q) of Panasonic NCR GA and of LG HG2 and Rch(T,SOC), Rdch (T, SOC) of Panasonic NCR GA and of LG HG2, with x axis is temperature (T), y axis is SOC and z axis is resistances (Rch or Rdch).

2.3.2.2 Half cells

In this section, the estimations of the concentration of Li intercalated in the negative electrode and the positive electrode active material are firstly presented. Then the estimation of the quantity of active materials are explained. These results provide the initial parameters for the thermal runaway model.

The x values in Li_xC_6 and $Li_x(NCA)O_2$ or $Li_x(NMC811)O_2$ is defined as the ratio between the lithium concentration (c_s) and the maximum lithium concentration (c_s^{max}) in the electrode. In the case of negative electrode, x presents the normalized concentration of Li intercalated in the negative electrode active material, denoted as c_{ne} . In the case of positive electrode, x addresses the conversion degree of the positive electrode active material, denoted as α .

For example, Figure 60 presents the x values at the 100%SOC and 0%SOC of Panasonic NCR GA cell with the voltage – capacity curves of cell electrodes.

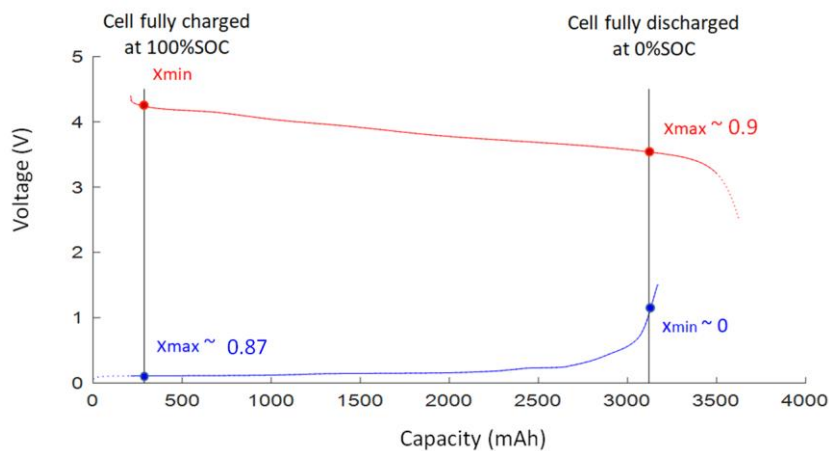


Figure 60: x values at the 100%SOC and 0%SOC of Panasonic NCR GA (red: positive electrode, blue: negative electrode).

For the negative electrode, we have calculated the x values based on the estimated maximum lithium concentration in full cell electrode, as presented in Table 18 and Table 19. For the positive electrode, it operates in a narrower stoichiometry range, thereby, we cannot precisely estimate its maximum concentration and its x values. Therefore, we will use the parameters found in the literature, as shown in Table 18 and Table 19.

Table 18: *x* values estimation at 100%SOC and 0%SOC of Panasonic NCR GA.

<i>Cell capacity = 3402mAh.</i>	Unit	Negative electrode	Positive electrode
The maximum lithium concentration in half cell (Surface of the half-cell negative = 1.1304 (cm ²))	mAh	5.72	-
The maximum lithium concentration in full cell electrode	mAh	3909	-
<i>x</i> values at 100%SOC (4.2V)	[-]	0.87	0.188 - 0.23 [119]
<i>x</i> values at 0%SOC (2.5V)	[-]	0.02	~0.9 [118]

Table 19: *x* values estimation at 100%SOC and 0%SOC of LG HG2.

<i>Cell capacity = 2892 mAh</i>	Unit	Negative electrode	Positive electrode
The maximum lithium concentration in half cell (Surface of the half-cell negative = 1.1304 (cm ²))	mAh	2.84	-
The maximum lithium concentration in full cell electrode	mAh	3215.35	-
<i>x</i> values at 100%SOC (4.2V)		0.899	0.21 – 0.26 [118, 148]
<i>x</i> values at 0%SOC (2.5V)		0	~0.9 [118]

The quantity of the active materials were estimated in Table 20.

Table 20: *Estimation of the quantity of the active materials of the selected technologies.*

	Unit	Panasonic NCR GA	LG HG2
Quantity of graphite (estimated from the estimation of the maximum electrode capacity)	g	10.5	8.64
Quantity of extracted electrolyte	g	2.223	2.48
Quantity of positive active materials	g	15.75	14.07

2.3.3 Thermal analysis

DSC thermal analysis can be a very powerful method to distinguish the thermal stability of cell components. For this thesis, DSC test (TA Instruments Q100) was made to study the thermal stability of cell separators. We have use the ramp of 5°C/min as similar with the increment of thermal abuse test in ARC. The results are shown in Figure 61.

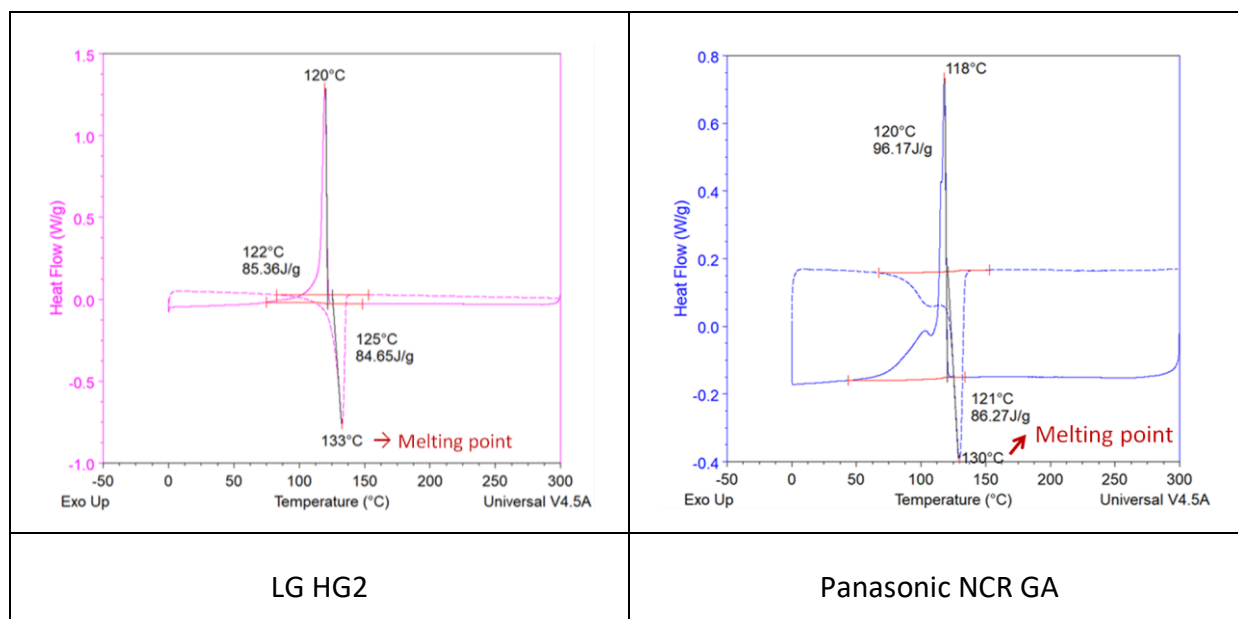


Figure 61: The melting points of the tested separators.

The mass of the tested samples of the LG's and Panasonic's separators were respectively 2.7 mg and 2 mg.

According to the SEM/EDX analysis results above, the LG HG2's separator technology is double-layer of PP/(PE,PP) with ceramic coating. This is one of the commonly used commercial separators with PE and PP based. They designed with a shutdown feature, by which two layers have different phase transition temperatures. As the temperature of the cell increases, the lower-melting component (PE) melts and provide a shutdown behaviour at 130 °C with little shrinkage until 170 °C when PP component melts [3]. This is coherent with the DSC analysis results as observed in Figure 61, the melting point of LG HG2's separator is at ~130°C.

The gap between 130 °C–170 °C can enhance the safety of the cell to some extent. When temperature continues increasing, the shrinkage follows the shutdown which leads to a

sharp increase in the cell resistance [115] and the internal short circuit (ISC) will occur once the positive electrode and negative electrode contact together. The ISC caused by shrinkage can produce massive heat generation so that the separator collapses quickly, whereas the ISC can also be mild and the separator may collapse much later. The collapse temperature of the PE/PP based separators is similar with that of the PP separator (170 °C). However, in case of LG HG2, its PP/(PE, PP) separator with ceramic coating could enhance the collapse temperature to be as high as 200–260 °C [3].

For the Panasonic NCR GA, according to the SEM/EDX analysis results, its separator technology is double-layer of PE with ceramic coating. Similarly, the lower-melting component (PE) melts as the temperature of the cell increases and provides a shutdown behaviour at ~130 °C, as seen in Figure 61 of the DSC analysis results. The thickness of this separator is more significant compared to that of LG HG2's, this factor combined with the ceramic coating may enhance the collapse temperature of this technology's separator.

2.4 Cell aging behaviour study

As described in section 1.3.6, aging of LIBs has a notable impact on the abusive behaviour of thermal runaway according to recent literature [8–13]. It is an inevitable degradation process which leads to capacity loss and internal impedance increase, thereby, loss of rate capability and cell performance during the whole lifetime of Li-ion batteries. It links closely to the inherent safety issues inside Li-ion batteries. Several studies confirmed that SEI growth driven aging process seems to play a critical role in thermal runaway. In the context of emerging higher capacity Li-ion batteries including Ni-rich high energy technologies, Li plating also seems to have a notable impact on the behaviour of Li-ion cells in thermal abuse conditions through increased risk of short circuit, and hence likely higher sensitivity to thermal runaway [9–11, 14, 15]. Both related phenomena in high energy LIB cells were focused in this research.

From the beginning of the work, an aging campaign of the selected technologies has been put in place since this step requires time. This campaign targets two aging mechanisms (Figure 62):

- on the one hand the predominant mechanism by SEI growth justifying a calendar aging testing protocol inspired by the work of the ANR SIMCAL project [149] completed with a cycling aging testing protocol reflecting aging from battery use at high temperature.
- on the other hand the Li plating mechanism with a campaign of cold cycling which can be inspired by the tests in progress carried out within the framework of the FUI MOBICUS project on LMO and NMC cells.

Several preliminary tests have been carried out to define a complete safety-focused aging campaign (Figure 62). Li plating aging protocol mocks up the cycling conditions at low temperature which accelerate the occurrence of Li deposition/plating and SEI-driven aging protocol replicates the storage/cycling conditions which accelerate the evolution of SEI but also minimize the occurrence of Li plating. These protocols are customized to take account of technologies studied and to achieve results that can be compared consistently in term of identical level of discharge capacity loss.

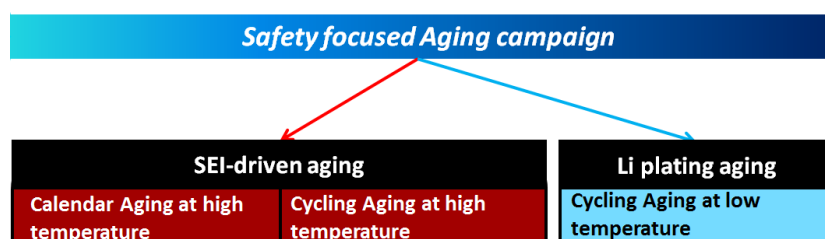


Figure 62: Safety-focus aging campaign

Knowledge of the state of aging of the cells before carrying out runaway tests is essential to allow better understanding and calibration of runaway phenomena. The quantification of SEI growth phenomena and loss of active matter are known in the Electrochemistry and Materials department thanks to the tools of Edouard *et al.* [150] based on the simulation of differential voltage. The phenomenon of Li plating is a phenomenon that has not been studied by IFPEN or INERIS until this thesis. Based on [80, 92, 93], non-destructive techniques of qualification and quantification of aging state has also been studied.

Post-mortem analyses were used to confirm and quantify the phenomenon on a batch of samples. Electrical measurement methods described in the literature [80] was evaluated and

X-ray tomography methods has also been used as non-destructive measurements. To achieve this, the work of the thesis benefits from a new microscanner set up in IFPEN which presents a better resolution than previous equipment. We were thus be able to detect the internal deformations of the stack of electrodes potentially induced by the accumulation of Li metal on the negatives and possibly the metallic deposits themselves, before carrying out the abusive tests.

The overall aging campaign includes: cell activation (check-up), aging protocols which are defined by preliminary tests, intermediate check-ups, cell storage and final check-up before post-mortem analysis or Thermal abuse tests.

In order to have comparable results, the check-up protocols stay the same for all cells and the charge/discharge C-rates of cycling aging are kept as the standard's. However, each safety-focus aging has its own specific aging protocols. To be clear, we have: SEI-driven calendar aging protocols, SEI-driven cycling aging protocols and finally Li deposition/plating aging protocols. These protocols will be defined based on firstly the bibliography studies and most importantly our pre-tests.

The safety-focused aging campaign was successfully completed. Subsequently, the two target aging mechanisms have been covered with their own defined aging protocols.

This campaign provided a batch of aged cells with known states and can be used to study the impact of aging on safety.

2.4.1 Check-ups and cell storage

The check-ups and storage conditions is presented in this section.

2.4.1.1 Check-ups:

To monitor the degradation of the cells, a uniform checkup procedure was performed periodically at 25 °C for all cells (Figure 63).

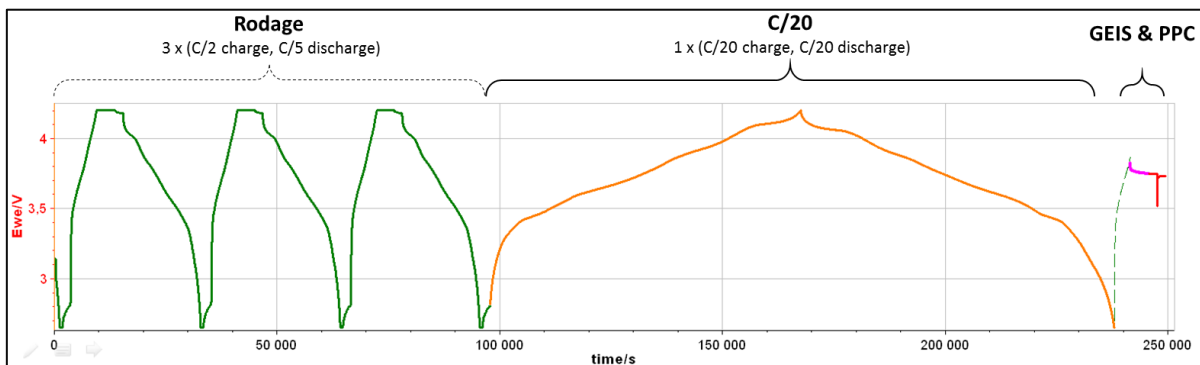


Figure 63: Check-up setup in 25 °C chamber (left) and Check-up protocol (right)

The C/20 provides the information on the actual charge/discharge capacity of the cell and the input for the simulation of cell differential voltage. The GEIS impedance analysis and HPPC resistance analysis provides information of ohmic contact, migration of Li^+ through SEI layers, charge-transfer impedance at electrode/electrolyte interfaces, and diffusion related processes [75].

2.4.1.2 Cell storage condition:

At the beginning of the project, we bought 2 lots of cells, which includes 180 Panasonic NCR GA cells and 200 LG HG2 cells. The cell storage conditions are considered to be important for keeping the cell states before and after the aging during a long time before thermal abuse test. According to bibliography, a properly designed and manufactured Li-ion cell has very low self-discharge rates commonly quoted in the range of 1 to 5 % per month when stored at 25 °C or below, and initially at approximately 50% SOC [4]. Storage at low voltages (low SOC), and/or low temperatures, reduces the magnitude of the calendar life aging effect, and

would thus, seem to indicate that storage at low SOC is preferable for maximizing cell life and keeping the cell state.

Therefore, in order to well maintain the cell state, we stored our cells at low SOC (~50 %) in low ambient temperature (5.5 °C - 6.5 °C).

2.4.2 SEI-driven aging

2.4.2.1 SEI-driven calendar aging

In research of the suitable storage conditions which accelerate the evolution of SEI, we decided to choose the most severe conditions of calendar aging for the first pre-test: the test cells will be calendar aged at 100 % SOC at maximum storage temperature (60 °C) with check-ups at 25 °C only at beginning and end of aging to limit any impact of the check-ups at 25°C.

Having the knowledge from SIMCAL project which has thoroughly investigated the battery degradation due to SEI evolution during the calendar aging [151], we decided that the SEI-driven calendar aging protocol is the same as this pre-test: during the calendar aging, the fully charged (100 % SOC) test cells would be stored under controlled conditions in climatic chambers of 60 °C with intermediate check-ups every 8 weeks until an expected level of aging, which are ~10 %, ~20 %, ~30 % discharge capacity loss.

Test setup and CU Planning

For calendar aging, no Li deposition was expected since the cells were not charged during aging, however, they were charged during periodic capacity check-ups (25 °C, charging rate: C/2). Therefore, we built the CU planning for this aging with the minimized number of check-ups made on the same test cells. To be specific, CU planning for Panasonic NCR 18650 GA is explained in Table 21.

After a storage duration of every 8 weeks, 6 selected cells were placed in the temperature chamber at 25 °C until they reached their thermodynamically equilibrium. Then, the check-up on these cells has been performed.

Table 21: CU planning of SEI-driven calendar aging for Panasonic NCR 18650 GA

	CU0	Storage	CU1	Storage	CU2	Storage	CU3	Storage	CU4	Storage	CU5	Storage	CU6	Storage	CU7	Storage	CU8
Number of cells ->	all	21	6	16	6	11	6	11	6	6	6	6	6	1	6	1	6
21 BAT 1530	☑		☑		☐		☐		☐		☐		☐		☐		☐
20 BAT 1525	☑		☑		☐		☐		☐		☐		☐		☐		☐
19 BAT 1524	☑		☑		☐		☐		☐		☐		☐		☐		☐
18 BAT 1517	☑		☑		☐		☐		☐		☐		☐		☐		☐
17 BAT 1516	☑		☑		☐		☐		☐		☐		☐		☐		☐
16 BAT 1513	☑		☑		☐		☐		☐		☐		☐		☐		☐
15 BAT 1512	☑		☑		☐		☐		☐		☐		☐		☐		☐
14 BAT 1507	☑		☑		☐		☐		☐		☐		☐		☐		☐
13 BAT 1506	☑		☑		☐		☐		☐		☐		☐		☐		☐
12 BAT 1501	☑		☑		☐		☐		☐		☐		☐		☐		☐
11 BAT 1500	☑		☑		☐		☐		☐		☐		☐		☐		☐
10 BAT 1480	☑		☑		☐		☐		☐		☐		☐		☐		☐
9 BAT 1479	☑		☑		☐		☐		☐		☐		☐		☐		☐
8 BAT 1471	☑		☑		☐		☐		☐		☐		☐		☐		☐
7 BAT 1470	☑		☑		☐		☐		☐		☐		☐		☐		☐
6 BAT 1465	☑		☑		☐		☐		☐		☐		☐		☐		☐
5 BAT 1464	☑		☑		☐		☐		☐		☐		☐		☐		☐
4 BAT 1459	☑		☑		☐		☐		☐		☐		☐		☐		☐
3 BAT 1458	☑		☑		☐		☐		☐		☐		☐		☐		☐
2 BAT 1445	☑		☑		☐		☐		☐		☐		☐		☐		☐
1 BAT 1444	☑		☑		☐		☐		☐		☐		☐		☐		☐
25 BAT 15xx	☑		☑		☐		☐		☐		☐		☐		☐		☐
24 BAT 15xx	☑		☑		☐		☐		☐		☐		☐		☐		☐
23 BAT 15xx	☑		☑		☐		☐		☐		☐		☐		☐		☐
22 BAT 15xx	☑		☑		☐		☐		☐		☐		☐		☐		☐

Note:
 Storage condition: 60°C, 100% SOC
 CU: Check-up at 25°C
 Total time: 448 (days) <=> 14,9 months
 ☐ 5 back-up cells are discharged & stored in cold chamber
 ☐ 1 discharged cell for analysis: Xray tomography --> SEI
 ☐ 2 charged cells for ARC test in INERIS
 ☐ 1 discharged cells for ARC test in INERIS
 ☐ 5 charged cells are put back into chamber of calendar aging

Results

This aging campaign was successfully carried out for the two technologies. The main obtained results in terms of capacity fading process and impedance increase of Panasonic NCR GA and LG HG2 are presented in Figure 64 and Figure 65.

The calendar aging occurred very slowly for both technologies. This observation confirms that these selected technologies are high quality products, there is very low cell-to-cell variation in the results of calendar aging.

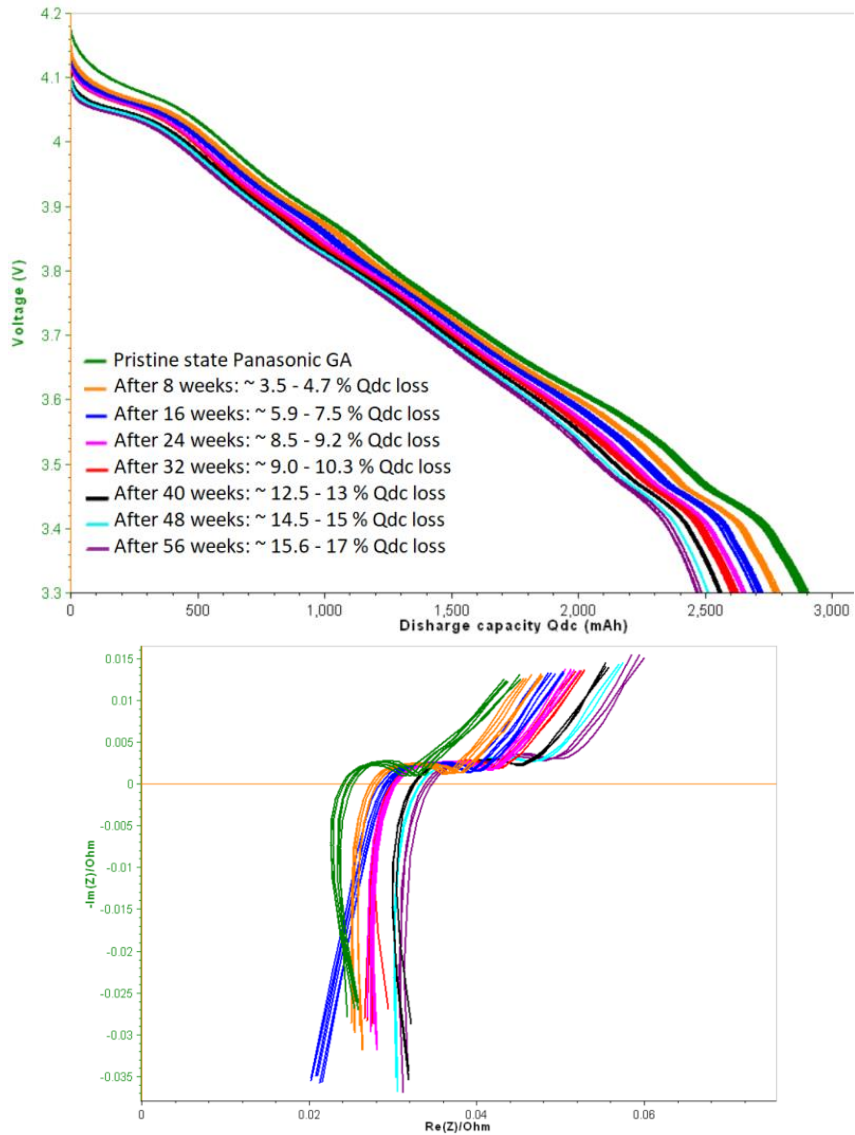
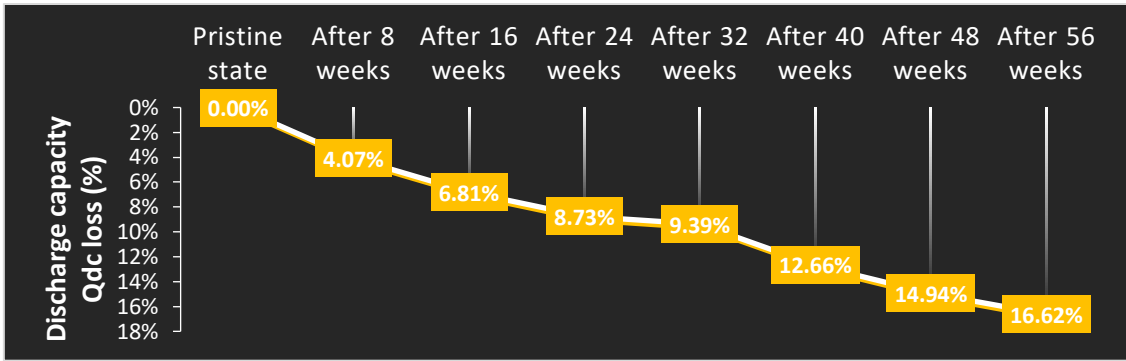


Figure 64: SEI-driven calendar aging of Panasonic 18650 GA (6 cells for each check-up): Discharge capacity loss (top), discharge profiles and cell impedance at the pristine and aged states (bottom).

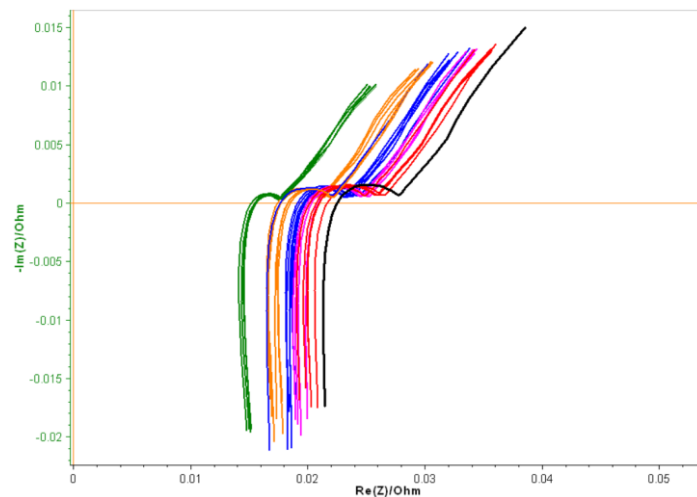
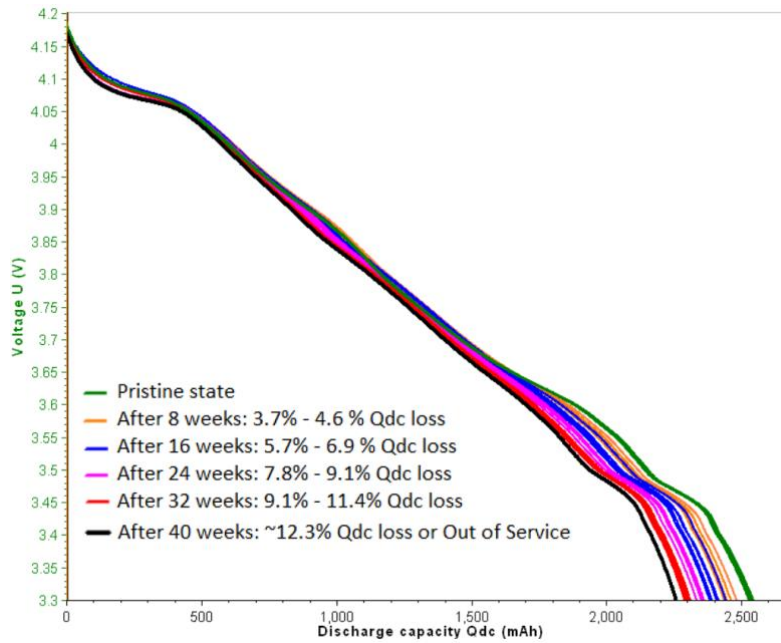
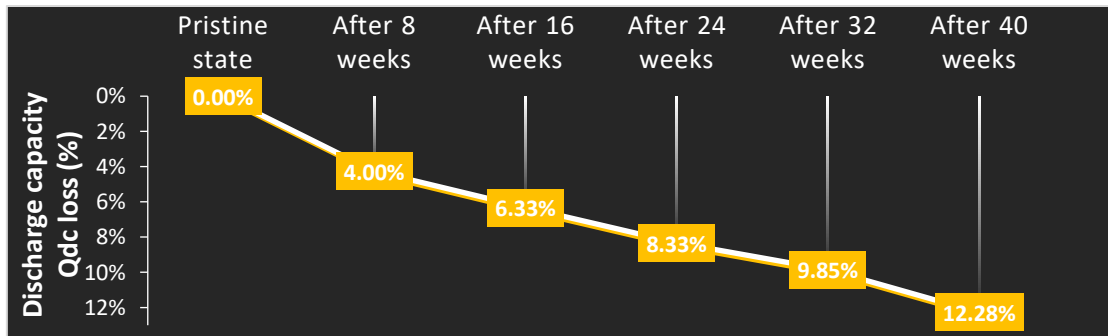


Figure 65: SEI-driven calendar aging of LG 18650 HG2 (6 cells for each check-up): Discharge capacity loss (top), discharge profiles and cell impedance at the pristine and aged states (bottom).

In case of Panasonic NCR GA (Figure 64), the cells successfully passed the whole calendar aging process until the end. After 56 weeks, we obtained a batch of aged cells with known states and which could be used to study the impact of calendar aging on safety.

In case of LG HG2 (Figure 65), after 40 weeks of calendar aging, some cells could not maintain the voltage at 100%SOC (~ 4.2V): They lost their voltage down to 0 – 1 V (reflecting out of service state). This might be due to the occurrence of soft internal short circuits during aging which might originally relates to the thin design of LG HG2's separator. Therefore, in the scope of the thesis timeline, these cells were not chosen to study the impact of calendar aging on safety.

2.4.2.2 SEI-driven cycling aging

Preliminary tests and defined protocols

Preliminary test dedicated to this purpose were not found necessary. Indeed, based on our knowledge that SEI growth will be dominant aging process, being accelerated under the cycling conditions at higher temperature, we can consider the results of reference cells cycled at 25 °C as the preference cycling results for this aging. Therefore, similarly as the case of SEI driven calendar aging, we choose the most severe SEI-driven cycling protocols for these test cells:

- Cycling at 45 °C (max cycling temperature);
- Standard cycling C-rate (C/2 charge, C/5 discharge) and 30min rest after every charge and after every discharge in order to have a stable SEI layer;
- Δ SOC: 0 – 85 % SOC, we intentionally avoid Li deposition in this aging and not exceed the temperature safety limit of the cell during each cycle, therefore, these cells are not cycling at high voltage range (85 – 100 % SOC).

Test setup and CU planning

Due to the limitation of time and equipment, we decided to age the tests cells by module of 8 cells connected in parallel, as shown in Figure 66:

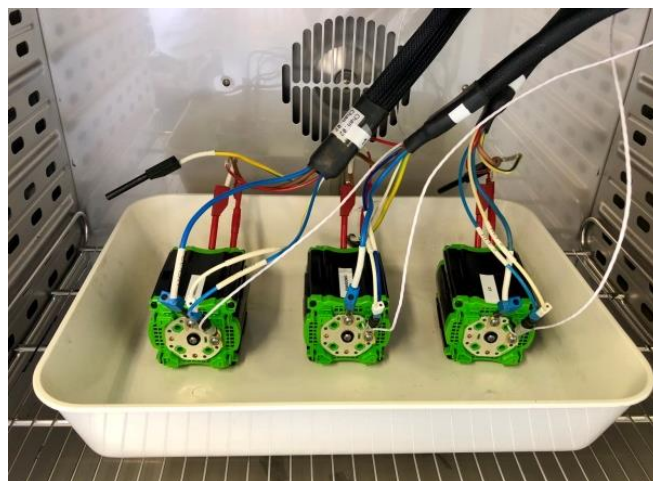


Figure 66: Test setup of cycling aging

Every 50 cycles, to spare time and also not interrupt the evolution of SEI at 45 °C, we include in the aging protocols the intermediate check-ups of 2 full cycles (Δ SOC 100 %) to control the level of aging. When the level of aging obtained by these intermediate check-ups passed a certain level, we dismantled the module and made a complete check-up at 25 °C for 6 cells of each technology. When we obtained the aged cells with the level of aging in term of discharge capacity loss we wanted, which are also ~10 %, ~20 %, ~30 % discharge capacity loss similarly as the calendar aging, the aging protocol was stopped.

Results and comparison between SEI-driven cycling and calendar aging

The impact of different aging condition (SEI-driven calendar and cycling aging) of Panasonic NCR GA is well observed in Figure 67. We found that different SEI-driven aging conditions have an impact on the electrochemical state of the battery. As observed in Figure 67, even though the aged cells reached the same level of aging (Q_{dc} loss ~ 16.5%), these cells exhibited different discharge profiles as seen in Figure 67. Moreover, the impedance evolution of these cells is also different. Therefore, it would be interesting to study this impact on the thermal runaway.

The origin of the capacity losses may be due to:

- Loss of lithium inventory (LLI) by the growth of the SEI
- Loss of positive active material (LAMpos)

- Loss of negative active material (LAMneg)

In order to integrate these SEI-driven aging into the models, we need to determine the LLI which allows us to estimate the quantity of SEI. In order to do that, we need to understand and to determine the LLI, LAMpos, LAMneg. There are two methods to do so, which are:

- Measurements of half-cells after dismantling in the discharged state of pristine and aged batteries:

- i. the residual capacity is measured on the positive half-cell which is directly related to the LLI during SEI formation (pristine state) and SEI growth after aging.

- ii. the capacity of the electrodes before and after aging are measured and compared to investigate the LAMpos and LAMneg.

- The differential voltage technique is used with the tool of Clément Edouard [150]. For this tool, the electrode potentials E^+ and E^- vs electrode capacity of pristine half-cells are the inputs. By adjusting on LLI in order to superimpose the peaks of the differential voltage of the pristine full cell with the differential voltage reconstructed from the half-cell electrodes. As the results of this tool, we obtained the LLI of cell formation and full cell balancing (Figure 68).

From this reconstruction, we gradually modify LLI, LAMpos and LAMneg to superimpose the reconstructed curve with the differential voltage curves of aged cells.

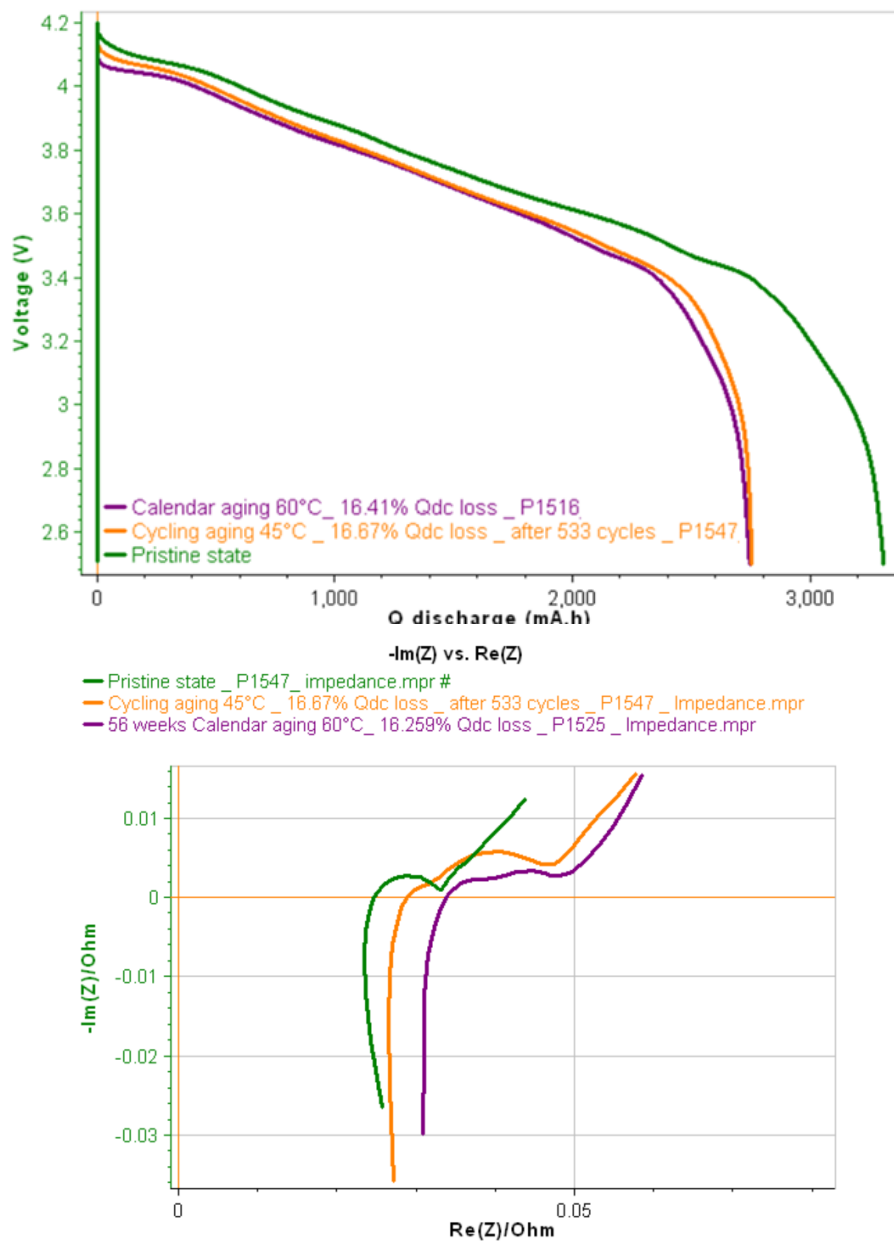


Figure 67: Discharge profiles (top) and cell impedances (bottom) comparison between SEI-driven calendar and cycling aging of Panasonic NCR GA

In the case of pristine state, we faced a problem for the first method: The residual capacity measured on the positive half-cell was too low. This is probably explained by a short circuit, even a very soft one, made while disassembling the cell. When a short-circuit is made, the voltage of the half-cell drops so the potential of the positive drops which forces its lithiation. Therefore, we lose information on the capacity which is directly related to the LLI. However,

the capacity and potential measurements of the electrode half-cells are correct, they can therefore be used.

For the second method of Clement's tool, it gives a very good result as seen in Figure 68, we see that all the peaks are superimposed and the capacity is good.

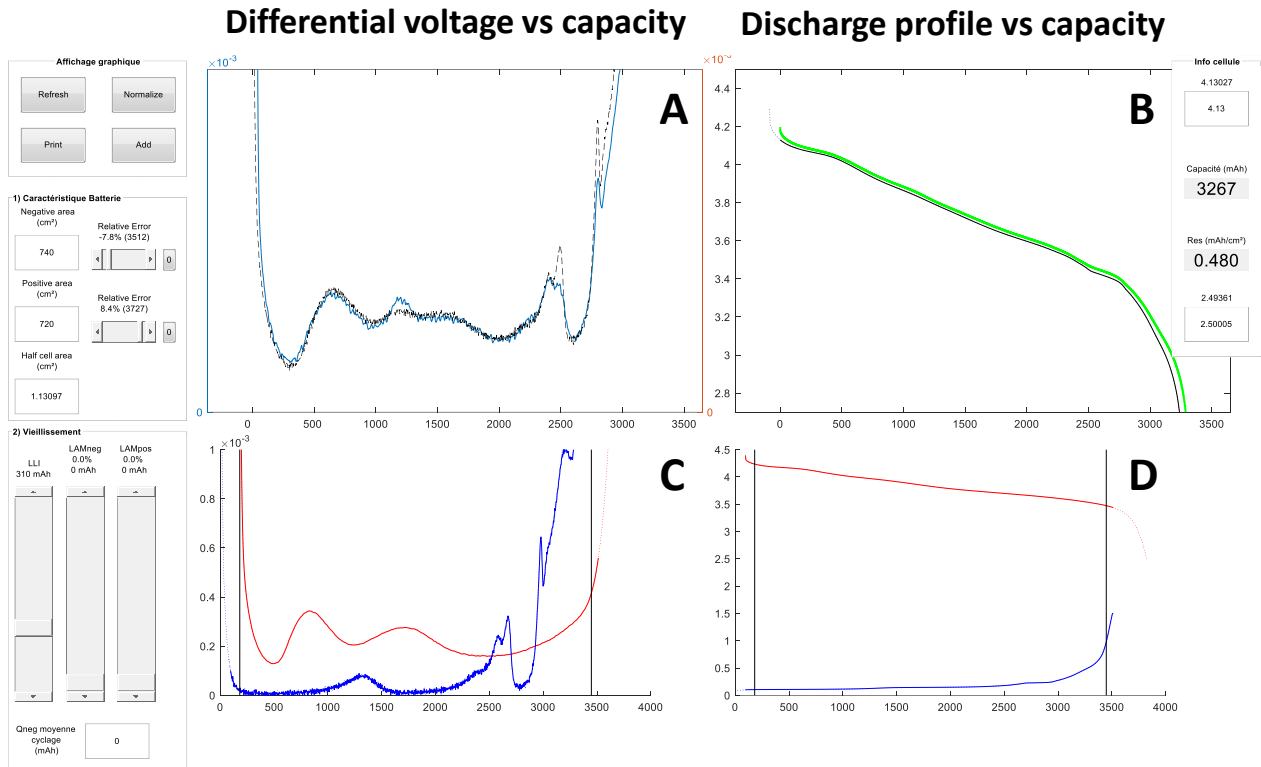


Figure 68: The differential voltage and discharge profiles vs capacity of pristine cell (A,B respectively) and of its electrode half-cells (C,D respectively) on Clément's tool interface.

We can therefore use this value of 310 mAh of LLI obtained from the tool as the amount of SEI in the model for pristine state, and also the reference to reconstruct the aged curves.

In the case of the aged states, for the first method, we obtained the residual values measured on the positive electrode are much larger. This is a good sign of probably no short circuit during dismantling. The results are below:

- LLI: There are 392 mAh for the calendar aging and 513 mAh for the cycling aging. Therefore values are all greater than 310 mAh (LLI of pristine state) which is due to the additional SEI produced during aging.

- LAMpos: The half-cells show that there is no loss of capacity of positive for the calendar aging but a loss of 9% positive electrode capacity for the cycling aging.
- LAMneg: The half-cells show a loss of 13.2% of capacity for calendar negative electrode and 21.1% of capacity for cycling aging.

We observed that the cycling aging has an impact on the aging of the electrodes.

By using the second method, we try to confirm these results with the discharge profile reconstruction and investigate the association of LLI / LAMpos / LAMneg which gives the total ~16.5% cell capacity loss in both cases.

For the calendar aged cell, the reconstruction of cell discharge profile and differential voltage by Clément's tool (Figure 69) gives the results below:

- LLI: 400 mAh therefore very close to the 392 mAh obtained on the first method.
- LAMpos: 0% similarly as the first method
- LAMneg: 360 mAh (10.2%) of instead of 513 mAh (13.2%) for the first method.

These are good results to confirm the identified association of LLI / LAMpos / LAMneg aging mechanisms and their proportion for calendar aging.

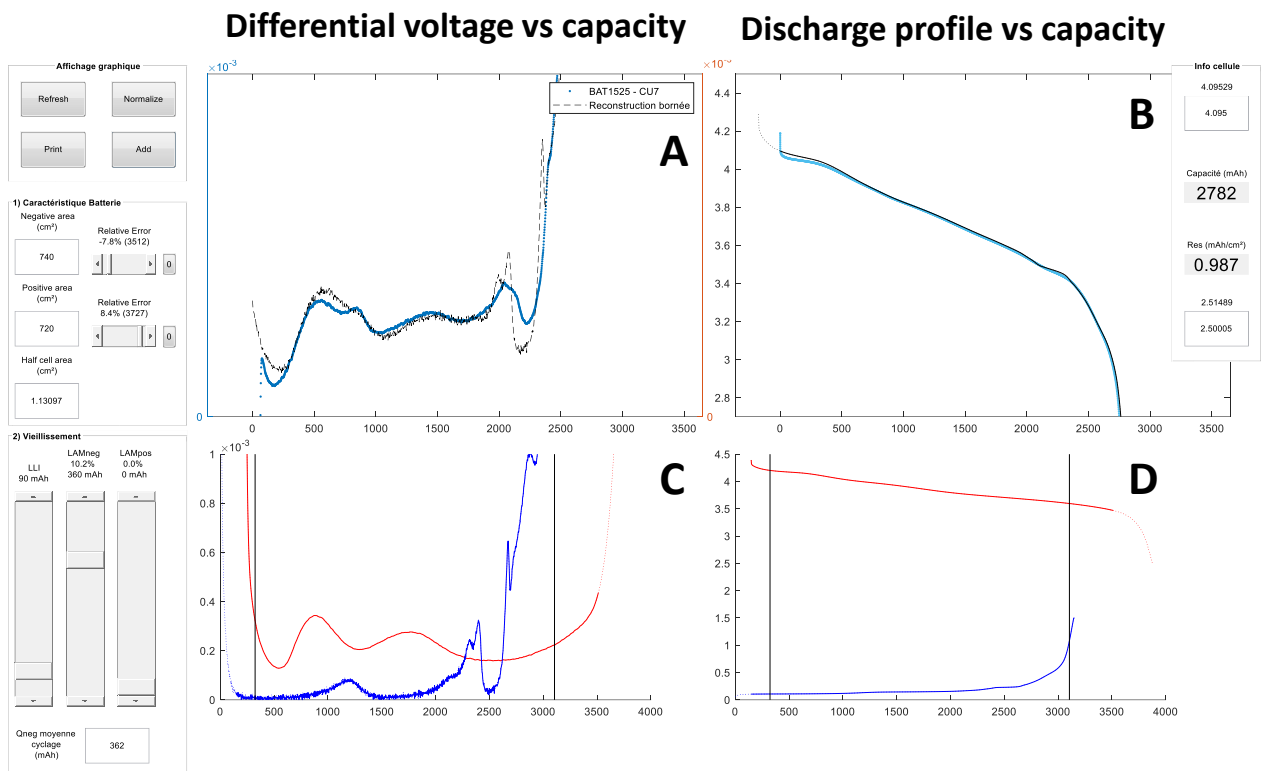


Figure 69: The differential voltage and discharge profiles vs capacity of calendar aged cell (A,B respectively) and of its electrode half-cells (C,D respectively) on Clément's tool interface.

However, as observed in Figure 69, the superposition of some peaks of the differential voltage vs capacity curve is not achieved. Here, we reach the limits of the tool because it was developed for non-blended electrodes which means that electrodes' aging is the same on all active materials. In our case, the negative is composed of graphite and silicon so if the loss of capacity of the negative electrode, LAMneg, is mainly due to silicon, the tool cannot work because the shape of the potential curve changes. This is also the reason why the tool failed for the case of cycling aged cell if it bases on the pristine electrode potentials.

Therefore, the reconstruction based on the aged negative electrode potential and the pristine positive electrode potential were carried out to not take into account the loss of LAMneg since it is already taken into account. With this method we obtained:

- LLI: 520 mAh which is very close to 515 mAh obtained in the first method.
- LAMpos: 6.8% (255 mAh) which is close to 9% (287 mAh) obtained with the first method.

Even though the reconstruction is not perfectly achieved, but this reconstruction confirms the measurements of half-cells. The final results are summarized in Table 22.

Table 22: The results of LLI, LAMpos, LAMneg of pristine, calendar aged and cycling aged cells.

	LLI (mAh)	LAMpos (mAh)	LAMneg (mAh)
Pristine	310	-	-
Calendar	392 (+ 82mAh)	0%	13.2%
Cycling	515 (+ 205 mAh)	9%	21.1%

2.4.3 Experimental evaluation of cell aging due to Li plating

2.4.3.1 Preliminary tests

The implementation of this study about Li deposition is new to our experience. Therefore, several pre-tests have been carried out in this campaign which dedicated to the study and validation of bibliography on this aging mechanism.

For the preliminary tests at the beginning of the thesis, we tried severe conditions of Li deposition aging on Panasonic NCR GA cells. The test cells have been aged at their minimum recommended temperature (-15 °C) by standard cycling C/2 charge and C/5 discharge at cold temperatures with 30 min rest after each cycle (Δ SOC: 100 %) continuously 83 cycles with check-ups at 25 °C only at the beginning and the end of aging. As expected, the test cell drastically aged and preliminary test by completion of this aging procedure with the temperature maintained from -15.5 °C to -14.4°C as seen in Figure 70, the tested cells P1 and P2 lost 31 – 37 % of its initial discharge capacity. We also obtained the combination of the hints of Li deposition as described in the bibliography (Figure 70). We also found that the stripping of Li is more observed in the first cycles at Li plating condition, than in the later cycles. Li stripping also appears more significantly at lower temperature than at the reference temperature of 25°C.

For conclusion, even though we do not have access to the analysis methods that can give us the direct or indirect evidence of Li deposition, the combination of the hints of Li deposition

and the differences electrochemical behaviours between this aging and SEI-driven aging can already be valuable for our result interpretation.

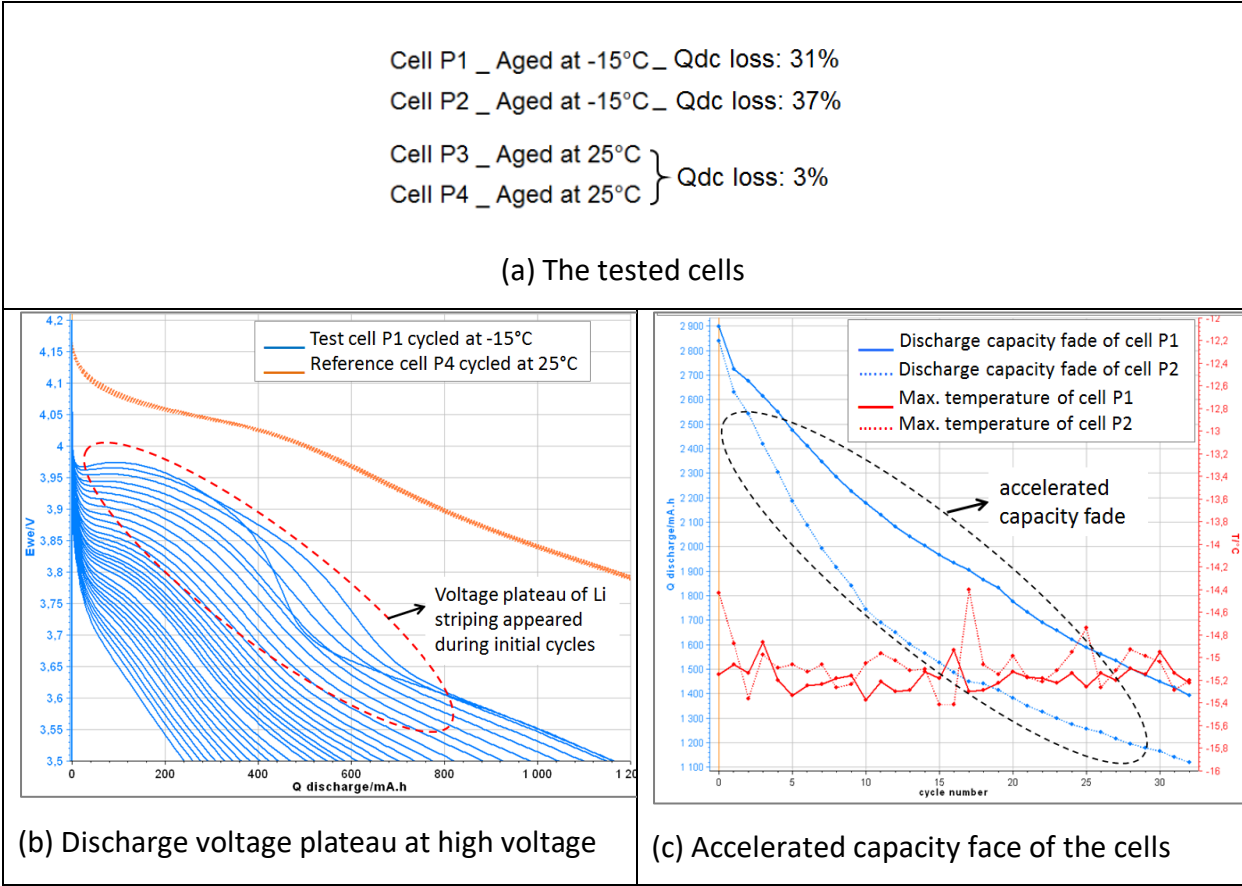


Figure 70: The Li plating of Panasonic NCR 18650 GA: The hints of Li deposition of aged cells (P1, P2) compared with reference cell (P4).

2.4.3.2 Defined protocols

After discussion, we selected the protocol of the pre-tests as the aging protocols defined for Panasonic NCR GA technology, which is: standard cycling (C/2 charge and C/5 discharge, ΔSOC: 100 %) at -15°C with 30 min rest after each cycle until a certain level of aging (discharge capacity loss of ~10 %, ~20 %, ~30 %, ~40 %, ...). Note that the check-ups at 25 °C will be made only at the beginning and the end of aging.

The Panasonic NCR GA technology has presented very repeatable aging results and thereby, we favoured this technology for the study of the impact of aging on the thermal runaway. The thermal safety of such cells (Panasonic NCR GA pristine and aged cells) was then

experimentally determined for comparison with expectations from the model to find out the influence of aging on battery safety. The details are shown in the following sections.

2.5 Thermal safety tests

Thermal abuse is the most direct way to challenge and pass the thermal stability limits of a Li-ion cell. Therefore, thermal safety test is carried out to subject the cell to external heating.

Studying the intrinsic thermal runaway process requires not only elevated temperature, but also an adiabatic environment and extended time to reach a self-sustaining thermal runaway condition. The quasi-adiabatic conditions in accelerating rate calorimetry (ARC) tests can be regarded as perfect thermal insulation conditions. Therefore, the results of ARC tests represent a worst-case scenario, since no thermal loss (that may and would occur to some extent in real operating conditions of a battery) can postpone the occurrence of the thermal runaway. Such adiabatic conditions also allow more easy and consistent comparisons between different technologies.

According to literatures [144], ARC tests are typically operated by the heat-wait-search (or seek) (HWS) algorithm. In such experiments, a cell is heated to a certain temperature (e.g. 30 °C) and if significant self-heating of the cell is detected (self-heating rate $SHR > 0.02$ °C/min) after defined wait and search periods, the ARC changes into the exothermic mode. In the exothermic mode, the calorimeter follows the temperature on the cell surface. Therefore, the conditions are quasi-adiabatic and no heat is allowed to be transferred from the cell to its surrounding. In case the SHR is not significant, the temperature is increased, for example by 5 °C and this step is repeated until significant exothermic reactions are detected. ARC HWS algorithm is illustrated in Figure 71:

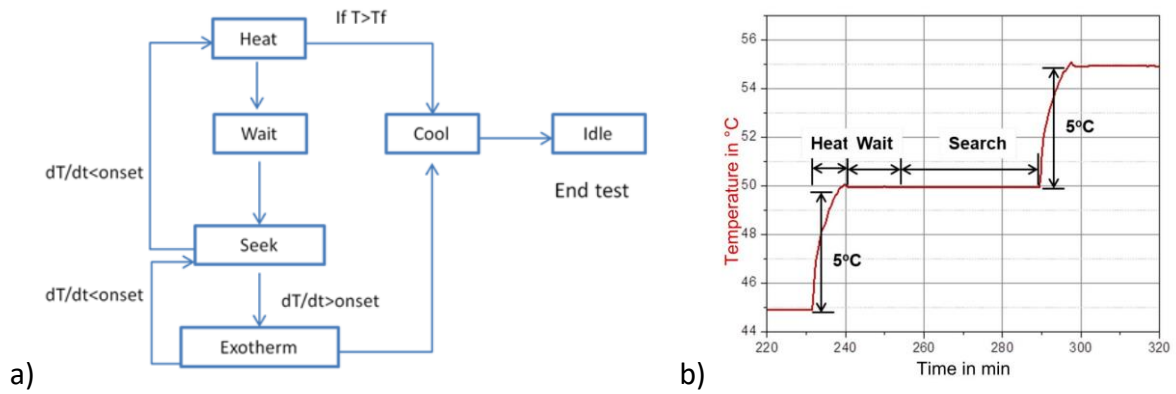


Figure 71: a) The heat-wait-seek or heat-wait-search (HWS) method,

b) Example of cell surface temperature curve during HWS experiment in an ARC. [144]

The Thermal runaway in pseudo-adiabatic condition of ARC is interesting to calibrate the exothermic reactions during the process of thermal runaway, avoiding the heat exchange with the environment. Therefore, our first approach was to perform the Thermal runaway in pseudo-adiabatic condition of ARC then in validation test (oven test) in order to respectively calibrate and validate the model.

2.5.1 Thermal safety test in pseudo-adiabatic condition of ARC

The exothermic reactions of Li-ion cells have been investigated by ARC on the cell level (operated by the heat-wait-search (HWS) algorithm) in BTC500 E1735 (ARC system). Pristine and aged cells obtained from the aging campaign, in known and quantified degradation states as assessed by electrical analysis, have undergone thermal safety tests on the STEEVE platform of INERIS. These tests make it possible to follow the triggering and the propagation of the thermal runaway within the elements during a thermal or electrical stress.

Inspired by [16], the results of ARC tests represent a worst case scenario, where the safety behaviour during the thermal runaway of the battery cell is mainly characterized by the three critical thresholds (T_1, T_2, T_3). These critical temperatures can be identified based on the evolution of cell skin temperature and confirmed by the cell self-heating temperature rate evolution (T_{rate}) during thermal runaway, where:

$$T_{rate} = dT/dt \quad (1)$$

Another important parameter is the pressure rate (P_{rate}) of BTC's vessel, which can be used to identify/assess phenomena like venting events, gas ignition, fire, and chemical explosion, where:

$$P_{rate} = dP/dt \tag{2}$$

In such experiments, the heat is not allowed to be transferred from the cell to its surroundings. The applied HWS test protocol is illustrated in Figure 72.

The system is firstly stabilized at a certain initial temperature (35 °C in this case), then the battery cell is heated at increments of 5 °C, while the system maintains the adiabatic conditions. After wait and search periods, if the self-heating rate is not significant ($T_{rate} < 0.03$ °C/min), the HWS loop will be resumed. Upon detection of a significant exothermic reaction, the ARC changes into the exothermic tracking mode, where it follows the cell temperature adiabatically. At this point, the test would come back to the HWS loop if the $T_{rate} < 0.01$ °C/min. Over 450 °C, the exothermic tracking mode continues until the end of thermal runaway.

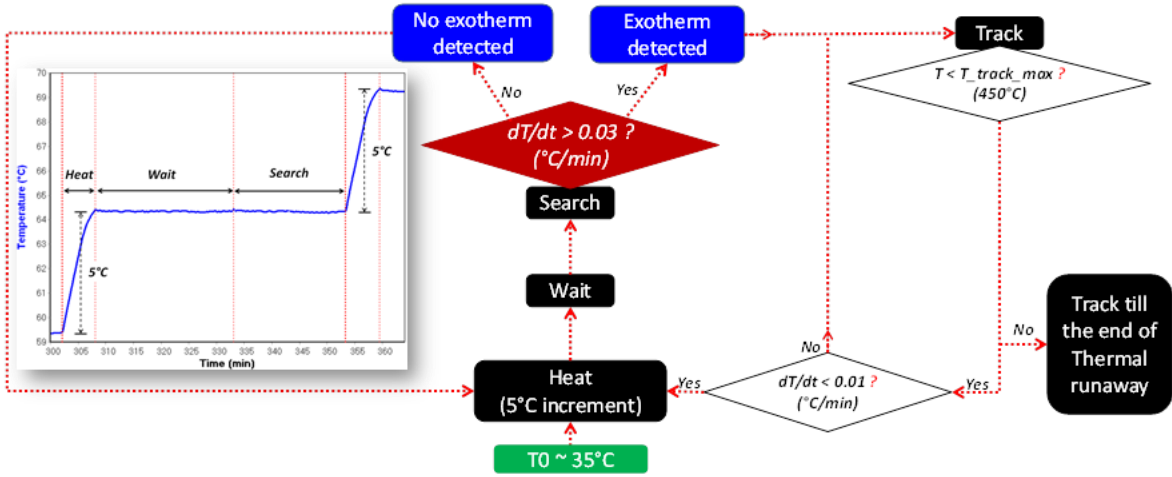


Figure 72: The applied HWS test protocol in quasi-adiabatic conditions.

These tests will make it possible to understand the processes involved in the thermal runaway of the batteries and to calibrate and validate the developed models. To go further in understanding the phenomenon, cells that have undergone runaway tests can also be analysed by X-ray tomography and then by post-mortem analysis. These analyses should

make it possible to detect the most important internal modification zones in the cells to locate the zones of initiation of the phenomenon, and to explain in some cases the differences observed during the tests of runaway on identical cells.

2.5.1.1 Test setup

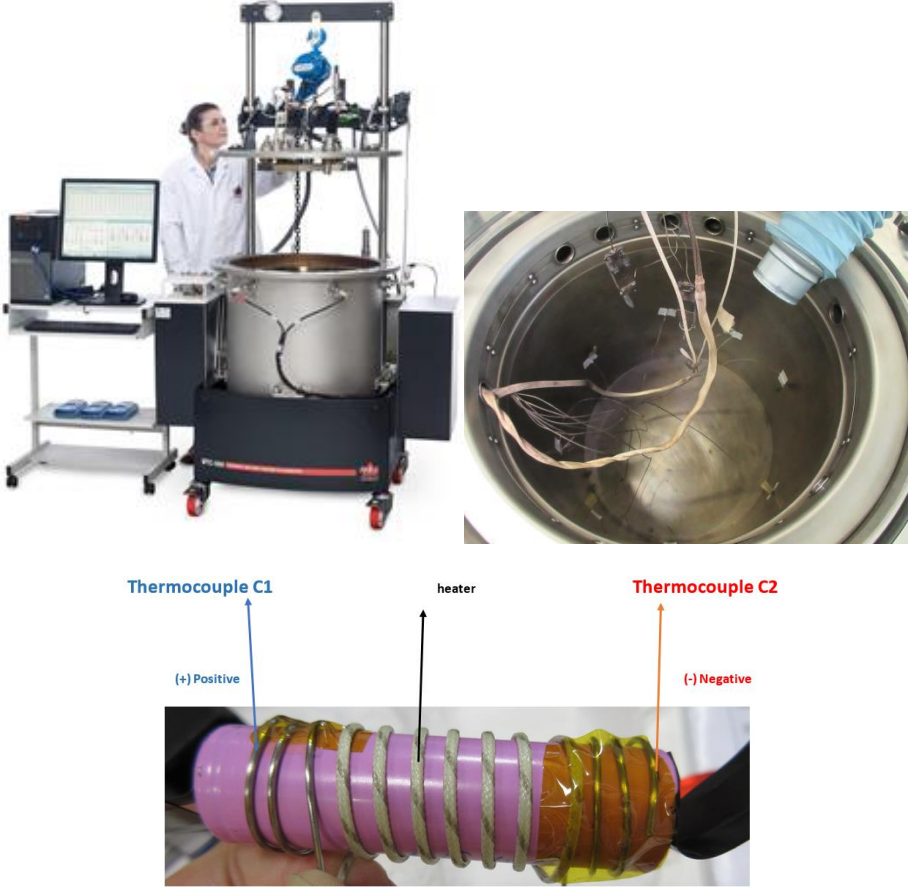


Figure 73: ARC and its vessel (Top). ARC test sensors (thermocouples) and heater setup on 18650 cells (Bottom).

These ARC HWS tests were performed with the cell setup as shown in Figure 73. The ARC are kept in the chamber of ~25°C.

The thermocouple C1 is near cell cap, therefore, its temperature will be strongly influenced by the activation of safety features during venting and combustion. Thereby, in this report, the results of different cells will be compared based only on the temperature of thermocouple C2.

2.5.1.2 HWS test results

The most important requirement of the HWS test in ARC BTC is to calibrate the model, which have the critical requirements below:

- adiabatic condition should be maintained during the whole test.
- important data need to be recorded, especially P_{heater} .
- the sensibility of exothermic detection should be respected ($0.03^{\circ}\text{C}/\text{min}$ as the limit).

It is important to note that the ARC is sensible to each 18650 technologies because the fit input to HWS protocol need to be optimized for each technology in order to stabilize and maintain the system in pseudo adiabatic condition during the thermal runaway test. Therefore, we have encountered these challenges below:

- New system of ARC (HEL 1735) required initial calibration for each technology in order to achieve a good test for model calibration. This new equipment, compared to the last one used in the works of Abada *et al.* [16], has bigger volume (0.0866 m^3), it reveals lower sensibility ($0.03^{\circ}\text{C}/\text{min}$ compared to $0.02^{\circ}\text{C}/\text{min}$).
- The time taken for effective calibration of the new ARC machine was unexpectedly long and more difficult than anticipated.

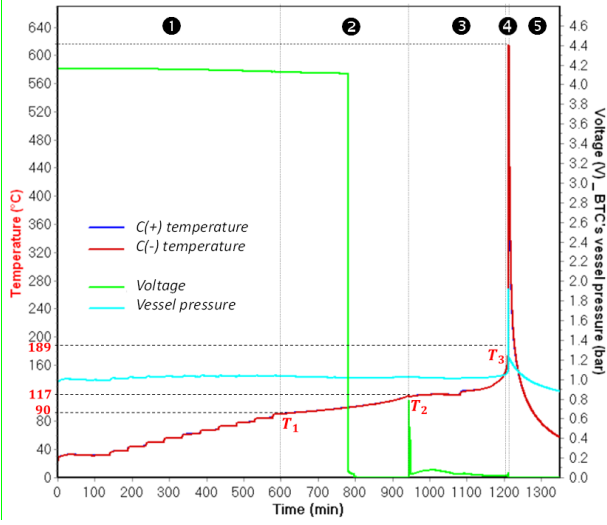
Finally we found a new strategy to cope with these non-adiabatic results, in order to calibrate and validate this model, as explained in Chapter 3.

However, qualitatively, our thermal safety tests results have confirmed about the reactivity of the thermal runaway of these technologies. The occurrence time of thermal runaway is strongly influenced by cell technology and SOC.

The stages during the thermal runaway of Ni-rich technologies

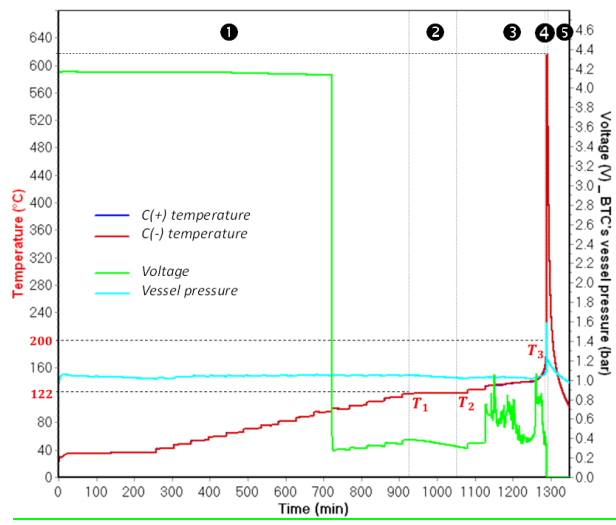
The tested cells are LG HG2 at 100% SOC and Panasonic NCR GA at 100% SOC. As observed in Figure 74, the thermal runaway of Pristine cells 100%SOC of these selected Ni-rich technologies are very reactive:

LG HG2 100%SOC

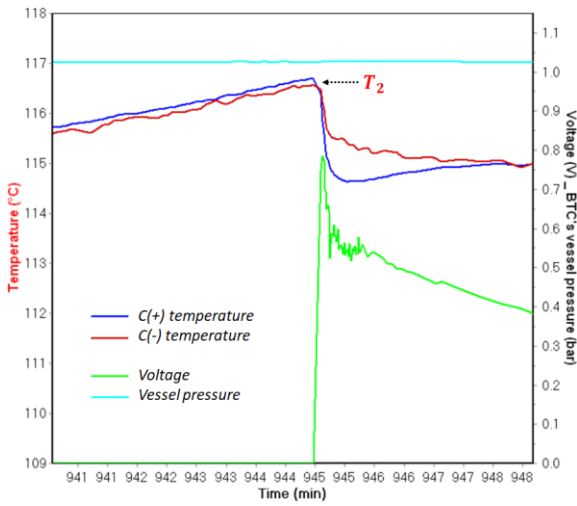


(a)

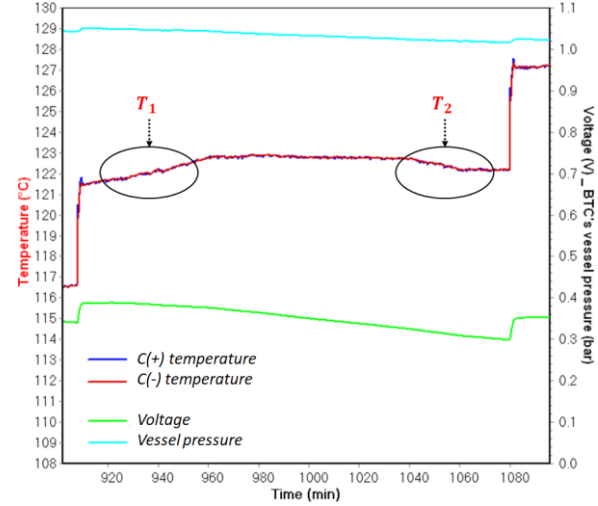
Panasonic NCR GA at 100% SOC



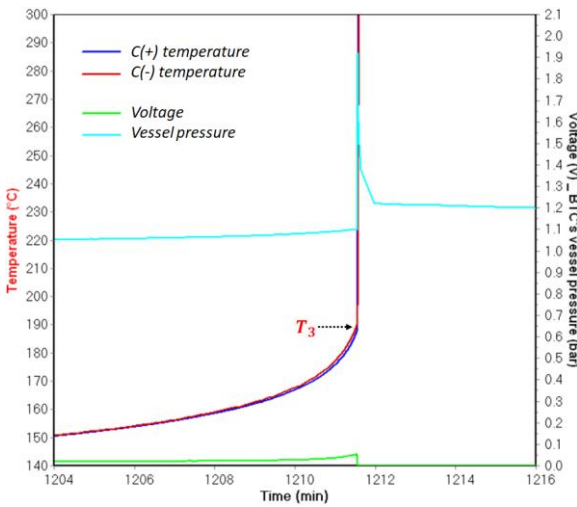
(b)



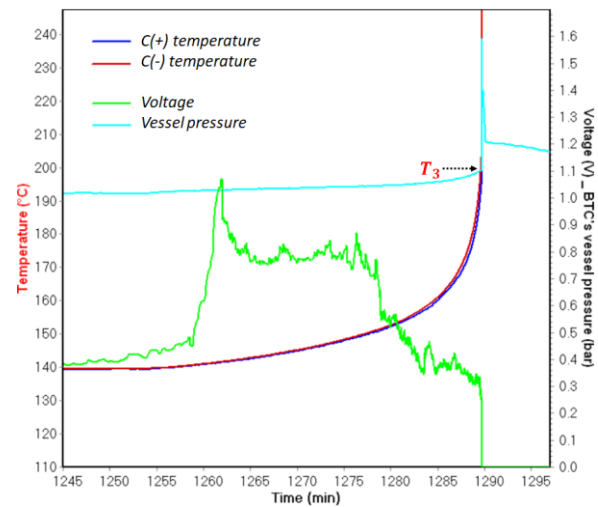
(c)



(d)



(e)



(f)

Figure 74: (a,b) The 5 stages in the evolution of cell temperatures obtained from the heat–wait–search (HWS) test of LG HG2 at 100% SOC and of Panasonic NCR GA at 100% SOC, respectively; (c,d) the initial observations of the endothermic reaction of separator melting of the LG HG2 at 100% SOC and Panasonic NCR GA at 100% SOC, respectively; (e,f) the final venting and hard ISC after the ceramic separator layer collapse occurs at T_3 for both the LG HG2 at 100% SOC and Panasonic NCR GA at 100% SOC. [106]

Having the technologies of negative electrodes of composites Graphite-SiOx, the selected technologies exhibit the influence of different positive electrode technologies on the onset time of thermal runaway.

As previously observed by Abada *et al.* for LFP/Graphite cells [16], the safety behaviour during the thermal runaway of the battery cell is mainly characterized by the three critical thresholds:

- T_1 is the temperature corresponding to the initial self-heating phenomenon detected. The detection of T_1 depends on the detection sensitivity of the testing device for the exothermic reaction, which is indicated in the testing program. In this work, the detection sensitivity for exothermic reactions is ≥ 0.03 °C/min;
- T_2 is the temperature referred to the initial observation of the endothermic reaction of the separator melting process;
- T_3 is the temperature corresponding to the sudden acceleration of temperature rate due to the final venting, indicated by the strongest gassing rate and the hard internal short-circuit (ISC) after the ceramic layer has collapsed.

Figure 74 gives an example of thermal runaway with the 5 stages indicated. Based on these three critical temperatures, the thermal runaway exothermic chain reactions can be analyzed in five stages in the evolution of the cell skin temperature, as described below.

Stage 1 corresponds to the safe region, where there is no cell self-heating or the cell self-heating is insignificant ($T_{rate} < 0.03$ °C/min in this research), and therefore not detected.

Stage 2 is the first reversible self-heating region, which begins from T_1 —the initial significant self-heating detected when $T_{rate} \geq 0.03$ °C/min . Above T_1 , the battery operation changes to an abnormal state caused by the main reactions listed below:

- Reactions of deposited Li and electrolytes, and “dead Li” formation;
- Initial decomposition of SEI (dominant reaction of this stage). This is regarded as the first side reaction during the full thermal runaway process. It occurs around 60–130 °C [3]. The exact temperature range depends upon cell chemistry, the thickness of SEI, and SOC level;
- SEI regeneration: Once the SEI decomposes, the intercalated Li in the graphite negative electrodes can contact the electrolyte again, thereby regenerating SEI.

Stage 3 is defined as the last reversible self-heating region, which starts from T_2 , the initial observation of the endothermic reaction of the separator melting process. Above this critical temperature, the separator loses its mechanical integrity then starts collapsing, which demonstrates the beginning of cell destruction at the component scale. This reaction depends on the composition and porous structure of different separator layers, as well as the separator thickness. It usually starts with the separator layer that has the lowest melting point. The melting points of commercial separators are about 110–130 °C for the polyethylene (PE) layer, 160–170 °C for the polypropylene (PP) layer, and 180–260 °C for the ceramic coating layer [3][117] . This leads to the soft internal short circuits (ISCs), and more importantly the decrease of cell temperature. Therefore, the separator is an important element in terms of safety. Its endothermic melting process can be initially observed by the decrease of cell temperature during tracking in adiabatic conditions and can be confirmed by the decrease of T_{rate} .

During stage 3, the temperature violently increases inside the battery due to these exothermic reactions:

- Further electrolyte balance reaction of SEI regeneration and decomposition at negative electrodes (dominant reactions at the beginning of this stage): Within the temperature range of about 120–250 °C, the SEI decomposition will not stop as long as there is sufficient regenerated SEI, meanwhile the SEI regeneration will not

increase because the surface of the negative electrode is still covered by a certain thickness of the SEI layer [107]. This exothermic process represents the balance reaction of SEI decomposition and regeneration, with the average thickness of SEI remaining at a stabilized level;

- The start of positive electrode decomposition and electrolyte oxidation (dominant reactions at the end of this stage): The highly exothermic decomposition of positive electrode starts at temperatures ranging 130–250 °C and produces oxygen [3, 4, 13, 108].

Therefore, stage 3 is also referred to as the heat accumulation and gas release process. During this stage, the cell might vent due to the cell's internal pressure increase caused by the solvent vaporization and the gases generated [152].

The beginning of the final venting is indicated by the strongest gassing rate and the hard ISC after the ceramic layer has collapsed, which simultaneously happen at a similar temperature level ($\sim T_3$). These two events lead to the accelerated heat accumulation and activate the battery combustion as soon as there is enough oxygen (mainly from the positive electrode decomposition reactions and from the air). This is the start of stage 4, the accelerated thermal runaway region, where the cell self-heating is accelerated and irreversible. This begins at T_3 and leads to the maximum temperature (T_{max}). During this stage, combustion occurs, vessel pressure aggressively increases, and venting and cell component ejection accelerate, causing fires and chemical explosion hazards due to the strong exothermic reactions below:

- Further highly exothermic decomposition of positive electrodes (~ 200 – 250 °C) [3][13]: Cells manufactured from the higher energy density positive electrode materials will be subjected to more severe exothermic reactions;
- Strong exothermic reaction between oxygen (released from positive electrode) and electrolytes [3][13];
- Decomposition of electrolytes (combustion reactions): A part of the carbonate electrolyte decomposes inside the cell and releases gases, whereas the other part evaporates and bursts out of the cell. During the final venting, the ultimate severity

of the reaction is dominated by the ignition of flammable vent gases. Auto-ignition temperatures of some typical organic electrolyte components are ~440 °C for ethyl methyl carbonate (EMC), ~445 °C for diethyl carbonate (DEC), ~455 °C for propylene carbonate (PC), ~458 °C for dimethyl carbonate (DMC), and ~465 °C for ethylene carbonate (EC) [4];

- Reactions between deposited Li and air (H₂O) diffused into the cell after venting;
- Reactions between deposited Li and the binder [3][10];
- Decomposition of negative electrodes with electrolytes [10]: The balance reaction of SEI decomposition and regeneration is broken as the temperature increases. Then, the graphite structure collapses;
- Binder reactions.

Stage 5 is the cooling down stage.

The chain exothermic reactions happen under near adiabatic conditions, where the exact reaction temperature highly depends on the cell chemistry and SOC level. Therefore, the temperature rate and duration of these thermal runaway stages are representative of the characteristics of the battery cell.

The initial significant self-heating of LG HG2 was detected at a lower temperature (~90 °C) compared to that of the Panasonic NCR GA (~122 °C). This might originally be due to the stronger initial SEI decomposition/regeneration reaction occurring in LG HG2 cells. Consequently, this demonstrates that the safe region (stage 1) of the Panasonic NCR GA is wider than that of LG HG2. Specifically, within the temperature range of 90 °C to 122 °C, the Panasonic NCR GA at 100% SOC is safer than LG HG2 at 100% SOC.

The cell self-heating temperature continues to increase throughout stage 2. The endothermic process of separator melting was initially observed at a similar temperature range for these selected technologies ($T_2 \sim 117$ °C for LG HG2 and $T_2 \sim 122$ °C for Panasonic NCR GA), as illustrated in Figure 74c,d. This might be because of the similarities of PE based in these separator technologies. However, these results are quite lower than the DSC analysis results of separator melting points at ~130°C. It is also seen that in case of Panasonic NCR GA, the first observation of separator melting is at the same temperature (~122 °C) as

the first exotherm detected. This means that this technology is safe and that the cell can increase to the temperature of separator melting without any thermal runaway exothermic reactions being detected.

Stage 3 corresponds to the heat accumulation and gas release process, where the self-heating rate of these Ni-rich technologies strongly increases. This is the last reversible self-heating region. It lasts about 267 min for the LG HG2 and about 235 min for the Panasonic NCR GA. The first venting events that occur during the opening of vent ports were observed at ~ 165 °C for the LG HG2 and at ~ 171 °C for the Panasonic NCR GA by the sudden changes of P_{rate} and cell temperature. The final venting and hard ISC of the Panasonic NCR GA occurred at higher temperature (~ 205 °C) than that of the LG HG2 (~ 190 °C), as shown in Figure 74e,f.

The severity of the thermal runaway accelerates during stage 4, thereby leading to the maximum temperature of ~ 615 °C for both technologies. Due to the limitation of the maximum temperature tolerance of the BTC, the maximum temperatures of these technologies cannot reach higher than ~ 615 °C. This intensive stage is caused by the combustion and explosive decomposition, so it lasts only ~ 28.5 s for LG HG2 and ~ 36 s for Panasonic NCR GA. During this stage, venting and cell component ejection accelerated.

The representative characteristics of the thermal runaway chain exothermic reactions of LG HG2 and Panasonic NCR GA at pristine state of 100% SOC are summarized in Figure 75 and Figure 76.

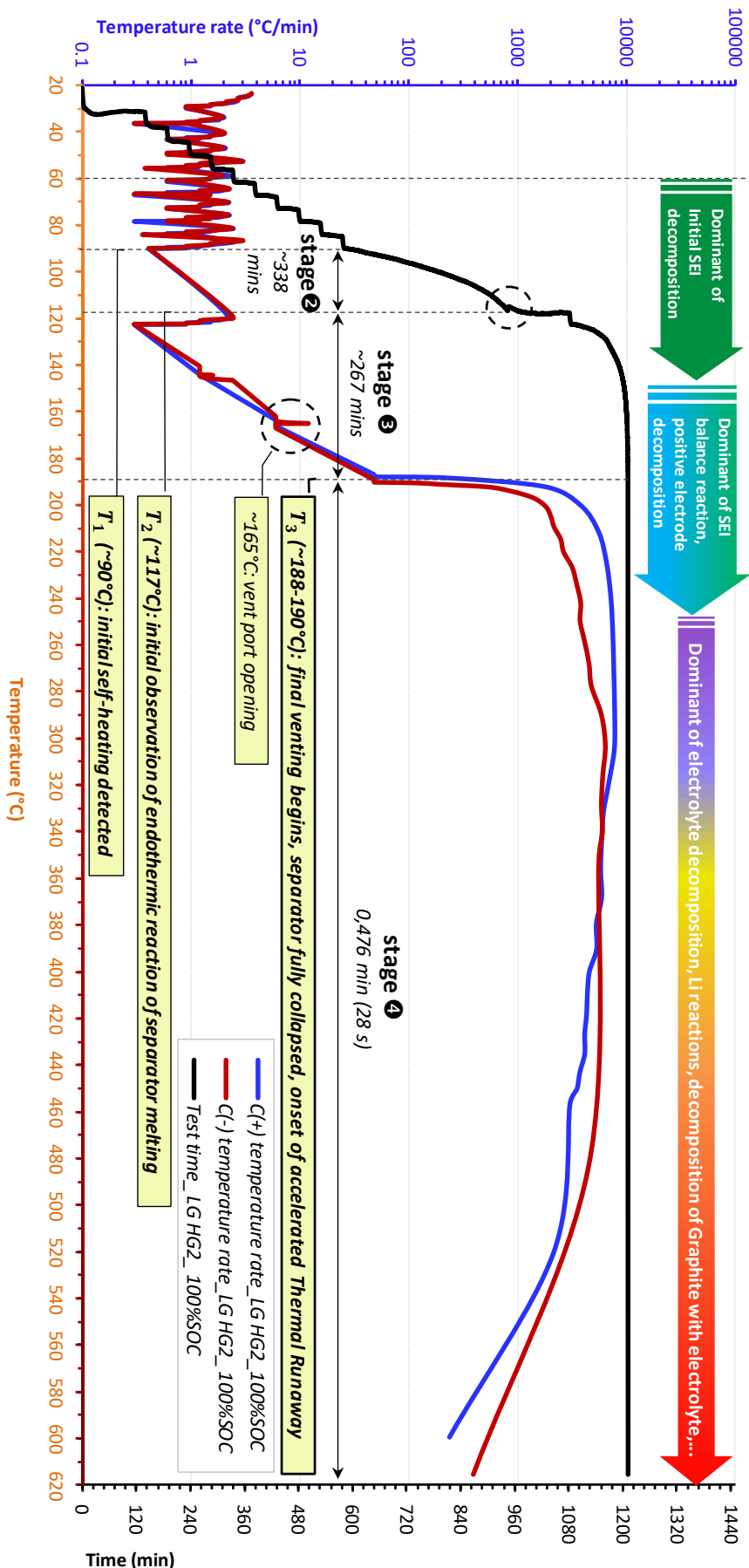


Figure 75: Temperature rates and test time versus temperature during the thermal runaway of the LG HG2 pristine cells at 100% SOC.

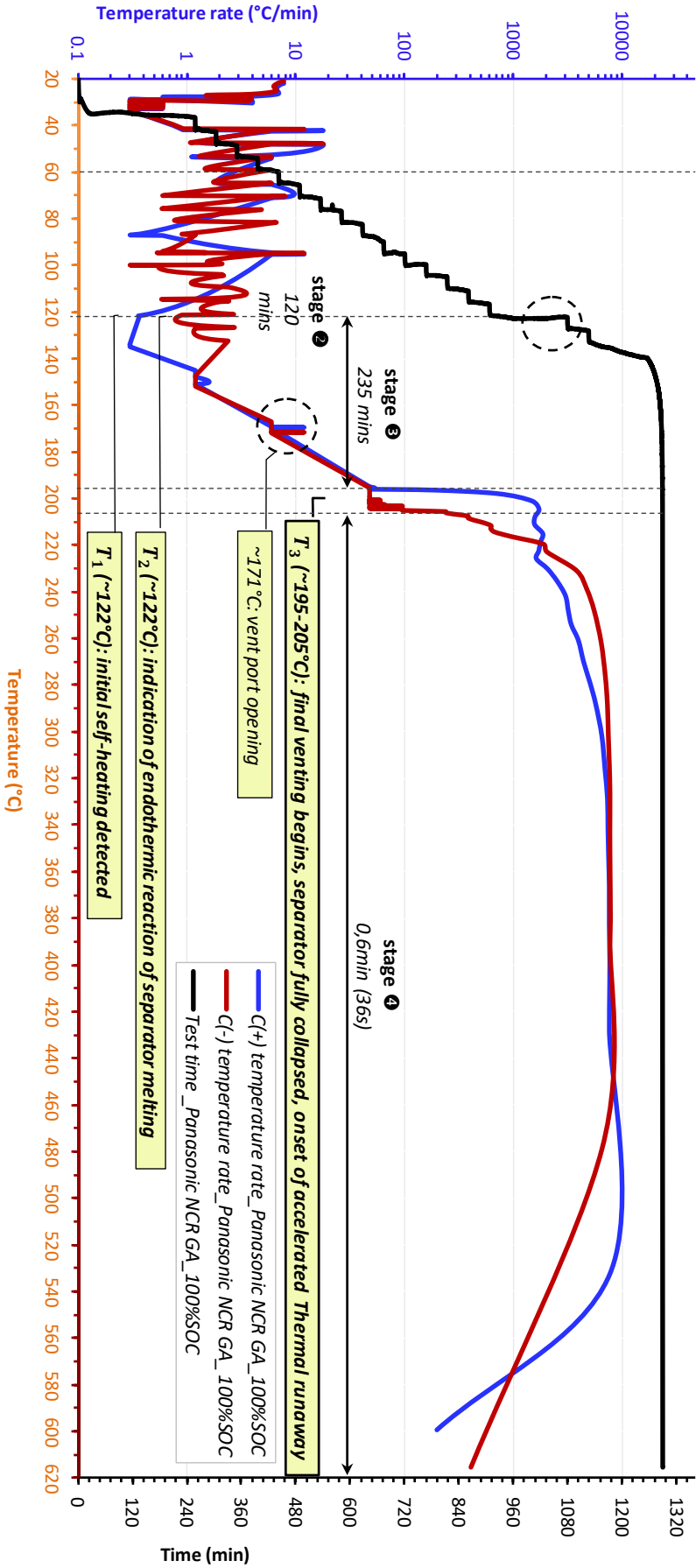


Figure 76: Temperature rates and test time versus temperature during the thermal runaway of the Panasonic NCR GA pristine cells at 100% SOC.

The factors impacting the thermal runaway of selected technologies

The severity of thermal runaway mainly depends on the cell technology, such as the chemical energy in the form of combustible materials stored in the battery (e.g., combustible electrode materials and flammable electrolytes), the shutdown mechanism of the separator, and the mechanical design of the safety features.

The severity of the thermal runaway also depends on the SOC level, which indicates the electrical energy is stored in the cell in the form of chemical potential energy.

Besides, the thermal abuse condition applied is also having a role in the severity of the thermal runaway.

The impact of electrode materials

The more energy a battery cell stores, the more energetic its thermal runaway can be. Therefore, the thermal runaway underpinning reactions of Ni-rich LIBs are very energetic because they have very high energy densities compared to other cell chemistries. Figure 77 illustrates the severity during the final stages of the thermal runaway for the selected Ni-rich technologies (result from this thesis) compared to the thermal runaway of a LFP/graphite battery from A123 Systems (result from previous thesis [16]). It is noteworthy that the ARC system used in this thesis is bigger in term of volume compared to that of the previous thesis. A similar type of separator was used, so the hard ISC occurred at similar temperatures (190–210 °C) for all these technologies. It is clearly seen that the Ni-rich LIBs are much more reactive.

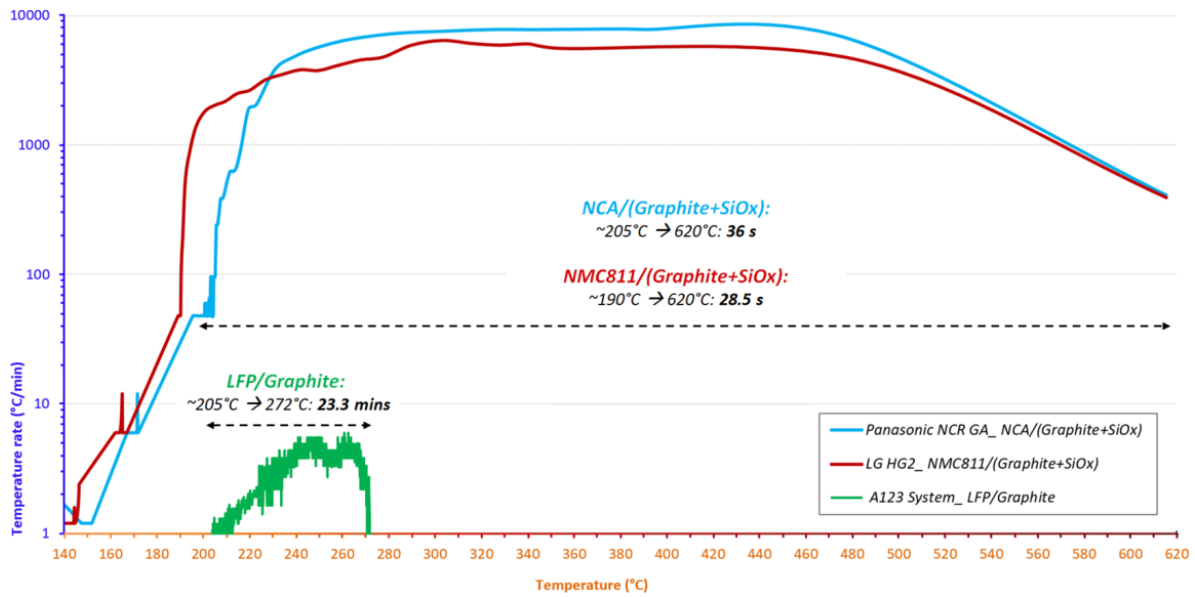


Figure 77: Comparison of the final stages of the thermal runaway of the selected Ni-rich technologies versus the “safest technology”, LiFePO_4 (LFP)/graphite.

Having similar technology to the negative electrode (graphite-SiOx composites), different positive electrode technologies (NMC811 in LG HG2 and NCA in Panasonic NCR GA) impacted the total duration and the severity of stage 4: With higher temperature rate, the NCA cell lasts ~36 s, while the NMC811 cell lasts 28.5 s, as shown in Figure 77. However, due to the stronger gassing from positive electrode decomposition of NMC811 technology and more amount of electrolyte stored in the cell (section 2.3.1.1), the final venting rate detected for LG HG2 is the most violent, as observed in Figure 79.

Upon further investigation, we found that the temperature rate during stage 4 of NCA technology reaches a higher value with longer duration, regardless of whether for 100% SOC or 50% SOC (Figure 81b). In general, NCA technology appears to be more reactive during the final stage of the thermal runaway than that of NMC811 technology.

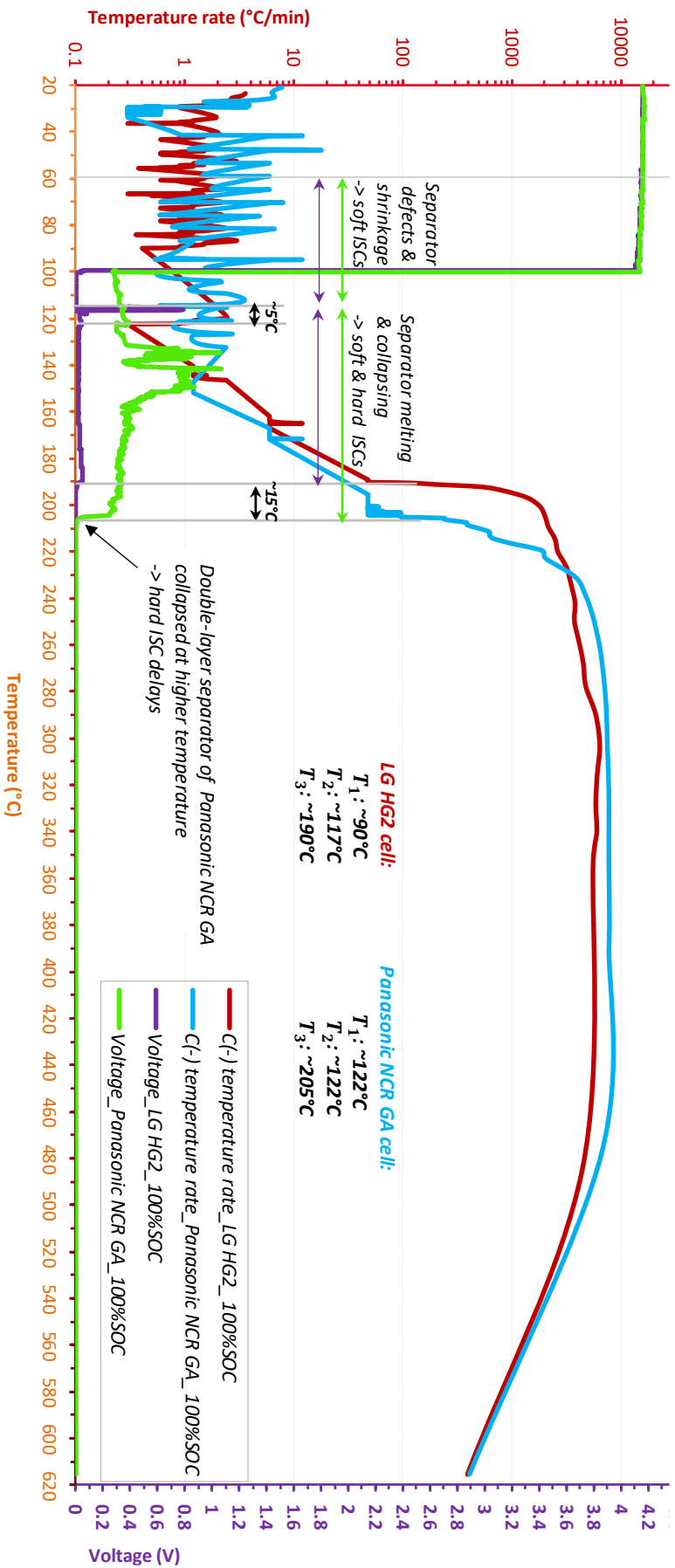


Figure 78: The C(-) temperature rate and cell voltage of LG HG2 and Panasonic NCR GA (at 100% SOC) versus C(-) temperature

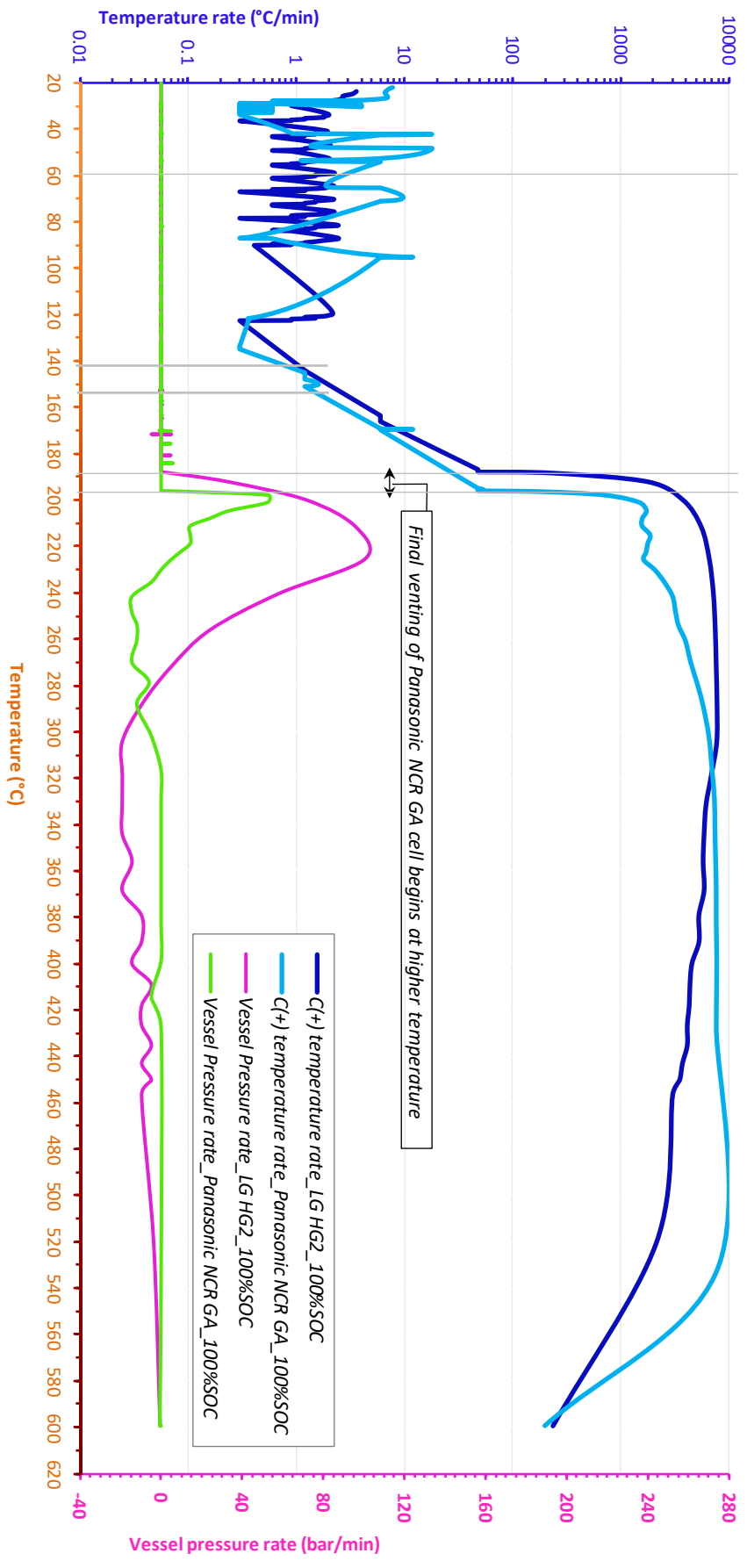


Figure 79: Temperature rate of C (+) and vessel pressure rate of LG HG2 and Panasonic NCR GA (at 100% SOC) versus C (+) temperature

The impact of separator

As described in 2.3.1.2, the two selected technologies have similar double-layer separator technologies: polymeric and ceramic layers. For LG HG2, the polymeric layer has a homogeneous porosity and the ceramic layer is mainly composed of grains. The separator total thickness is $\sim 13 \mu\text{m}$. For Panasonic NCR GA, the porosity of its separator polymeric layer has lower homogeneity. The ceramic layer is composed of long fibers in a mixture with different grains. The separator total thickness is $\sim 38 \mu\text{m}$, which is significantly thicker than the separator for LG HG2.

Therefore, even though the melting point of these technologies' separators are similar ($\sim 130^\circ\text{C}$) as analysed in 2.3.3, the Panasonic NCR GA's separator fully collapses at higher temperature, which leads to the delay of final venting, as shown in Figure 79, and also to the delay of hard ISC ($\sim 205^\circ\text{C}$ compared to $\sim 190^\circ\text{C}$ for LG HG2), as observed in Figure 78. Therefore, stage 4 of Panasonic NCR GA starts at a higher temperature. As a conclusion, the separator technology has a strong impact on the occurrence of the thermal runaway.

The impact of SOC

For any given cell, the most severe thermal runaway process is achieved when that cell contains its maximum electrical energy (100% SOC or overcharged) [19]. To better understand the impact of SOC level on the thermal runaway of LG HG2 and Panasonic NCR GA, these cells were subjected to thermal safety tests at two different levels of SOC: 100% and 50%. The impact of SOC on the thermal runaway can be observed in Figure 80 and Figure 81. Through testing of multiple batteries, we confirmed that lower SOC level leads to ISC delay, and thereby shifts the initial self-heating as well as the activation of stage 4 to higher temperatures, as shown in Figure 80. Therefore, T_1 , T_2 , and T_3 are increased for cells at reduced SOC. Additionally, as similarly proven in Figure 80, cells at 50% SOC require more time before undergoing thermal runaway, and their thermal runaway processes can only be activated at higher temperature. Moreover, their stage 4 is less severe, showing a lower temperature rate and shorter duration. Therefore, the pristine cells at 50% SOC are less reactive.

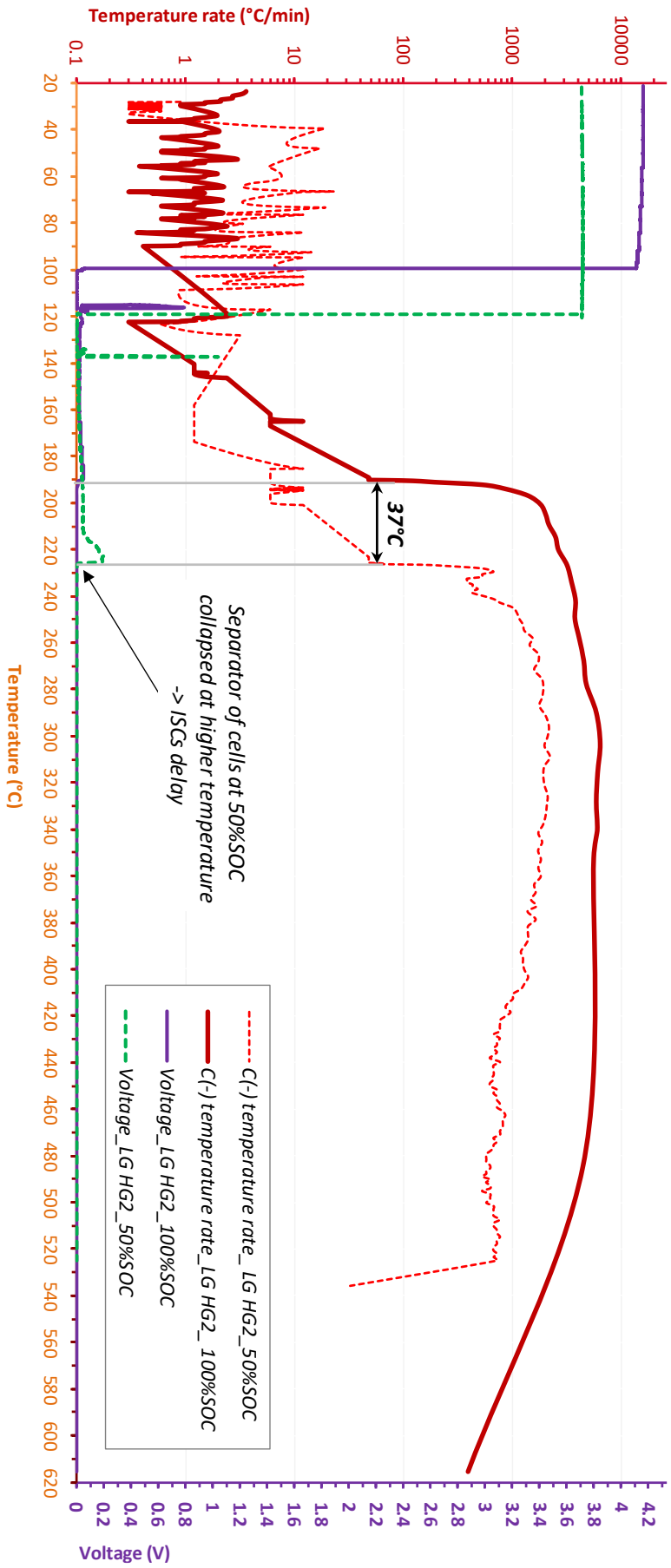


Figure 80: The C (-) temperature rate and voltage of LG HG2 at 50% and 100% SOC versus C (-) temperature.

This SOC dependency shift is stronger for the LG HG2 technology, and the maximum temperature is also reduced with reduced SOC (~615 °C for LG HG2 100% SOC and ~535 °C for LG HG2 50% SOC). However, all tested cells clearly exhibit stage 3 and stage 4, with the same temperature rate of ~6 °C/min at the beginning of vent port opening and ~48 °C/min at T_3 , regardless of SOC and cell technology (Figure 81b).

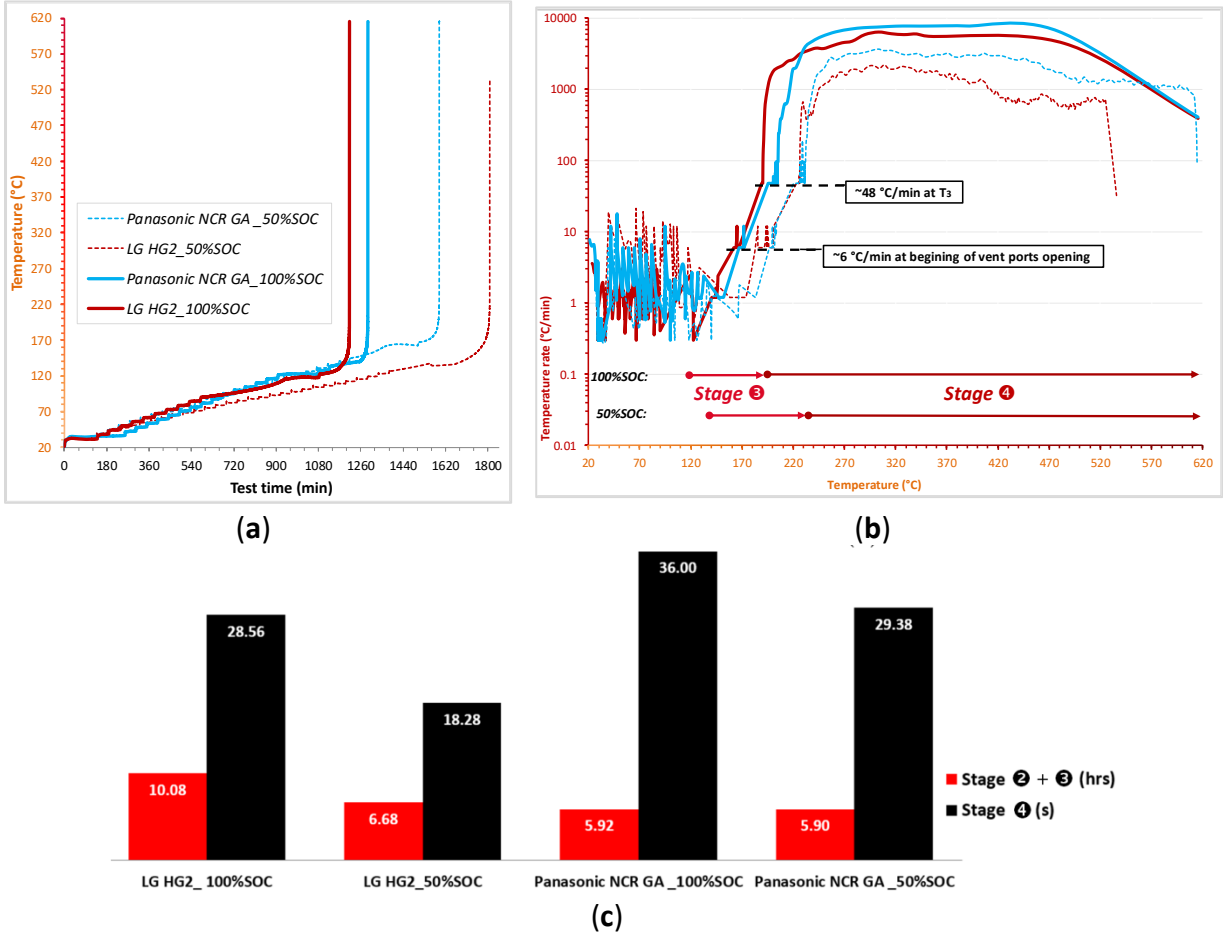


Figure 81: (a) Temperature profiles versus test time and (b) temperature rate versus temperature of the 50% and 100% SOC LG HG2 and Panasonic NCR GA cells. (c) Duration of the reversible self-heating region (stage 2 + 3) and duration of the irreversible self-heating region (stage 4) during thermal runaway of the presented cells.

Further analysis of the venting during the thermal runaway pertaining to tested cells

During the thermal runaway process, venting events lead to gas release and cell component ejection. The remaining cells were weighed after having undergone thermal runaway (residuals). As shown in Figure 82, the mass loss of pristine cells at 50% SOC is lower than

that of pristine cells at 100% SOC. This additionally confirms the lower reactivity of cells with reduced SOC, which is coherent with the findings in literatures [74, 95, 124–128].

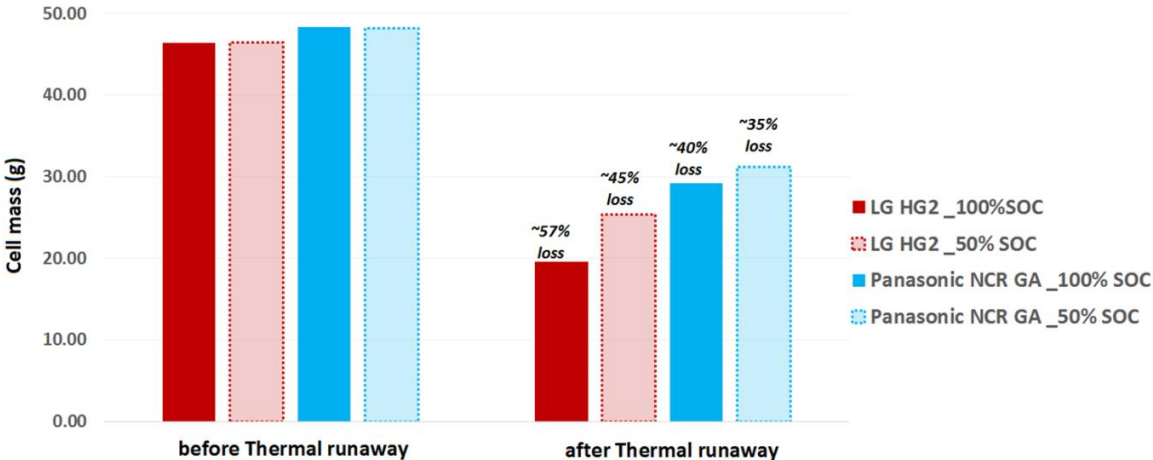


Figure 82: Cell mass before and after thermal runaway.

Looking deeper into the impact of SOC on the venting mechanism, and although these cells have different safety feature designs, we observed in Figure 83 that during final venting of all cells, the vent ports fully opened; however, the gasket seal collapsed only in the case of cells with 50% SOC. This is also confirmed by the residues of the dead cells after the thermal runaway (presented in Table 23). This could be explained by the delay of hard ISC in case of 50% SOC, as well as the shift of final venting to higher temperature, where stronger exothermic reactions occur with higher reaction rates, and eventually the pressure rate acceleration during stage 4 collapses the gasket seal. Therefore, the jelly roll of 50% SOC cells was violently ejected (Table 23). This also explains why the duration of stage 4 is shorter for 50% SOC.

We also observed in Figure 83 that the moment of final venting has occurred right after the hard ISC for all the tested cells. These events initiated the final stage of the thermal runaway. This shows the important role of the hard ISC to the acceleration of the venting and globally to the thermal runaway.

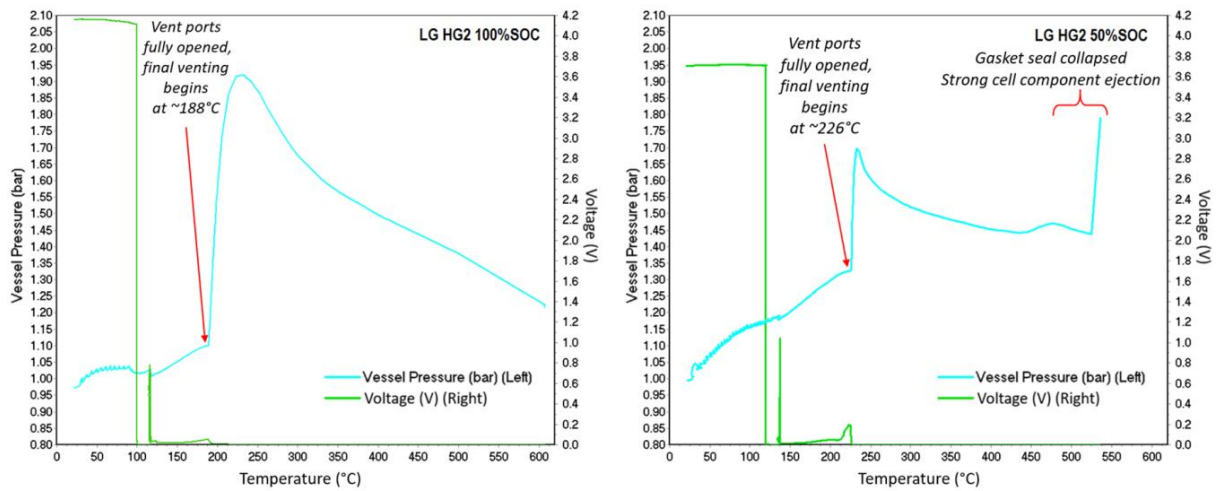
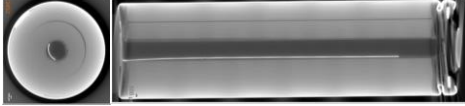

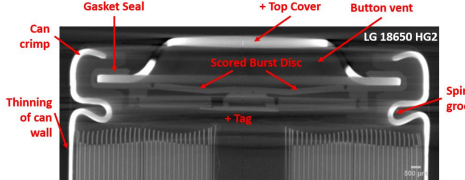
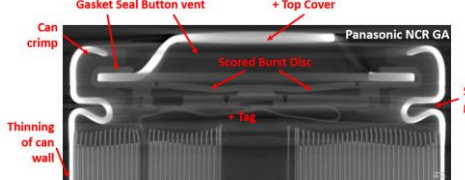






Figure 83: Cell voltage and vessel pressure (bar) versus temperature for LG HG2 100% SOC and 50% SOC.

The presence of a stiff centre tube and a metal bar to allow pressure equalization can be clearly observed in Table 21 in the design of the Panasonic cells and LG cells, respectively (the open centre core), preventing winding ejection during thermal runaway. However, these approaches do not work effectively for cells at reduced SOC.

However, at reduced SOC, it is acknowledgeable that the metal tube in case of Panasonic NCR GA helps the ejection of the jelly roll together as a compact matter, and therefore, reduced the component ejection into the surrounding environment than the case of metal bar in LG HG2 case. Therefore, it is better to have the metal tube in the core of the cell.

Table 23: The impact of safety features and SOC on venting and component ejection mechanisms, as seen through the pictures of LG HG2 and Panasonic NCR GA (50% and 100% SOC) after thermal runaway.

	LG 18650 HG2	Panasonic NCR GA
Cell internal structure global view		
Original design of safety features near cell gasket		
The 100% SOC cells after thermal runaway		
The 50% SOC cells after thermal runaway		

2.5.1.3 Main findings about the thermal runaway of Ni-rich LIBs

We performed the thermal abuse tests on the two selected Ni-rich LIBs charged to different levels of SOC (100% and 50%) at pristine states in quasi-adiabatic condition (ARC). The obtained results first confirmed the proposed complete thermal runaway exothermic chain reactions, then discovered the different factors impacting the thermal runaway kinetics, and furthermore demonstrated the relationship between safety features and SOC with venting and component ejection mechanisms. The main findings are below:

- (1) For all tested SOC levels, the initial significant self-heating of Panasonic NCR GA was always detected at a higher temperature. Therefore, the safe region of this technology is wider than that of LG HG2. This might originally be due to the stronger initial SEI decomposition/regeneration reaction occurring in LG HG2 cells.

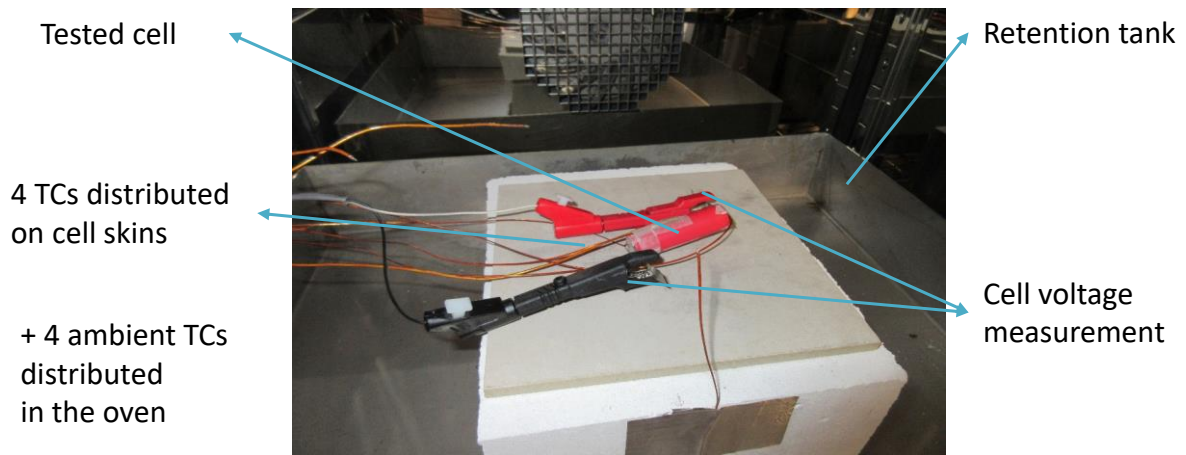
- (2) As a critical element in terms of safety, the separator technology significantly impacts the reversible self-heating stages and the onset of the accelerated thermal runaway. Having a 3-fold thicker separator, Panasonic NCR GA exhibited the final venting and hard ISC at the higher temperatures which were ~ 205 °C for 100% SOC compared to ~ 190 °C for the LG HG2, and ~ 228 °C for 50% SOC compared to ~ 222 °C for the LG HG2.
- (3) Regardless of SOC, the positive electrode material strongly influences the severity during the final stage of thermal runaway. NCA technology appears to be more reactive, with a higher self-heating temperature rate over a longer duration (Figure 14c). However, the final venting of LG HG2 is the most violent due to the stronger gassing from positive electrode decomposition due to NMC811 technology compared to NCA technology.
- (4) The impact of SOC on the thermal runaway was significantly observed for all selected Ni-rich technologies. We found that the cells at reduced SOC were less reactive. They required more time before undergoing thermal runaway and their accelerated thermal runaway stage had lower temperature rates over a shorter duration and were only activated at higher temperature, thereby meaning their gasket seal collapsed and they exhibited cell jellyroll ejection but lower mass loss after the thermal runaway.
- (5) All tested cells exhibited the same self-heating temperature rate of ~ 6 °C/min at the beginning of vent port opening and ~ 48 °C/min at the onset of the accelerated thermal runaway (T_3).

2.5.2 Thermal safety test in Oven (Oven test)

After calibrating the thermal runaway model for the studied technologies with the HWS tests in the BTC, it is necessary to validate this model by another type of thermal abuse test, which would reflect more realistic thermal abuse conditions in real life of a battery (eg. “non-adiabatic”). In this research, thermal abuse test in Oven (so-called Oven test) is used, for both new cells and aged cells, to validate the model and investigate the impacts of aging on the thermal runaway.

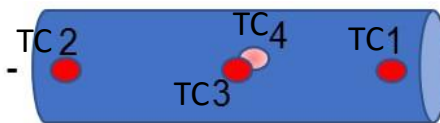
2.5.2.1 Test setup

The oven tests were carried out in STEEVE platform of INERIS to validate the model of thermal runaway at the cell scale. The experimental set up is illustrated in Figure 84.



TC5 : Oven ambient _ Above the cell

TC7 : Oven ambient _
Negative terminal side



TC6 : Oven ambient _
Positive terminal side

TC8 : Oven ambient _ Under the cell

Figure 84: The experimental set up of Oven test (top) and the thermocouples (TCs) distribution on the cell skin and in the ambient air.

The tested cell is installed in the oven on a retention tank. The cell is heated by the ambient air in the oven. The cell voltage and cell skin temperatures are continuously monitored throughout the test using 4 thermocouples distributed over the cell skin, as shown in Figure 84:

- 1 thermocouple on the negative terminal side
- 1 thermocouple on the positive terminal
- 2 other thermocouples positioned in the middle of the cell body

A video camera is scheduled to record the progress of the test.

2.5.2.2 Test protocol

The regulation of the set point is done on the surface temperature of the cell (regulation on the cell sample), the steps of the operating protocol are as follows:

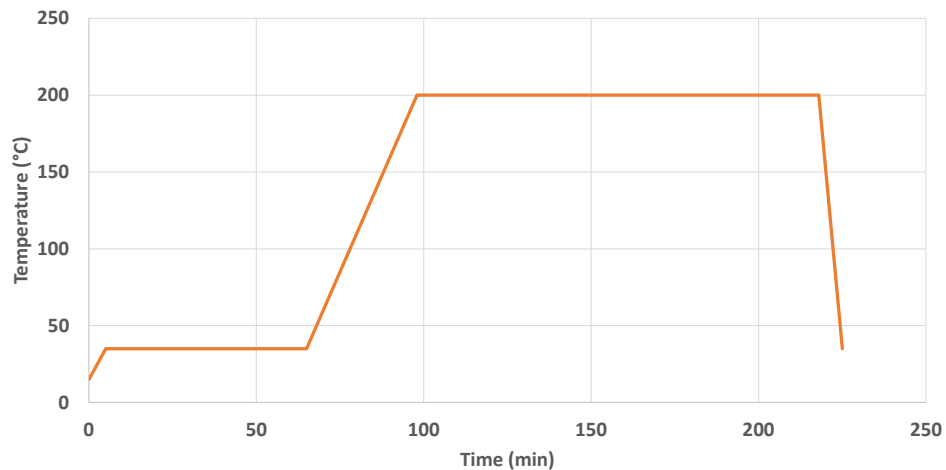


Figure 85: Oven test protocol

1. the oven is preheated to 35 ° C; this temperature is maintained for 60 minutes.
2. a ramp is applied up to 200 ° C (or until destruction of the cell) with a heating rate of 5 ° C / min.
3. If the destruction of the cell has not taken place before 200 ° C, a stabilization period of 120 minutes at 200 ° C is applied. After this period, the oven stops heating, and the cell temperature drops.

In the event of a fire, the oven is shut down.

2.5.2.3 Cell characteristics before and after oven test

To investigate the characteristic of the cells before and after the oven tests, we have following the procedure including: taking photos of cells → measure the mass, dimensions and voltage of the cell. The results relating to the tested cells are presented in Table 24.

The thermal runaway occurred for all tested cells. We observed that the width dimensions increase for all cells and the mass loss in case of aged cells are more significant. This might be due to the more severe venting and cell components ejection.

Table 24: Cell characteristic before and after the oven test.

		Before test			After test			
		Mass (g)	Dimensions (mm)	Voltage (V)	Mass (g)	Mass loss (%)	Dimensions (mm)	Voltage (V)
Panasonic NCR GA	Pristine P1706	48.76	18x65	4.16	28.37	41.82	18x67	Not measurable
	Pristine P1723	48.7	18x65	4.16	18.71	61.58	18x69	Not measurable
	Calendar aging P1530	48.6	18x65	4.13	17.9	63.17	18x68	Not measurable
	Cycling aging P1555	48.65	18x65	4.15	10.64	78.13	18x71	Not measurable
LG HG2	Pristine L1715	46.08	18x65	4.14	9.15	80.14	18x68	Not measurable
	Pristine L1714	46.28	18x65	4.15	9.93	78.54	19.6x68	Not measurable

2.5.2.4 Oven test result analysis

As we can see in Figure 86 (left), the preheating time between two different oven tests are different depending on the initial temperature of the cell, which lead to the delay in term of time between tests. To easily compare different oven test results, we excluded the preheating and stabilization time and came up with the new timeline termed $\Delta Time(t)$:

$$\Delta Time(t) = Time(t) - \sum (Time_{preheating\ to\ 35^{\circ}C} + Time_{stabilization\ at\ 35^{\circ}C})$$

With this new timeline, we can also visibly compare the thermal runaway process, especially the heating time before the accelerated thermal runaway, as seen in Figure 86 (right).

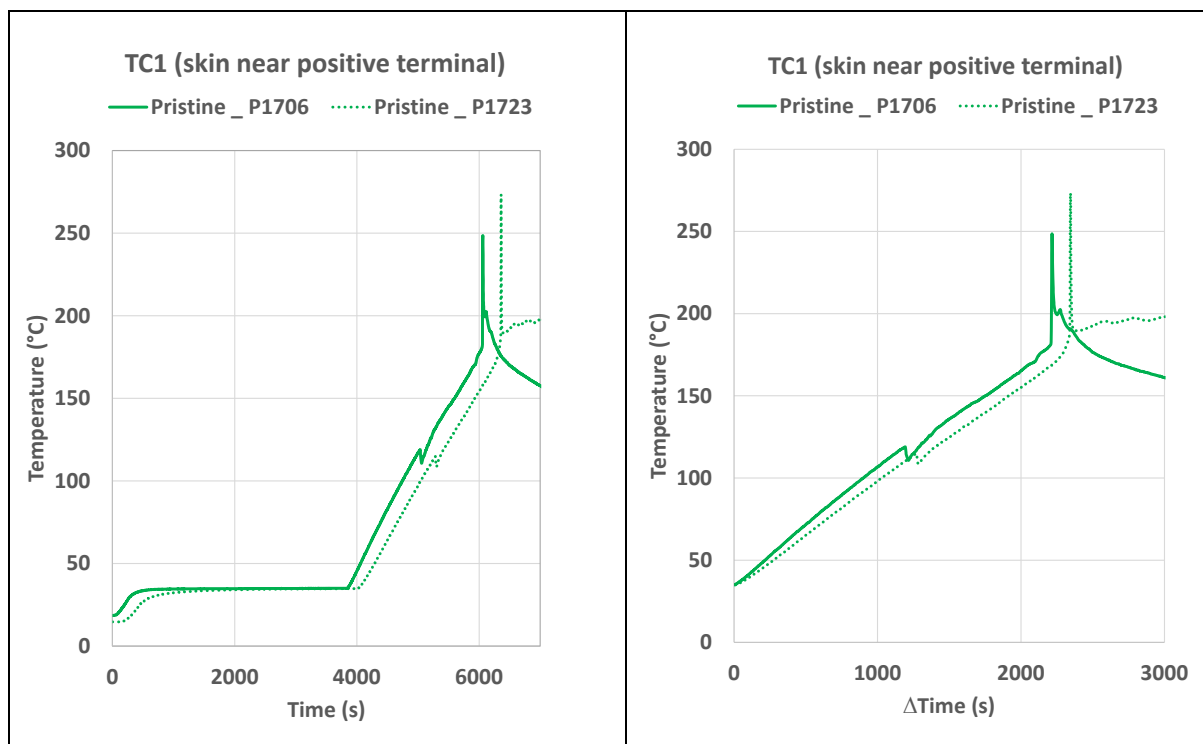


Figure 86: Example of the thermocouple temperatures rough data of 2 different oven tests (Pristine Panasonic NCR GA), plotting with test time (left) and Δ Time (right).

2.5.2.5 Oven test results of Panasonic NCR GA at pristine state

For pristine Panasonic NCR GA cells, two oven tests were made on cell P1706 and P1723. The temperature and voltage evolution of the two tested cells are presented in Figure 87 and Figure 88. It can be seen that the thermal behaviours of the two cells are quite similar. In Figure 88, the cell voltage drops occur at the similar test time, around 1000s, which might be the sign of the CID response. After that the venting occurred at around 1200s which corresponds to the temperature of $\sim 111^{\circ}\text{C}$, as observed in the temperature evolution of TC1 in Figure 87 for both tested cells. We also observed in Figure 87 that the moment of the accelerated thermal runaway (T_3) was delayed for the P1723 cell compared to that of the P1706 cell. This can be explained due to the lower temperature heating in case of oven test of P1723 cell as shown in Figure 87.

The maximum temperatures reached by these cells are in the range of $650^{\circ}\text{C} - 720^{\circ}\text{C}$. The hard ISC when cell voltage reach 0V are sooner in case of cell P1706 compared to that of the other tested cells as seen in Figure 88.

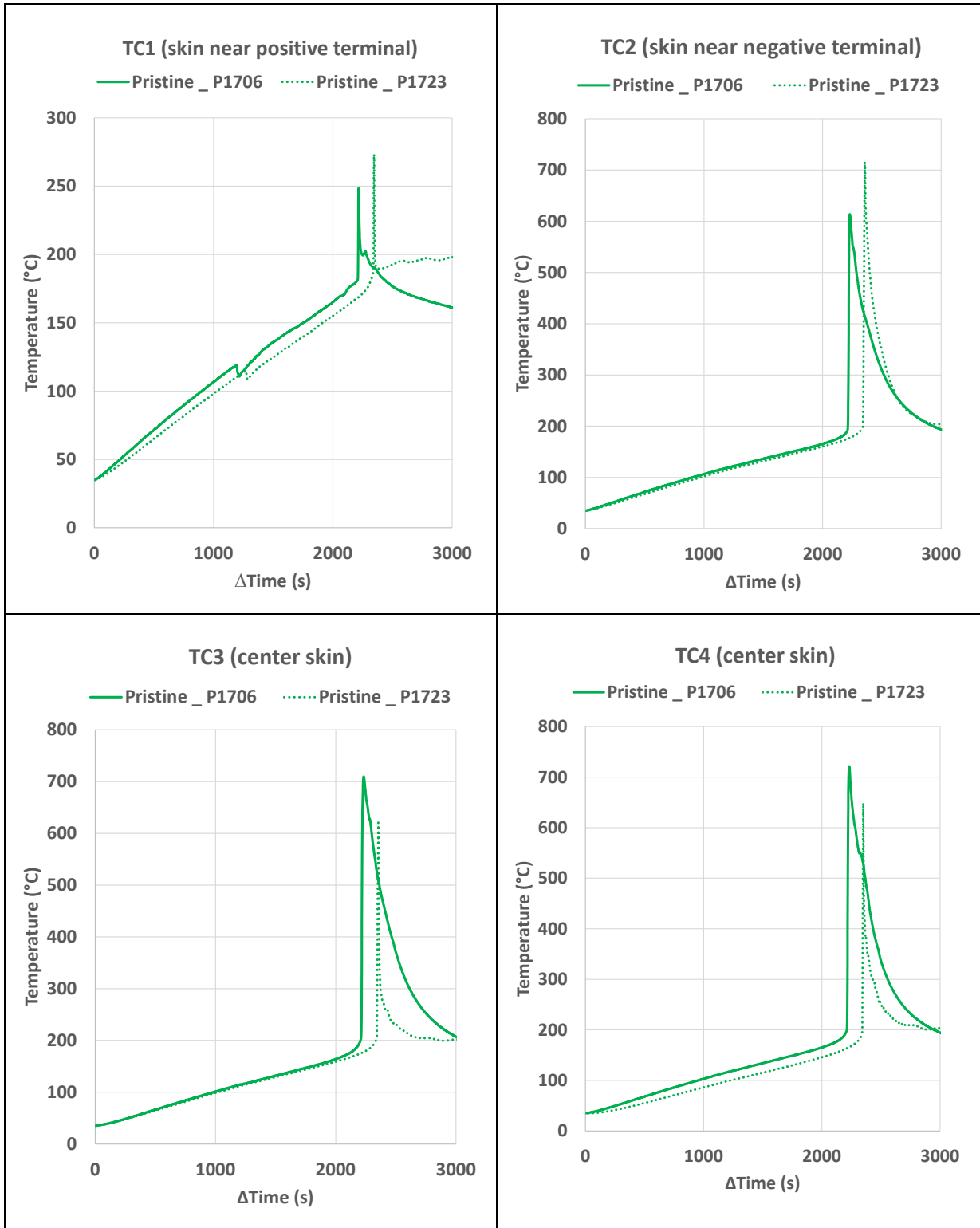


Figure 87: Temperature evolution of the TCs distributed on the skin of pristine Panasonic NCR GA tested cells.

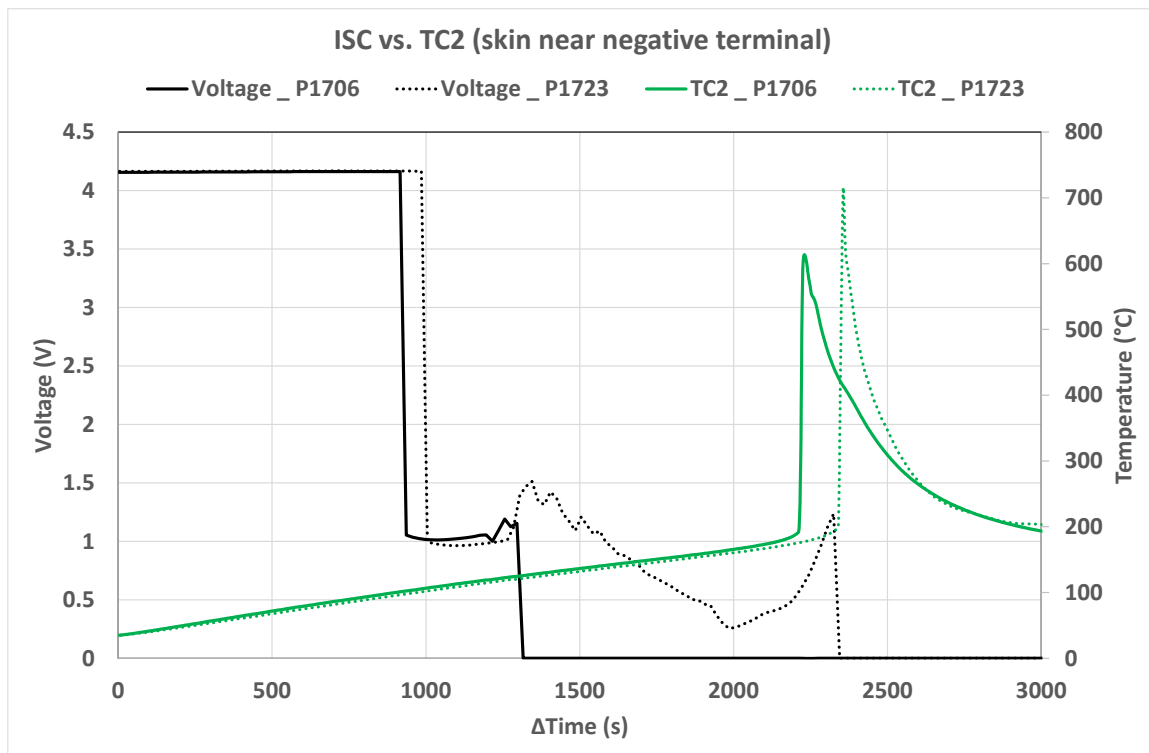


Figure 88: Temperature evolution and voltage of pristine Panasonic NCR GA tested cells.

2.5.2.6 Oven test results of LG HG2 at pristine state

The temperature evolution of two pristine LG HG2 tested cells (L1714 and L1715) are presented in Figure 89 in comparison with the results of the two pristine Panasonic NCR GA cells. We observed that the thermal runaway of the two LG HG2 cells occurred sooner than that of the Panasonic NCR GA cells. This finding is coherent with the HWS tests results in 2.5.1.

In Figure 90, the LG HG2 cell voltage drops also occur at the similar test time, around 1500s, which relates to the CID response. After that the venting occurred at around 1650s which corresponds to the temperature of $\sim 138^{\circ}\text{C}$, as observed in the temperature evolution of TC1 in Figure 90 for both LG HG2 tested cells. Therefore, the venting of LG HG2 pristine cells occurred later and at higher temperature than that of Panasonic NCR GA pristine cells.

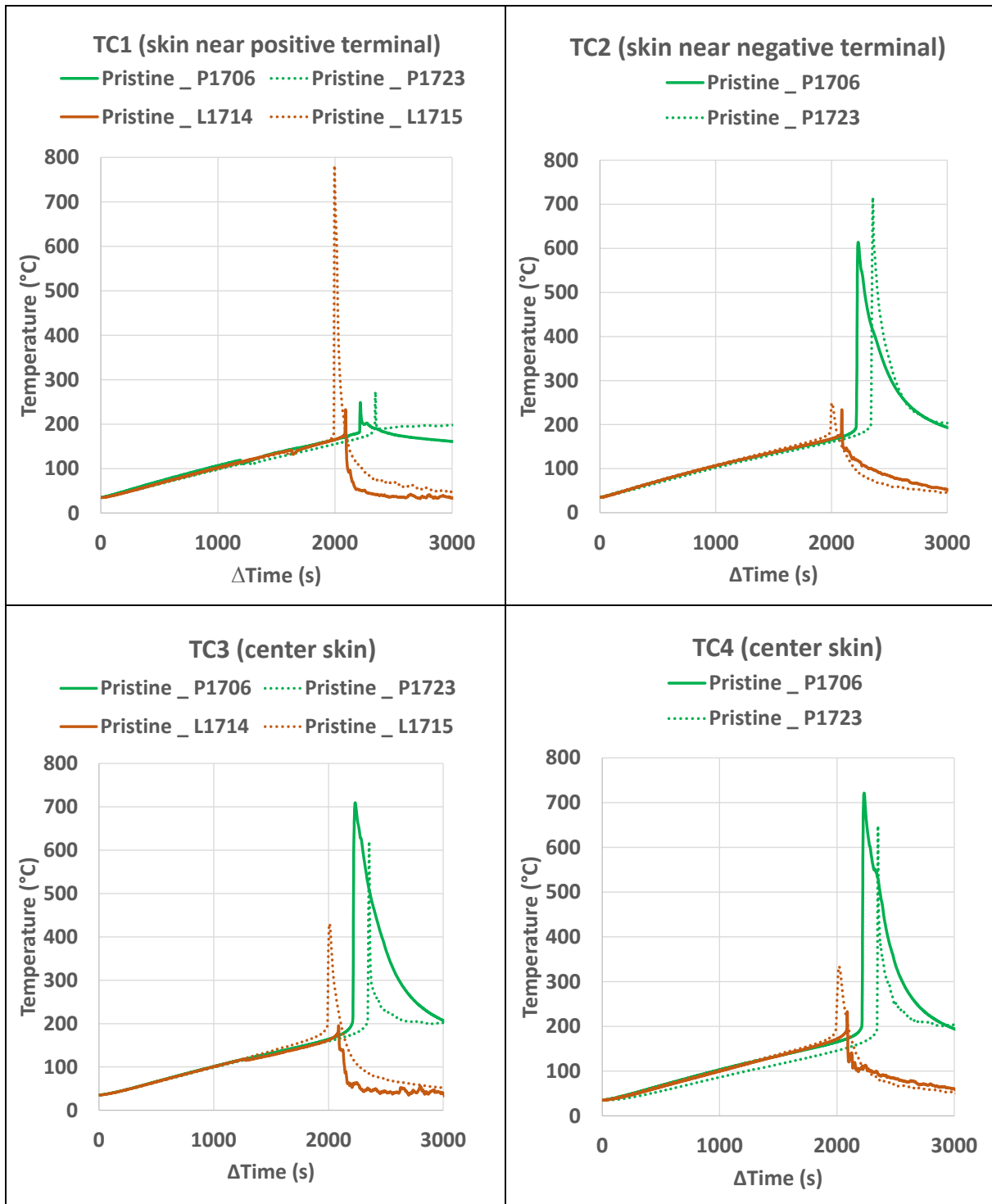


Figure 89: Temperature evolution of the TCs distributed on the skin of pristine LG HG2 and Panasonic NCR GA tested cells.

We also observed that the moment of the accelerated thermal runaway (T_3) was slightly delayed for the L1714 cell compared to that of the L1715 cell. Due to the limited operability of the locking system of the oven door, it is noteworthy that, during the accelerated thermal runaway of L1714 cell, the oven door opened. Due to this accidental thermal loss during the

accelerated thermal runaway, there is a huge drop in the temperature measured at the cell skin of L1714 cell. The oven test of L1715 was better performed, the maximum temperatures reached of L1715 is $\sim 800^{\circ}\text{C}$.

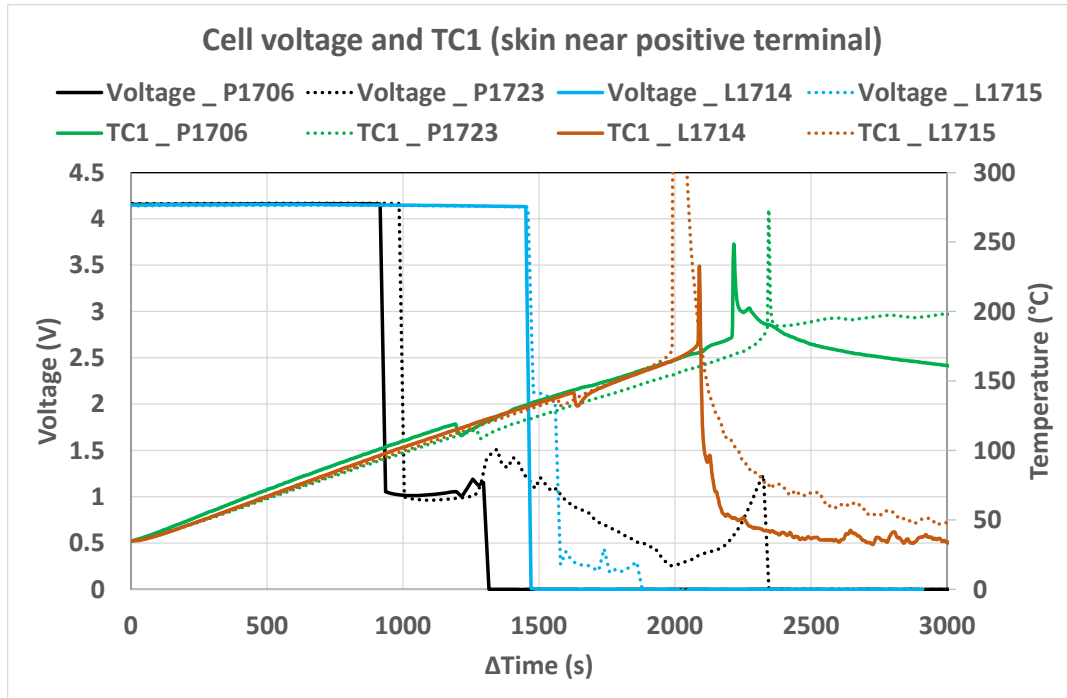


Figure 90: Temperature evolution and voltage behaviours of pristine LG HG2 cells compared to that of pristine Panasonic NCR GA cells.

2.5.2.7 Influence of calendar aging and cycling aging on the thermal runaway

The temperature evolution of the pristine Panasonic NCR GA cell (P1706) in comparison with the results of calendar aging Panasonic NCR GA cell (P1530) and cycling aging Panasonic NCR GA cell (P1555) are presented in Figure 92. The critical temperature T_3 and the venting temperature (T_{vent}) as well as their occurrence times (tT_3 and tT_{vent}) are shown in Table 25. We observed that the thermal runaway of the two aged cells are delayed compared to that of the pristine cell. It is also noteworthy that the venting occurred at around 1200s at $\sim 111^{\circ}\text{C}$ in case of pristine cells, while this event happened later (1519s and 1801s) and at higher temperatures (129°C and 144°C) in case of calendar aged cell and cycling aged cell, respectively, as seen in Figure 91. Consequently, the venting of cycling aged cells is delayed compared to that of calendar aged cell.

During the accelerated thermal runaway of the 2 aged cells, the oven door opened. Due to this issue, there is a huge drop in the temperature measured at the cell skin of two aged cells during their accelerated thermal runaway.

Table 25: Occurrence times and critical temperature of Panasonic NCR GA tested cells.

Panasonic NCR GA	tTvent (s)	Tvent (°C)	tT3 (s)	T3 (°C)
Pristine (cell P1706)	1214	111	2211	196
Calendar aging (cell P1530) 16.26% discharge capacity loss	1519	129	2307	199
Cycling aging (cell P1555) 16.67% discharge capacity loss	1801	144	2329	198

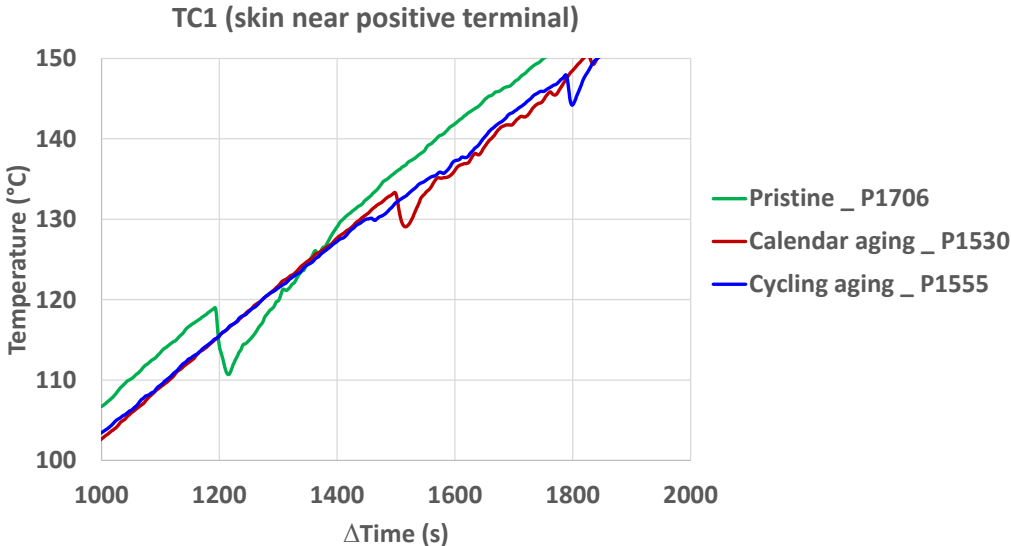


Figure 91: The venting of the Panasonic NCR GA pristine and aged tested cells.

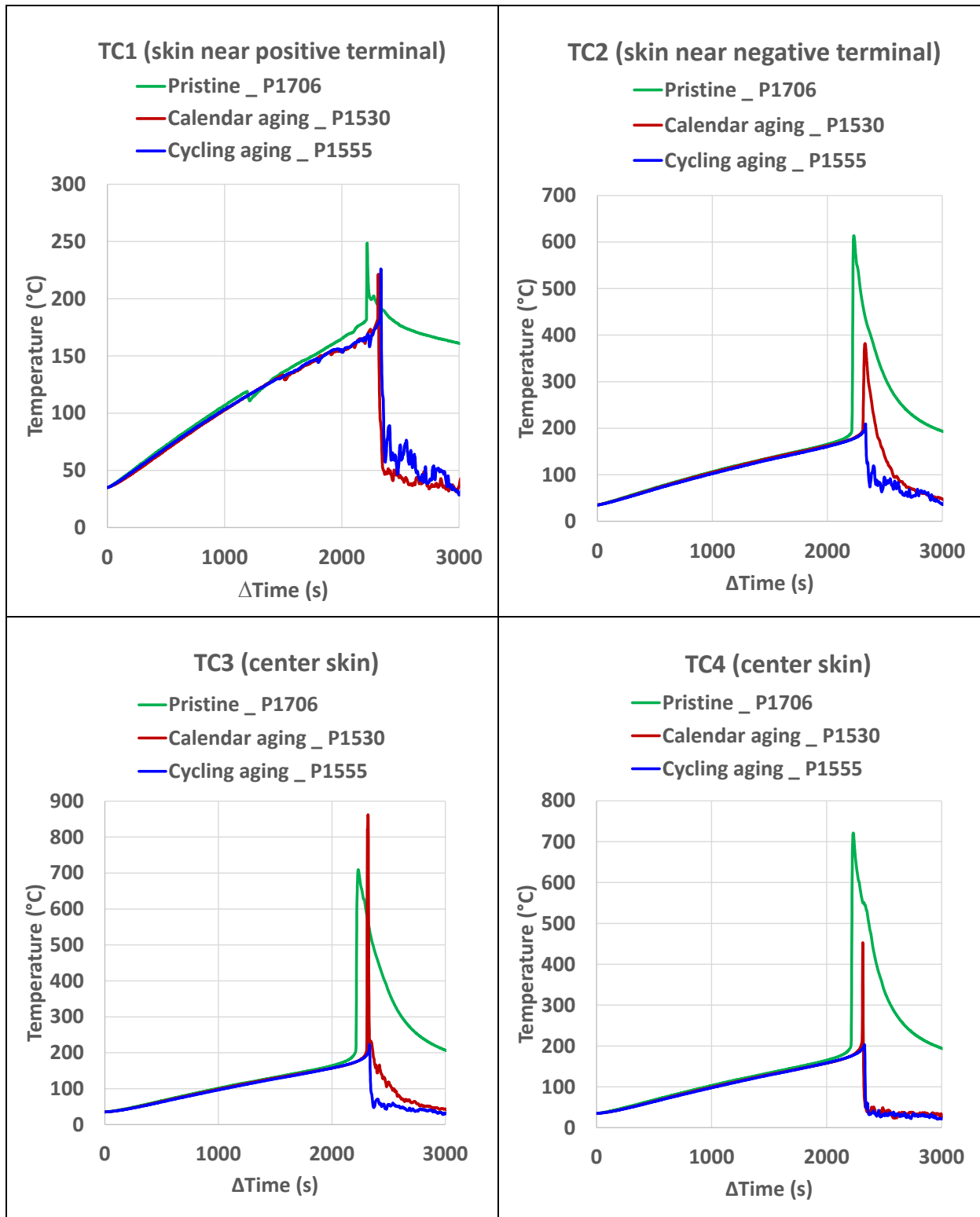


Figure 92: Temperature evolution of the TCs distributed on the skin of pristine, calendar aging and cycling aging Panasonic NCR GA tested cells.

2.6 Conclusions

Experimental study has launched in all 3 processes: Multi-scale cell analysis, Safety-focused aging campaign and Thermal safety tests in ARC BTC as well as in Oven with the interesting presented results.

The choice of Li-ion batteries technologies studied is well confirmed by multi-scale analysis of pristine cells. The two selected commercial 18650 Ni-rich LIBs, namely a Panasonic NCR GA and a LG HG2, which were based on NCA and NMC811, respectively, for positive electrodes, in combination with graphite-SiO_x composite negative electrodes. They are all very reactive technologies with high Ni content in positive electrode materials in combination with the novel negative electrode technologies: Graphite-SiO_x composites.

The safety-focused aging campaign has been finished with promising results. The dedicating aging monitoring activity has led to the development of a specific analysing tool for faster diagnosis of capacity fade due to aging, considering the vast amount of data produced.

Safety thermal tests in adiabatic condition with the new ARC (BTC500 E1735) has led us to a clearer understanding of the thermal runaway of the selected cells at pristine states and different SOC levels (50 % and 100 %). First, the results confirmed the proposed complete thermal runaway exothermic chain reactions for high-energy, Ni-rich LIBs. Then, the different factors impacting the thermal runaway kinetics are addressed. Finally, the relationship between safety features and SOC towards venting and component ejection mechanisms are demonstrated.

At pristine state, regardless of technology, cells at reduced SOC are less reactive. Regardless of SOC levels, the Panasonic NCR GA battery technology had a wider safe region than that of the LG HG2 battery. This technology also delayed the hard internal short circuit and shifted the final venting to a higher temperature. However, above this critical temperature, it exhibited the most severe irreversible self-heating stage, with the highest self-heating temperature rate over the longest duration.

The detailed findings will help to adjust and calibrate the multiphysics modelling tool as needed under COMSOL, which so far has been calibrated for lithium iron phosphate $LiFePO_4$ (LFP) cells developed by [16].

Due to the failure of BTC since the 2nd year of the thesis, the HWS tests were not made for aged cells. However, with the Oven tests, the thermal runaway of the aged cells were investigated. The oven tests will also contribute to the validation of the thermal runaway model, which would reflect more realistic thermal abuse conditions in real life of a battery (eg. “non-adiabatic”).

Chapter 3. Model construction, calibration and validation

“To avoid situations in which you might make mistakes may be the biggest mistake of all.”

- Peter McWilliams

Contents

3.1	Introduction	165
3.2	Model construction	167
3.2.1	Electrical-thermal sub-model	167
3.2.2	Thermal runaway process sub-model	168
3.2.3	Energy balance sub-model	178
3.2.4	Thermal exchange sub-model.....	181
3.2.5	Integration of SEI-driven Aging.....	186
3.3	Model calibration.....	187
3.3.1	Electrical-thermal sub-model calibration	188
3.3.2	Cell thermal properties characterization.....	191
3.3.3	Thermal exchange sub-model calibration	194
3.3.4	Thermal runaway process sub-model calibration.....	196
3.4	Model validation	208
3.4.1	Model validation results of Panasonic NCR GA Pristine cell 100%SOC	209
3.4.1	Model validation results of LG HG2 Pristine cell 100%SOC	214
3.4.2	Model limitation	221
3.5	Conclusion.....	222

3.1 Introduction

The objective of this chapter is to develop an extended model of the thermal runaway at the cell scale to simulate the temperature evolution of Li-ion batteries under thermal abuse conditions, with the support from the experimental results from chapter 2 of the thesis.

In a first part, the construction of the electrical-chemical-thermal model, including 3 sub-models of electrical-thermal sub-model, thermal runaway process sub-model and energy balance sub-model, will be described.

For the thermal runaway process sub-model, 4 main exothermic degradation reactions were considered in the thermal runaway 3D model of Li-ion battery in the works of Kim *et al.* [137] and calibrated for LFP/Graphite technology in Abada *et al.* [13, 16, 138]:

1. SEI decomposition
2. Decomposition reaction between the intercalated lithium and electrolyte solvent at the negative electrode (SEI formation)
3. Decomposition reactions at the positive electrode
4. Electrolyte combustion reaction

This sub-model has been extended in this thesis, as illustrated in Figure 93, by adding new phenomena (5), (6) below in order to account respectively: i) for internal short circuiting, ii) lithium-ion cell degassing (eg. venting):

5. Hard internal short circuit (ISC)
6. Venting

The phenomena 1 to 5 are all exothermic. Reactions 1 to 4 may release gases which increase the internal pressure of the cell and may lead to venting. The reaction between the electrolyte and the fluorinated binder is neglected in the works of Kim *et al.* [137] and Abada *et al.* [13, 16, 138] as well as in this work for simplification purposes, although fluorinated binders may be involved in some exothermic reactions at the anode side [153].

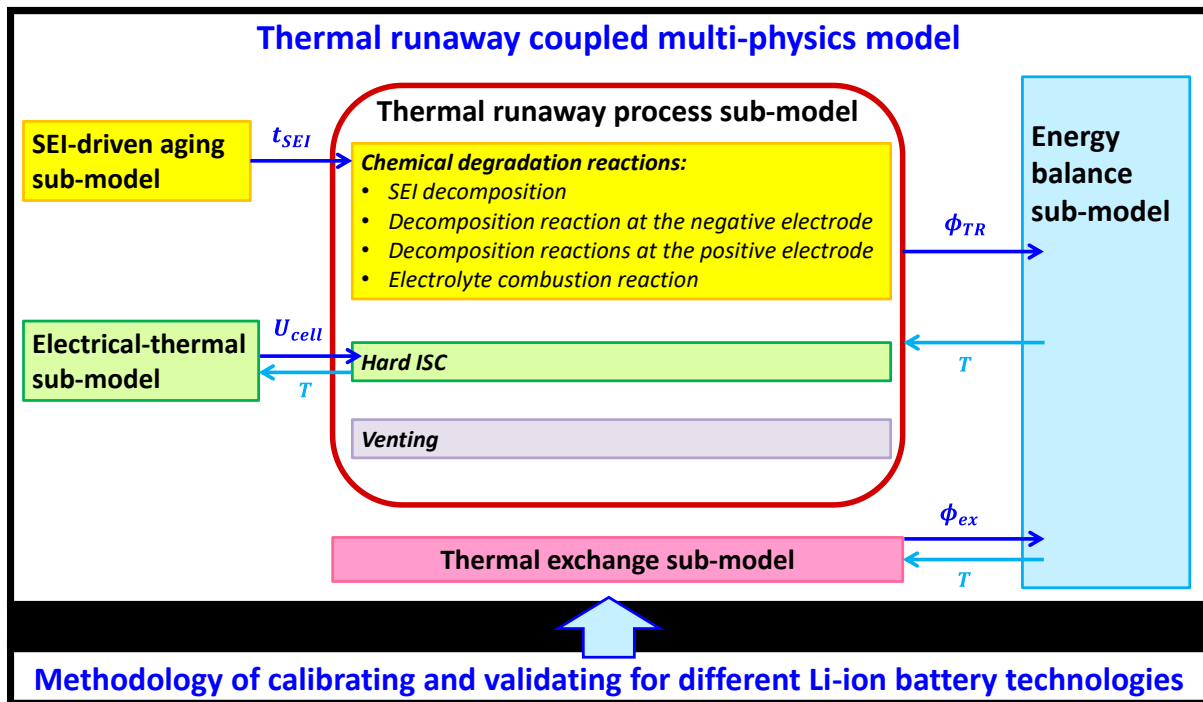


Figure 93: Thermal runaway coupled multi-physics model.

The thermal runaway model is calibrated based on the HWS tests in BTC. Therefore, in the second part of this chapter, thermal exchange sub-model is introduced to cope with practical difficulties of maintaining the pseudo-adiabatic condition during the thermal abuse tests in the ARC BTC system which were presented in chapter 2: abnormal thermal response of BTC has been observed and led to non-adiabatic condition during HWS tests, which alters the test results. This sub-model is designed to compensate this deviation. The integration of the SEI-driven aging which bases on the simplified electrochemical model developed within IFPEN [154], is also presented. This sub-model allows to study the influence of aging on the thermal runaway.

In a third part, the calibration of the thermal runaway model on the COMSOL Multiphysics software platform for NMC811/Graphite-SiOx (LG HG2) and NCA/Graphite-SiOx (Panasonic NCR GA) chemistries is described, with the determination of the subsequent parameters of all the sub-models. The geometries and physical parameters of the studied cells are also implemented. At the end, the calibration results of the thermal runaway model for the two selected technologies are discussed.

In a final part, the validation of the thermal runaway model developed at cell scale, as calibrated with parameters entailing the specific characteristics of Ni-rich chemistries of the two selected technologies, based on the comparison with the experimental data of Oven tests is detailed.

Therefore, the final deliverable of this chapter is a multi-dimensional multi-physics model of a Li-ion cell accounting for the triggering of thermal runaway under abuse thermal condition.

3.2 Model construction

The extended thermal runaway model includes 3 sub-models of electrical-thermal sub-model, thermal runaway process sub-model and energy balance sub-model. The electrical-thermal sub-model was used to represent the thermal-electrical behaviour of the cell. The thermo-chemical reactions during the thermal runaway were represented by dimensionless 0D model based on Hatchard *et al.* [136], Kim *et al.* [137] and Abada *et al.* [13, 16, 138].

3.2.1 Electrical-thermal sub-model

In this work, the second-order resistor-capacitor equivalent circuit model (2RC-ECM) is used in electrical modelling of LIB cells, thanks to its high computation efficiency, easy implementation and good simulation of the battery dynamic behaviours [155, 156]. As shown in Figure 94, this enhanced battery model is composed of the open circuit voltage (OCV), the Ohmic internal resistance R_0 , two parallel RC networks connected in series (i.e., R_1-C_1 and R_2-C_2). The model input is the applied current being $I(t)$ and the model output is the battery terminal voltage (U_{cell}).

The electric dynamic behaviour is significantly influenced by cell temperature, denoted T , notably through its internal resistance value as well as in terms of actual cell capacity or cell voltage [156]. Therefore, the OCV was considered as a function of battery SOC, which is denoted by $OCV(SOC)$. Similarly, the SOC and temperature dependencies were also taken into account for cell internal resistances, which are denoted by $R_0(SOC, T)$, $R_1(SOC, T)$, $R_2(SOC, T)$.

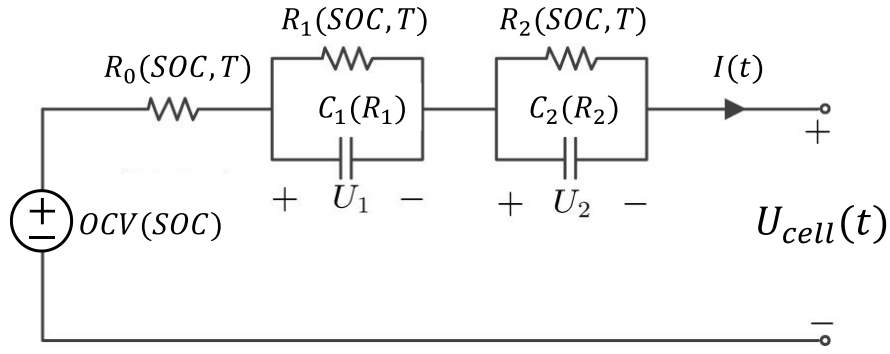


Figure 94: Second-order resistor-capacitor equivalent circuit model (2RC-ECM) of LIB, inspired by [156].

The SOC variation is expressed as in (Eq. 1), it is highly dependent on the cell actual capacity and the applied current.

$$SOC(t) = SOC(t_0) + \frac{1}{Q_{cell}} \int_{t_0}^t I(t) dt \quad (Eq. 1)$$

According to the Kirchhoff's laws, we can construct the set of equations for mathematically describing the relationships linking capacitor, voltage, and current of this battery, as follows:

$$\begin{cases} U_{cell}(t) = OCV(SOC, T) + R_0 \cdot I(t) + U_1 + U_2 & (Eq. 2) \\ \frac{dU_1(t)}{dt} = \frac{I(t)}{C_1} - \frac{U_1}{R_1 C_1}, & \text{with } C_1 = \frac{\tau_1}{R_1} & (Eq. 3) \\ \frac{dU_2(t)}{dt} = \frac{I(t)}{C_2} - \frac{U_2}{R_2 C_2}, & \text{with } C_2 = \frac{\tau_2}{R_2} & (Eq. 4) \end{cases}$$

3.2.2 Thermal runaway process sub-model

As mentioned in the introduction, this thermal runaway process sub-model is essentially based on the identified chemical degradation reactions introduced in Hatchard *et al.* [136] which were calibrated and validated for LiCoO₂/Graphite technology in Kim *et al.* [137] and for LFP/Graphite technology in Abada *et al.* [13, 16, 138], the venting recently defined in Coman *et al.* [139, 140], and the self-discharge introduced in the work of Petit *et al.* [138]. The main chemical degradation reactions and phenomena occurred during the thermal runaway which were taken into account in this “extended” model are:

1. SEI decomposition

2. Negative electrode decomposition (SEI formation reaction)
3. Positive electrode decomposition
4. Electrolyte decomposition
5. Hard internal short circuit (ISC)
6. Venting

This model is able to predict the global heat flow generated from these reactions during the thermal runaway, ϕ_{TR} , using (Eq. 5):

$$\phi_{TR} = \phi_{SEI} + \phi_{ne} + \phi_{pe} + \phi_e + \phi_{ISC} + \phi_{vent} \quad (Eq. 5)$$

Where:

- ϕ_{SEI} is the heat flow generated from the SEI decomposition reaction [W].
- ϕ_{ne} is the heat flow generated from the interface electrolyte/negative electrode reaction of SEI formation [W].
- ϕ_{pe} is the heat flow generated from the interface electrolyte/positive electrode reaction [W].
- ϕ_e is the heat flow generated from the degradation reaction of the electrolyte [W].
- ϕ_{ISC} is the heat flow generated from the hard ISC [W].
- ϕ_{vent} is the heat flow generated from the venting [W].

The electro-chemical-thermal model, resulting from coupling an electrochemical model with a thermal model, is used to reflect the heat and gas mass flows generated within the cell by the 4 electrochemical degradation reactions in terms of a set of thermal equations. These equations can describe the temporal evolution of the concentration of the species involved in these exothermic reactions ($c_{species}$) and also express the thermochemical kinetics (reaction activation energy E_a and frequency factor A) and various parameters of material transport with temperature dependency, through the temperature dependence of the reaction rate R which is addressed using Arrhenius law. For each reaction i , the reaction rate R_i is evaluated as the volumetric reaction rates (Eq. 6).

$$R_i = A_i \cdot \exp\left(-\frac{E_{a_i}}{k_B \cdot T}\right) \cdot (c_{species})^m = -\frac{dc_{species}}{dt} \quad (Eq. 6)$$

Except the venting, these main thermal runaway reactions are all exothermic.

3.2.2.1 Solid electrolyte interface decomposition reaction

Active particles of the negative electrode are protected from direct reaction with the electrolyte solvent by the ionically conducting SEI layer. According to the literatures [107, 137, 157], unstable SEI can exothermically decompose at approximately 60°C. Inspired by [13, 16, 136–138], the heat flow generated by this unstable SEI stabilization reaction, ϕ_{SEI} , is determined in our model by (Eq. 7):

$$\phi_{SEI} = h_{SEI} \cdot w_{ne} \cdot R_{SEI} \quad (Eq. 7)$$

Where:

- h_{SEI} is the specific enthalpy of the reaction (the heat released by the metastable SEI reaction per mass of active material in the negative electrode) [J/kg].
- w_{ne} is the mass of active material in the negative electrode [kg].
- R_{SEI} is the reaction rate [1/s], which is defined as (Eq. 8):

$$R_{SEI} = A_{SEI} \cdot \exp\left(-\frac{E_{aSEI}}{k_B \cdot T}\right) \cdot (c_{SEI})^{m_{SEI}} = -\frac{dc_{SEI}}{dt} \quad (Eq. 8)$$

Where:

- A_{SEI} is the reaction frequency factor [1/s].
- E_{aSEI} is the thermal reaction activation energy [J].
- m_{SEI} is the reaction order [-].
- k_B is the Boltzmann constant $1.380 \cdot 10^{-23}$ [m².kg/s²/K].
- c_{SEI} is the normalized concentration of lithium-containing unstable species in the SEI [-].

3.2.2.2 Decomposition reaction between the intercalated lithium and electrolyte solvent at the negative electrode

The solvent decomposition reaction on the negative electrode/electrolyte interface is responsible for initial SEI layer built up during battery formation and the SEI growth due to aging. Inspired by [13, 16, 136–138], this exothermal reaction leads to the generated heat flow, ϕ_{ne} , described in (Eq. 9):

$$\phi_{ne} = h_{ne} \cdot w_{ne} \cdot R_{ne} \quad (\text{Eq. 9})$$

Where:

- h_{ne} is the reaction specific enthalpy [J/kg].
- w_{ne} is the mass of the active material in the negative electrode [kg].
- R_{ne} is the reaction rate [1/s], which is assumed to be limited by the diffusion, and valuated as follow:

$$R_{ne} = A_{ne} \cdot \exp\left(-\frac{E_{ane}}{k_B \cdot T}\right) \cdot (c_{ne})^{m_{ne}} \cdot \exp\left(-\frac{t_{SEI}}{t_{SEI,ref}}\right) = \frac{dc_{ne}}{dt} = -\frac{dt_{SEI}}{dt} \quad (\text{Eq. 10})$$

Where:

- A_{ne} is the reaction frequency factor [1/s].
- E_{ane} is the reaction activation energy [J].
- m_{ne} is the reaction order [-].
- c_{ne} is the normalized concentration of Li intercalated in the negative electrode [-]. Note that this value depends on the state of charge of the cell at the beginning of positive degradation reaction.
- t_{SEI} is the normalized thickness of the SEI [-].
- $t_{SEI,ref}$ is a dimensionless quantity to account for diffusive limitation [-].

This decomposition reaction (Eq. 10) leads to the growth of SEI layer and consequently the change of the amount of intercalated Li in the negative electrode. These changes are important during the process of cell aging. However, there are very different time constants

reflecting the thermal runaway vs the aging process of the cell during its operation. Therefore, for simplification purpose in the thermal runaway modelling work, it is assumed that the behaviour of the cell during the thermal runaway is not impacted by those changes.

The “ $\exp\left(-\frac{t_{SEI}}{t_{SEI,ref}}\right)$ ” expression addresses the diffusion limitation of the SEI growth to this reaction [136, 137], which also indicates that the bigger the SEI layer (higher t_{SEI}) is, the slower this reaction will be. It is to be noted that the exothermal stabilization of the SEI is already taken into account in these mechanism and no extra terms have to be added in (Eq. 7).

3.2.2.3 Reactions at the positive electrode

Positive electrode active materials in their oxidized state can exothermically react with the electrolyte. Or in another case, they exothermically decompose and produce oxygen that can react exothermically with the electrolyte [136, 137]. A number of studies [3, 4, 13, 108] show that these exothermic reactions begin at a range of temperatures from approximately 130 to 250 °C. Inspired by [13, 16, 136–138], the heat flow released by the electrolyte decomposition reaction on the positive electrode, ϕ_{pe} , is determined from (Eq. 11):

$$\phi_{pe} = h_{pe} \cdot w_{pe} \cdot R_{pe} \quad (Eq. 11)$$

Where:

- h_{pe} is the reaction specific enthalpy [J/kg].
- w_{pe} is the mass of active material in the positive electrode [kg].
- R_{pe} is the reaction rate [1/s], which is obtained by (Eq. 12):

$$R_{pe} = A_{pe} \cdot \exp\left(-\frac{E_{ape}}{k_B \cdot T}\right) \cdot (\alpha)^{m_{pe}^{p1}} \cdot (1 - \alpha)^{m_{pe}^{p2}} = \frac{d\alpha}{dt} \quad (Eq. 12)$$

Where:

- A_{pe} is the reaction frequency factor [1/s].
- E_{ape} is the reaction activation energy [J].

- α is the decomposition reaction advancement, which addresses the conversion degree of the positive electrode active material [-]. α evolves in the range of [0..1]. Note that the initial value of this parameter depends on the state of charge of the cell at the beginning of positive degradation reaction.
- m_{pe}^{p1} is the reaction order of α . The expression $(\alpha)^{m_{pe}^{p1}}$ represents the exothermic reaction between the electrolyte and the conversion part of the positive electrode active materials.
- m_{pe}^{p2} is the reaction order of $(1 - \alpha)$. The expression $(1 - \alpha)^{m_{pe}^{p2}}$ represents the exothermic reaction between the electrolyte and the non-conversion part of the positive electrode active materials.

3.2.2.4 Electrolyte combustion reaction

At high temperature, the electrolyte becomes unstable and is oxidized due to the contact with available oxygen released by cell internal reactions or from ambient air during cell venting. Inspired by [13, 16, 136–138], this exothermic reaction leads to the released heat flow, ϕ_e , which is evaluated by (Eq. 13):

$$\phi_e = h_e \cdot w_e \cdot R_e \quad (\text{Eq. 13})$$

Where:

- h_e is the reaction specific enthalpy [J/kg].
- w_e is the mass of electrolyte in the cell [kg].
- R_e is the reaction rate [1/s], which is estimated by (Eq. 14):

$$R_e = A_e \cdot \exp\left(-\frac{E_{ae}}{k_B \cdot T}\right) \cdot (c_e)^{m_e} = -\frac{dc_e}{dt} \quad (\text{Eq. 14})$$

Where:

- A_e is the reaction frequency factor [1/s].
- E_{ae} is the reaction activation energy [J].

- m_e is the reaction order [-].
- c_e is the dimensionless concentration of electrolyte [-].

This electrolyte decomposition reaction leads to the decrease of the electrolyte quantity, thereby, the c_e dimensionless variable decreases.

3.2.2.5 Hard internal short circuit

As cell temperature increases, the separator melts and collapses, subsequently the cell undergoes internal short-circuit leading to the voltage drop to 0V. The hard ISC energy is released inside the cell as heat. Inspired by [13, 138], the ISC heat flow, ϕ_{ec} , is given by (Eq. 15):

$$\phi_{ec} = U_{cell} \cdot I_{TR} \quad (Eq. 15)$$

Where:

- U_{cell} is the cell voltage [V].
- I_{TR} is the discharge current [A], which is expressed as (Eq. 16):

$$I_{TR} = A_{ec} \cdot \exp\left(-\frac{E_{aec}}{k_B \cdot T}\right) \cdot U_{cell} \cdot Q_{cell} \cdot k \quad (Eq. 16)$$

Where:

- A_{ec} is the frequency factor of the hard ISC [s^{-1}].
- E_{aec} is the activation energy of the hard ISC [J].
- Q_{cell} is the cell actual capacity [Ah].
- $k = -3600 [V^{-1}]$

We considered the loss of cell capacity due to the positive electrode decomposition reaction. The residual capacity, Q_{cell} , is reduced compared to the initial cell capacity (Q_{cell}^0), as reflected by (Eq. 17):

$$Q_{cell} = F_{Q_{res}} \cdot Q_{cell}^0 \quad (Eq. 17)$$

Where:

- $F_{Q_{res}}$ is the ratio between the instantaneous residual capacity and the initial cell capacity. this parameter is estimated as a function of the advancement of positive electrode decomposition reaction, as described in (Eq. 18):

$$F_{Q_{res}} = F_{Q_{res}}^{inf} + \left(1 - \frac{\alpha - \alpha^0}{1 - \alpha^0}\right) \cdot (1 - F_{Q_{res}}^{inf}) \quad (Eq. 18)$$

Where:

- $F_{Q_{res}}^{inf}$ is the ratio between the capacity after the positive electrode is fully decomposed and the initial capacity [-].
- α^0 is the initial positive reaction decomposition advancement [-].

3.2.2.6 Venting

Due to the gases released from the exothermic decomposition reactions, the pressure inside the cell increases. The venting occurs when cell internal pressure becomes higher than the burst pressure of the safety vent. The venting occurs once the vent opens. Inspired by the lumped approach following the works from Coman *et al.* [139, 140] and Petit *et al.* [138], this event is mathematically described in this thesis based on the consideration of the amount of gas generation. The energy loss due to heat flow drop in the cell during venting, Φ_{vent} , is addressed in (Eq. 19):

$$\Phi_{vent} = R \cdot T \cdot \frac{dy}{dt} \quad (Eq. 19)$$

Where:

- y is the amount of gas ejected due to venting [mol].

The vent opens when the difference between the internal cell pressure and the ambient pressure reaches the burst pressure of the venting device (Eq. 20):

$$(P_{cell} - P_{amb}) \geq P_{burst} \quad (Eq. 20)$$

Where:

- P_{cell} is the cell internal pressure [bar].
- P_{amb} is the ambient pressure [bar].
- P_{burst} is the burst pressure of the venting device [bar].

The cell pressure P_{cell} depends on the amount of gas generated inside the cell and the amount of gas released during venting, as well as the cell temperature, as described in (Eq. 21):

$$P_{cell} = P_0 + \frac{R \cdot T}{1e5 \cdot V_h} (n_{SEI} + n_{ne} + n_{pe} + n_e - y) \quad (Eq. 21)$$

Where:

- P_0 is the internal pressure before gas release [bar].
- V_h is the headspace volume of the cell [m³].
- n_{SEI} is the amount of gas formed by the SEI decomposition reaction [mol].
- n_{ne} is the amount of gas formed by the solvent reduction on the negative electrode [mol].
- n_{pe} is the amount of gas formed by the electrolyte decomposition on the positive electrode [mol].
- n_e is the amount of gas formed by the electrolyte decomposition [mol].

Inspired by Coman *et al.* [139, 140], the amount of gas escaping the cell due to venting, y , is evaluated from (Eq. 22):

$$\frac{dy}{dt} = \frac{dn_{out}}{dt} + \frac{dn_{gas}}{dt} \quad (Eq. 22)$$

Where:

- n_{out} is the quantity of gas leaving the cell while venting occurs due to the pressure difference between the cell and the ambient (transient event) [mol].
- n_{gas} is the total amount of gas emitted from the decomposition reactions and released while the vent is opened [mol].

When venting begins, the quantity of the gas leaving the cell due to the pressure difference between the cell and the ambience, n_{out} , can be calculated by using the isentropic flow equation for a gas passing through a nozzle (Eq. 23):

$$\frac{dn_{out}}{dt} = \frac{V_{vent} \cdot P_{vent} \cdot A_{vent}}{R \cdot T_{vent}} \quad (Eq. 23)$$

Where:

- V_{vent} is the velocity of the gas escaping the cell [m/s].
- P_{vent} is the pressure of the gas escaping the cell [bar]
- A_{vent} is the cross-section area of the pressure disk opening [m²].
- R is the gas constant, 8.314 [J/(mol.K)]
- T_{vent} is the temperature at the outlet [K].

These parameters are assessed as follows from equations (Eq. 24), (Eq. 25), (Eq. 26):

$$P_{vent} = \frac{P_{cell}}{\left(1 + \frac{\gamma - 1}{2} \cdot M^2\right)^{\frac{\gamma - 1}{\gamma}}} \quad (Eq. 24)$$

$$T_{vent} = \frac{T}{1 + \frac{\gamma - 1}{2} \cdot M^2} \quad (Eq. 25)$$

$$V_{vent} = M \cdot \sqrt{\frac{\gamma \cdot R \cdot T}{M_{gas}}} \quad (Eq. 26)$$

Where:

- γ is the specific heat capacity ratio of the gas formed (C_p/C_v).
- M_{gas} is the molar mass of gas formed [kg/mol].
- M is the Mach number, the ratio of the speed of the flow to the speed of sound, which is defined as (Eq. 27):

$$\left\{ \begin{array}{l} M = 0, \quad \text{if vent is closed} \\ M = \min \left(\sqrt{\frac{2}{\gamma - 1} \cdot \left[\left(\frac{P_{cell}}{P_{amb}} \right)^{\frac{\gamma-1}{\gamma}} - 1 \right]}, 1 \right) \end{array} \right. \quad (\text{Eq. 27})$$

When there is no venting, $M = 0$ leads to $P_{vent} = P_{cell}$, $T_{vent} = T$, $V_{vent} = 0$ hence $m_{out} = 0$. When the pressure of the cell stabilises with the ambient pressure ($P_{cell} = P_{amb}$), $M = 0$, hence $m_{out} = 0$.

While the vent is opened, the gas emitted from the decomposition reactions releases and this amount of gas can be calculated from (Eq. 28):

$$\frac{dn_{gas}}{dt} = \begin{cases} 0, & \text{if vent is closed} \\ \frac{dn_{SEI}}{dt} + \frac{dn_{neg}}{dt} + \frac{dn_{pos}}{dt} + \frac{dn_{ne}}{dt}, & \text{if vent is opened} \end{cases} \quad (\text{Eq. 28})$$

In which, the amount of gas formed by the decomposition reaction i , n_i , is given by (Eq. 29):

$$\frac{dn_i}{dt} = R_i \cdot w_i \cdot V g_i \quad (\text{Eq. 29})$$

Where:

- R_i is the reaction rate of reaction i [1/s].
- w_i is the mass of reactant relative to reaction i [kg].
- $V g_i$ is the amount of gas produced by reaction i relative to its mass of reactant [mol/kg].

3.2.3 Energy balance sub-model

In this sub-model, the energy balance is mathematically modelled. The energy balance models can be classified dimensionally into 0D, 1D, 2D or 3D, which refers to the number of independent space variables of which the modelled system is function of.

3.2.3.1 0D energy balance model

0D energy balance model has no spatial dependency. It is given by an ordinary differential equation of the average temperature of cell skin (Eq. 30), which is a function of only one

variable (time in this case). It means that this 0D energy balance model is only time dependent.

$$M_{cell} \cdot C_{p,average} \cdot \frac{dT}{dt} = \phi_{TR} + P_{heater} \quad (Eq. 30)$$

Where:

- M_{cell} is the cell mass [kg]. This mass is considered constant even in case venting occurs.
- $C_{p,average}$ is the average heat capacity of the cell [J/(kg.K)].
- P_{heater} is the heat flow profile sent by the BTC heater winding around the cell to heat up the cell [W].
- ϕ_{TR} is the global heat flow generated from the reactions occurred during the thermal runaway.

This model does not consider the spatial dimensions, thereby, the battery cell is seen as a point whose temperature is the average temperature of the battery cell. Therefore, the heat transfers (radiation and convection) exchange between the cell and its surrounding are represented by a single effective exchange coefficient. Consequently, 0D model faces its limits where the approach of homogenized average thermal properties is no longer valid. This type of model is sometimes sufficient to properly simulate cell-scale thermal behaviour under normal operating conditions. In case of thermal abuse conditions during the thermal runaway, it is then necessary to develop 3D energy balance model, as clearly shown, by various researchers [13, 16, 137, 138]. However, 0D simulation is essential to allows us to calibrate the different reactions during the thermal runaway in the most efficient way, before going to 3D model calibration and validation.

3.2.3.2 3D energy balance model

Further to time dependence capability, 3D model allows for spatial dependency requirements. Therefore, the model is extended to three dimensions so we could consider the geometrical features. It is obtained from energy conservation law by the well-known partial differential equation of the temperature (Eq. 31), which is describing temperature as

a function of different independent variables (time, spatial coordinates). Therefore, this 3D model is able to consider different heat sources in the core of the battery cell.

In the core of the cell, the thermal conduction is assumed to dominate the internal heat transport in the cell because the convective heat through the net flow of electrolyte and production gas is limited [137]. So inside the cell, the heat is dissipated by conduction, therefore, the energy balance is expressed as in (Eq. 31):

$$\rho \cdot C_{p,average} \frac{\partial T}{\partial t} = \phi_{TR} + k_r \frac{\partial^2 T}{\partial x^2} + k_r \frac{\partial^2 T}{\partial y^2} + k_z \frac{\partial^2 T}{\partial z^2} \quad (Eq. 31)$$

Where:

- ϕ_{TR} is the heat flow density generated from the reactions during the thermal runaway [W/m³].
- k_r, k_z are the thermal conductivities in the radial and vertical directions of the cylindrical cell [W/(m.K)].

Inspired by [138], in this 3D model, the ISC is considered as a global mechanism. It means that the battery cell goes to ISC in a uniform manner, where the heat flow generated from this reaction, ϕ_{ec} , is estimated based on the cell average temperature, $T_{average}$, as written in (Eq. 32):

$$\phi_{ec} = U_{cell} \cdot I_{TR} = U_{cell} \cdot \left[A_{ec} \cdot \exp\left(-\frac{E_{aec}}{k_B \cdot T_{average}}\right) \cdot U_{cell} \cdot Q_{cell} \cdot k \right] \quad (Eq. 32)$$

Similarly for the venting, it is considered as a global event, and thereby, its heat flow, Φ_{vent} in (Eq. 33), is calculated based on the cell average temperature:

$$\Phi_{vent} = R \cdot T_{average} \cdot \frac{dy}{dt} \quad (Eq. 33)$$

Even though it is possible to set up and solve a 3D energy balance model of a battery cell, such a model would require a relatively large amount of computational resources to be used in practice. By exploiting the symmetry of the selected batteries (cylindrical cells), the model can be solved much faster. Because these batteries are structurally symmetric around its

axis, i.e., it's axisymmetric, we assumed that there are temperature variations in the radial (r) and vertical (z) directions only and not in the angular direction. Therefore, the model was then solved with the 2D axisymmetric modelling approach (Figure 95) in the rz-plane instead of the full 3D model, which has saved considerable memory and most importantly accelerated the computation time.

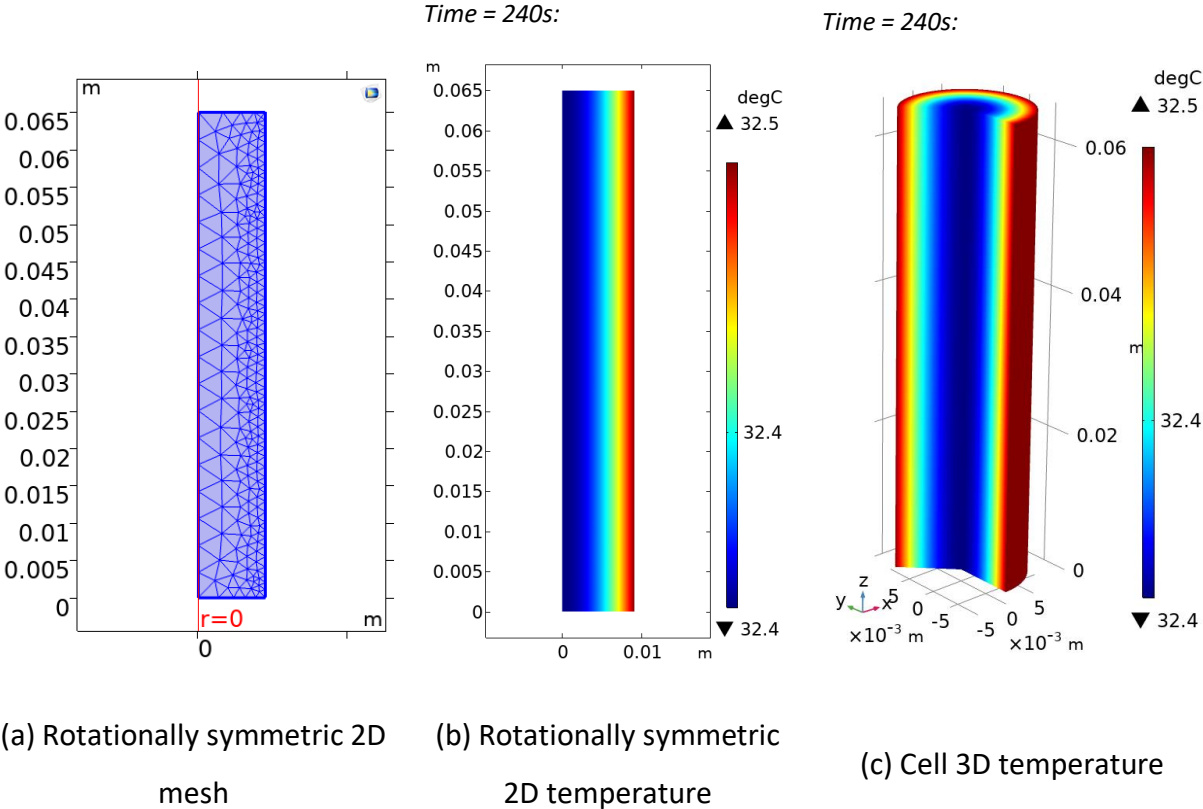


Figure 95: Rotationally symmetric 2D approach for 3D thermal model.

The electro-chemical-thermal sub-models have been well coupled with the energy balance sub-model to achieve a multi-physics predictive 3D model of the thermal runaway.

Overall, the proper combination of 0D and 3D thermal runaway simulations represents a time-efficient tool for assessing the behaviours of battery cell during the thermal runaway, especially during the model calibration process presented in section 3.5.

3.2.4 Thermal exchange sub-model

In this section, we outline the construction of the thermal exchange sub-model in the COMSOL Multiphysics software platform.

3.2.4.1 Thermal exchange sub-model accounting the non-ideal adiabatic condition during HWS test in BTC

Facing the technical difficulties in maintaining the pseudo-adiabatic condition during the thermal abuse tests in ARC BTC for model calibration, we developed this thermal exchange sub-model to take into account the thermal loss/gain resulting from the non-ideal adiabatic conditions which actually occurred during HWS test in the BTC. This model also further fits for the cooling step of the HWS protocol (link with chapter 2) which is activated after the thermal runaway, where pseudo-adiabatic environment does not prevail any longer. The heat flow exchange between the cell and its surrounding is denoted as ϕ_{ex} .

In the 0D model, this heat flow exchange is implemented into the energy balanced equation as follow:

$$M_{cell} \cdot C_{p,average} \cdot \frac{dT}{dt} = \phi_{TR} + P_{heater} + \phi_{ex} \quad (Eq. 34)$$

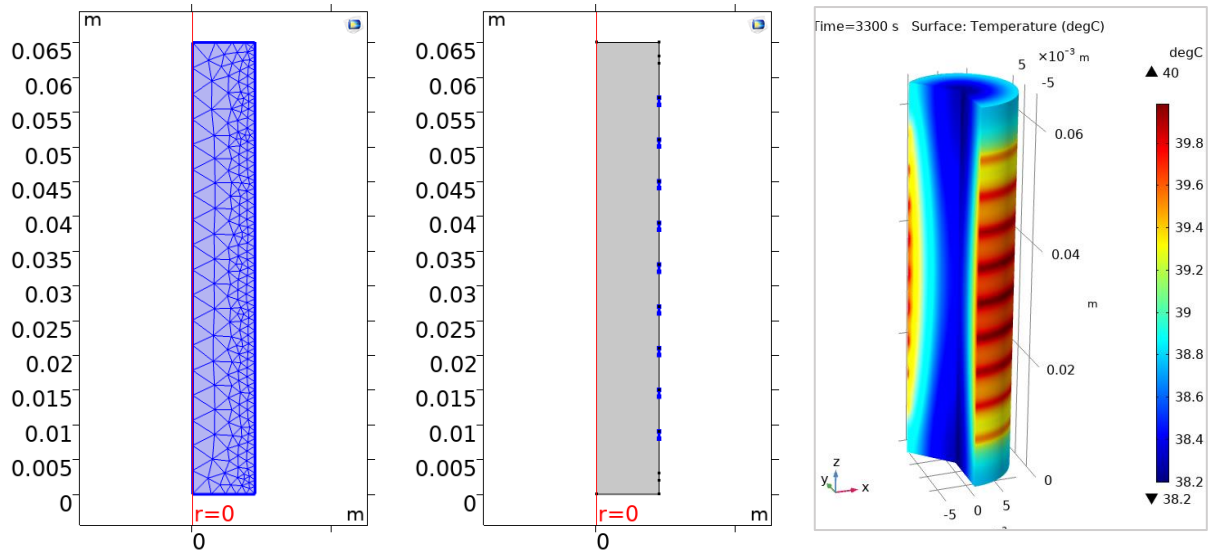
Where ϕ_{ex} is addressed in (Eq. 35):

$$\phi_{ex} = -\beta \cdot P_{heater} - h_{ex} \cdot A_{cell} \cdot (T - T_{amb}) \quad (Eq. 35)$$

In which:

- The expression $\beta \cdot P_{heater}$ corresponds to the heat loss of the heater winding around the cell during the heat steps in the HWS protocol, which the cell did not received.
- The expression $h_{ex} \cdot A_{cell} \cdot (T - T_{amb})$ corresponds to the heat exchange between the cell and its surrounding.

In the 3D model, the heat exchange is implemented at the boundary between the cell skin and the surrounding environment. The positions of the heater winding around the cell were also modelled with the 2D axisymmetric modelling approach in the rz-plane as shown in Figure 96.



(a) Rotationally symmetric 2D mesh (b) Heat source positions received from heater (blue) (c) 3D cell model temperature during thermal abuse test

Figure 96: The positions of the heater winding around the cell modelled with the rotationally symmetric 2D approach.

At this boundary, the heat exchange combines different modes of heat transfer which is expressed as the boundary conditions as shown in (Eq. 36):

$$\begin{aligned}
 \phi_{exchange_n} &= -k_n \frac{\partial T}{\partial n} \\
 &= \begin{cases} h_{conv}(T_{skin} - T_{amb}) + \varepsilon\sigma(T_{skin}^4 - T_{amb}^4) \\ h_{conv}(T_{skin} - T_{amb}) + \varepsilon\sigma(T_{skin}^4 - T_{amb}^4) + \frac{(1-\beta) \cdot P_{heater}}{A_{heater}} \end{cases} \text{ at heater position} & (Eq. 36) \\
 &= \begin{cases} h_{ex}(T_{skin} - T_{amb}) \\ h_{ex}(T_{skin} - T_{amb}) + \frac{(1-\beta) \cdot P_{heater}}{A_{heater}} \end{cases} \text{ at heater position}
 \end{aligned}$$

Where:

- $\phi_{exchange_n}$ represents the exchange heat flow from the cell core in the direction n [W].
- h_{conv} is the convective heat transfer coefficient [W/(m².K)].
- ε is the emissivity of the cell surface [-].

- σ is the Stefan-Boltzmann's constant [$W/(m^2.K^4)$].

The expression $\beta \cdot \frac{P_{heater}}{A_{heater}}$ corresponds to the heat loss of the heater winding around the cell during the heat steps in the HWS protocol, which the cell did not received.

The expression " $h_{conv}(T_{skin} - T_{amb}) + \varepsilon\sigma(T_{skin}^4 - T_{amb}^4)$ " is the sum of the convective heat flux out to ambient and the radiative heat out to ambient from cell surface. To simplify, this sum is written as the convective heat flux $h_{ex}(T_{skin} - T_{amb})$ in this research where h_{ex} is the effective heat transfer coefficient (Eq. 36). Since we model the thermal runaway at the cell scale, this simplification has very small impact, but it may provide inaccuracies if this model is used to study the propagation of thermal runaway between the cells.

3.2.4.2 Thermal exchange sub-model simulating the oven test

This sub-model is used for validation procedure and parametric study. This numerical simulation tool is based on the Oven tests that were presented in chapter 2, therefore it is also called as Oven test sub-model. This simulation tool is developed on COMSOL multi-physics platform, as shown in Figure 97.

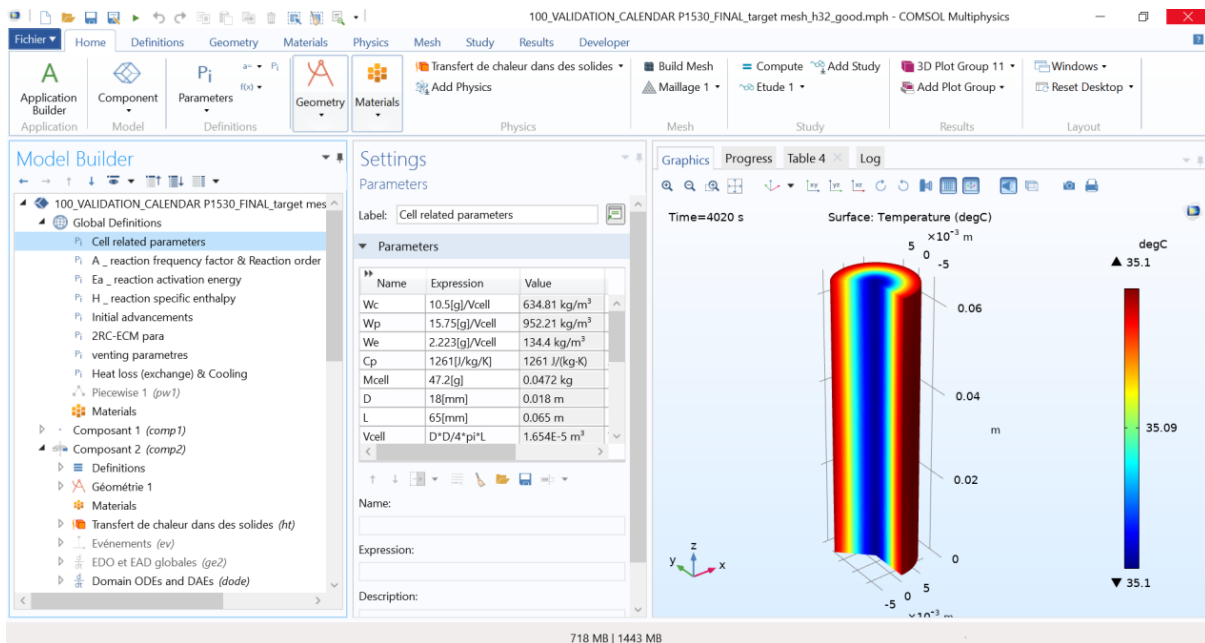


Figure 97: The 3D oven test simulation tool to validate the developed thermal runaway model.

The cell skin temperatures are continuously monitored throughout the oven test using 4 thermocouples distributed over the cell skin, as shown in Figure 98.

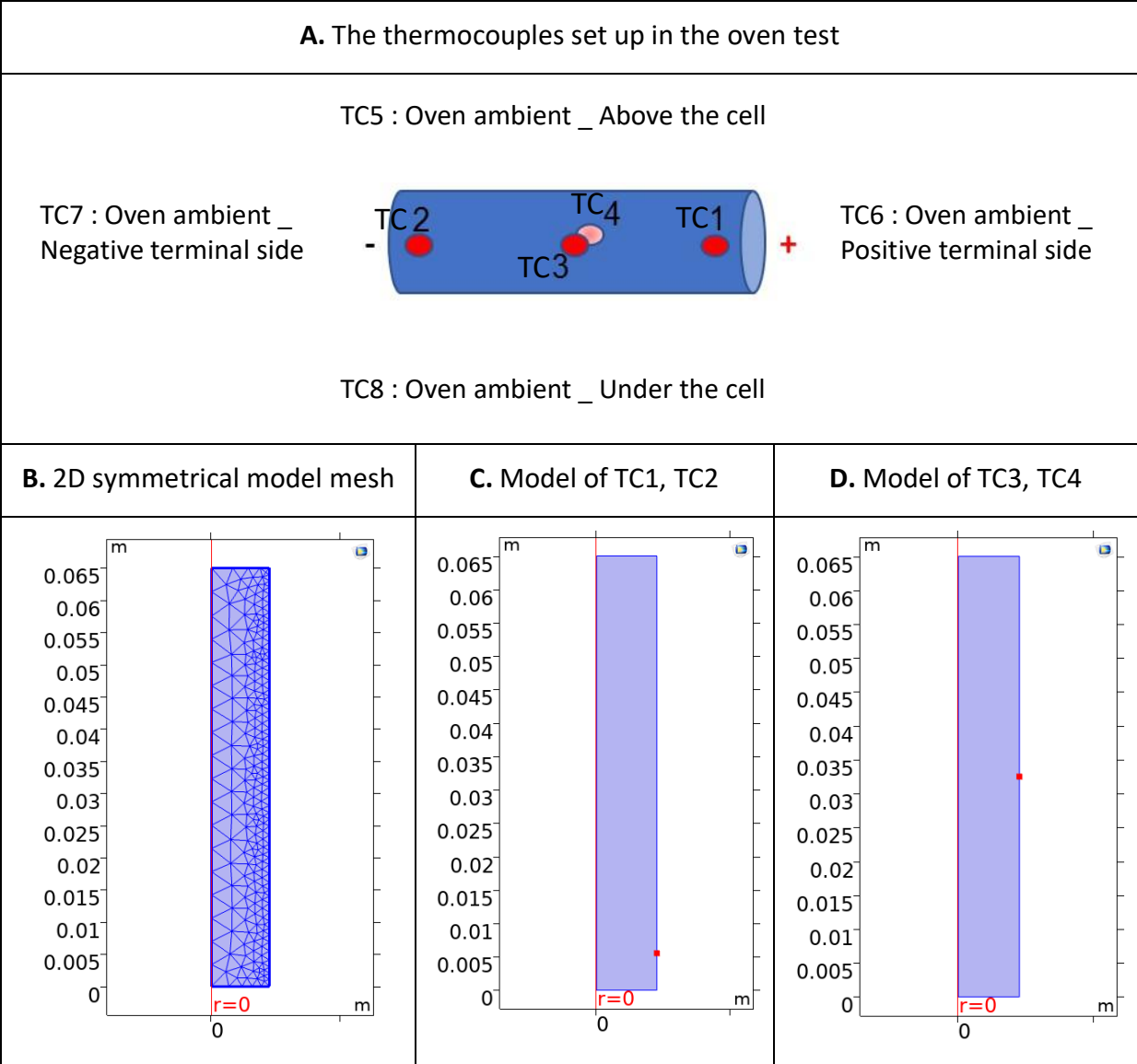


Figure 98: The thermocouples set up in the oven test (A) and their models distributed over the cell skin (red points in (C) and (D)). (B) The 2D symmetrical mesh used in the model.

Due to the symmetrical characteristic of the 3D model, the TC1 and TC2 is both modeled by the red point position in Figure 98.B. Moreover, due to the 2D symmetrical approach taken in the model, the TC3 and TC4 is both modeled by the red point position in Figure 98.D.

The cell is heated by the ambient air in the oven. The implementation of the convective heat transfer into the 3D thermal model to simulate the Oven test will be described here.

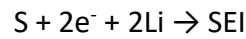
$$\phi_{exchange} = h_{ex} \cdot (T_{ramp} - T) \tag{Eq. 37}$$

This convective heat flux is implemented into the 3D thermal model as a boundary condition.

3.2.5 Integration of SEI-driven Aging

The integration of aging is based on the simplified electrochemical model developed within IFPEN [154] in which the Li-ion battery cell is considered as a superposition of the three solid porous media represented by the negative electrode, the separator and the positive electrode. In this simplified aging model, the loss of cyclable lithium by the evolution of the SEI layer is considered to be the predominant mechanism in the first stage of cell capacity loss.

This layer growth due to the solvent (S) reduction on the surface of the active material particles of the negative electrode, which is simplified according to the following reaction:



The amount of SEI formed (n_{SEI}) can be expressed using Faraday's law as a function of the cell capacity loss C:

$$n_{SEI} = \frac{1}{2F} C \quad (Eq. 38)$$

Therefore, the volume variation of the SEI growth can be expressed by (Eq. 39):

$$dV_{SEI} = \frac{M_{SEI}}{\rho_{SEI}} dn_{SEI} = \frac{M_{SEI}}{\rho_{SEI}} \cdot \frac{1}{2F} dC \quad (Eq. 39)$$

Where:

- M_{SEI} is the molar mass of the SEI layer [kg/mol].
- ρ_{SEI} is the density of the SEI [kg/m³].

With the assumption that the radius of the graphite particle (active material of the negative electrode) is very large compared to that of the formed SEI, we can estimate the average growth of the SEI thickness (t_{SEI}) by equation (Eq. 40).

$$dt_{SEI} \approx \frac{M_{SEI}}{\rho_{SEI} \cdot S_n} \cdot dC \cdot \frac{1}{2F} \quad (Eq. 40)$$

Where:

S_n is the electroactive surface of the negative electrode [m²], which is evaluated by (Eq. 41):

$$S_n = \frac{3\delta_n A}{R_{s,n}} \varepsilon_{s,n} \quad (Eq. 41)$$

In which:

- $\varepsilon_{s,n}$ is the volume fraction of graphite in the negative electrode.
- δ_n is the thickness of the negative electrode [m].
- A is the area of the electrode (assumed to be flat) [m²].
- $R_{s,n}$ is the radius of the particle of the negative electrode [m].

After integration, we obtain the relationship between the thickness growth of the SEI layer (Δt_{SEI}) and the loss of capacity (ΔC) that the cell has undergone during aging:

$$\Delta t_{SEI} \approx \frac{M_{SEI}}{\rho_{SEI} \cdot S_n} \cdot \Delta C \cdot \frac{1}{2F} \quad (Eq. 42)$$

This equation makes it possible to address the current thickness of the SEI layer during aging from its initial thickness by application of (Eq. 43):

$$t_{SEI} \approx t_{SEI_{initial}} + \Delta t_{SEI} \quad (Eq. 43)$$

3.3 Model calibration

Calibration of models is essential and is based on reliable measurements. If the method of calibration of the SEI-driven aging model is already established, it is not the same for the thermal runaway model. In this section, the calibration process of each sub-model will be presented. The model parameters were extracted both from the experimental study carried out within our project and also from literature.

3.3.1 Electrical-thermal sub-model calibration

The 2RC-ECM electrical-thermal model was described in section 3.2.1. For this model, as explained in chapter 2, the OCV(capacity) data of the selected batteries has been extracted thanks to GITT test (every 5% capacity increment) at 25°C in order to estimate the OCV(SOC) of pristine cells. We have also obtained the electrical-thermal experimental data of cell charge/discharge resistances depending on different temperatures and SOC (presented in chapter 2, denoted as $R_{ch}(SOC, T)$ and $R_{dch}(SOC, T)$, respectively) from previous studies in IFPEN.

Before being integrated into the extended thermal runaway model, identifying all the other parameters in the 2RC-ECM electrical-thermal model are necessarily required. Therefore, we have calibrated and validated this model by 2 different tests below:

To calibrate the model parameters during the stable current as well as during the dynamic current, we applied the current profile as shown in Figure 99. The ambient temperature was around 25°C.

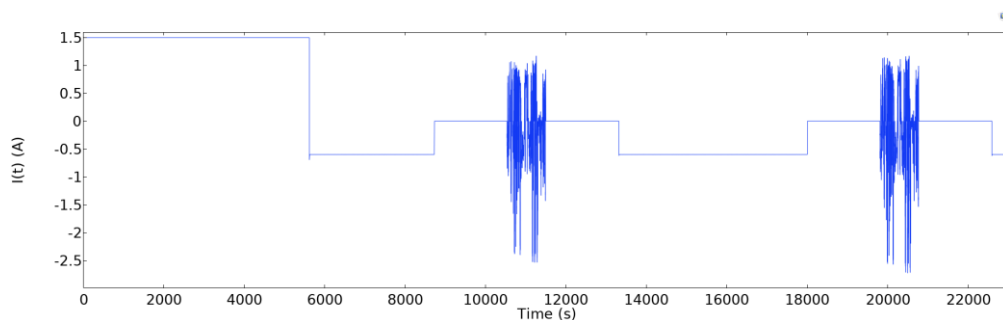


Figure 99: Current $I(t)$ applied in the 2RC-ECM electrical-thermal model of LG HG2.

By assuming that at ~25°C, the cell actual capacity does not change significantly while going through this profile $I(t)$, we calibrated the parameters for this model. It can be observed that the model well predicted the battery voltage, as shown in Figure 100.

The calibration results of the 2 selected technologies are presented in Table 26. The parameters $\tau_1 = R_1 \cdot C_1$ and $\tau_2 = R_2 \cdot C_2$ are adjusted to model the transient behaviours of the battery for different time constants.

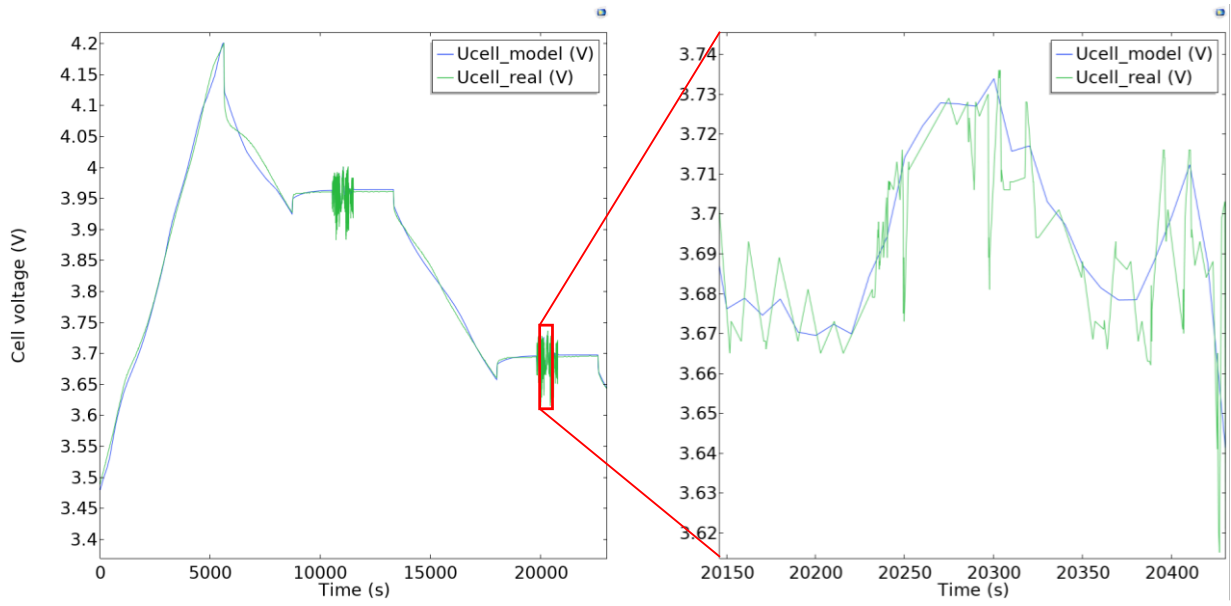


Figure 100: 2RC-ECM model cell voltage calibration result of LG HG2.

Table 26: The calibrated parameters for the electrical-thermal sub-model.

Pristine	Unit	LG HG2	Panasonic NCR GA
$R0_{ratio_ch} = \frac{R0_{ch}(SOC, T)}{R_{ch}(SOC, T)}$	[-]	0.5	0.5
$R0_{ratio_dch} = \frac{R0_{dch}(SOC, T)}{R_{dch}(SOC, T)}$	[-]	0.5	0.5
$R1_{ratio_ch} = \frac{R1_{ch}(SOC, T)}{R_{ch}(SOC, T)}$	[-]	0.25	0.3
$R1_{ratio_dch} = \frac{R1_{dch}(SOC, T)}{R_{dch}(SOC, T)}$	[-]	0.25	0.3
$R2_{ratio_ch} = \frac{R2_{ch}(SOC, T)}{R_{ch}(SOC, T)}$	[-]	0.25	0.2
$R2_{ratio_dch} = \frac{R2_{dch}(SOC, T)}{R_{dch}(SOC, T)}$	[-]	0.25	0.2
τ_1	s	10	10
τ_2	s	100	100

These calibrated results were validated by another test, which is the standard cycling (C/2 charge and C/5 discharge) at 25°C. The results are presented in Figure 101:

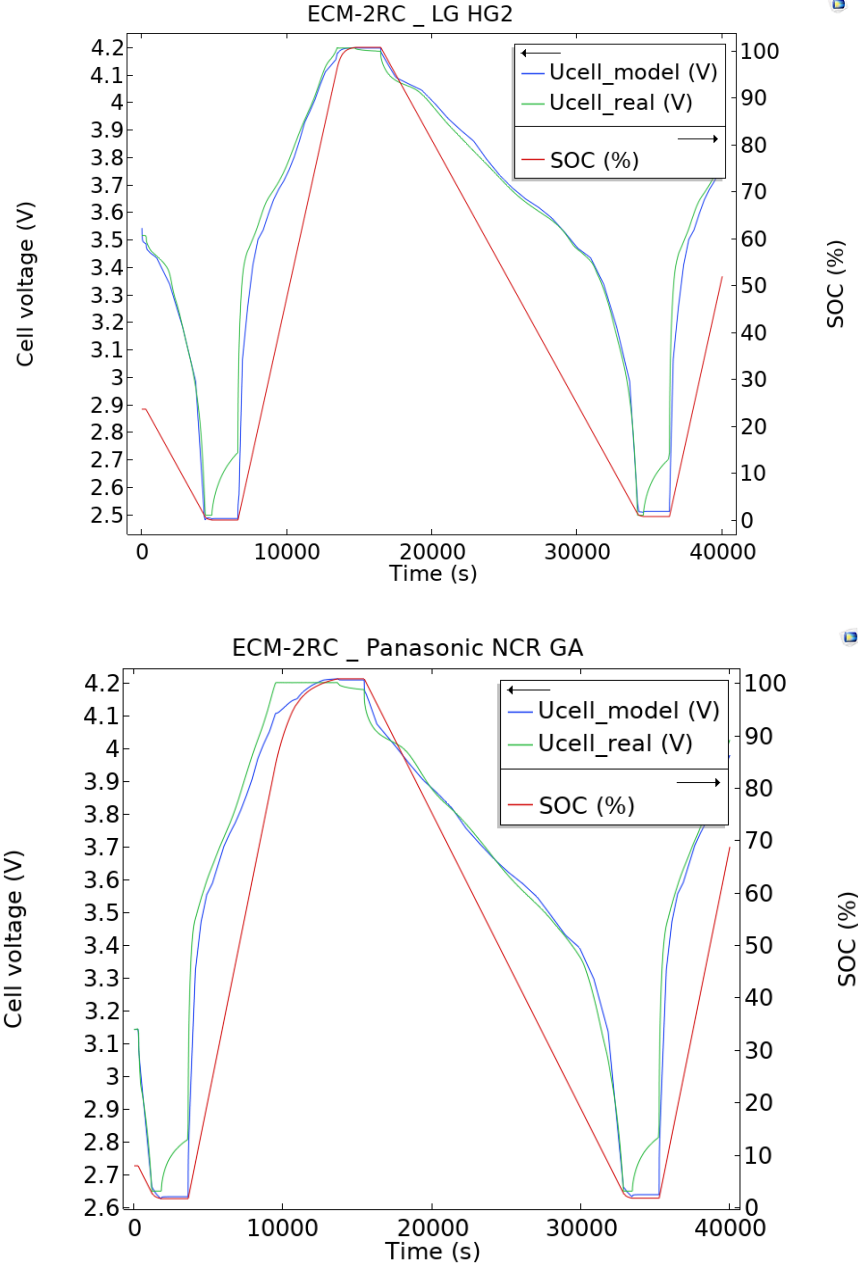


Figure 101: Cell voltage comparison between 2RC-ECM model result and experimental data of LG HG2 pristine cell and Panasonic NCR GA cell.

This electrical-thermal sub-model was being coupled with the other sub-models in the extended thermal runaway model to account for the heat generation due to the hard ISC, with the computed current I_{TR} added to the input current of the cell. There are some identified limitations of this electrical-thermal model relating to different factors below:

- During the thermal runaway, the hard ISC occurred at very higher temperature compared to the highest temperature investigated for the temperature-dependency of cell resistance, which is 40°C. Therefore, there must be a gap between the cell resistance during the thermal runaway in the model vs in real life.
- The tests used for the calibration and validation of this electrical-thermal model were made at ~25°C.
- The hard ISC during the thermal runaway usually drops the cell voltage down to 0V. However, the GITT tests made to estimate the OCV(SOC) could not go down to 0V, hence the OCV(SOC) corresponding to 0V was not measured. To cope with this difficulty, we added a data point in the look-up table of OCV(SOC): OCV = 0V ⇔ SOC = -20%. Similarly, we added a data point in the look-up tables of the cell charge/discharge resistances which correspond to -20%SOC.

3.3.2 Cell thermal properties characterization

In order to model the thermal behaviour of the battery cell, the thermal characterization, including the estimation of cell heat capacity (C_p) and thermal conductivity properties, were carried out, since these data are keys parameters and need to be adjusted for each LIB technology of interest.

3.3.2.1 Heat capacity of the selected technologies

The heat capacity of the cell is a critical parameter in the thermal model of a Li-ion battery. This parameter can be estimated based on knowing all the heat capacities of the cell components, as described in (Eq. 44).

$$C_p = \frac{\sum_{i=1}^n C_{p,i} m_i}{\sum_{i=1}^n m_i} \quad (\text{Eq. 44})$$

Where:

- $C_{p,i}$ is the heat capacity of component i [J/(kg.K)].
- m_i is the mass of component i [kg].

However, the use of this equation is not practical since we do not know the heat capacity of each component in the cell. Therefore, we used a simplified estimation equation (Eq. 45) by using the thermal calorimetric tests in ARC to determine the amount of energy lost or gained by the cell (Q) to go from an initial temperature $T_{initial}$ to a final temperature T_{final} .

$$C_p \approx \frac{Q}{M_{cell}(T_{final} - T_{initial})} = \frac{Q}{M_{cell} \cdot \Delta T} \quad (Eq. 45)$$

To apply this equation, the thermal analysis tests were performed on the selected cells at pristine states, in pseudo-adiabatic conditions in the ARC, which consisted of 5 temperature increments of 5°C ($\Delta T1, \Delta T2, \Delta T3, \Delta T4, \Delta T5$) starting from ~33°C to 63°C. We have limited this temperature range because above ~60°C, the exothermic reaction inside the cell might start to occur and then impact the estimation result of cell heat capacity.

Q in this case is equivalent to the energy sent to the cell for each temperature increment. The cell skin temperature and the temperature surrounding the cell in the ARC vessel were maintained similar throughout the tests to assure the pseudo-adiabatic condition. Then an averaging process was taking place to estimate the average heat capacity of the cell following the equation below:

$$C_{p,average} \approx \frac{C_p^{\Delta T1} + C_p^{\Delta T2} + C_p^{\Delta T3} + C_p^{\Delta T4} + C_p^{\Delta T5}}{5} \quad (Eq. 46)$$

To support the data processing, I have developed a tool on RStudio software in order to estimate the C_p through these thermal calorimetric tests (Annex), the results are shown in Figure 102.

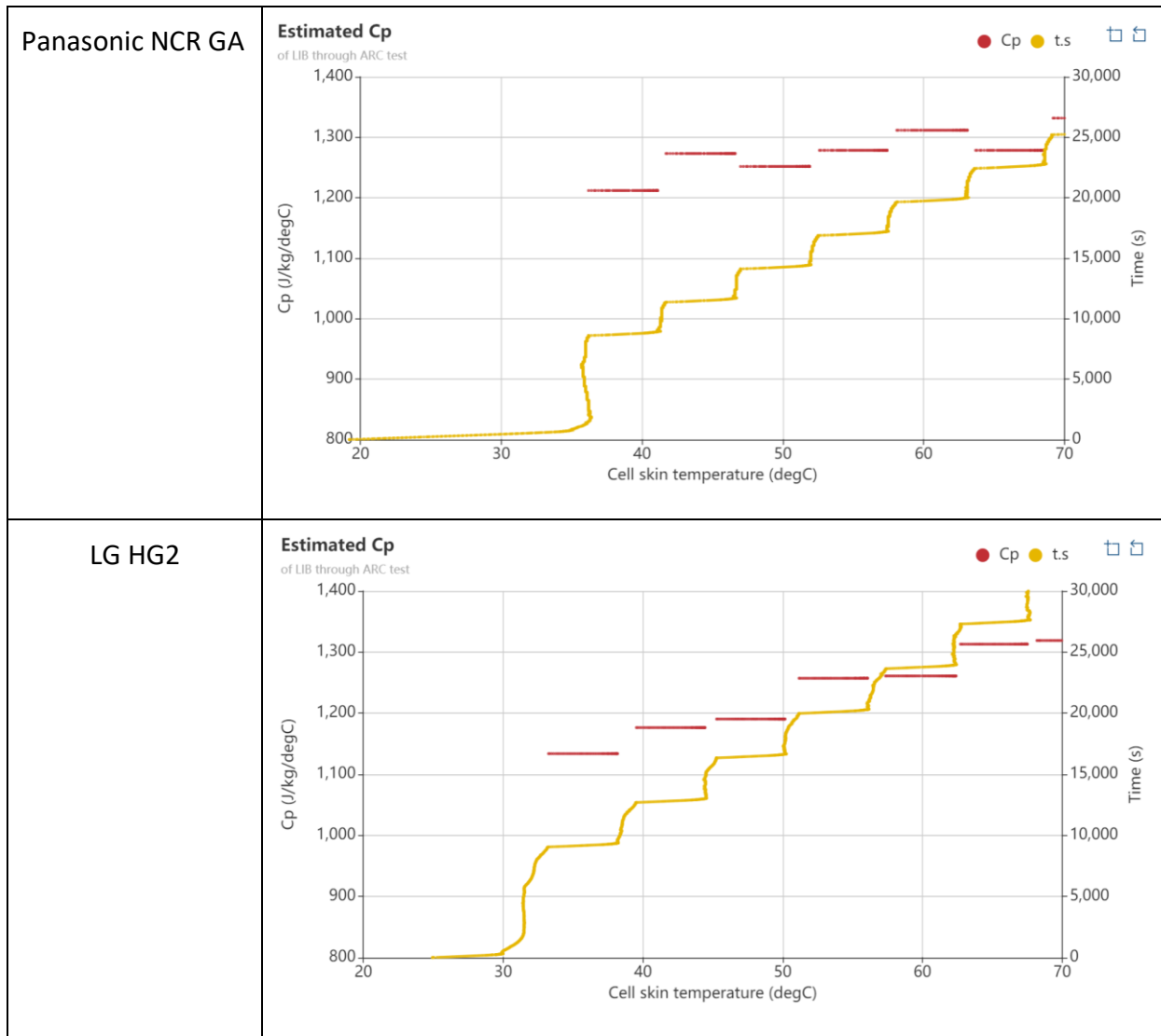


Figure 102: The estimated C_p of the selected technologies

The estimated results of the average C_p of these selected technologies are compiled in Table 27, values are found consistent with similar data obtained by Maleki *et al.* [153] for 18650 cells.

Table 27: Average heat capacity of the selected cells

Parameter	Unit	Sony US GR LiCoO ₂ /Graphite	LG HG2 NMC811/(Graphite+SiOx)	Panasonic NCR GA NCA/(Graphite+SiOx)
Average C_p	J/(kg.K)	1280 [153]	1196	1261

These results also confirmed that there is no thermally alerting sign of any reaction before 60°C for both technologies at pristine states.

3.3.2.2 Thermal conductivity

The cell skin and the cell core are two distinct regions, which induces the anisotropic nature of the thermal conductivity in the battery. In the previous works of Abada *et al.* [13, 16, 138], the equivalent thermal parameters k_r , k_z were determined by fitting experimental data obtained in pseudo-adiabatic conditions of ARC with a simple thermal model. However, due to the technical difficulties of maintaining the pseudo-adiabatic conditions in the BTC, our experimental data were not precise enough to assess these anisotropic heat conductivities. As a consequence, we relied on the literature values of the 18650 cell obtained previously in several studies [158–160]. Based on the work results of Worwood *et al.* [158], the used thermal properties in this thesis are displayed in Table 28.

Table 28: Thermal conductivity of the selected cells

Parameter	Unit	Sony US GR LiCoO ₂ /Graphite	LG HG2 NMC811/(Graphite+SiOx)	Panasonic NCR GA NCA/(Graphite+SiOx)
k_r	W/(m.K)	0.25 [153, 158]	0.25	0.25
k_z	W/(m.K)	30 [153, 158]	30	30

3.3.3 Thermal exchange sub-model calibration

In this section, the calibration of the required parameters of the thermal exchange sub-model is presented.

3.3.3.1 Calibration of the thermal exchange sub-model accounting the non-ideal adiabatic condition during HWS test in BTC

As described in section 3.2, this thermal exchange sub-model allows us to calibrate the model when the adiabatic condition of the ARC tests was not well maintained. The parameters in question are the heat exchange coefficient h_{ex} and the heat loss ratio β of the heater winding around the cell during the heat steps in the HWS protocol, which were used in (Eq. 35) and (Eq. 36). These parameters were determined by fitting the thermal abuse test

data obtained in pseudo-adiabatic conditions of BTC with the model. The fitted results are in Table 29.

Table 29: Thermal exchange sub-model parameters

Parameter	Unit	LG HG2 NMC811/(Graphite+SiOx)	Panasonic NCR GA NCA/(Graphite+SiOx)
h_{ex}	W/K/m ²	8	8
β	[-]	0.35	0

The comparison example between the thermal runaway model with and without this sub-model is shown in Figure 103.

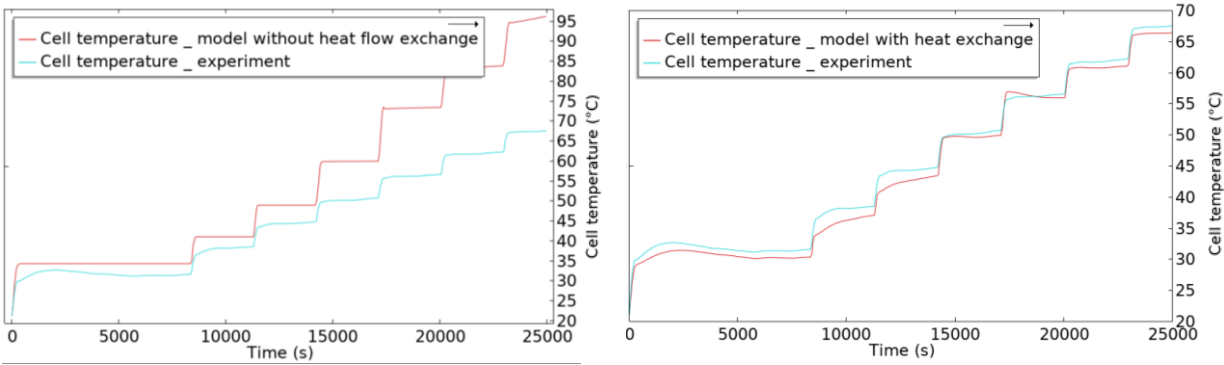


Figure 103: The comparison between the thermal runaway model with and without heat exchange.

3.3.3.2 Calibration of the thermal exchange sub-model simulating the oven test

The calibration of the heat transfer coefficient for the Oven test sub-model is necessary for each technology studied. Based on the simulations of the temperature evolution of pristine Panasonic NCR GA (cell P1706) and LG HG2 (cell L1715) cells from the beginning of the test till 5900s with different heat transfer coefficients, we identified that in the case of the weak heat exchanges ($h = 12 \text{ W.K}^{-1}.\text{m}^{-2}$ and $h = 22 \text{ W.K}^{-1}.\text{m}^{-2}$), the simulated temperatures is very low compared to the test data, as shown in Figure 104 for example in case of Panasonic NCR GA cells.

Finally, we observed that the temperature evolution simulated in case of $h = 32 \text{ W.K}^{-1}.\text{m}^{-2}$ for Panasonic NCR GA cells and $h = 27 \text{ W.K}^{-1}.\text{m}^{-2}$ for LG HG2 cells are close to the experimental data. Therefore, we chose these values for our simulation study of Panasonic NCR GA and LG HG2, respectively.

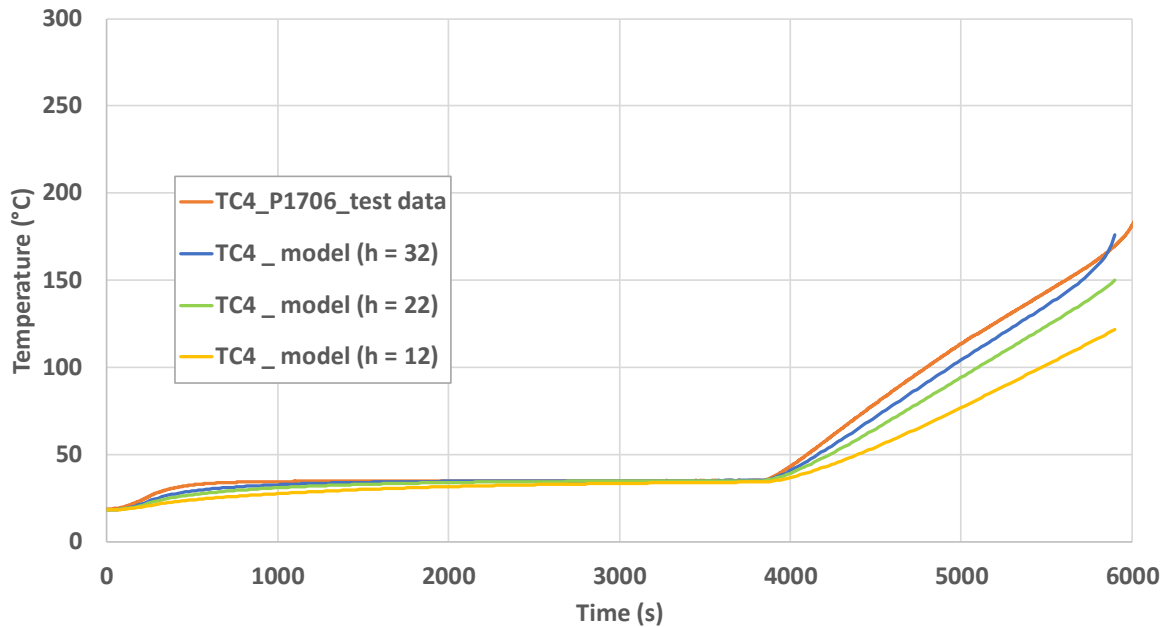


Figure 104: Comparison of the measured and simulated (by use of oven test sub-model) cell skin temperature TC4 in the oven test according to different heat transfer coefficient h [$\text{W.K}^{-1}.\text{m}^{-2}$] for oven test sub-model calibration purposes.

3.3.4 Thermal runaway process sub-model calibration

It is possible to determine the kinetics of the degradation reactions of the battery cell using thermal safety tests on cell level where the entire cell is tested [136, 137]. The Heat-Wait-Search thermal safety test in accelerated rate calorimetry (ARC) used for model calibration were described in chapter 2. This test is important for the calibration of the model since the cell is tested under pseudo-adiabatic condition; the integrity of the entire cell allows the best fit. In order to calibrate the thermal runaway reaction model, a proper combination process of 0D simulations and 3D simulations was applied in this study which represents a time-efficient tool for assessing the behaviours of battery cell during the thermal runaway.

The thermal runaway of Li-ion batteries mostly occurs as a cascading reactions process. However, it is difficult to identify these various reactions separately in the experiments with BTC, especially since:

- the first two exothermic reactions related to the SEI and the negative electrode are correlated and occur in proximate time slot.
- the reaction of the positive electrode is coupled with the oxidation of the electrolyte solvent. These two reactions, at their accelerated rates, will eventually trigger the hard ISC. For the selected Ni-rich high energy density, these 3 reactions nearly accelerated at the same time during the final stage of the thermal runaway.

The total use of the kinetic literature data relating to these exothermic phenomena does not make it possible to characterize the kinetic parameters of the various reactions. Moreover, the kinetic data are not currently fully available in the open literature for the selected technologies. Therefore, we carried out the calibration of the thermal runaway reaction model by fitting data based on the existing literature data in combination with use of experimental results obtained from thermal abuse tests in the BTC.

As shown in Figure 105, the process started with the 0D calibration model because it saves computational time for similar accuracy as a 3D model. With the optimum time step, 0D model takes only ~2 min per simulation. This makes it possible to calibrate the thermal runaway reaction model in time-efficient manner under conditions representative of abusive thermal tests carried out in the BTC. In which, the heating power sent to the cell from the heater winding around the cell represents the input heat source of the model. The average cell surface temperature, recorded during the thermal abuse test in BTC, represents the output of the model.

After obtaining a good calibration fit from 0D calibration model, step 2 is to apply this fit to calibrate the 3D model, as described in Figure 105. To be efficient, the 3D model with the simplified mesh was firstly calibrated then came to the 3D model with the complex mesh at the end.

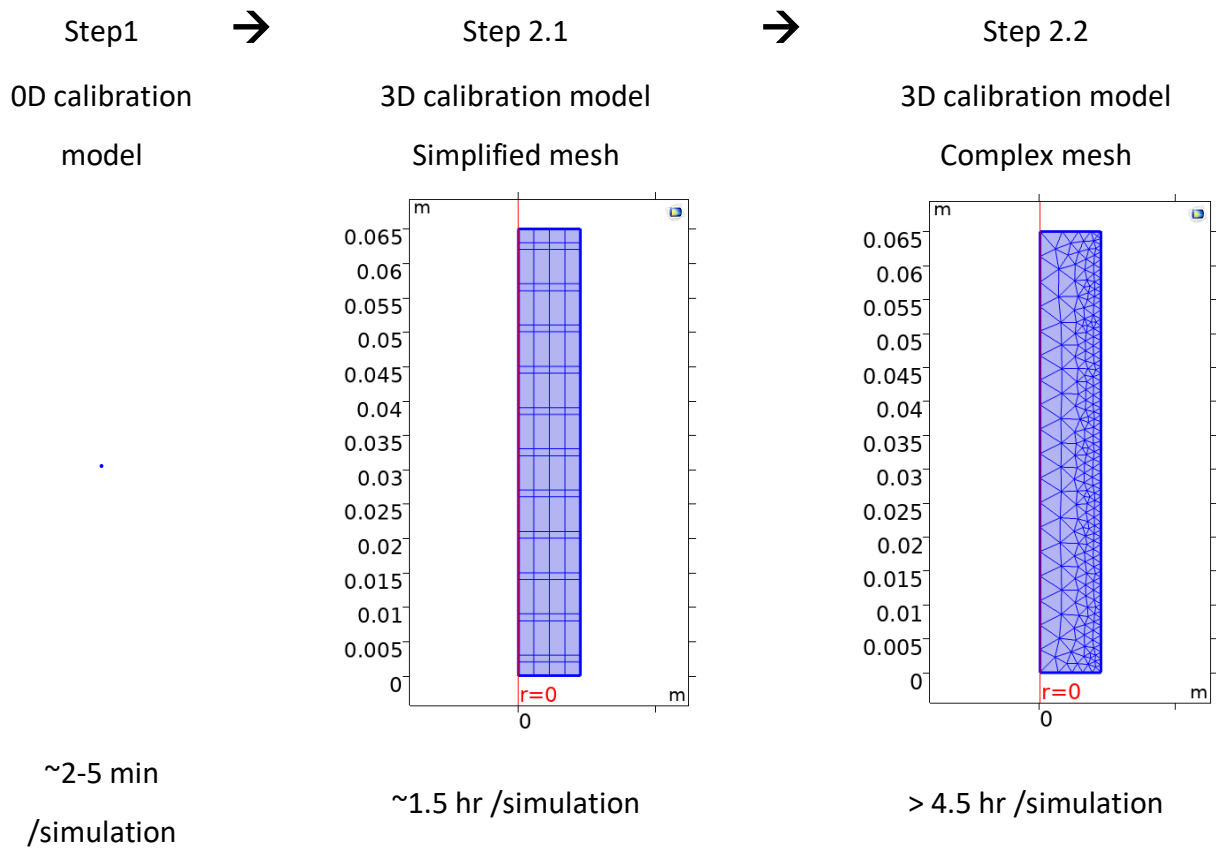


Figure 105: Thermal runaway reaction model calibration process.

In order to properly compare cell temperature model predictions with the experimental data of the cell skin temperature measured by thermocouples C1 and C2 during the thermal abuse tests in BTC, the TC position was set at coordinates $(r,z) = (0.009,0.0055)$ in the cell geometry introduced in the 3D calibration model, as presented in Figure 106.

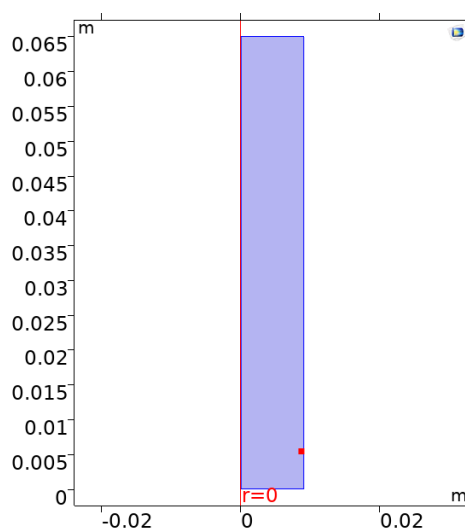


Figure 106: The TC position in the 3D calibration model (red point).

The overall calibration results of cell temperature evolution are found in Figure 107.

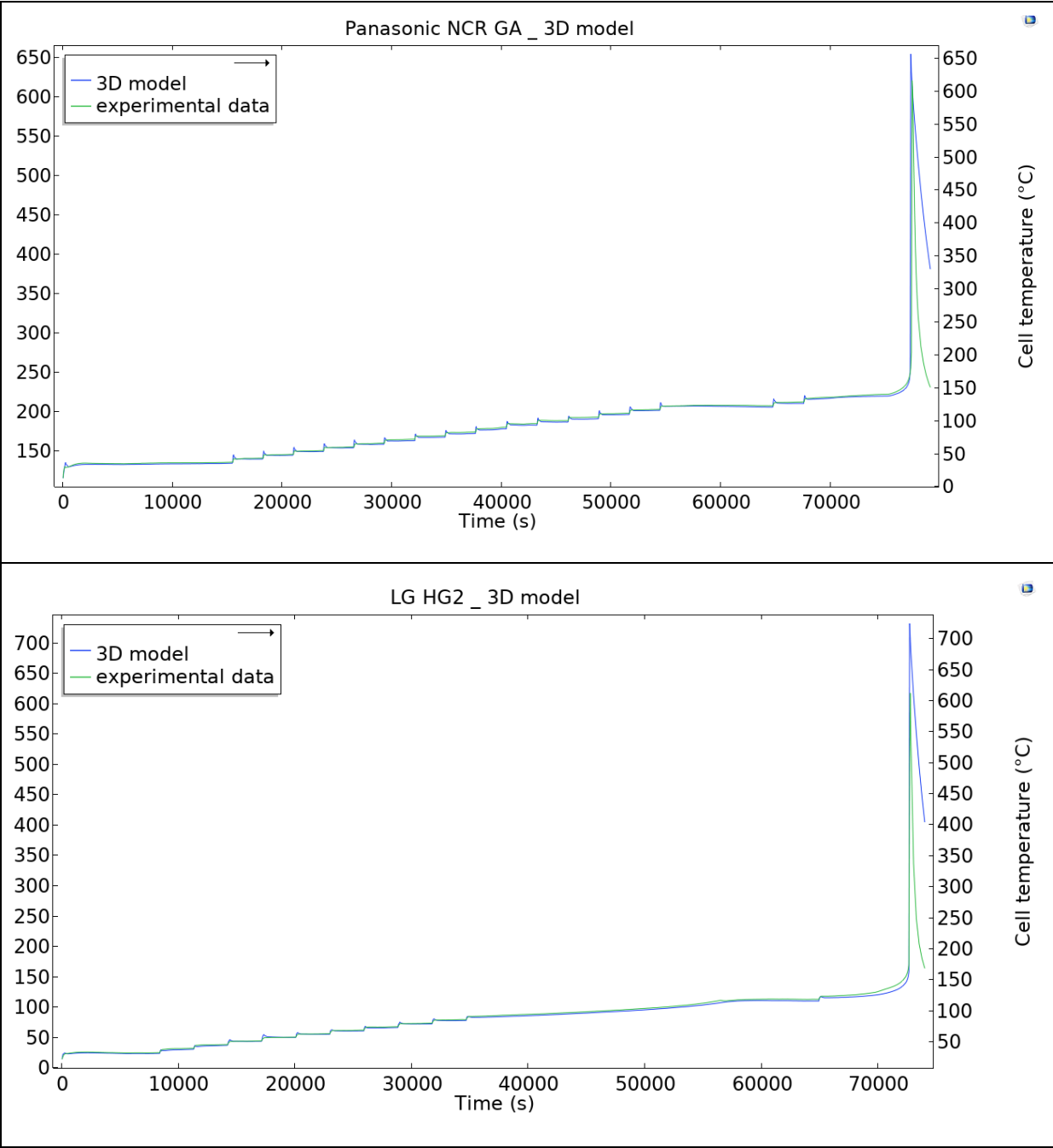


Figure 107: Calibration results of Panasonic NCR GA (top) and LG HG2 (bottom)

We observed that the 3D model seems to over predict the skin temperature as reflected by the TC measurements in the Heat step of HWS experiments, as shown in Figure 108.

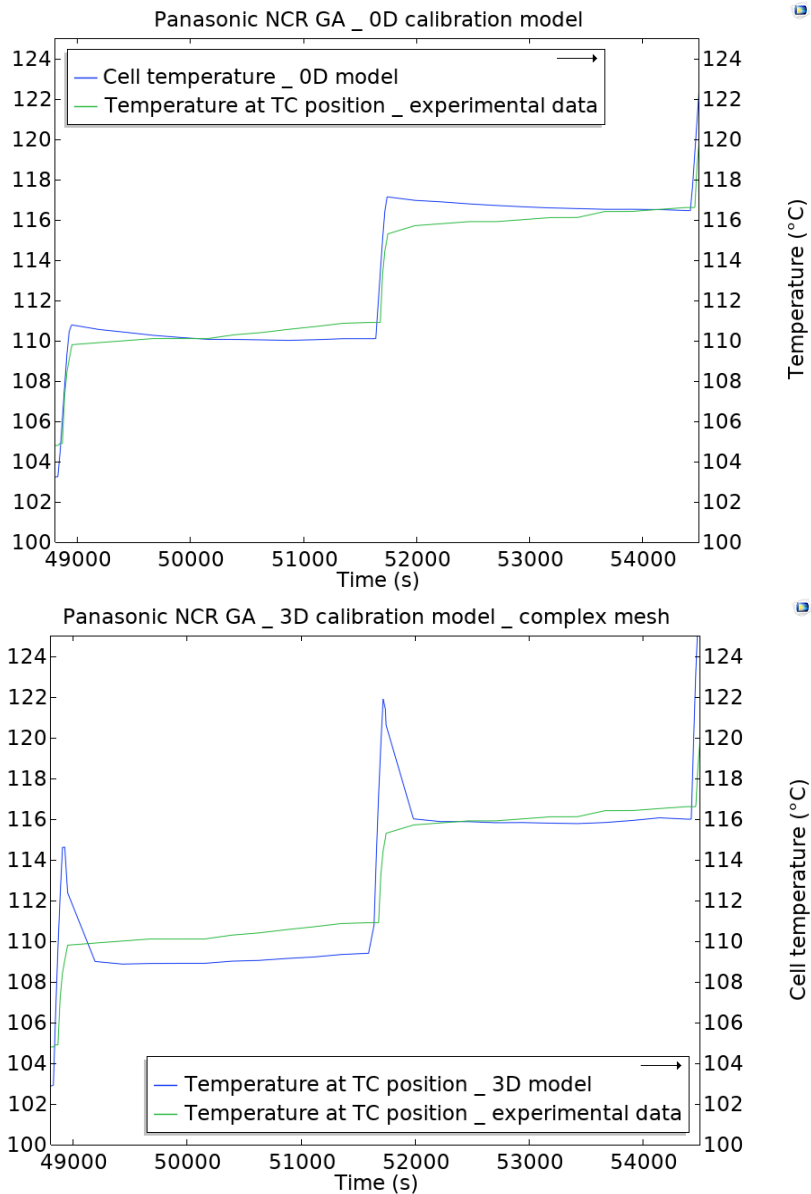


Figure 108: The temperature overshoot at the TC position in the 3D model.

This might be due to the limitation of the 3D model built, in which the cell skin specific thermal property (vs cell core material) is not properly taken into account and therefore, the 3D simulation of the heat flow conduction from the heater to the nearby skin area and to the cell core during the heating step is not accurately modelled. As shown in Figure 109, in the model, at the beginning of heating, the temperature gradient is stronger on the cell surface direction compared to that of the direction towards the cell core. However, this might not be the case in real life.

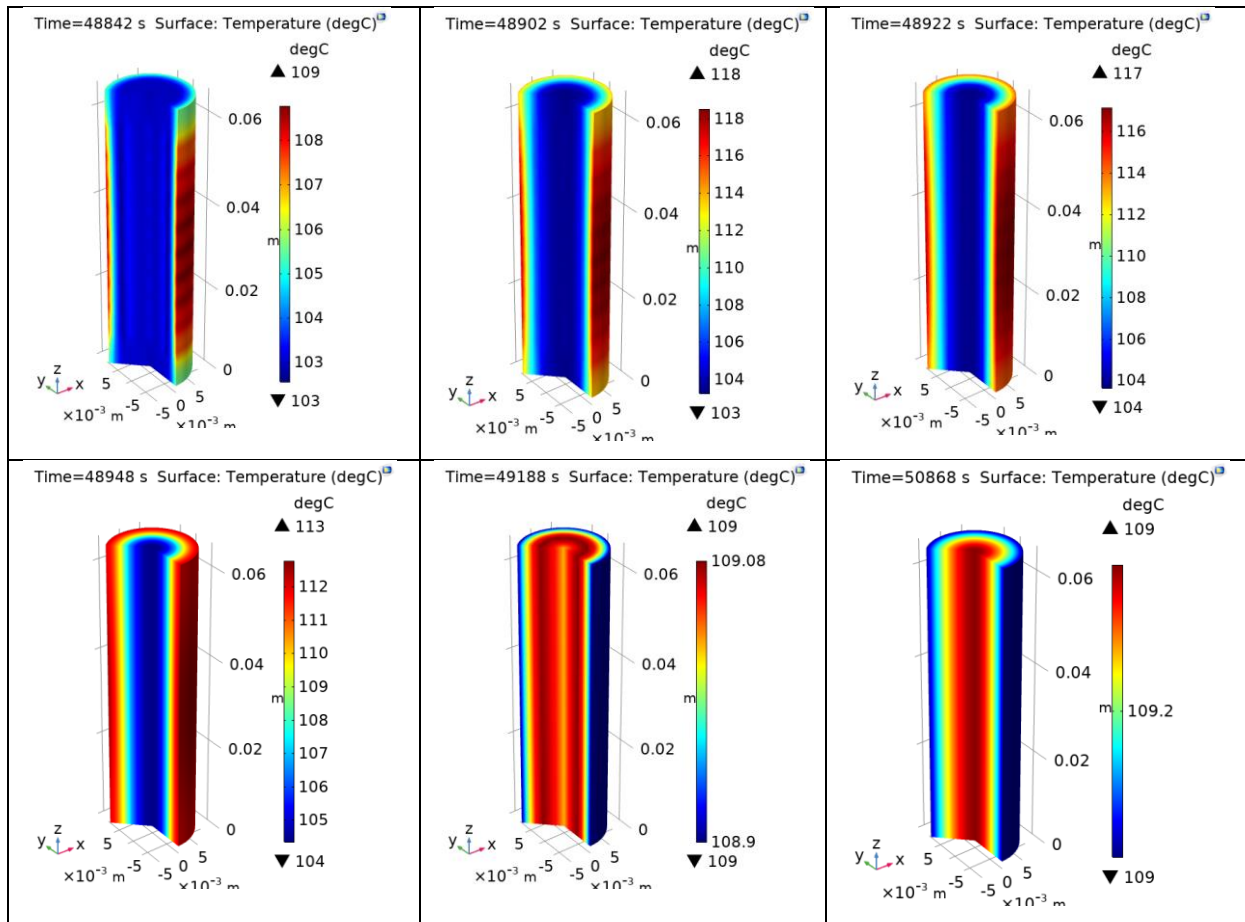


Figure 109: The cell temperature during Heat step in 3D calibration model.

3.3.4.1 Chemical degradation reactions

The chemical degradation reactions were modelled by the equations in 3.2.2, in which we need to identify the parameters below:

- the reaction kinetic parameters (E_a , A): These kinetic parameters are respectively the activation energy and the reaction factor. In this study, these kinetic parameters of the different reactions are based on data from the literature and then were adjusted with the experimental data from the BTC.
- the order of reactions (m): Assuming all reactions are pseudo-first order.
- the dimensionless initial values of the concentrations of the various constituents: provided from Chapter 2.
- the amount of heat released during each reaction (H): These amounts of heat were adjusted. This is justified because the amount of heat released during the

thermal runaway depends closely to the composition of the cell components, especially the electrolyte and the positive active materials. The compositions of cell components are not the same from product line to product line, even if they have similar chemistries. Moreover, we cannot be sure if the cells investigated in the literatures are exactly like our selected commercial cells. Additionally, there can be variation among values between different literatures as well. Therefore, adjustment of this parameter is necessary. However, we tried to remain close to literature values.

During the simulations, we therefore adjusted the reaction kinetics, as well as the heat released by the chemical reactions, while calibrating the right moment of hard ISC and the appropriate amount of gas produced and ejected, so that the average temperature estimated by the model corresponds as well as possible to the experimental curve of the test in the BTC. The results are shown below.

The parameters values related to the SEI degradation reaction and the electrolyte reduction on a graphite based negative electrode are in Table 30.

Table 30: Model parameters of the negative materials reaction

Parameter	Unit	Graphite [137, 161]	Graphite [16]	LG HG2	Panasonic NCR GA
h_{SEI}	[J/kg]	2.57e5	2.57e5	2.313e5	2.056e5
A_{SEI}	[1/s]	1.67e15	1.67e15	1.67e15	1.67e15
Ea_{SEI}	[J]	2.24e-19	2.29e-19	2.15e-19	2.15e-19
m_{SEI}	[-]	1	1	1	1
$c_{SEI,0}$	[-]	0.15	0.15	0.15	0.15
h_{ne}	[J/kg]	1.71e6	1.71e5	2.51e5	2.06e5
A_{ne}	[1/s]	2.50e13	2.50e13	3.25e13	2.5e13
Ea_{ne}	[J]	2.24e-19	2.19e-19	2.15e-19	2.15e-19
m_{ne}	[-]	1	1	1	1
c_{ne}	[-]	0.75	0.75	0.89	0.87
t_{SEI0}	[-]	0.033	0.033	0.033	0.033

The parameters values of the positive electrode materials are shown in Table 31. The initial value of the positive electrode decomposition reaction advancement α is usually set to be close to 0.3 for a fully charged NMC or NCA cell.

Table 31: Model parameters of the positive materials reaction

Parameter	Unit	NCA [161]	LG HG2	Panasonic NCR GA
h_{pe}	[J/kg]	2.18e5	2.245e6	2.18e6
A_{pe}	[1/s]	7.25e16	2.1e17	1.07e17
Ea_{pe}	[J]	2.16e-19	2.78e-19	2.79e-19
m_{pe}	[-]	1	1	1
α_0	[-]	0.04	0.19	0.19

The parameters values of the electrolyte are presented in Table 32. It is noteworthy that these values all linked to electrolyte and therefore are valid for LiPF₆ diluted in organic solvent mixture.

Table 32: Model parameters of the electrolyte reaction

Parameter	Unit	[137, 161]	A123 [16]	LG HG2	Panasonic NCR GA
h_e	[J/kg]	1.55e5	6.2e5	1.596e6	1.55e6
A_e	[1/s]	5.14e25	5.14e25	1.49e26	7.60e25
Ea_e	[J]	4.55e-19	4.48e-19	4.149e-19	4.104e-19
m_e	[-]	1	1	1	1
c_{e0}	[-]	1	1	1	1

Figure 110 presents the calibration results of these chemical degradation reactions during the thermal runaway of Panasonic NCR GA and LG HG2, respectively. The results are corresponding to our knowledge from bibliography study. The first 2 reactions relating to the SEI and the negative electrode were occurred at ~60°C. The positive electrode

decomposition reactions started at $\sim 130^{\circ}\text{C}$. The latest reactions come to the decomposition of the electrolyte starting at $\sim 140^{\circ}\text{C}$.

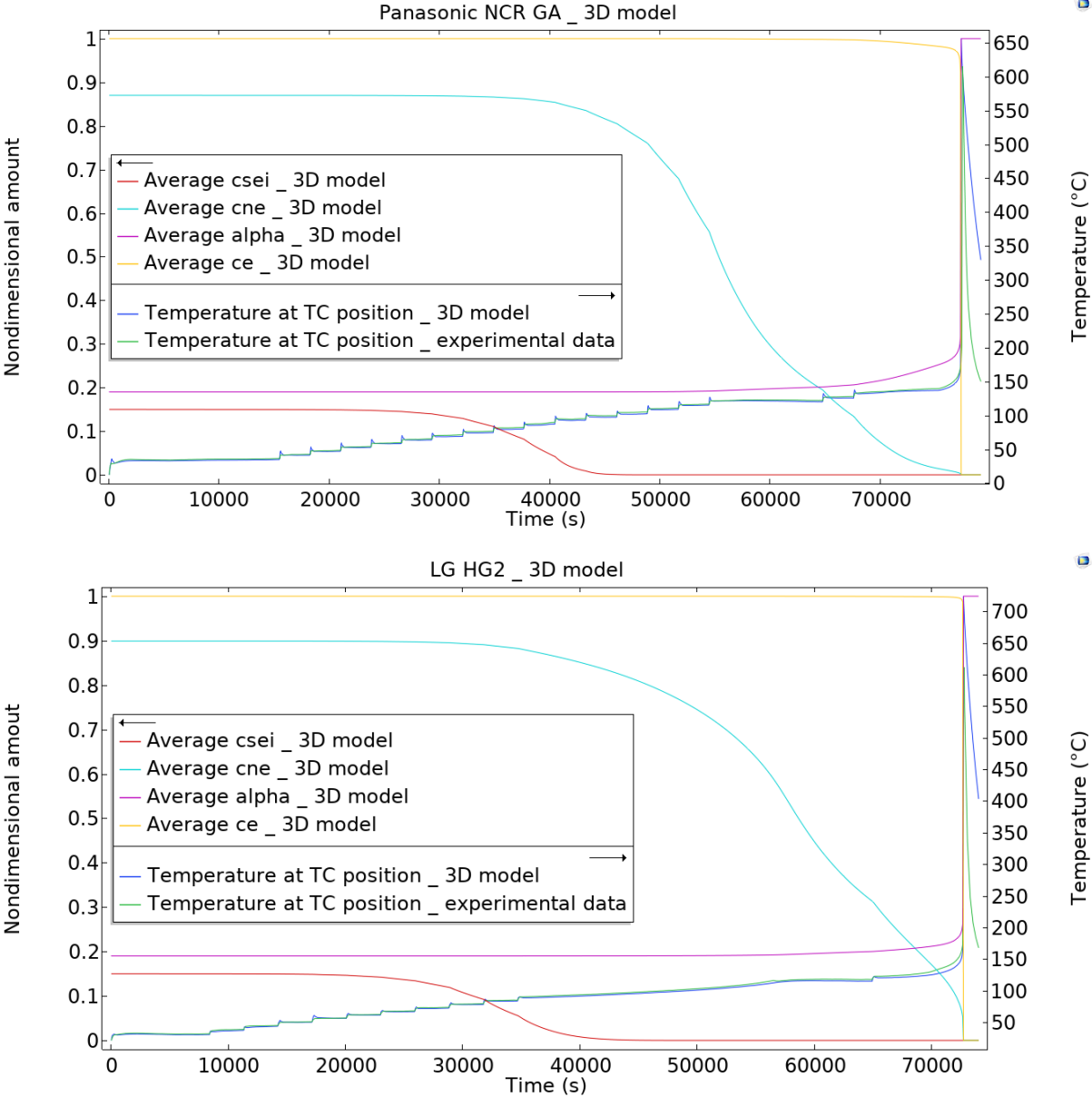


Figure 110: Chemical degradation reaction calibration results of Panasonic NCR GA (top) and LG HG2 (bottom).

3.3.4.2 Hard ISC calibration

The calibration of the hard ISC during the final stage of the thermal runaway includes the adjustment of the kinetic parameters of the hard ISC. The parameters are shown in Table 33.

Figure 111 shows the calibration results of the hard ISC of Panasonic NCR GA and LG HG2, respectively. The event was well correlated with the experimental data.

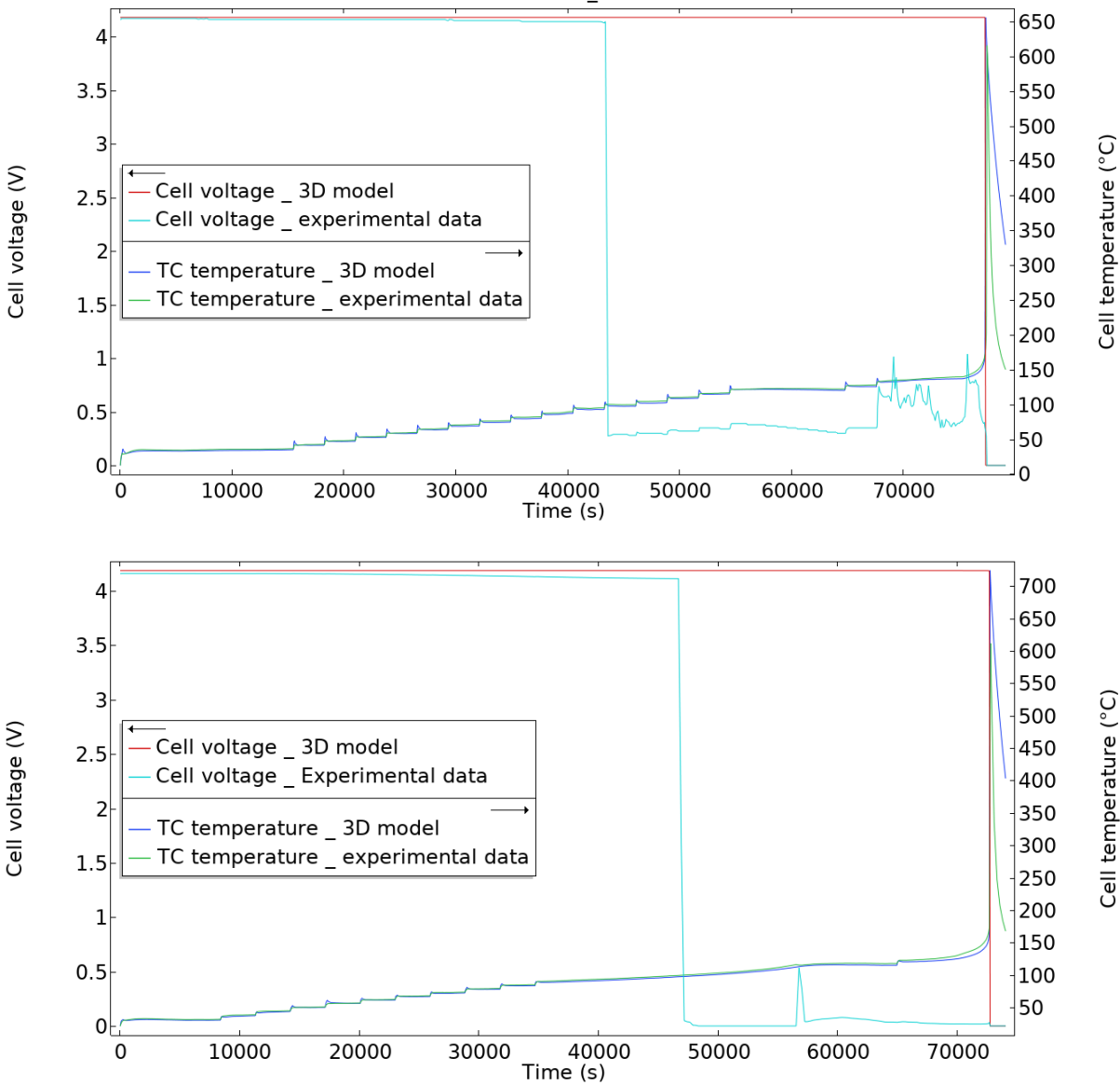


Figure 111: Hard ISC calibration results of Panasonic NCR GA (top) and LG HG2 (bottom)

Table 33: The fitting parameters of the hard ISC of LG HG2 and Panasonic NCR GA model.

Parameter	Unit	Saft [138]	LG HG2	Panasonic NCR GA
A_{ec}	[1/s]	1.67e10	4.83e10	2e10
Ea_{ec}	[J]	2.07e-19	2.835e-19	3.1878e-19
F_{Qres_inf}	[-]	0.15	0.15	0.15

3.3.4.3 Venting calibration

Due to some technical issues of the BTC, we did not fully obtain the accurate measurement of the pressure of the ARC vessel during the whole thermal abuse tests. Therefore, to cope with this problem, we calibrated the venting physical model based on the criteria below:

- the amount of matter ejected from the cell is less than the total mass loss measured from the experiment.
- the calibration parameters are corresponding to the existing literature and the thermal abuse test of Samsung 18650 cells from the internal project of IFPEN/INERIS.

When the venting occurs, the cell internal pressure will drop very quickly and after venting, it will be as the pressure of the ARC vessel. However, we do not have the accurate data of the pressure of the ARC vessel at the moment after venting, therefore, this calibration also based on the assumption that when venting occurs, the ARC vessel pressure is equal to the initial value of the ARC vessel pressure at the beginning of the test, which is ~ 0.97 bar. We also assumed that the initial pressure inside the cell is similar to the initial value of P_{amb} (~ 0.97 bar) which is also closed to this value in [139].

The calibration results are presented in Table 34. It also confirmed that the amount of gas ejected from the cell is less than the total mass loss measured from the experiment.

Table 34: Calibration results and comparison between the amount of ejected gas modelled and the cell mass loss from experiment. ^(a) adjusted values

Parameter	Unit	LG HG2	Panasonic NCR GA
M_{gas}	[kg/mol]	0.84 [139]	0.84 [139]
γ		1.3 [139]	1.3 [139]
P_{burst}	[bar]	12 ^(a)	21.8 ^(a)
V_{gsei}	[mol/kg]	0.14 ^(a)	0.1 ^(a)
V_{gn}	[mol/kg]	0.14 ^(a)	0.1 ^(a)
V_{gp}	[mol/kg]	2.5 ^(a)	1.2 ^(a)
V_{ge}	[mol/kg]	2 ^(a)	2 ^(a)
Head space volume/Cell volume	%	7 ^(a)	7 ^(a)
Centre tube volume/Cell volume	%	5 ^(a)	5 ^(a)
Amount of ejected gas (Calibration model)	[g]	20.4	11
Cell mass loss (Experimental measurement)	[g]	25.5	19

Figure 112 shows the calibration results of the venting of Panasonic NCR GA and LG HG2, respectively. It is noteworthy that the order of magnitude of the bursting pressures values are coherent as compared to scale values published in Mier *et al.* [162] which is in order of 18 to 20 bar for 18650 cells.

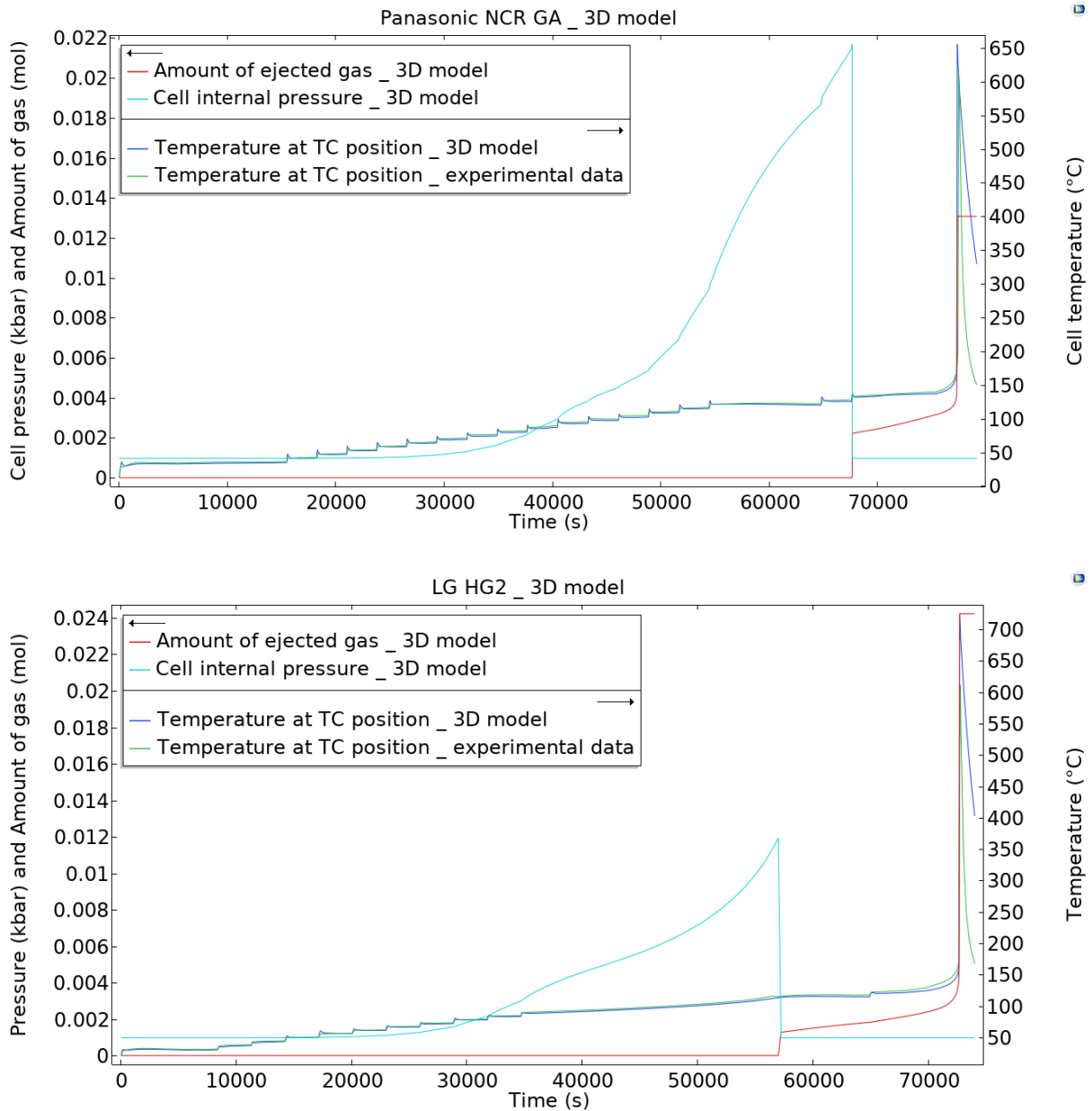


Figure 112: Venting calibration results of Panasonic NCR GA (top) and LG HG2 (bottom).

3.4 Model validation

In this section, we outline the validation results of the thermal runaway model based on the simulations using the thermal exchange sub-model of oven test developed on COMSOL Multi-physics software platform presented in 3.2.4.

As explained in chapter 2, the preheating time between two different oven tests are different depending on the initial temperature of the cell, which lead to the delay in term of time between tests. In order to easily compare the simulation results with different oven

test results, we based on the new timeline termed $\Delta Time(t)$, which excluded the preheating and stabilization time and accounted only for the heating time:

$$\Delta Time(t) = Time(t) - \sum (Time_{preheating\ to\ 35^{\circ}C} + Time_{stabilization\ at\ 35^{\circ}C})$$

3.4.1 Model validation results of Panasonic NCR GA Pristine cell 100%SOC

With simulations of oven abuse test, the three-dimensional (3D) extended model predicts that the accelerated thermal runaway process initially propagates in the azimuthal and longitudinal directions to form a hollow cylinder-shaped reaction zone, as shown in Figure 113, which is coherent with the simulation results of Kim *et al.* [137].

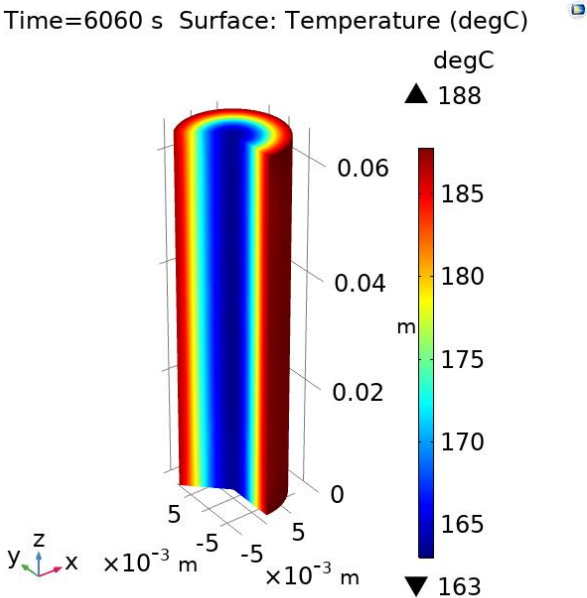


Figure 113: The hollow cylinder-shaped reaction zone before the accelerated thermal runaway process.

The comparison between the simulation results of the model and the experimental data of Oven test on the pristine cell Panasonic 100%SOC is presented in Figure 114. In real oven test, TC1 is near the positive terminal, it means that it is near the occurrence of venting and component ejection during the thermal runaway, therefore, its monitored temperature might be lower due to the endothermic venting events, as seen in Figure 114 (top). In another hand, the TC3,4 are symmetrical and close to each other so their measured temperatures are likely to be close to each other, as seen in Figure 114 (bottom).

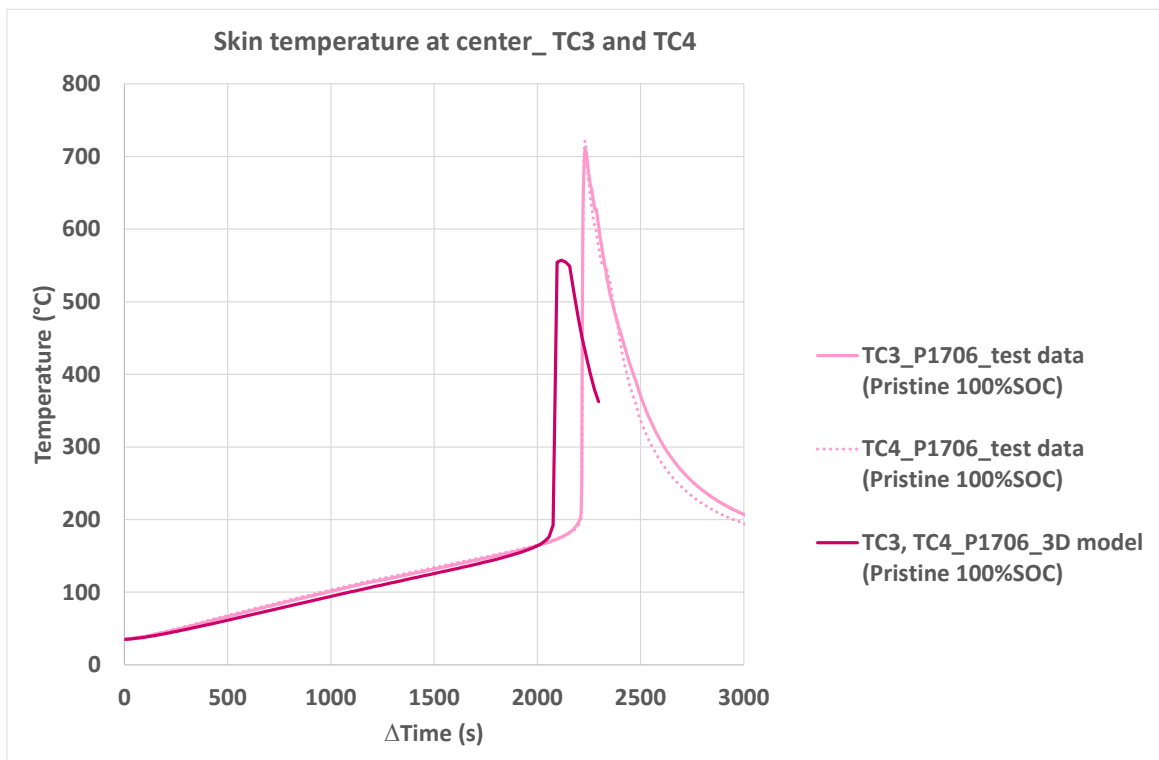
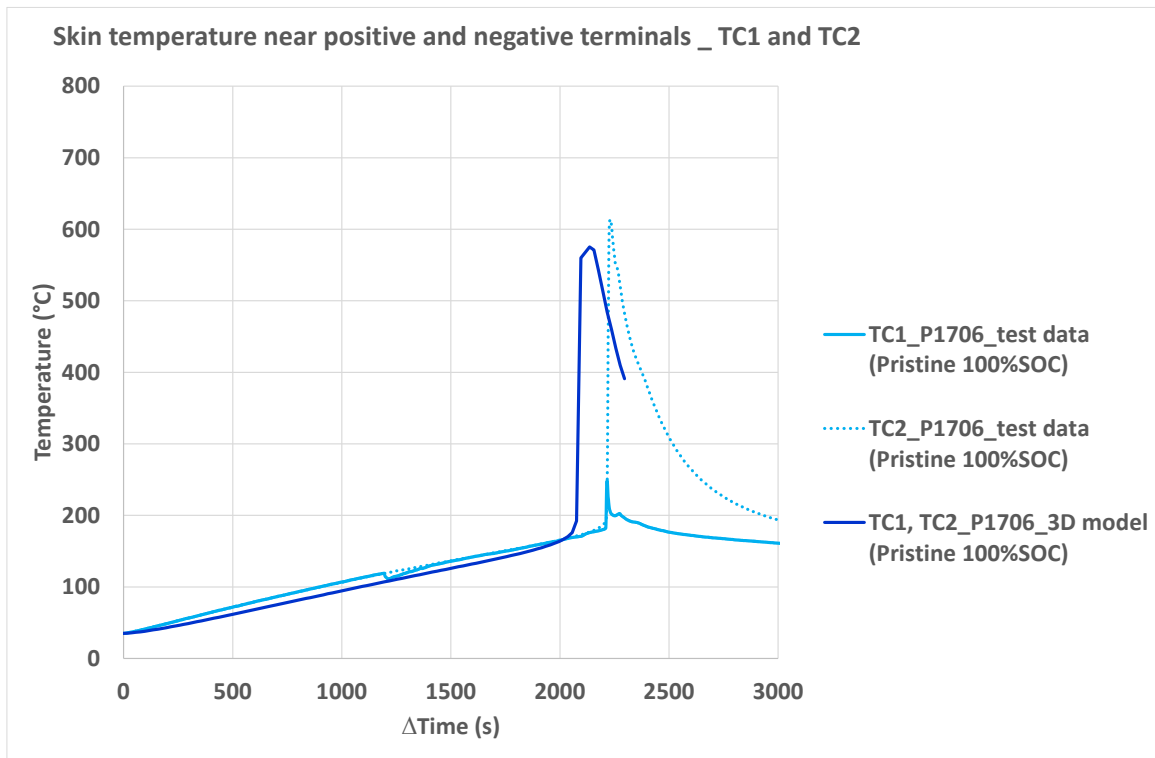


Figure 114: The skin temperature evolution of the TC1,TC2 (top) and TC3,TC4 (bottom) in the oven test vs simulation results.

However, due to the limitation of the model, the influence of venting on the TC1 cannot be taken into account. Therefore, to simplify and consistently compare the simulation results vs the oven test skin TCs measured data, we base our analysis on the average skin temperature term T_{avg} ($^{\circ}C$) determined as below:

$$T_{avg} = \frac{TC1 + TC2 + TC3 + TC4}{4}$$

Figure 115 shows the average skin temperature evaluated at the skin surface of the pristine P1706 Panasonic NCR GA cell as the result of the 4 TCs responses during the actual test performed in the oven, in comparison with the simulated average skin temperature obtained from the 3D model. The critical temperature T_3 (representation of the onset of the accelerated thermal runaway, described in chapter 2), the maximum temperature reached T_{max} and times to these temperatures, are identified and shown in Table 35. The model gives satisfactory results in term of critical temperature T_3 and the maximum average skin temperature reached, with small differences of $3.7^{\circ}C$ (-1.9%) and $4.8^{\circ}C$ (-0.9%), respectively. However, the model predicted the moment of the accelerated thermal runaway quite early (135s in advance) as compared to real onset time of this accelerated thermal runaway process in the oven test. However, the model calibration gives particularly good prediction for the moment of the accelerated thermal runaway. As the main differences between configurations for validation and calibration concern the exchange with the ambient, this delay result in the validation may be suspected in the parameters of the heat-exchange sub-model. This delay may also link to the kinetic parameters of the positive electrode decomposition reaction and the electrolyte reaction, which are estimated quite early ($120^{\circ}C$ and $139^{\circ}C$, respectively), as observed in Figure 116 and Table 36.

Table 35: The critical temperature T_3 , the maximum temperature reached T_{max} and times to these temperatures identified from the oven test vs simulation results of Panasonic NCR GA pristine cell 100%SOC.

Pristine 100%SOC	T3 ($^{\circ}C$)	Tmax ($^{\circ}C$)	tT3 (s)	tTmax (s)
Oven test data	196.0	562.0	2211	2231

3D model	192.3	557.2	2076	2096
Off set values (model/test data)	- 3.7 (-1,9%)	- 4.8 (-0,9%)	- 135 (-6,1%)	- 135 (-6,1%)

As also observed in Table 36, the SEI and negative electrode decomposition reactions occurred at around 56°C – 63°C, which is in agreement with the findings available in the literatures [3] [107].

Table 36: The temperature range and occurrence time of the exothermic chemical reactions of pristine cell 100%SOC and the related bibliography sections.

100%SOC	Onset temperature (°C)	End temperature (°C)	Onset time (s)	End time (s)	Related bibliography section
cSEI	56	146.5	416	1816	1.4.2.2
cne	63	557.0	536	2096	1.4.2.2
α	120	557.0	1416	2096	1.4.2.3
ce	139	557.0	1716	2096	1.4.2.4

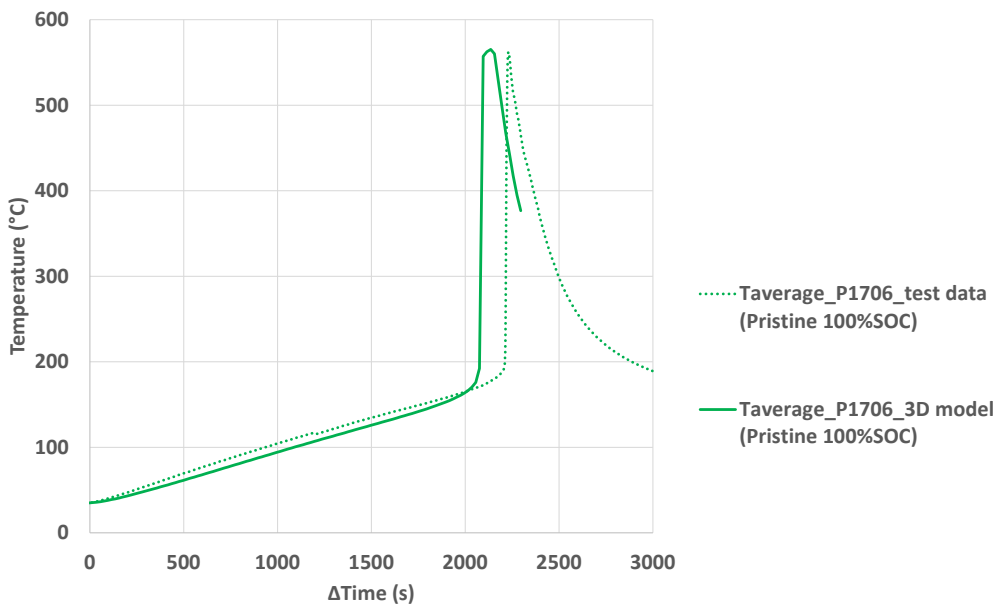


Figure 115: The average skin temperature evolution of the oven test in the oven vs simulation results.

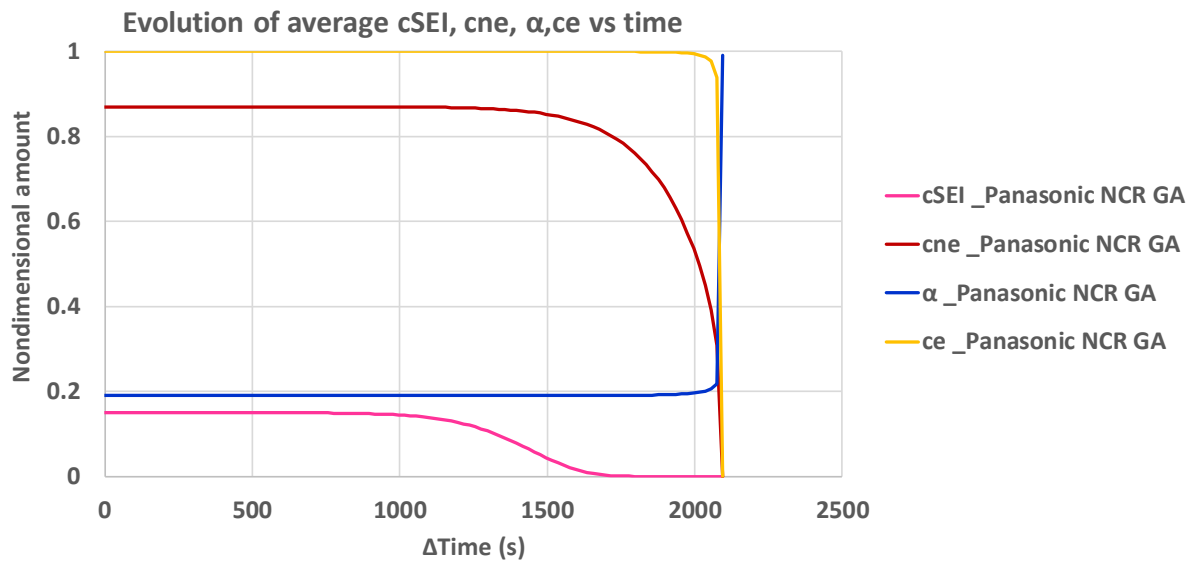


Figure 116: Simulation results of the evolution of the chemical species concentration c_{SEI} , c_{ne} , c_e and the conversion degree α of the pristine Panasonic NCR GA cell 100%SOC.

The cell voltage measured during the oven test and the hard ISC simulated with the thermal runaway model are shown in Figure 117. It can be seen that the hard ISC modelled delay notably compared to that in real test for this cell. However, for the repeatability test on cell P1723, this delay reveals smaller. This relates to the process of the soft ISCs inside the cells before the hard ISC occurred, which might depend on different factors such as the separator defects and the electrolyte and gas vaporation in the cell.

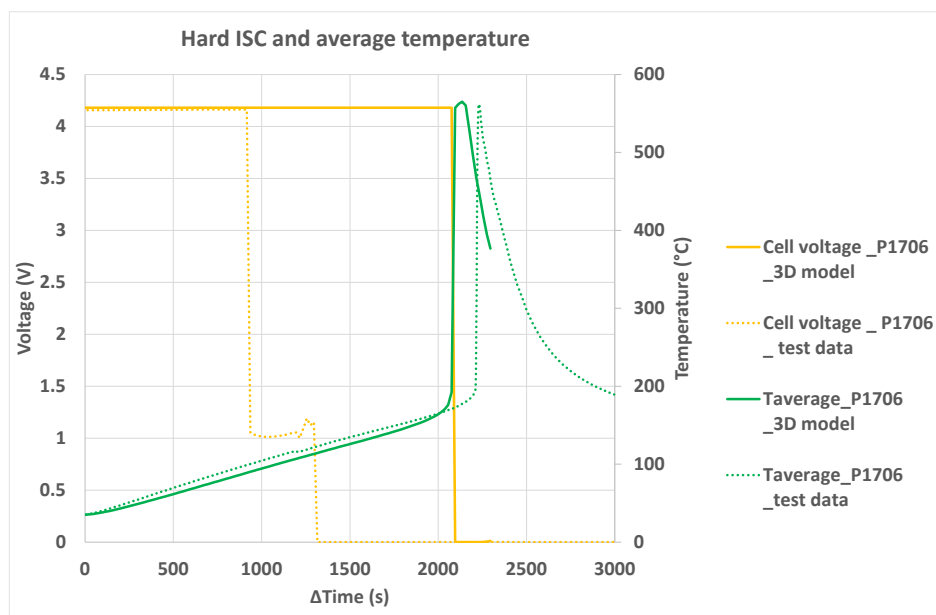


Figure 117: The hard ISC simulation result vs the cell voltage measured in oven test.

3.4.1 Model validation results of LG HG2 Pristine cell 100%SOC

Figure 118 shows the average skin temperature evaluated at the skin surface of the pristine L1715 LG HG2 cell as the result of the actual test performed in the oven and the simulated average skin temperature obtained from the 3D model, in comparison with that of pristine P1706 Panasonic NCR GA cell.

It is noteworthy that, during the accelerated thermal runaway of the pristine L1715 LG HG2 cell, the oven door has opened which caused thermal losses and strongly impacted the accuracy of the monitored skin temperatures. Due to this incident, a huge drop in the temperature measured at the cell skin of the L1715 cell, which is visible in Figure 118. These heat losses cannot be taken into account in the model.

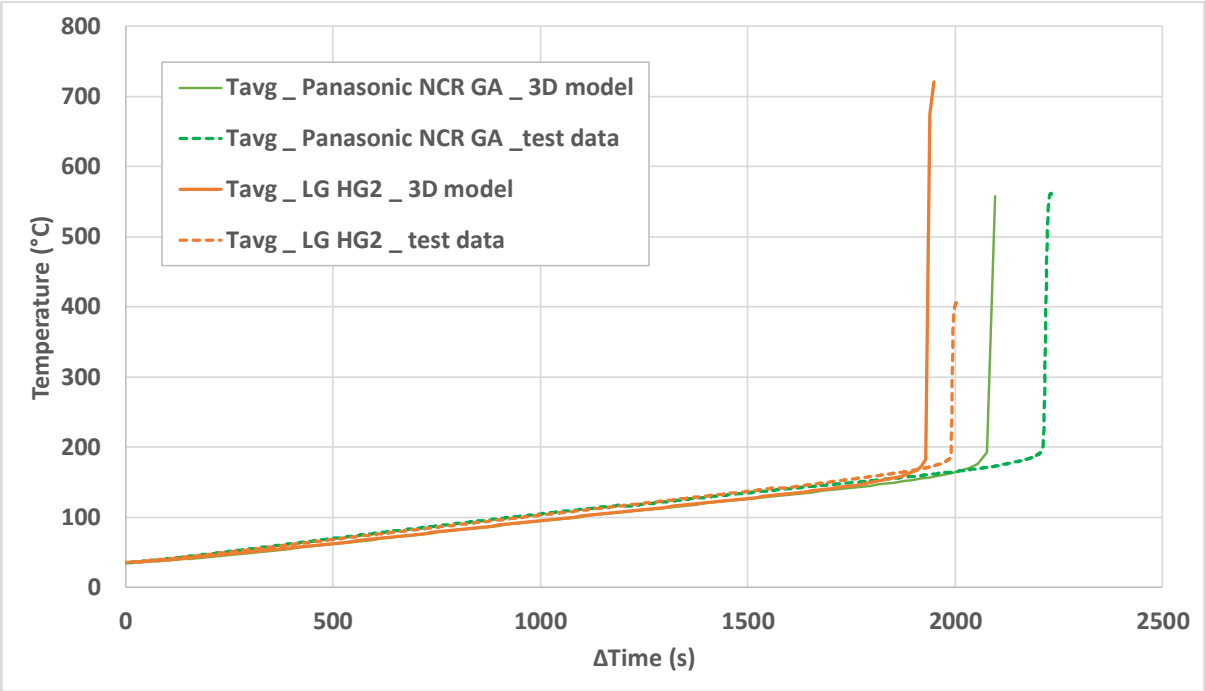


Figure 118: The average skin temperature evolution of the oven test data vs simulation results of pristine 100%SOC Panasonic NCR GA and LG HG2 cells.

The critical temperature T_3 , the maximum temperature reached T_{max} and times to these temperatures, are identified and shown in Table 37.

The model gives excellent agreement results in term of critical temperature T_3 for both technologies, especially for LG HG2 cell with the difference of 0.2%. Moreover, the model

predicted the moment of the accelerated thermal runaway of LG HG2 less early (53s (2.7%) in advance) as compared to the offset of Panasonic NCR GA cell (135s (6.1%) in advance). This is thanks to the better calibration of the kinetic parameters of the positive electrode decomposition reaction and the electrolyte reaction in case of LG HG2 technology, which are estimated quite later (132°C and 149.4°C, respectively), as observed in Table 38 and Figure 121.

Table 37: The critical temperature T_3 , the maximum temperature reached T_{max} and times to these temperatures identified from the oven test vs simulation results of pristine Panasonic NCR GA and LG HG2 cells.

Pristine 100%SOC		Panasonic NCR GA	LG HG2
<i>3D model</i>	T3 (°C)	192.3	181.5
	Tmax (°C)	557.2	723.0
<i>Oven test data</i>	T3 (°C)	196.0	181.1
	Tmax (°C)	562.0	-
<i>Off set values (model/test data)</i>	$\Delta T3$ (°C)	-3.7 (-1.9%)	0.4 (0.2%)
	$\Delta Tmax$ (°C)	-4.8 (-0.8%)	-
<i>3D model</i>	tT3 (s)	2076	1929
	tTmax (s)	2096	1949
<i>Oven test data</i>	tT3 (s)	2211	1982
	tTmax (s)	2231	2003
<i>Off set values (model/test data)</i>	$\Delta tT3$ (s)	-135 (-6.1%)	-53 (-2.7%)
	$\Delta tTmax$ (s)	-135 (-6.05%)	-54 (-2.7%)

According to the simulation results demonstrated in Table 38 and Figure 121, a clearer picture of the exothermic chemical chain reactions occurs inside the Ni-rich tested cells during the thermal runaway in oven test are drawn:

As the temperature increases up to around 56-57°C, the unstable components of the SEI at the negative electrode (tracked by the variable c_{SEI}) firstly decompose after 416-419s of

heating. This initial exothermic reaction provides a small temperature boost to the other reactants inside the cell, which activates the decomposition reaction between the intercalated lithium (tracked by the variable c_{ne}) and the electrolyte solvent at around 63-67.4°C after 536-579s of heating.

Table 38: The temperature range and occurrence time of the exothermic chemical reactions occurred during the thermal runaway of pristine and calendar aged cells.

Pristine 100%SOC		Onset temperature (°C)	End temperature (°C)	Onset time (s)	End time (s)
cSEI	Panasonic NCR GA	56.0	146.5	416	1816
	LG HG2	57.1	147.4	419	1779
cne	Panasonic NCR GA	63.0	557.0	536	2096
	LG HG2	67.4	672.0	579	1939
α	Panasonic NCR GA	120.0	557.0	1416	2096
	LG HG2	132.0	672.0	1579	1939
ce	Panasonic NCR GA	139.0	557.0	1716	2096
	LG HG2	149.4	672.0	1799	1939

The two reactions above provide heat to the initiation of the exothermic reactions at the positive electrode (tracked by the variable α) at a temperature of about 120°C after 1416s of heating for Panasonic NCR GA cell and about 132°C after 1579s of heating for LG HG2 cell. At the temperature of around 139°C for Panasonic NCR GA cell and around 149.4°C for LG HG2, the electrolyte decomposition reaction initiates (tracked by the variable c_e).

As the temperature evolves, alpha increases as the decomposition reactions at the positive electrode proceeds, while c_{SEI} , c_{ne} and c_e decrease as the decomposition reactions at the negative electrode and the electrolyte decomposition reactions occur. The decomposition reaction of the unstable SEI components at the negative electrode ends around 147°C for both technologies. The remain reactions continue to heat the cell until the critical temperature T_3 , of about 192°C for Panasonic NCR GA cell and about 181.5°C for LG HG2

cell, is reached at which the reactions at the positive electrode and the electrolyte reaction accelerate, causing the remaining intercalated lithium at the negative electrode (tracked by c_{ne}) to react much faster and the cell goes to the accelerated thermal runaway. Therefore, even though the decomposition reaction between the intercalated lithium and electrolyte solvent at the negative electrode take place at lower temperatures (63-67.4°C), they proceed relatively slowly until being accelerated by the reactions at the positive electrode and the electrolyte. This reaction consequently leads to the collapse of graphite structure in the negative electrode active particles.

Therefore, there are 3 main exothermic reactions during the accelerated thermal runaway: the positive electrode/electrolyte decomposition reaction, the intercalated lithium at the negative electrode/electrolyte decomposition reaction and the electrolyte combustion reaction, reacting simultaneously, which are responsible for the extreme temperatures reached at the accelerated stage of the thermal runaway. This is illustrated through Figure 120. It is also noteworthy that these findings are aligned with the works of Hatchard *et al.* [136].

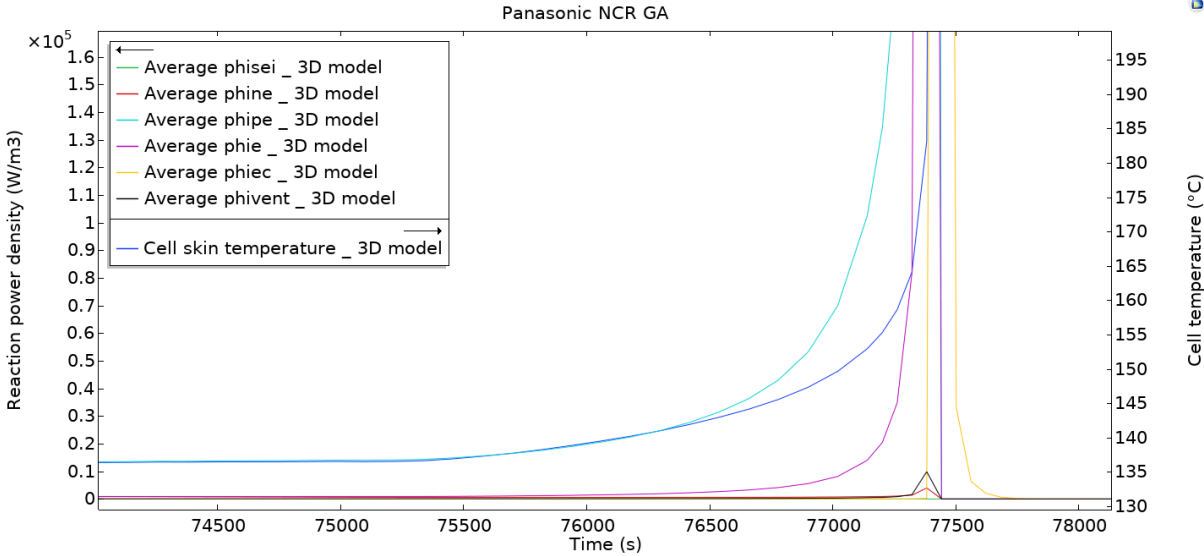


Figure 119: Heat flows contributing to the accelerated thermal runaway.

According to the simulation results shown in Figure 120 and Table 39, the venting of Panasonic NCR GA cell occurred during the accelerated thermal runaway, which is very violent and very late, while the venting of LG HG2 cell occurred sooner. The 3D model

estimated the amount of ejected gas is 7.73 g in case of Panasonic NCR GA cell, which is notably smaller compared to the test measurement mass loss data (20.3 g). The amount of ejected gas predicted in case of LG HG2 is much higher (20.72g), which is ~20% closer to the mass loss experimental data compared to the case of Panasonic NCR GA cell. Additionally, as compared to the first venting signal shown in the oven tests presented in Table 39, the venting was modelled more accurately for LG HG2 compared to that of Panasonic NCR GA cell.

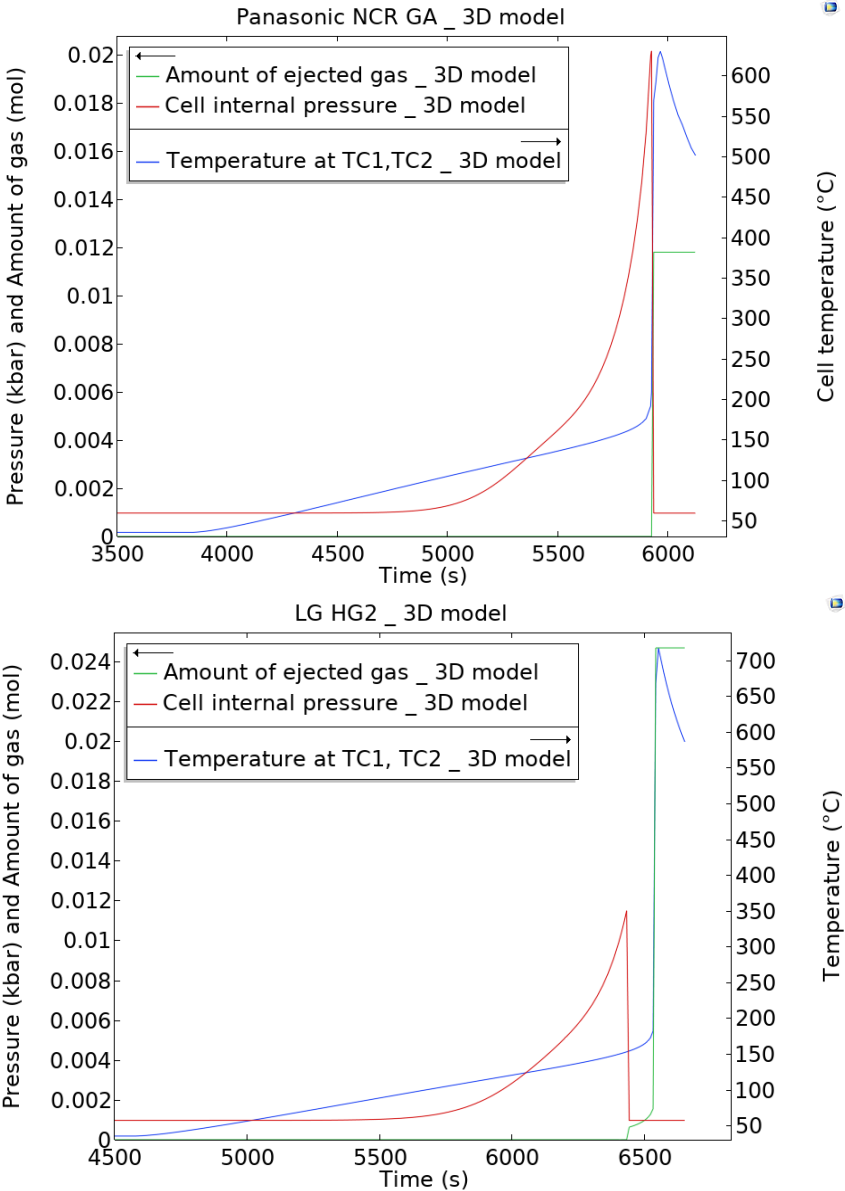


Figure 120: The venting simulated by 3D model of Panasonic NCR GA and LG HG2 pristine cells 100%SOC.

Moreover, the simulation results showed that LG HG2 produced and released more gas. This finding is coherent with the recorded venting event during these oven tests.

Table 39: The amount of ejected gas (simulation results vs test measurements).

Pristine 100%SOC		Panasonic NCR GA	LG HG2
<i>3D model</i>	Tvent (°C)	557	153
<i>Oven test data</i>	Tvent (°C)	111	132
<i>Off set values</i>	$\Delta T3$ (°C)	446 (401%)	21 (15.9%)
<i>3D model</i>	tTvent (s)	2096	1839
<i>Oven test data</i>	tTvent (s)	1214	1578
<i>Off set values</i>	$\Delta tTvent$ (s)	882 (72%)	261 (16.5%)
<i>3D model</i>	Ejected gas (g)	7.73	20.72
<i>Oven test data</i>	Mass loss (g)	20.30	36.93
<i>Off set values</i>	(g)	-12.57 (62%)	-16.21 (43.9%)

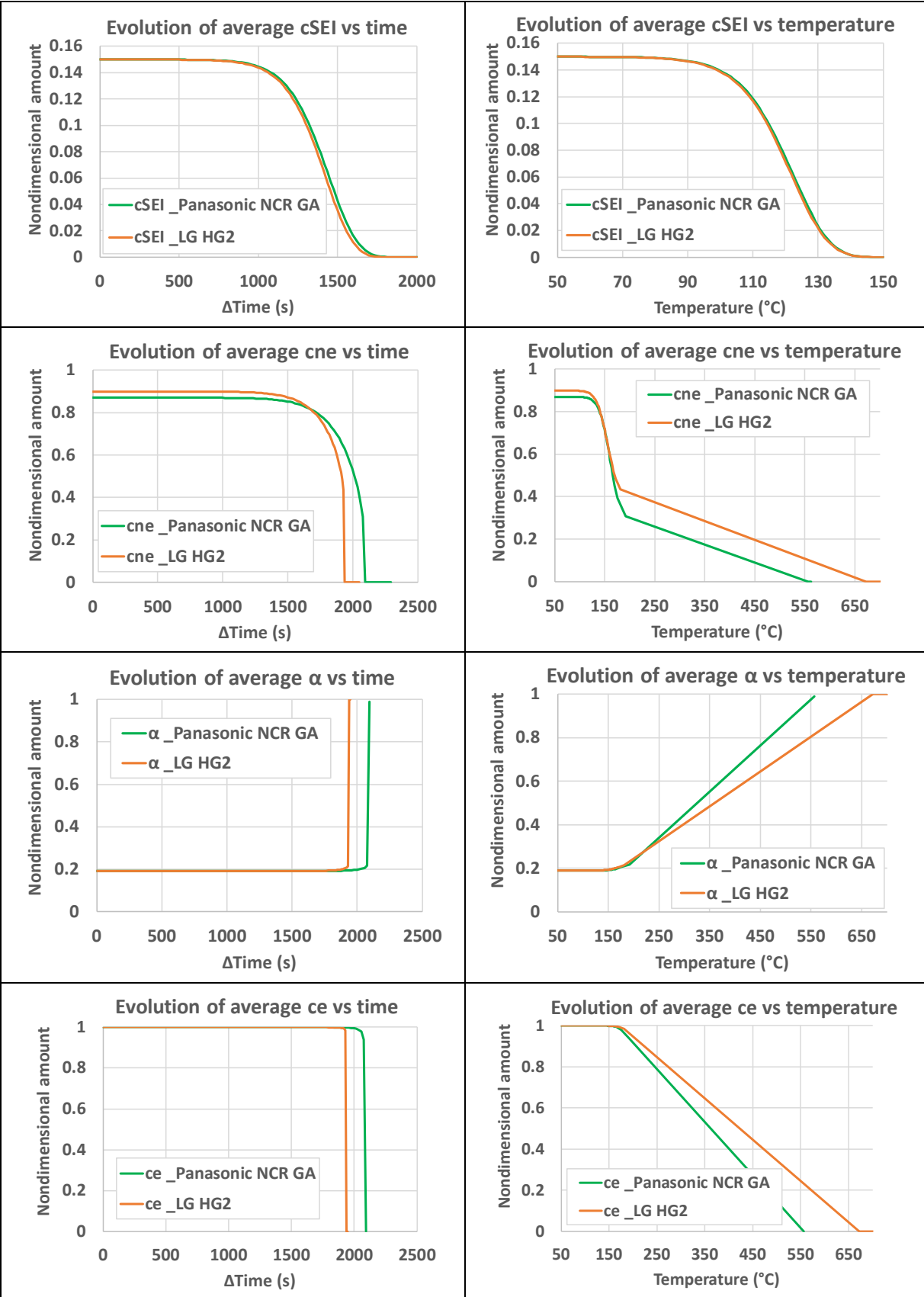


Figure 121: Evolution of c_{SEI} , c_{ne} , α , c_e vs time / vs average skin temperature of pristine cells.

3.4.2 Model limitation

There are several limitations in the model, which are linked to the identified factors below:

The cell reactive materials (cell components) variation:

Although the tested cells are from the same product line (Panasonic NCR GA), their composition may vary slightly from one cell to another. Especially the variation in the quality and quantity of the electrolyte in each cell, since its solvent is involved in all in the degradation reaction at the interface of the negative electrode, at the interface of the positive electrode and in the decomposition reaction of the electrolyte.

The sensitivity of the chemical reactions during the thermal runaway:

It is difficult to adjust the kinetics of chained exothermic reactions pertaining to this phenomenon. These parameters are very sensitive, especially since these reactions are intrinsically linked and some usually occurred and accelerated at closely time.

The calibration based on HWS test in the BTC:

The kinetic parameters are calibrated based on the HWS test in the pseudo-adiabatic of the BTC. Even though the model has taken into account the heat exchange, the quality of the calibrated kinetic parameters may be reduced since the BTC devices do not maintain the pseudo-adiabatic condition throughout the whole test, thereby, it cannot repeat the same quality and sensitivity from test to test.

The lacking of HWS tests for calibration purposes:

The model was calibrated based on only a single HWS test for each technology due to the failure of BTC in the second year. This lacking of repeatable tests makes it difficult for the calibration process of the thermal runaway.

The melting of the separator:

This links closely to the critical temperature T_2 , which is not taken into account in the model. Instead, the model can only account for the heat release due to the self-discharge of the cell during the accelerated thermal runaway.

The venting:

We tried to calibrate this venting event in the model. It occurs as soon as the pressure inside the cell exceeds the critical pressure. However, the pressure monitoring could not be performed well in the BTC, therefore the critical pressure was not very well calibrated. In the works of Mier et al. [152, 162], they have also shown that critical burst overpressure of the venting cap may vary in case of 18650 cells and its value follows a normal distribution.

3.5 Conclusion

Following final orientation given to the thermal runaway model development activities the extended thermal runaway model has been fully constructed on COMSOL Multi-physics platform. This model is able to predict the temperature evolution of the cell as well as the hard ISC and venting.

Firstly, this model was calibrated for the selected Ni-rich technologies based on HWS test in pseudo-adiabatic condition of BTC. Then, the ultimate strategy adopted to evaluate the performance of the model and contribute to its overall validation was reported. The 3D extended thermal runaway model, calibrated for Panasonic NCR GA and LG HG2 technologies, is validated through 3D oven test sub-model developed in this chapter. The imperfections and limitations as well as the advantages of the model were highlighted.

Thanks to this modelling works, a clearer picture of the exothermic chemical chain reactions occurs inside the Ni-rich tested cells during the thermal runaway was drawn. The model gives excellent agreement results in term of critical temperature T_3 for both technologies, especially for LG HG2 cell with the difference of 0.2%. However, it predicted the moment of the accelerated thermal runaway quite early (2.7% in case of LG HG2 and 6.1% in case of Panasonic NCR GA). The predictions of the models on the venting were not well calibrated, especially in case of Panasonic NCR GA.

After validation, this extended model of Panasonic NCR GA and LG HG2 can now be used to simulate the thermal runaway of these technologies to assess the impact of main parameters pertaining to cell states. Some parametric study using this model will be presented in chapter 4.

Chapter 4. SOC and SOH parametric study

“Don't let PERFECT be the enemy of the GOOD.”

- Voltaire

Contents

- 4.1 Introduction 225
- 4.2 Impact of SOC on the thermal runaway overall phenomenology..... 226
- 4.3 Impact of SEI thickness growth by calendar aging on the thermal runaway 230
- 4.4 Impact of SEI growth influenced by calendar aging and cycling aging..... 235
 - 4.4.1 Thermal runaway of cycling aged cell _ Scenario (I) 236
 - 4.4.2 Thermal runaway of cycling aged cell _ Scenario (II) 237
 - 4.4.3 Comparison between the simulation results with the experimental data 238
- 4.5 Simulation conclusions and perspectives..... 245

4.1 Introduction

After validation, a parametric study using this developed model has been carried out to assess the impact factors relating to state of charge (SOC) and aging (state of health (SOH)) on the thermal runaway.

In the first part of this chapter, the impact of the SOC level onto the thermal runaway process of Ni-rich tested cells is explored making use of the calibrated model.

In two further sections, the analysis of the SEI-driven aging overall impact on the thermal runaway of Ni-rich cells is investigated based on a parametric study and relating simulations performed with the model. Firstly, the impact of SEI thickness growth due to calendar aging at high temperature on the thermal runaway is confirmed. Secondly, the impact of SEI growth from two different aging mechanisms of calendar aging and cycling aging by assuming different scenarios of the SEI produced from cycling aging is detailed.

The aging sub-model carried out in this section is targeted mainly towards the Panasonic NCR GA (NCA chemistry), for the following reasons:

- The aging campaign of Panasonic NCA GA cells were more successfully carried out.
- The levels of aging achieved of Panasonic NCR GA cells were higher which is more consistent with the intended purpose to study the impact of aging on the thermal runaway for a significant variation domain of cell aging.
- We successfully aged few cells with different SEI-driven aging at high temperature: Calendar aging and cycling aging, with the same level of discharge capacity loss (~16%). This allowed to compare the impact of these different aging mechanisms on the thermal stability of the battery.
- Experimental work (Oven tests) at the aged states of Panasonic NCR GA technology occurred to reveal the most complete one available for such a purpose.

4.2 Impact of SOC on the thermal runaway overall phenomenology

The 3D oven test simulation tool was used to simulate the thermal runaway of pristine cells Panasonic NCR GA at 100%SOC, 50%SOC and 0 %SOC. There are 2 different parameters to be adjusted in the model for different SOC levels which are the normalized concentration of Li intercalated in the negative electrode (c_{ne}) and the conversion degree (α) of the positive electrode active material, which were obtained in chapter 2. These SOC-dependence parameters of 100%SOC, 50%SOC and 0%SOC are shown in Table 40.

Table 40: Parameters set for SOC levels.

Initial SOC (%)	100	50	0
$\alpha(0)$	0.19	0.390	0.97
$c_{ne}(0)$	0.87	0.425	0.02

Figure 122 shows the simulated average skin temperature of the pristine Panasonic NCR GA cells at different levels of SOC. The critical temperature T_3 , the maximum temperature reached T_{max} and times to these temperatures, are identified in Table 41.

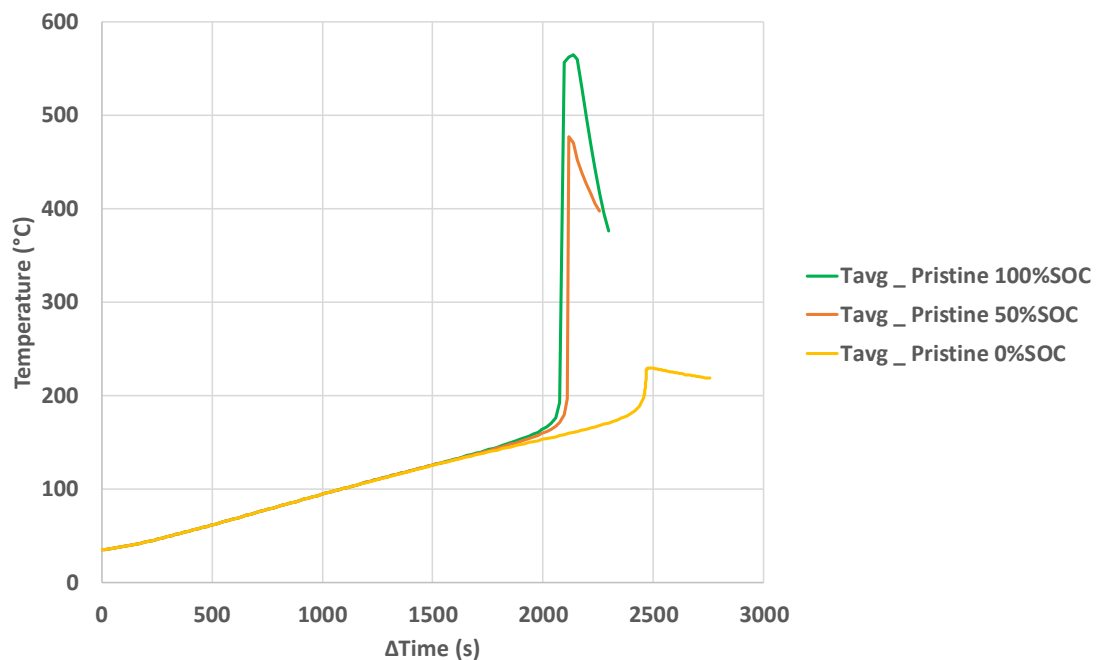


Figure 122: Simulation results of the average skin temperature evolution of pristine cells at different SOC levels.

The model results are coherent with the findings in the experimental work in Chapter 2 as well as the finding in the literatures [74, 95, 124–128], which confirms that the safety of the LIBs increases with decreasing SOC. The accelerated thermal runaway is delayed and occurs at higher temperature in case of cells at lower SOC. The model also shows that the SOC-dependency is observed to be very strong with the SOC range below 50%. Consequently, the maximum average skin temperature reached is decreased with decreased SOC.

Table 41: The critical temperature T_3 , the maximum temperature reached T_{max} and times to these temperatures identified from the oven test vs simulation results.

Pristine		100%SOC	50%SOC	0%SOC
<i>3D model</i>	T3 (°C)	192.3	197	206
	Tmax (°C)	557.2	477	228
<i>Oven test data</i>	T3 (°C)	196.0	-	-
	Tmax (°C)	562.0	-	-
<i>3D model</i>	tT3 (s)	2076	2096	2462
	tTmax (s)	2096	2116	2469
<i>Oven test data</i>	tT3 (s)	2211	-	-
	tTmax (s)	2231	-	-

Figure 123 and Table 42 present the evolution, the temperature range and occurrence time of the exothermic chemical reactions of pristine cells at different SOC. It shows that these reactions are less intense (maximum temperature drops from 557 to 228 °C from 100% SOC to 0% SOC) and also notably delayed in case of reduced SOC batteries (thermal runaway delayed about 400 s in the case of 0% SOC batteries).

Table 42: The temperature range and occurrence time of the exothermal chemical reactions.

Panasonic NCR GA Pristine		Onset temperature (°C)	End temperature (°C)	Onset time (s)	End time (s)
cSEI	100%SOC	56	146.5	416	1816
	50%SOC	56	146.5	416	1836
	0%SOC	56	145.3	416	1856
cne	100%SOC	63	557.0	536	2096
	50%SOC	72	477.0	656	2116
	0%SOC	78	229.0	756	2480
α	100%SOC	120	557.0	1416	2096
	50%SOC	120	477.0	1416	2116
	0%SOC	140	229.6	1756	2484
ce	100%SOC	139	557.0	1716	2096
	50%SOC	139	477.0	1716	2116
	0%SOC	140	229.6	1756	2484

Besides the heat released by exothermic chemical reactions, the hard ISC after the collapse of separator also releases a large amount of stored electric energy, which is strongly related to the SOC level of the tested cells. Therefore, the cell with increased SOC can trigger the thermal runaway instantly once the separator collapses, the exothermal chemical reactions accelerate simultaneously and overlap each other, as observed in Figure 123 and Table 42.

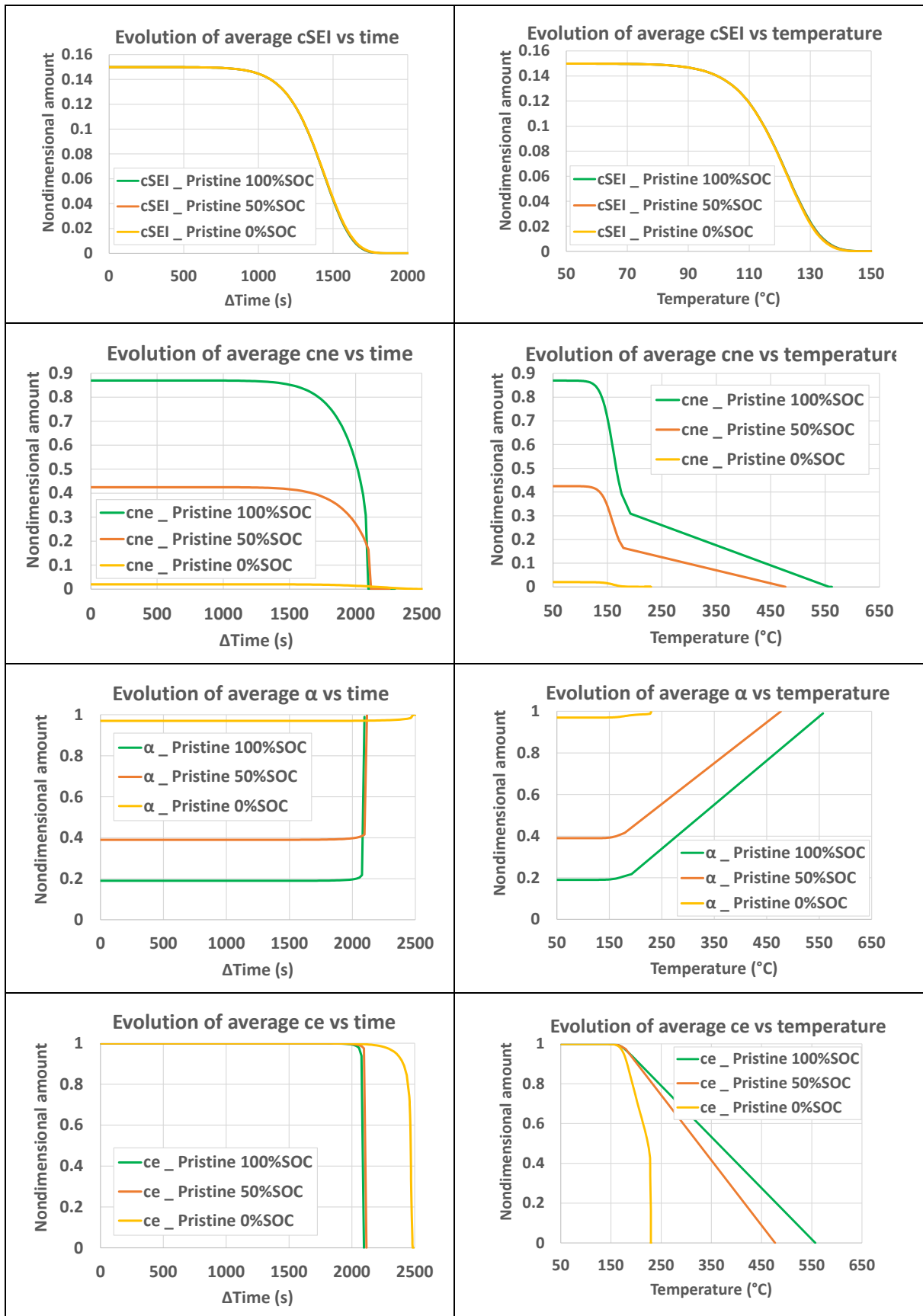


Figure 123: Evolution of c_{SEI} , c_{ne} , α , c_e vs time / vs average skin temperature of pristine cells

4.3 Impact of SEI thickness growth by calendar aging on the thermal runaway

In this section, the 3D oven test simulation tool was used to simulate the thermal runaway of a calendar aged Panasonic cell (cell P1530) at 16.26% discharge capacity loss which is the highest aging level obtained, and results compared with experimental data. The estimation of SEI thickness growth through calendar aging are summarised in Table 43.

Table 43: Estimation of the SEI thickness growth through calendar aging

Parameters	Unit	Panasonic NCR GA
M_{SEI}	kg/mol	0.162
ρ_{SEI}	kg/m^3	1690
$\epsilon_{s,n}$	[-]	0.62 [163]
δ_n	m	8.4e-5
A	m^2	0.0773
$R_{s,n}$	m	10e-6
$\delta_{SEI,0}$	m	5e-9
$t_{SEI,0}$	[-]	0.033
Capacity loss due to SEI growth calendar aging (LLI)	Ah	0.082
δ_{SEI} calendar aging (16.26% capacity loss)	m	1.26e-7
t_{SEI} calendar aging (16.26% capacity loss)	[-]	0.834

The critical temperatures identified are shown in Table 44. The model gives satisfactory results for the critical temperature T_3 , with small differences of 3.7°C (1.9%) and 3°C (1.5%) for the case of pristine cell and calendar aged cell, respectively. Additionally, the model was able to predict that the thermal runaway occurrence is delayed for calendar aged cell. This can be explained due to diffusion limitation increase due to the increased thickness of SEI layer in case of calendar aged cell. This result is consistent with the experimental data of the

oven test and the findings in the works of Abada *et al.* [16], as well as of Lammer *et al.* [132][133][134].

Table 44: The critical temperature T_3 , the maximum temperature reached T_{max} and times to these temperatures identified from the oven test vs simulation results of pristine cell and calendar aging cell.

100%SOC		Pristine	Calendar aging
<i>3D model</i>	T3 (°C)	192.3	196.0
	Tmax (°C)	557.2	558.0
<i>Oven test data</i>	T3 (°C)	196.0	199.0
	Tmax (°C)	562.0	-
<i>Off set values (model/test data)</i>	$\Delta T3$ (°C)	-3.7 (-1.9%)	-3.0 (-1.5%)
	$\Delta Tmax$ (°C)	-4.8 (-0.8%)	-
<i>3D model</i>	tT3 (s)	2076	2110
	tTmax (s)	2096	2130
<i>Oven test data</i>	tT3 (s)	2211	2307
	tTmax (s)	2231	2314
<i>Off set values (model/test data)</i>	$\Delta tT3$ (s)	-135 (-6.1%)	-197 (-9.3%)
	$\Delta tTmax$ (s)	-135 (-6.05%)	-184 (-7.9%)

Figure 124 shows the average skin temperature calculated at the skin surface of the pristine (P1706) and calendar aged (P1530) cells as determined from the 4 skin TC responses obtained during the oven tests. It is compared with the simulated average skin temperature from the 3D model. In can be seen that the overall evolutions of temperatures between pristine and aged cells are qualitatively well predicted by the model. However, due to the limited operability of the locking system of the oven door, it is important to note that during the accelerated thermal runaway of the calendar aged cell, the oven door opened which caused unexpected thermal losses. This issue unfortunately impacted the accuracy of the monitored skin temperatures of the calendar aged cell as it caused a drop in the

temperature measured at the cell skin, which is visible in Figure 124 for calendar aging curve during the accelerated thermal runaway. These heat losses are obviously not taken into account in the model which assumes ideal behaviour of the oven test during heating process, hence clearly explaining the overestimation of the surface temperature of the cell simulated under these operating conditions.

Moreover, the model still predicted the moment of the accelerated thermal runaway quite early (135s (6.1%) in advance in case of pristine cell and 197s (9.3%) in advance in case of calendar aged cell). This delay is linked to the kinetic parameters of the positive electrode decomposition reaction and the electrolyte reaction, which are estimated quite early (120-121°C and 139°C, respectively) for both cells, as observed in Table 45.

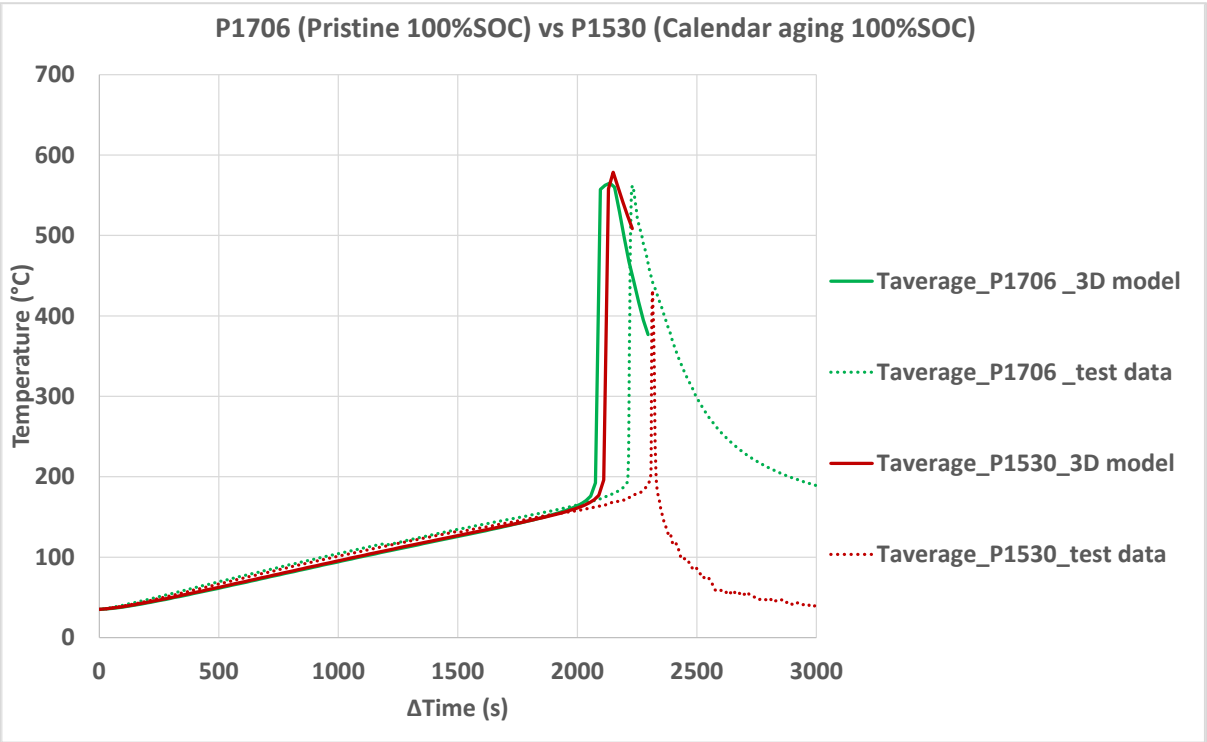


Figure 124: The average skin temperature of pristine cell and calendar aging cell of the simulation results vs oven test data.

Consequently, as shown in Table 45 and Figure 125, the decomposition reaction of the negative electrode of the calendar aged cell occurred at higher temperature compared to that of pristine cell (72.4°C > 63°C) and delayed 114s compared to that of pristine cell. This delay relates to the delay in degradation reaction of the negative electrode, as shown in Table 45 (cne) and Figure 125, which can be explained by the increased diffusional

limitations of Li ions due to the thicker SEI layer formed from calendar aging. Moreover, the heat released by the calendar aged cells is slightly more important and their temperature increases faster during the more accelerated thermal runaway than that of pristine cell.

Table 45: The temperature range and occurrence time of the exothermic chemical reactions occurred during the thermal runaway of pristine and calendar aged cells.

100%SOC		Onset temperature (°C)	End temperature (°C)	Onset time (s)	End time (s)
cSEI	Pristine	56.0	146.5	416	1816
	Calendar aging	56.7	146.0	410	1810
cne	Pristine	63.0	557.0	536	2096
	Calendar aging	72.4	558.0	650	2130
α	Pristine	120.0	557.0	1416	2096
	Calendar aging	121.5	558.0	1410	2130
ce	Pristine	139.0	557.0	1716	2096
	Calendar aging	138.5	558.0	1690	2130

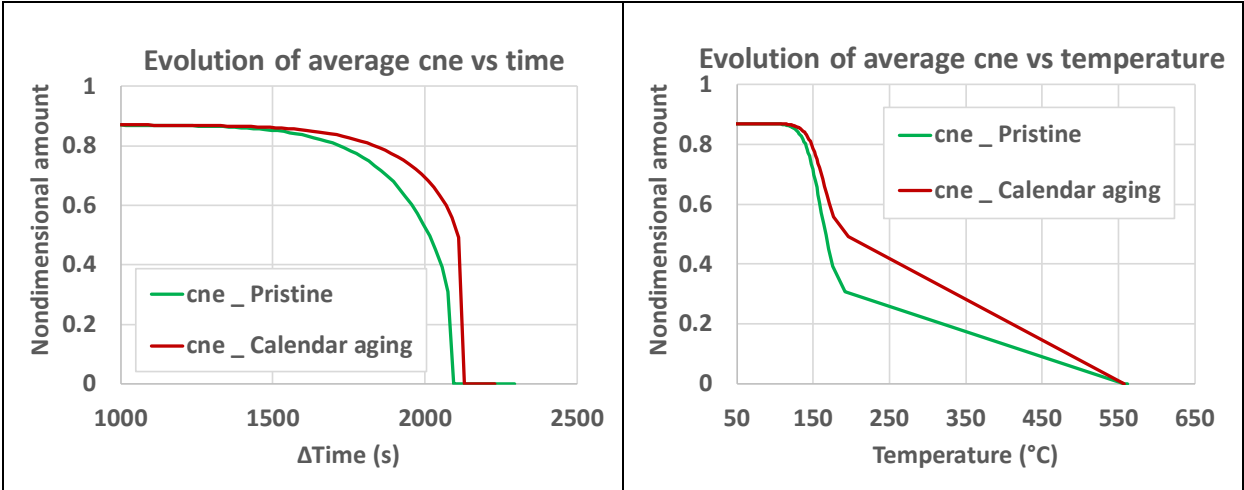


Figure 125: The evolution of the average c_{ne} vs time / vs average skin temperature of pristine and calendar aged cells.

According to the simulation results shown in Figure 126, the venting of both cells occurred during the accelerated thermal runaway, which is very violent and late compared to the first venting signal shown in the oven tests (~122°C).

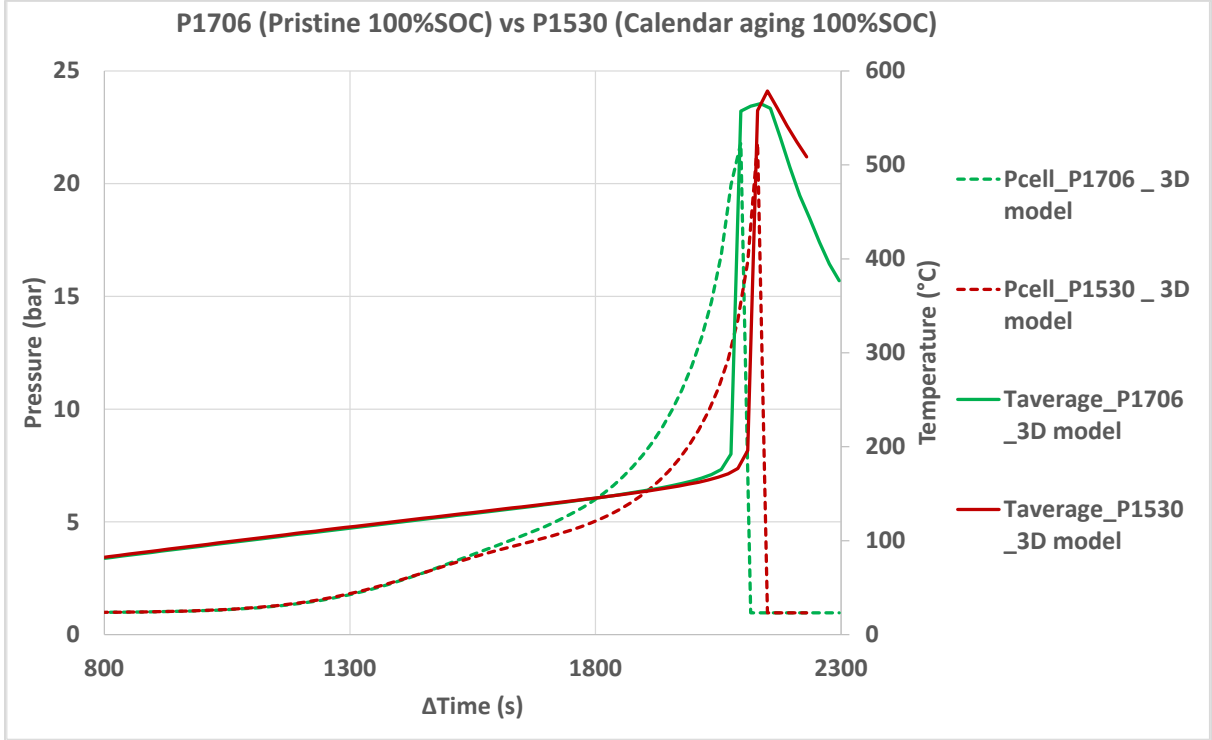


Figure 126: Cell internal pressure and average skin temperature of the pristine and calendar aged Panasonic NCR GA cells.

The amount of ejected gas modelled and the cell mass loss from experiment are shown in Table 46. The simulation results show that the calendar aging produced and released more gas, hence its venting is more violent. This finding is coherent with the recorded venting event during these oven tests.

Table 46: Comparison between the amount of ejected gas modelled and the cell mass loss from experiment.

100%SOC Panasonic NCR GA	Unit	Pristine _ P1706	Calendar aging _ P1530
Cell mass loss (Oven test measurement)	[g]	20.30	30.7
Amount of ejected gas (3D model)	[g]	7.73	9.5

4.4 Impact of SEI growth influenced by calendar aging and cycling aging

Two cells with different SEI-driven aging mechanisms were aged during this study, calendar aging at high temperature (cell P1530) and cycling aging at high temperature (cell P1555), with the same level of discharge capacity loss (16%). Thanks to the tool developed at IFPEN during the work of the C. Edouard thesis focused to the modelling of aging [154], which was described in chapter 2, the amount of LLI (loss of lithium inventory), LAMpos (loss of active materials at the positive electrode), LAMneg (loss of active materials at the negative electrode) of these cells were analyzed as summarized in Table 47.

Table 47: Analysis of capacity loss due to LLI, LAMpos and LAMneg for pristine, calendar aging and cycling aging Panasonic NCR GA cells.

	LLI (mAh)	LAMpos (mAh)	LAMneg (mAh)
Pristine	310	-	-
Calendar aged cell	392 (+ 82)	0%	13.2%
Cycling aged cell	515 (+ 205)	9%	21.1%

During cycling aging, the graphite exhibits volume expansion /contraction during lithiation / delithiation of 5 % – 10 %. Therefore, the SEI cracks and SEI reformation due to these volume changes of the graphite negative electrode during cycling operations are the major cause of Li consumption [56]. Graphite negative electrodes exhibit a largely linear expansion from 0 % to 25 % lithiation SOC, only minor volume changes between 25 % and 50 % lithiation SOC, and another linear expansion above 50 % lithiation SOC, where the LiC₆ phase formation begins. Therefore, due to stress from these volume changes, the SEI layer should be physically strong or flexible enough to accommodate the volume change of the negative electrode during the cycling process [56]. Osswald *et al.* [10] found that higher temperatures and higher currents lead to stronger local consideration of charge distribution and also higher self-heating, especially during charging.

Therefore, we assume that the cycling aging at high temperature produced more SEI unstable than SEI stable. Moreover, the SEI layer due to cycling aging is more porous and thereby, lower diffusional limitations of Li ions, compared to that of SEI layer due to calendar aging.

However, for cycling aging in real life, we know that some part of newly formed SEI is stable but some other part is unstable, but we do not know the real proportion between the unstable SEI vs the stable SEI produced. Therefore, in order to investigate the impact of cycling aging to the thermal runaway, we will simulate the thermal runaway of the cycling aged cell with 2 different scenarios below:

4.4.1 Thermal runaway of cycling aged cell _ Scenario (I)

Compared with the calendar aged cell with the same level of discharge capacity loss, this studied scenario relies on the following assumptions and related selection of parameter values:

- More SEI unstable produced from cycling aging than that in case of calendar aging. Which means that $c_{SEI,0}$ (the initial normalized concentration of unstable SEI containing Li) of cycling aged cell is higher than the $c_{SEI,0}$ of calendar aged cell.
- However, the SEI layer produced from cycling aging have the same thickness as in case of calendar aging, which means that $t_{SEI,0}$ of cycling aged cell is similar as the $t_{SEI,0}$ of calendar aged cell.
- The diffusivity of SEI layer from cycling aging is similar as in case of calendar aging, which means that $t_{SEI,ref}$ of cycling aged cell is similar as the $t_{SEI,ref}$ of calendar aged cell.

Therefore, compared to the case of pristine cell, the different parameters for this scenario of cycling aging are shown in Table 48.

Table 48: The different parameters for scenario I of cycling aged cell vs pristine cell.

100%SOC	$c_{SEI,0}$	$t_{SEI,0}$
Pristine	0.150	0.033
Cycling aging (I)	0.375	0.834

4.4.2 Thermal runaway of cycling aged cell _ Scenario (II)

Compared with the calendar aged cell with the same level of discharge capacity loss, this studied scenario relies on the following assumptions and relating set of parameter values:

- More SEI unstable produced from cycling aging than that in case of calendar aging. Which means that $c_{SEI,0}$ (the initial normalized concentration of unstable SEI containing Li) of cycling aged cell is higher than the $c_{SEI,0}$ of calendar aged cell.
- The SEI layer produced from cycling aging have the higher thickness than in case of calendar aging, which means that $t_{SEI,0}$ of cycling aged cell is thicker than the $t_{SEI,0}$ of calendar aged cell.
- SEI layer from cycling aging is assumed to be more porous, therefore, the diffusivity of SEI layer from cycling aging is also proportionally higher than in case of calendar aging, which means that $t_{SEI,ref}$ of cycling aged cell is higher than the $t_{SEI,ref}$ of calendar aged cell.

In this scenario, the thickness of SEI formed due to cycling aging, $t_{SEI,0}$, is estimated in Table 49.

Table 49: Estimation of the SEI thickness growth through cycling aging

Parameters	Unit	Panasonic NCR GA
M_{SEI}	kg/mol	0.162
ρ_{SEI}	kg/m^3	1690
$\epsilon_{s,n}$	[-]	0.62 [163]
δ_n	m	8.4e-5
A	m^2	0.0773
$R_{s,n}$	m	10e-6
$\delta_{SEI,0}$	m	5e-9
$t_{SEI,0}$	[-]	0.033
Capacity loss due to SEI growth cycling aging (LLI)	Ah	0.205
δ_{SEI} cycling aging (16.67% capacity loss)	m	3.09e-7
$t_{SEI,0}$ cycling aging (16.67% capacity loss)	[-]	2.04

Therefore, compared to the case of pristine cell and cycling aging scenario I, the different parameters for this scenario of cycling aging are shown in Table 50.

Table 50: The different parameters for scenario II of cycling aged cell vs pristine cell.

100%SOC	$c_{SEI,0}$	$t_{SEI,0}$	$t_{SEI,ref}$
Pristine	0.15	0.033	1
Cycling aging (I)	0.375	0.834	1
Cycling aging (II)	0.375	2.04	2.446

4.4.3 Comparison between the simulation results with the experimental data

The simulation results of the 2 cycling aging scenarios above will firstly be compared with the experimental data of Oven test made in INERIS, in order to explore the accuracy of the

thermal runaway simulation of SEI-driven cycling aging. Then these results will also be compared to the case of calendar aging, in order to study the impact of these different aging mechanisms to the thermal runaway.

Figure 127 shows the average skin temperature measured at the skin surface of the pristine (P1706), calendar aged (P1530) and cycling aged (P1555) cells thanks to the 4 skin TCs during the oven tests, in comparison with the simulated average skin temperature from the 3D model. The model results show an increased delay before thermal runaway in case of calendar aging and an even more increased delay in the case of cycling aging. This is consistent with experimental data.

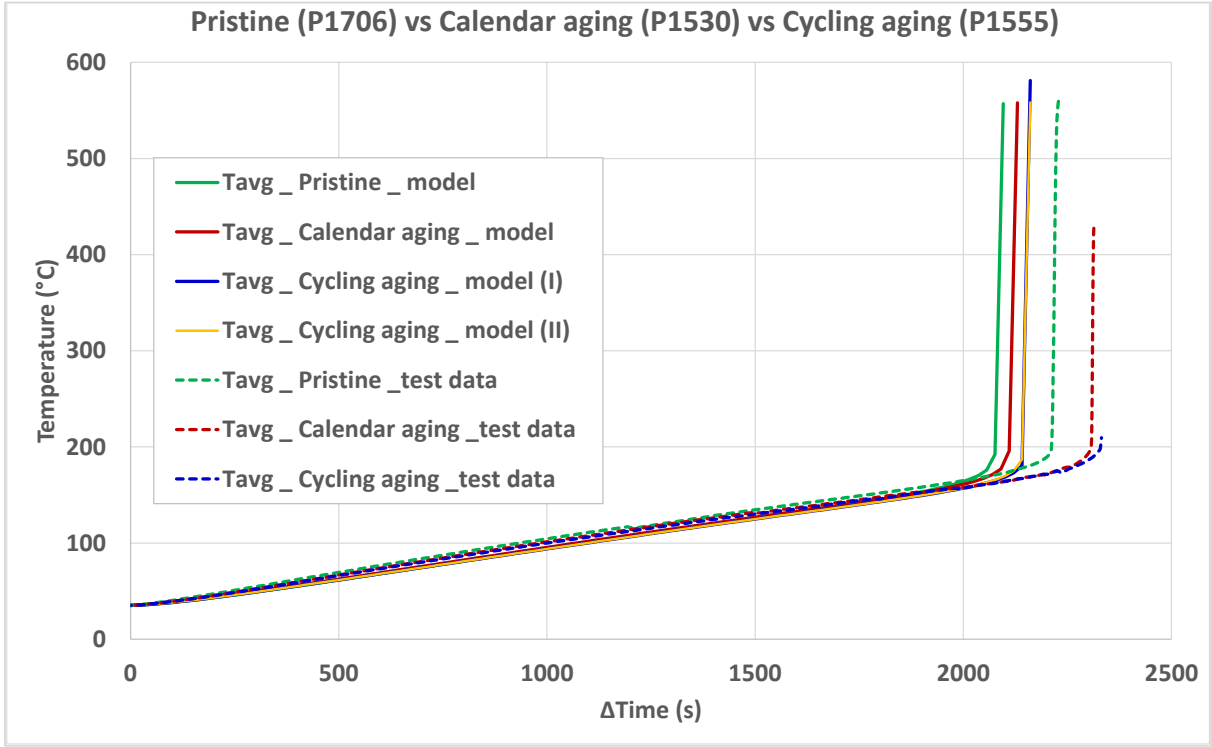


Figure 127: The average skin temperature of pristine cell 100%SOC, calendar aging cell 100%SOC and cycling aging cell 100%SOC of the simulation results vs oven test data.

However, as previously, due to the limited operability of the locking system of the oven door, it is noteworthy that, during the accelerated thermal runaway of the cycling aged cell, the oven door also opened which also caused thermal losses similarly as the case of the oven test of calendar aged cell. This issue unfortunately strongly impacted the accuracy of the monitored skin temperatures of the cycling aged causing a drop in the temperature

measured at the cell skin of cycling aged cell, which is visible in Figure 127. These heat losses cannot be taken into account in the model.

Table 51: The critical temperature T_3 , the maximum temperature reached T_{max} and times to these temperatures identified from the oven test vs simulation results of pristine cell, calendar aged cell and cycling aged cell.

100%SOC		Pristine	Calendar aging	Cycling aging	
				Scenario (I)	Scenario (II)
3D model	T3 (°C)	192.3	196	180.0	187.0
	Tmax (°C)	557.2	558	581.0	558.3
Oven test data	T3 (°C)	196.0	199	198.0	
	Tmax (°C)	562.0	-	-	
Off set values (model/test data)	$\Delta T3$ (°C)	-3.7 (-1.9%)	-3.0 (-1.5%)	-18 (-9%)	-11 (-5.5%)
	$\Delta Tmax$ (°C)	-4.8 (-0.8%)	-	-	-
3D model	tT3 (s)	2076.0	2110	2141.0	2141.0
	tTmax (s)	2096.0	2130	2161.0	2161.0
Oven test data	tT3 (s)	2211.0	2307	2329.0	
	tTmax (s)	2231.0	2314	2331.0	
Off set values (model/test data)	$\Delta tT3$ (s)	-135 (-6.1%)	-197 (-8.5%)	-188 (-8%)	-188 (-8%)
	$\Delta tTmax$ (s)	-135 (-6.1%)	-184 (-7.9%)	-170 (-7.3%)	-170 (-7.3%)

Table 51 presents the critical temperatures identified from the oven test vs simulation results of these investigated cells. We see that the predictions of T_3 of both cycling aging models are all lower than the physical oven test (180°C and 187°C vs 198°C). However, the prediction of T_3 of the scenario II is more accurate. Even though they predicted different values of the critical temperature T_3 , it is interestingly noticed that both cycling aging model scenarios predict the same occurrence time of the accelerated thermal runaway (2141s).

As observed in Table 52 and Figure 128, due to the higher $c_{SEI,0}$, the SEI reaction of the cycling aging scenarios occurred earlier and at a bit lower temperatures ($\sim 52^\circ\text{C}$) than that of the other cases ($\sim 56^\circ\text{C}$). In addition, due to the higher diffusion limit corresponding to the higher $t_{SEI,0}$, the negative electrode decomposition reaction of these cycling aging scenarios occurred later and at the same level of temperature compared to the case of calendar aging ($\sim 72^\circ\text{C}$). However, it is noticeable that the maximum average skin temperature simulated for cycling aging scenario II is higher than that for cycling aging scenario I. This can be explained due to the slower negative electrode decomposition reaction of scenario II from 661s to 2161s than that of scenario I. This also led to the slower positive electrode decomposition and electrolyte reactions, as seen in Figure 128. The slower electrolyte reaction in the scenario II reflects a better fit with observations resulting from the actual test because we found more electrolyte ejected outside of cycling aged cell at the end of the thermal runaway. Therefore, it comes out from our simulations that the scenario II of cycling aging looks closer to the reality than scenario I.

Above of all that, the model predicted the moment of the accelerated thermal runaway (t_{T_3}) quite early for all three cases (135s (6.1%) in advance in case of pristine cell, 197s (8.5%) in advance in case of calendar aged cell and 188s (8%) in advance in case of cycling aged cell). This delay may be suspected in the parameters of the heat-exchange sub-model. It can also link to the kinetic parameters of the positive electrode decomposition reaction and the electrolyte reaction, which are estimated early ($120\text{-}123^\circ\text{C}$ and 139°C , respectively) for all cells, as observed in Table 52 and Figure 128.

Table 52: The temperature range and occurrence time of the exothermic chemical reactions occurred during the thermal runaway of pristine, calendar aged and cycling aged cells.

100%SOC		Onset temperature (°C)	End temperature (°C)	Onset time (s)	End time (s)
cSEI	Pristine	56.0	146.5	416	1816
	Calendar aging	56.7	146.0	410	1810
	Cycling aging (I)	52.0	146.8	341	1861
	Cycling aging (II)	51.6	146.9	341	1861
cne	Pristine	63.0	557.0	536	2096
	Calendar aging	72.4	558.0	650	2130
	Cycling aging (I)	72.0	581.0	661	2161
	Cycling aging (II)	72.0	558.0	661	2161
α	Pristine	120.0	557.0	1416	2096
	Calendar aging	121.5	558.0	1410	2130
	Cycling aging (I)	122.7	581.0	1461	2161
	Cycling aging (II)	122.7	558.0	1461	2161
ce	Pristine	139.0	557.0	1716	2096
	Calendar aging	138.5	558.0	1690	2130
	Cycling aging (I)	138.2	581.0	1721	2161
	Cycling aging (II)	138.2	558.0	1721	2161

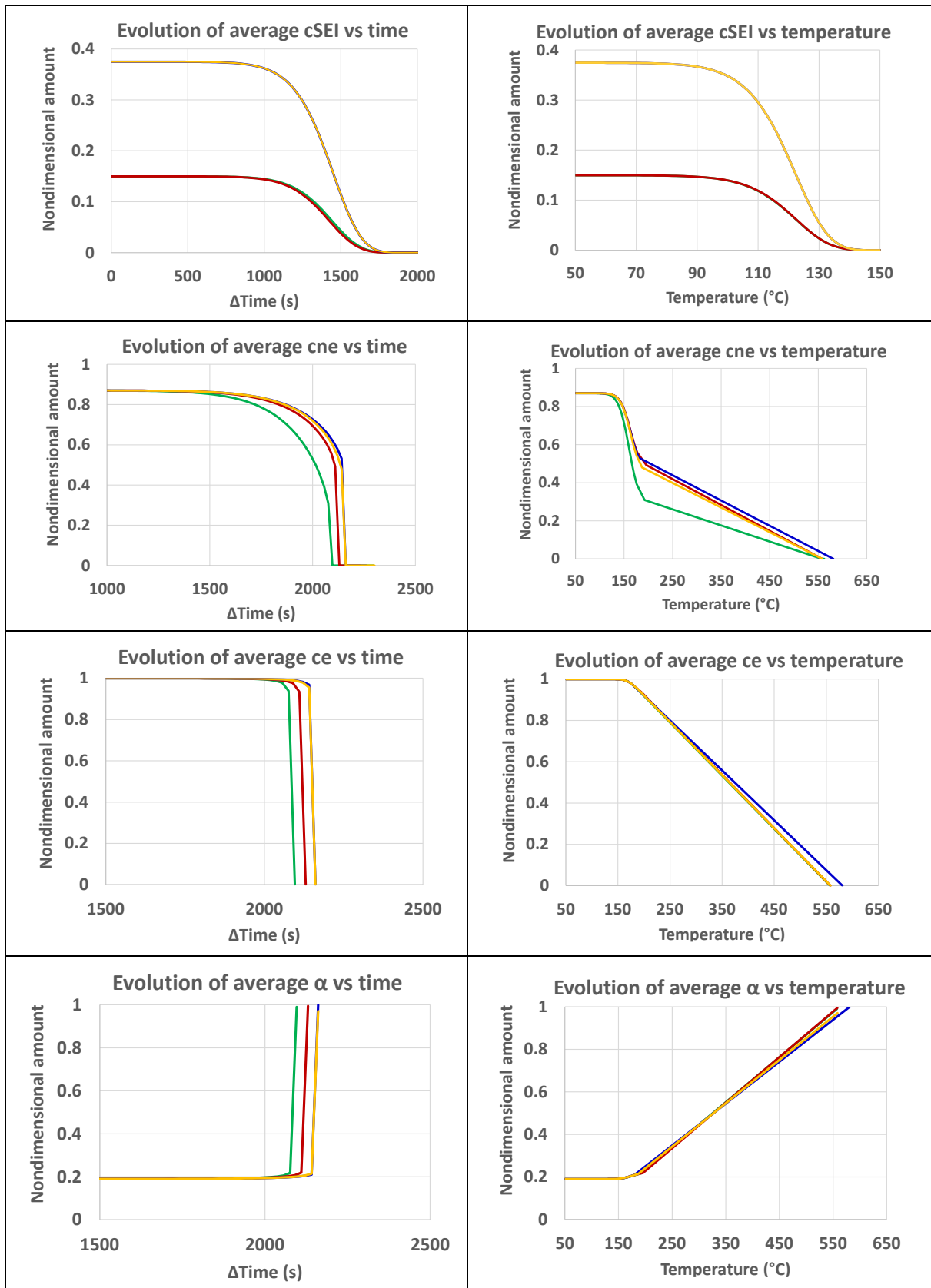


Figure 128: Evolution of c_{SEI} , c_{ne} , α , c_e vs time / vs average skin temperature of pristine cell (green curves), calendar aged cell (red curves) and cycling aged cell scenario I (blue curves), cycling aging scenario II (yellow curves).

According to the simulation results, we observed that at the same level of aging, cells calendar aged by storage at 60 °C triggered the accelerated thermal runaway earlier than the cycling aged cell. However, the accelerated thermal runaway of the cycling aged cell appeared to be less reactive than cycling aged cells.

The amount of ejected gas modelled and the cell mass loss from experiments are presented in Table 53. The simulation results show that the cycling aging released more gas compared to the pristine cell, which is consistent with the cell mass loss trend of the oven tests measurements. However, the simulation results also show that the cycling aging cell released a bit less gas compared to the calendar aged cell, which is not consistent with the cell mass loss trend of the oven tests measurements. Therefore, both cycling aging models did not simulate well the amount of ejected gas during the thermal runaway.

Table 53: Comparison between the amount of ejected gas modelled and the cell mass loss from experiment.

100%SOC	Unit	Pristine _ P1706	Calendar aging _ P1530	Cycling aging _ P1555
Cell mass loss (Oven test measurement)	[g]	20.30	30.7	38.01
Amount of ejected gas (3D model)	[g]	7.73	9.5	9.10 (scenario I)
				7.91 (scenario II)

4.5 Simulation conclusions and perspectives

The thermal runaway model validation and parametric simulation study carried out in this chapter has focused on Panasonic NCR GA technology, in particular for NCA/Graphite-SiO_x chemistry.

Thanks to this 3D oven test simulation tool, the parametric study made it possible to investigate the impact of SOC level on the thermal runaway. It also allowed to compare the occurrence time and temperature range of the exothermic chemical reactions of different cells. The model results are consistent with our findings with HWS tests as well as the finding in the literatures [74, 95, 124–128], which confirmed that the safety of the LIBs increases with decreasing SOC.

With strong assumptions, we were able to investigate the impact of SEI thickness due to calendar aging and 2 cycling aging corresponding to the quality of SEI. The results of which were compared, with real validation oven test data obtained so far. Therefore, the impact of between different aging mechanisms assumptions was studied. The 3D model predicted the moment of the accelerated thermal runaway (t_{T_3}) quite early for all three cases (6.1% in case of pristine cell, 8.5% in case of calendar aged cell and 8% in case of cycling aged cell). According to the simulation results and the oven test data, we observed that at the same level of aging, cells calendar aged by storage at 60 °C triggered the accelerated thermal runaway earlier than the cycling aged cell. However, the accelerated thermal runaway of the calendar aged cell appeared to be less reactive than cycling aged cells.

Last but not least, this model makes it possible to explore more scenarios of cells undergoing thermal runaway process in specified conditions for which adequate parameterization can be defined in relation with underpinning physics, especially the information we cannot get from a dedicated HWS test which may give more insights on the mechanisms at play during the thermal runaway.

Conclusions and perspectives

This thesis, entitled "Understanding and modelling the thermal runaway of Li-ion batteries", is part of a long-term collaboration between IFPEN, INERIS and LRCS (UPJV). The first goal of the thesis was to understand the thermal runaway phenomenon of Li-ion batteries at cell scale, while taking into account the effect of high energy density Ni-rich commercial technologies and the underpinning mechanisms and relationship between aging and safety. Furthermore, in order to better predict and prevent this phenomenon in real-life application, the second goal of the thesis was to develop a predictive consolidated 3D thermal runaway model and the implementation of test protocols for model calibration and validation. To achieve the goals of the thesis, the scientific strategy applied was the combination between modelling and experimental studies.

With an intense bibliography study since the beginning, the state-of-the-art bibliography review explored almost all aspects relating to the thesis works. As guideline for this thesis, some main conclusions have been drawn thanks to this study regarding the thermal runaway process, technology choice, experimental methodology and modelling approach. The outlines of this study were detailed in Chapter 1 of this manuscript.

The bibliography study allowed us to select the Li-ion battery technologies. Ni-rich chemistries are widespread for their safety issues, but little work has been published on the modelling of its thermal runaway. In addition, in order to be able to compare the influence of parameters related to cell chemistry, our study also compared between NMC811 and NCA chemistries. Therefore, the choice of Li-ion batteries technologies studied is the two selected commercial 18650 Ni-rich LIBs, namely Panasonic NCR GA and LG HG2, which were based on NCA and NMC811, respectively, for positive electrodes, in combination with graphite-SiO_x composite negative electrodes.

The implementation of the thermal runaway modelling and experimental studies coupling strategy was exposed in the second and third chapter of the manuscript, detailing the modelling activities and the design of experiments associated with the stages of calibration and validation of the developed model.

The exploitation of the experimental results has been discussed in the second chapter of the manuscript. These tests have significantly enriched our understanding of the thermal runaway phenomenon of the selected chemistries. Besides helping to adjust and calibrate the developed

model for the technologies studied, the safety thermal abuse HWS tests in pseudo-adiabatic condition of the ARC (BTC500 E1735) has also led us to a clearer understanding of the thermal runaway of the selected cells at pristine states and established the 5 stages during the thermal runaway process for high energy Ni-rich LIBs as well as addressed different factors impacting the thermal runaway kinetics. Regardless of SOC levels, the Panasonic NCR GA battery technology had a wider safe region than that of the LG HG2 battery. This technology also delayed the hard internal short circuit and shifted the final venting to a higher temperature. However, above this critical temperature, it exhibited the most severe irreversible self-heating stage, with the highest self-heating temperature rate over the longest duration. This experimental works have been published in WEVJ (World Electric Vehicle Journal) as article, which is entitled “Understanding the Thermal Runaway of Ni-Rich Lithium-Ion Batteries” [106].

Due to the failure of BTC since the 2nd year of the thesis, the HWS tests were not made for aged cells. However, with the Oven tests, the thermal runaway of the aged cells was investigated. The oven tests contributed to the validation of the thermal runaway model, which have reflected more realistic thermal abuse conditions in real life of a battery (eg. “non-adiabatic”).

The extended thermal runaway model has been fully constructed on COMSOL Multi-physics platform. The development, calibration and validation of the thermal runaway model at the cell scale were described in the third chapter of the manuscript. The abusive tests carried out in the BTC made it possible to establish the necessary database for the calibration of the thermal runaway model for the target chemistries. Relying on parameter values from the literature and our experimental data, the model parameters were adjusted. As for the validation of the model, it was carried out thanks to the overheating tests in the oven. The imperfections and limitations as well as the advantages of the model were also highlighted.

Thanks to the 3D oven test simulation tool developed, the parametric study presented in chapter 4 has investigated the impact of SOC level and SEI-driven aging on the thermal runaway.

The simulation results on the impact of SOC were coherent with the findings in our experimental works as well as the finding in the literatures [74, 95, 124–128], which confirmed that the safety of the LIBs increases with decreasing SOC and the accelerated thermal runaway delay and occurred

at higher temperature in case of cells at reduced SOCs. It also allowed to compare the occurrence time and temperature range of the exothermic chemical reactions of different cells.

For the impacts of SEI-driven calendar and cycling aging on the thermal runaway, a simplified aging sub-model was integrated which assumes that the growth of the SEI layer is the predominant mechanism. To obtain data for this sub-model, various experimental protocols have been developed at IFPEN and INERIS such as: the cell characterization and SEI-driven calendar and cycling aging campaigns were carried out at IFPEN, while the experiments relating to thermal abuse tests were carried out in the “STEEVE” platform at INERIS. With strong assumptions for parametric studies relating to the impact of SEI thickness due to calendar aging and due to the different scenarios of cycling aging corresponding to the quality of SEI were investigated. The model gives satisfactory results for the critical temperature T_3 , with small differences of 1.9%, 1.5% and 5.5% for the case of pristine cell, calendar aged cell and cycling aged cell, respectively. Additionally, the model was able to predict that the thermal runaway occurrence is delayed for aged cells compared to the pristine cells. This can be explained due to diffusion limitation increase due to the increased thickness of SEI layer in case of aged cell. This result is consistent with the experimental data of the oven test and the findings in the literatures [16][132][133][134].

However, the simulation results have predicted the moment of the accelerated thermal runaway quite early (6.1% in advance in case of pristine cell, 9.3% in advance in case of calendar aged cell and 8% in advance in case of cycling aged cell). This delay may be suspected in the parameters of the heat-exchange sub-model. It can also link to the kinetic parameters of the positive electrode decomposition reaction and the electrolyte reaction.

Furthermore, according to the experimental and simulation results, we found that:

- The first exothermic reactions of aged cells occur at a higher temperature than that for pristine cells. However, the accelerated thermal runaway has been shown to be more violent in case of aged cells.
- At the same level of aging, cells calendar aged by storage at 60 °C triggered the accelerated thermal runaway earlier than the cycling aged cell. However, the accelerated thermal runaway of the calendar aged cell appeared to be less reactive than cycling aged cells.

Overall, this thesis work provides a predictive tool capable of helping to prevent thermal runaway and design safer Li-ion batteries. The scaling of the cell to the modulus of the model, it is necessary to deepen research in order to arrive at an experimental method suitable for the study of the propagation of thermal runaway within the module. As safety control of Li-ion battery is critical and urgent, it is believed that the effort in modelling thermal runaway phenomenon is worth to be emphasized for a long time. The development of multi-physics and multi-scale models is the selected way, to pave the way for future optimization of Li-ion battery safety management system at module or pack levels. Further studies in this direction are on-going within the collaboration between IFPEN/INERIS/LRCS. Some perspectives can be put forward for the future research to improve the current thermal runaway model, as discussed below:

- The current model only takes into account the heat released due to the hard internal short circuits occurred at the onset of accelerated thermal runaway and considered it as a global mechanism which is estimated based on the cell average temperature. The melting process of separator and the local heat released due to the internal short circuits is lacking. Therefore, the model can be improved by taking into account the thermal point of view of these short circuits at the localized overheating.
- The kinetic parameters are calibrated based on the HWS test in the pseudo-adiabatic of the BTC. Even though the model has taken into account the heat exchange, the quality of the calibrated kinetic parameters will be improved if the BTC devices maintain better the pseudo-adiabatic condition throughout the whole test.
- The venting calibration could be improved taken into consideration through improving BTC vessel pressure monitoring involving the estimation of the critical pressure linked to the venting and the mass loss monitoring after the first exothermic detection.
- It would also be remarkably interesting to perform gas analyses in real time in order to characterize the escaping gases and thus consolidate the identification of the reactions that take place continuously. Thus, we can legitimately think that we can improve the calibration of the model and obtain more satisfactory predictions.
- For the oven test, it is important to note that the model validation procedure could be improved by improving the operability of the locking system of the oven door to prevent the unexpected thermal losses.

- In order to achieve a safe operation of LIBs, our findings demonstrate that Battery Management System should monitor and control the state of charge and aging history of batteries with high attention to the safety aspects.
- Due to the limited time and the technical issue of BTC, we were not able to perform the thermal abuse tests on li plating aged cells and integrate its impact on the thermal runaway. This could be interesting to explore this impact by the developed model with the support of future experimental tests.
- Beyond the model, the characterization of pristine and aged cells after thermal abuse tests had provided interesting information and opened up other perspectives such as the impact of mental tube presence in the cell core, the cell cap design. More analyzes and post-mortem observations can provide knowledge in terms of degradation of the different components of Li-ion batteries under abusive thermal conditions.

Last but not least, knowledge in terms of initiation and evolution of the thermal runaway Ni-rich Li-ion batteries have been enriched thanks to the combination of experimental and modelling studies. The developed model can be used as a simulation tool to explore more scenarios of cells undergoing thermal runaway process in specified conditions for which adequate parameterization can be defined in relation with underpinning physics. This contributes to the future Li-ion battery safety management system in depth.

Résumé de thèse en français

Contexte

La batterie lithium-ion (LIB) est l'une des technologies de stockage d'énergie les plus prometteuses aujourd'hui, grâce à leurs densités d'énergie spécifiques élevées et à leurs performances de cyclage stables. Néanmoins de difficiles défis restent à relever pour la technologie LIB : (i) la mise au point de variantes à moindre coût, (ii) l'obtention de performances plus élevées avec une durée de vie plus longue (> 10 ans pour les applications automobiles), (iii) tout en autorisant une charge rapide (<20 min pour 80% état de charge (SOC)), et enfin (iv) permettre leur cyclage à basse température. Dans le même temps, ces améliorations attendues ne doivent pas compromettre les performances de sécurité, qui doivent rester excellentes dans toutes les situations.

Aujourd'hui, les LIBs disponibles commercialement contiennent des électrolytes inflammables (base solvantée), et donc non seulement elles stockent l'énergie « utilisable » stockée sous une forme électrochimique, mais elles stockent également de l'énergie chimique non fonctionnelle sous forme de matériaux combustibles. Par conséquent, lorsque les LIB ne fonctionnent pas correctement (en dehors des plages de fonctionnement autorisées par leurs fabricants, ou en raison de défauts des cellules), les énergies électrochimiques et chimiques à l'intérieur des cellules peuvent être involontairement libérées et ainsi conduire à des émissions incontrôlées de gaz et aérosols inflammables, et/ou provoquer des incendies ou même des explosions. Lors de ces incidents, la défaillance catastrophique la plus énergétique d'un système LIB est un emballement thermique consécutif à l'occurrence de réactions exothermiques qui s'enchaînent en cascade. Ceci est caractérisé par un déficit d'évacuation d'énergie par rapport à l'accumulation d'énergie dans les cellules sous l'action d'un stress d'origine thermique, mécanique ou électrique, conduisant à une surchauffe incontrôlable du système de batterie. Par conséquent, comprendre le plus précisément possible les causes et les processus de l'emballement thermique devient un enjeu crucial pour améliorer la sécurité des batteries au li-ion, perfectionner les outils la maîtrise des risques et augmenter leur fiabilité dans le temps.

La sécurité des batteries devient encore plus critique avec l'émergence de LIBs riches en Ni qui commencent à arriver sur le marché. Cette nouvelle génération de batteries présente une densité d'énergie particulièrement élevée et corrélativement contient des matières actives plus intrinsèquement réactives qui pourraient éventuellement conduire, en cas d'emballement thermique, à des événements plus catastrophiques que dans le cas de systèmes moins performants.

Selon la littérature récente, le vieillissement des cellules au li-ion a également un impact notable sur l'occurrence et les conséquences potentielles de l'emballement thermique tant redouté. Il est étroitement lié aux problèmes de sécurité inhérents aux batteries Li-ion. Plusieurs études ont

confirmé que le vieillissement (calendaire, par cyclage) provoquant un accroissement progressif de la SEI (*Solid Electrolyte Interphase*) semble jouer un rôle critique dans l'emballement thermique. Par ailleurs, dans le contexte de l'émergence de batteries Li-ion de plus grande capacité, notamment celles impliquant l'utilisation de matières actives cathodiques dopées en Ni, les dépôts de lithium métal (*lithium plating*) constituent un autre phénomène lié au vieillissement susceptible d'avoir un impact notable sur le comportement des cellules Li-ion et augmenter leur sensibilité à l'emballement thermique. Par conséquent, ces deux principaux mécanismes de vieillissement des batteries au Li-ion évoqués que sont la croissance SEI et le *Lithium plating* impactent clairement leur sécurité de fonctionnement.

Dans ce contexte, inspirée par les travaux menés dans un cadre collaboratif de long terme mené à l'initiative d'IFPEN, INERIS, LRCS (et de quelques autres organismes), ainsi que par les avancées obtenues par d'autres chercheurs, cette thèse vise à approfondir la compréhension et la modélisation de ce phénomène multiphysique complexe, mettant en scène le processus d'amorçage de l'emballement thermique à l'échelle de la cellule, lorsque qu'une réactivité potentiellement exacerbée des nouvelles technologies de LIBs riches en Ni est en jeu et en tenant compte du phénomène complexe et multiforme du vieillissement des cellules qui survient tout au long du cycle de vie. L'objectif in fine est de comprendre les clés du succès de batteries Li-ion à haute énergie intrinsèquement plus sûres pendant l'utilisation.

Stratégie de recherche et orientation scientifique

La méthodologie pour étudier l'emballement thermique des batteries au lithium dans cette thèse s'est structurée autour de 3 lots de travaux principaux (WP), combinant analyse de l'état de l'art, études expérimentales et développement de modèles d'emballement thermique :

- Le premier WP traite de l'étude de l'effet des technologies à haute densité d'énergie sur la sécurité : Matériaux d'électrode positive riches en Ni, associés avec une nouvelle technologie d'électrode négative : Composites S_xO_x -Graphite ;
- Le deuxième WP vise à comprendre les mécanismes sous-jacents et la relation entre le vieillissement calendaire et cyclique et la sécurité des LIBs en se concentrant sur 2 mécanismes de dégradation dus au vieillissement : l'évolution SEI en fonction de la température et du placage de Li (dans des conditions de basse température) ;
- Le WP final traite du développement d'un modèle 3D d'emballement thermique consolidé et de la mise en œuvre de protocoles de tests et d'outils de simulation numérique pour l'étalonnage et la validation du modèle.

Cette stratégie de recherche en trois étapes repose sur les réalisations de plusieurs projets achevés dans un passé récent et sur la combinaison et les synergies offertes par des études expérimentales et de modélisation combinées (Figure 1):

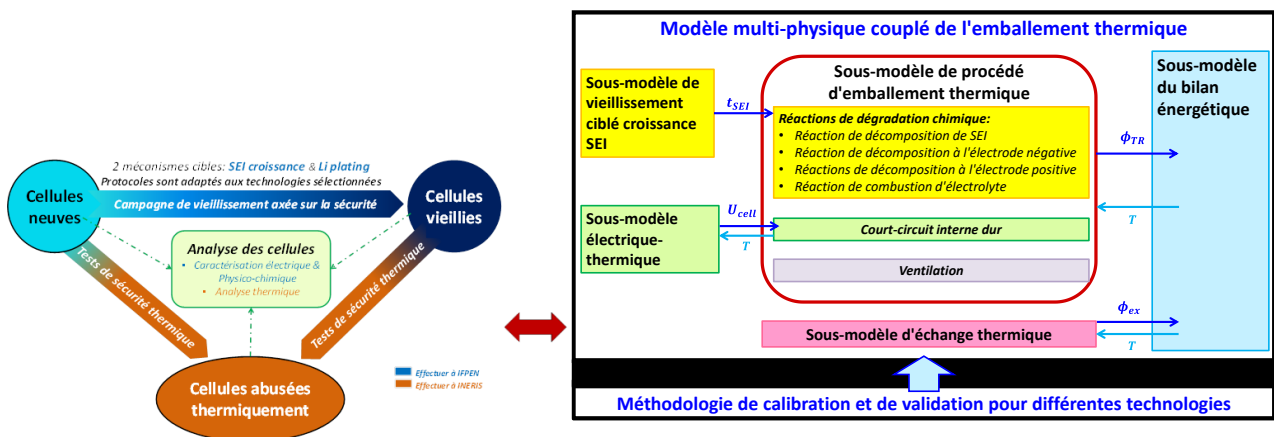


Figure 1: Illustration de la stratégie de recherche : Approches expérimentales (à gauche) combinées à des travaux de modélisation (à droite)

Etudes expérimentales visant une compréhension améliorée du phénomène d'emballement thermique des accumulateurs au lithium-ion neufs et usagés

Cet événement complexe implique des phénomènes multi-échelles allant de la physico-chimie interne aux réactions des divers composants de la batterie (électrodes, électrolytes et séparateur) et à la propagation thermique du noyau de la cellule et des dispositifs de sécurité (CID, PTC, système d'évent, ...) jusqu'à l'enveloppe externe.

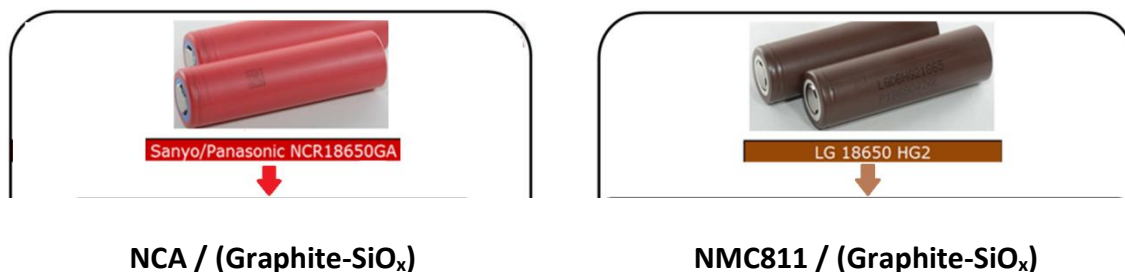


Figure 2 : les cellules au lithium-ion sélectionnées.

L'analyse multi-échelle des cellules a compris l'examen des cellules dans leurs états neufs, leurs états vieillis ainsi que leur comportement dans le cadre de situations provoquées de stress thermique (Deux technologies étudiées, cf. Figure 2). Concernant l'impact du vieillissement sur la sécurité des LIBs, une campagne d'essais a été réalisée à l'IFPEN pour vieillir artificiellement (de manière contrôlable et quantifiable) des échantillons de batteries, en ciblant deux mécanismes spécifiques du vieillissement, l'un se traduisant par une croissance de la SEI (vieillessement calendaire et par cyclage) et l'autre par des dépôts de Li Métal au niveau de l'anode (*Lithium plating*). Enfin, des tests d'analyse thermique du comportement des cellules neuves et vieilles ont été menés sur la plate-forme STEEVE de l'INERIS pour qualifier la résistance des batteries ainsi vieilles au phénomène d'emballement thermique (BTC, essais en étuve). Les compositions

d'électrodes positives et négatives ont été identifiées par des mesures semi-quantitatives SEM-EDX. Les résultats des analyses ont confirmé que les technologies sélectionnées pour la thèse sont des technologies riches en Ni, comme le montre la figure 2, ce qui est cohérent avec notre priorité de sélection.

Etude du vieillissement des cellules

Plusieurs tests préliminaires ont été réalisés pour définir une campagne complète de vieillissement axée sur la sécurité (Figure 3). Le protocole de vieillissement de type *Li plating* simule les conditions de cyclage à basse température qui accélèrent l'occurrence de dépôts indésirables de lithium métal et le protocole de vieillissement provoquant une augmentation de la SEI reproduit les conditions de stockage (vieillissement dit calendaire) et de cyclage (lié à l'utilisation) qui accélèrent l'évolution de SEI. Les protocoles ont été adaptés pour prendre en compte la spécificité des technologies étudiées et pour obtenir des résultats comparables de manière cohérente en termes de niveau identique de perte de capacité de décharge dans des délais raisonnables.

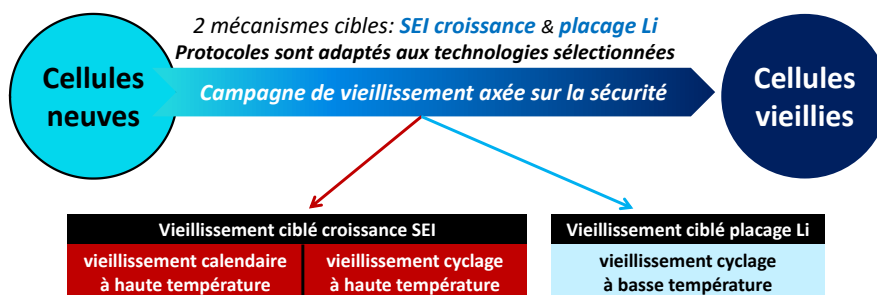


Figure 3 : Approche expérimentale de l'effet du vieillissement des cellules au lithium-ion : phénoménologies étudiées

La campagne de vieillissement a été menée avec succès pour les deux technologies étudiées. Les principaux résultats obtenus en termes de processus d'évanouissement de capacité et d'augmentation d'impédance de Panasonic NCR GA et LG HG2 sont présentés sur la figure 4.

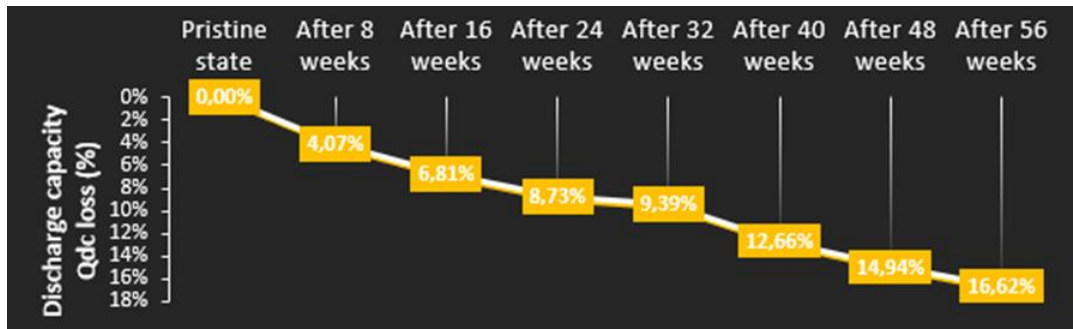


Figure 4 : Vieillesse liée à l'évolution de la SEI des cellules Panasonic 18650 GA : Perte de capacité à différents stades du vieillissement (évaluée via contrôle séquentiel de lots de 6 cellules).

Le vieillissement calendaire s'est produit très lentement pour les deux technologies. Cette observation confirme que ces technologies sélectionnées sont des produits de haute qualité, et homogènes : il existe une très faible variation de cellule à cellule dans les résultats du vieillissement calendaire.

Dans le cas de Panasonic NCR GA (Figure 5), les cellules ont subi avec succès le processus de vieillissement jusqu'à l'atteinte de la capacité résiduelle ultime visée. Après 56 semaines, nous avons obtenu un lot de cellules âgées avec des états connus et qui pourraient être utilisées pour étudier l'impact du vieillissement calendaire sur la sécurité. Dans le cas du LG HG2, après 40 semaines de vieillissement calendaire, certaines cellules ne sont révélées en défaut : tension résiduelle dans l'intervalle $[0 - 1]$ V. Cela pourrait être dû à la survenue de courts-circuits internes « doux » au cours du processus de vieillissement, peut-être en raison de la technologie « couche mince » du séparateur de LG HG2. Pour cette raison, les cellules Panasonic NCR GA (pour lesquelles ce constat n'a pas été observé) ont été privilégiées pour étudier l'impact du vieillissement calendaire des LIBs sur leur sécurité d'usage.

L'impact des différentes conditions de vieillissement (calendaire et par cyclage sur l'évolution de la SEI et des conséquences sur les performances de décharges) des cellules Panasonic NCR GA est clairement observé entre cellules neuves et vieilles comme illustré à la figure 5. Comme observé sur cette figure 5, même si les cellules âgées ont atteint le même niveau de vieillissement (perte de Qdc $\sim 16,5\%$), on constate aussi que ces cellules vieilles présentent des profils de décharge légèrement différents. Il est donc intéressant d'étudier cet impact sur l'emballage thermique.

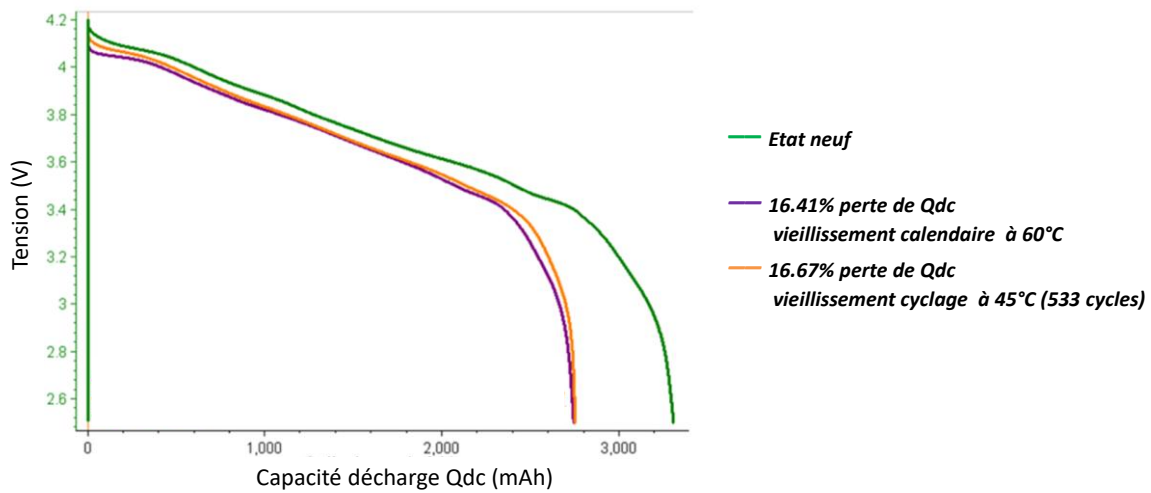


Figure 5: Comparaison des profils de décharge dus au vieillissement des cellules Panasonic NCR GA par effet calendaire ou de cyclage

Test d'échauffement dans Accelerated Rate Calorimeter

Le calorimètre BTC (*Accelerated Rate Calorimeter* ou ARC), conçu spécifiquement par son fabricant pour tester les batteries) disponible à l'INERIS a donc été utilisé pour étudier le comportement des batteries soumises à un stress thermique contrôlé pour observer et qualifier l'occurrence de l'emballement thermique en conditions pseudo-adiabatiques. Les tests ont été réalisés sur les deux technologies de LIBs riches en Ni sélectionnées, chargés à deux niveaux de SOC (100% et 50%) dans des états vierges (ARC). Comme observé sur la figure 6, l'emballement thermique des cellules neuves (à 100% SOC) de ces technologies riches en Ni sélectionnées se manifeste de manière abrupte.

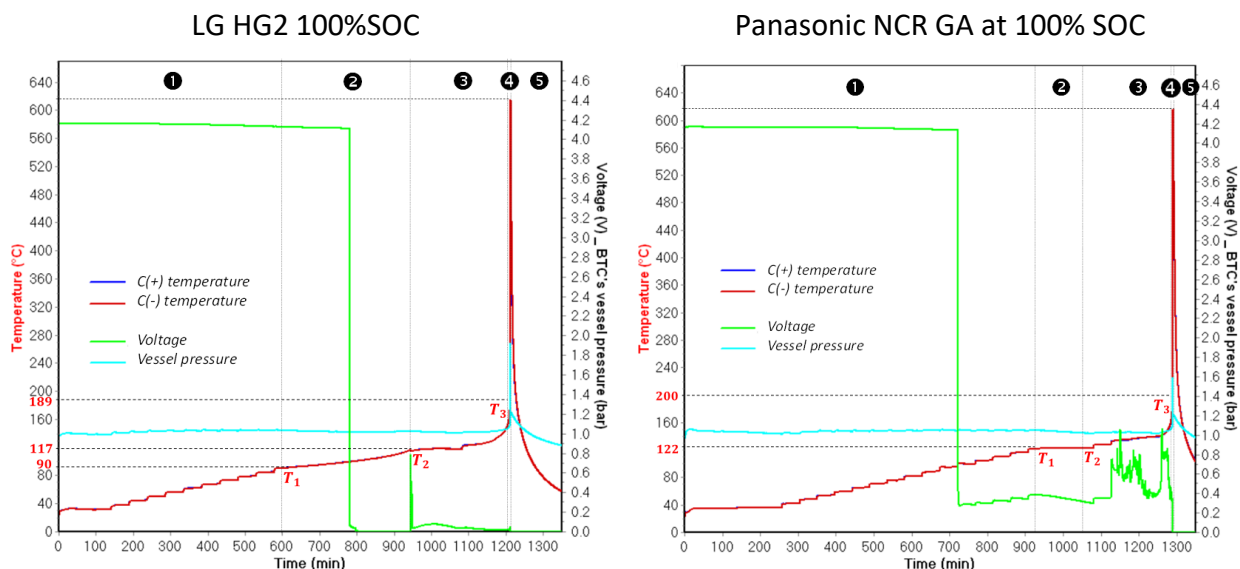


Figure 6 : Illustration des 5 changements d'états observables lors du processus de test abusif induit par "heat-wait-search" (HWS) des cellules LG HG2 et Panasonic NCR GA chargées à 100% SOC.

Trois seuils de température critique vis-à-vis de la sécurité des batteries étudiées sont en particulier identifiables lors du processus d'emballement thermique induit par l'essai abusif :

T₁ est la température correspondant au phénomène d'auto-échauffement initial détecté. La détection de T₁ dépend de la sensibilité de détection du dispositif de test pour la réaction exothermique, qui est sélectionnée dans le programme de test. Dans ce travail, la sensibilité de détection des réactions exothermiques est $\geq 0,03 \text{ }^\circ\text{C} / \text{min}$;

T₂ est la température rapportée à l'observation initiale de la réaction endothermique du processus de fusion du séparateur ;

T₃ est la température correspondant à l'accélération soudaine du taux de température due à la ventilation finale, indiquée par le taux de gazage le plus élevé et le court-circuit interne dur (ISC) après l'effondrement de la couche de céramique.

La figure 6 donne un exemple d'emballement thermique avec les 5 étapes indiquées. Sur la base de ces trois températures critiques, l'occurrence en cascade des réactions exothermiques menant à l'emballement thermique final permet de consolider cinq étapes distinctes dans l'évolution de la température de peau des cellules ainsi testées.

Les résultats obtenus, ont aussi permis une analyse des différents facteurs ayant un impact sur la cinétique d'emballement thermique. Ils ont en outre démontré la relation entre les caractéristiques de sécurité et l'état de charge (%SOC) avec les mécanismes d'éjection des composants associés au déclenchement du dispositif d'évent ». Les principaux enseignements sont les suivants :

(1) Pour tous les niveaux de SOC testés, l'auto-échauffement significatif initial de Panasonic NCR GA (chimie de la positive NCA) a toujours été détecté à une température plus élevée que celle de l'autre technologie LG HG2 (chimie de la positive NMC811). Par conséquent, la zone de sécurité de cette technologie est plus large que celle du LG HG2.

(2) En tant qu'élément critique en termes de sécurité, la technologie du séparateur a un impact significatif sur les étages d'auto-échauffement dans leur période réversible et sur le déclenchement de l'emballement thermique auto-accélééré. Ayant un séparateur 3 fois plus épais, la Panasonic NCR GA subit l'ouverture de l'évent et du court-circuit interne aux températures plus élevées comparativement à la Panasonic NCR GA.

(3) Indépendamment de l'état de charge (%SOC), le matériau de l'électrode positive influence fortement la gravité lors de la dernière étape de l'emballement thermique. La technologie NCA semble être plus réactive, avec un taux de température d'auto-échauffement plus élevé sur une durée plus longue. Cependant, l'éjection de gaz et aérosols lors du *venting* de la LG HG2 est la plus violente en raison de la décomposition

plus rapide des matériaux de l'électrode positive due à la technologie NMC811 par rapport à la technologie NCA.

(4) L'impact de l'état de charge (%SOC) sur l'emballage thermique a été observé de manière significative pour toutes les technologies riches en Ni sélectionnées. Nous avons constaté sans surprise que les cellules à SOC réduit (50%SOC) étaient moins réactives que les cellules à pleine charge(100%SOC).

Test d'échauffement libre sous loi de chauffe pilotée (test en étuve)

Dans cette autre approche expérimentale, les batteries sont sollicitées thermiquement en conditions de stress thermique davantage représentatives de situations réelles, du fait que les pertes thermiques ne sont pas « compensées » : l'essai est réalisé en étuve dont la loi de chauffe est programmable. Ce type d'essai a été utilisé en complément des essais d'emballage thermique précédents menés en conditions pseudo-adiabatiques notamment pour fournir des données de calibration du modèle d'emballage thermique. Ces tests ont été effectués à la fois pour les cellules neuves et les cellules vieilles, pour valider d'une part le modèle et d'autre part consolider l'analyse des impacts du vieillissement sur l'emballage thermique.

L'évolution de la température de deux cellules testées LG HG2 à l'état neuf est présentée à la figure 7 en comparaison avec les résultats des deux cellules GA Panasonic NCR testées dans les mêmes conditions (état neuf). Nous avons observé que l'emballage thermique des deux cellules LG HG2 s'est produit plus tôt que dans le cas des cellules Panasonic NCR GA. Ces résultats sont cohérents avec les résultats des tests en ARC (HWS). De plus, le dégazage des cellules vierges LG HG2 par ouverture de l'évent s'est produit plus tard et à une température plus élevée que dans le cas des cellules neuves Panasonic NCR GA.

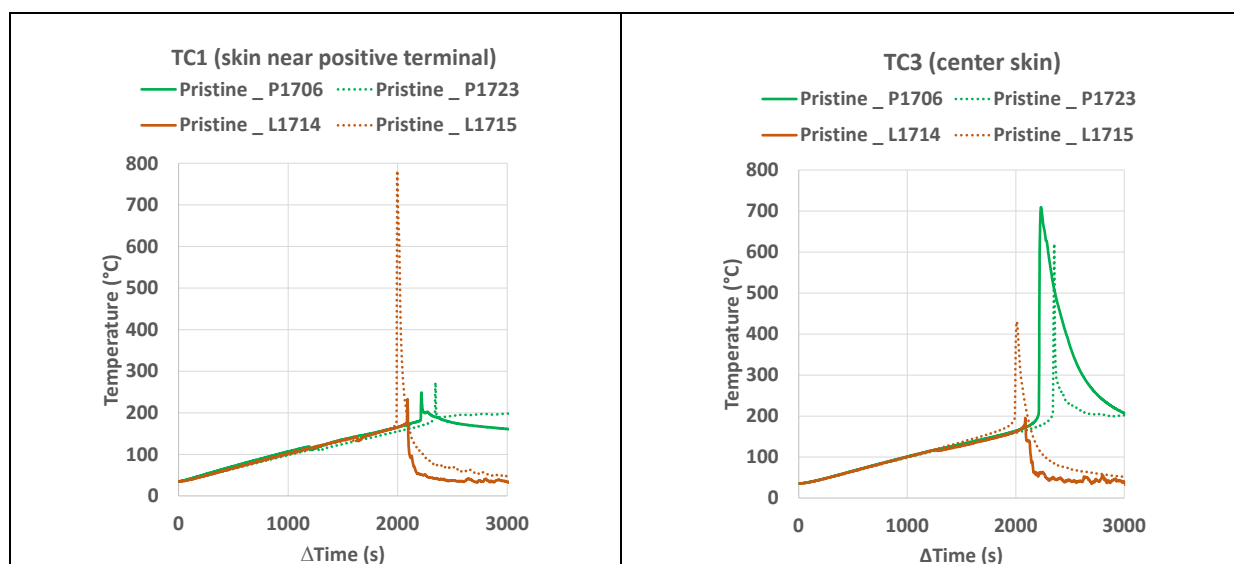


Figure 7 : Évolution de la température des TC distribués à la surface des cellules testées LG HG2 (marron) et Panasonic NCR GA (vertes)..

Nous avons également effectué des tests en étuve sur les deux cellules Panasonic NCR GA ayant subi pour l'une un vieillissement de type calendaire et pour l'autre un vieillissement par cyclage avec un même niveau de vieillissement in fine (~ 16% de perte de capacité de décharge). L'emballage thermique s'est produit pour toutes les cellules testées. Nous avons observé un gonflement de toutes les cellules (augmentation du diamètre apparent) et la perte de masse constatée après emballage est plus importante dans le cas des cellules vieilles. Cela peut être attribué à une éjection de matières plus importante lors du dégazage par l'événement dans le cas des cellules vieilles. Par ailleurs, l'emballage thermique des deux cellules vieilles est retardé par rapport à l'occurrence de celui de la cellule neuve de référence, comme on le voit dans le tableau 1. De plus, le dégazage de la cellule vieillie par cyclage s'est révélé plus tardif que dans le cas de la cellule ayant subi un vieillissement de type calendaire.

Table 54: Occurrence times and critical temperature of Panasonic NCR GA tested cells.

Panasonic NCR GA	tTvent (s)	Tvent (°C)	tT3 (s)	T3 (°C)
Cellule neuve	1214	111	2211	196
Cellule ayant subi un vieillissement calendaire	1519	129	2307	199
Cellule ayant subi un vieillissement par cyclage	1801	144	2329	198

Construction et calibration du modèle

La construction du modèle 3D étendu d'emballage thermique comprend un modèle électrochimique-thermique, γ compris 3 sous-modèles couplés dont i) un sous-modèle électrothermique, ii) un sous-modèle de processus d'emballage thermique et iii) un sous-modèle de bilan énergétique, comme illustré à la figure 8.

Dans le sous-modèle de processus d'emballage thermique sont intégrées les quatre réactions principales de dégradation exothermique reprises du modèle 3D d'emballage thermique de la batterie Li-ion développé par Kim et al. et pour lesquelles les paramètres sous-jacents avaient été calibrés pour la technologie LFP / Graphite dans le cadre des travaux menés par Abada et al. Ces réactions intégrées dans le modèle sont :

1. Décomposition de la SEI
2. Réaction de décomposition entre le lithium intercalé et le solvant de l'électrolyte au niveau de l'électrode négative (formation de SEI)
3. Réactions de décomposition à l'électrode positive
4. Réaction de combustion d'électrolyte

Ce sous-modèle a été étendu dans cette thèse, en ajoutant de nouveaux phénomènes (5), (6) ci-dessous afin de tenir compte respectivement : i) des courts-circuits internes, ii) du dégazage des cellules lithium-ion (cf figure 8) :

5. Court-circuit interne franc (ISC)

6. Venting

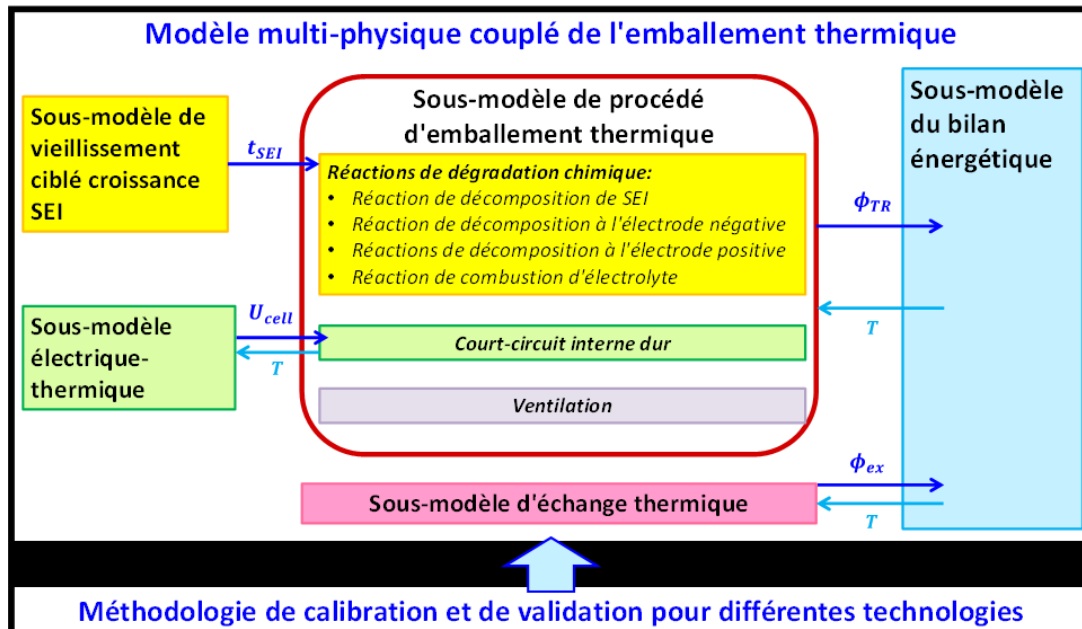


Figure 8 : Modèle d'emballage thermique avec ses couplages multiphysiques

Le modèle d'emballage thermique est calibré sur la base des tests HWS en BTC. Par conséquent, un sous-modèle d'échange thermique est introduit pour faire face aux difficultés pratiques de maintien de la condition pseudo-adiabatique pendant les tests d'abus thermique dans le système ARC du BTC : En effet, une réponse thermique anormale du BTC a été observée et a conduit à constater un défaut rémanent d'adiabaticité lors des tests HWS, ce qui donne ses résultats bruts lors de l'essai en BTC s'écartant sensiblement des conditions de pseudo-adiabaticité recherchées. Ce sous-modèle a donc été conçu pour « compenser » cet écart d'adiabaticité observée et permettre une utilisation cohérente des résultats des tests malgré les difficultés rencontrées.

L'intégration du vieillissement associé à l'accroissement de la SEI basé sur le modèle électrochimique simplifié développé au sein d'IFPEN, a également été rajoutée. Ce sous-modèle permet d'étudier l'influence du vieillissement sur l'emballage thermique (hors lithium plating)

Le modèle d'emballage thermique a été développé sur la plate-forme logicielle COMSOL Multiphysics, comme illustré à la figure 9.

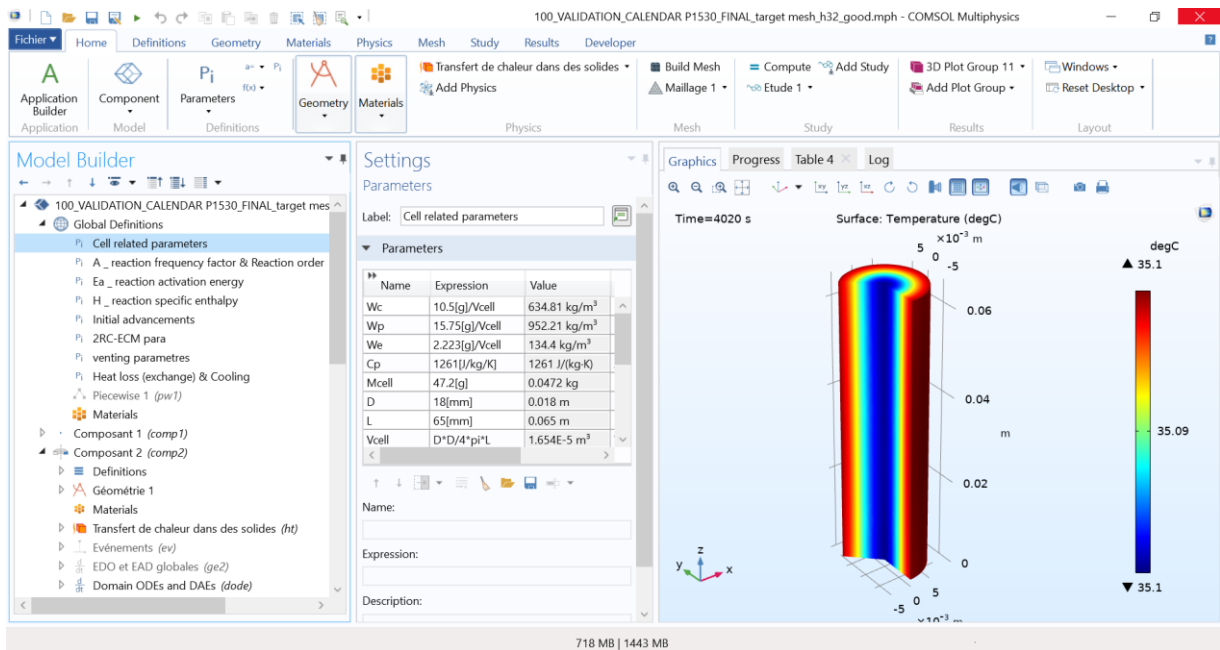


Figure 9 : Outil de simulation numérique pour la calibration et la validation du modèle

Les résultats d'étalonnage globaux basés sur les tests HWS des chimies NMC811 / Graphite-SiOx (LG HG2) et NCA / Graphite-SiOx (Panasonic NCR GA) sont présentés à la figure 10.

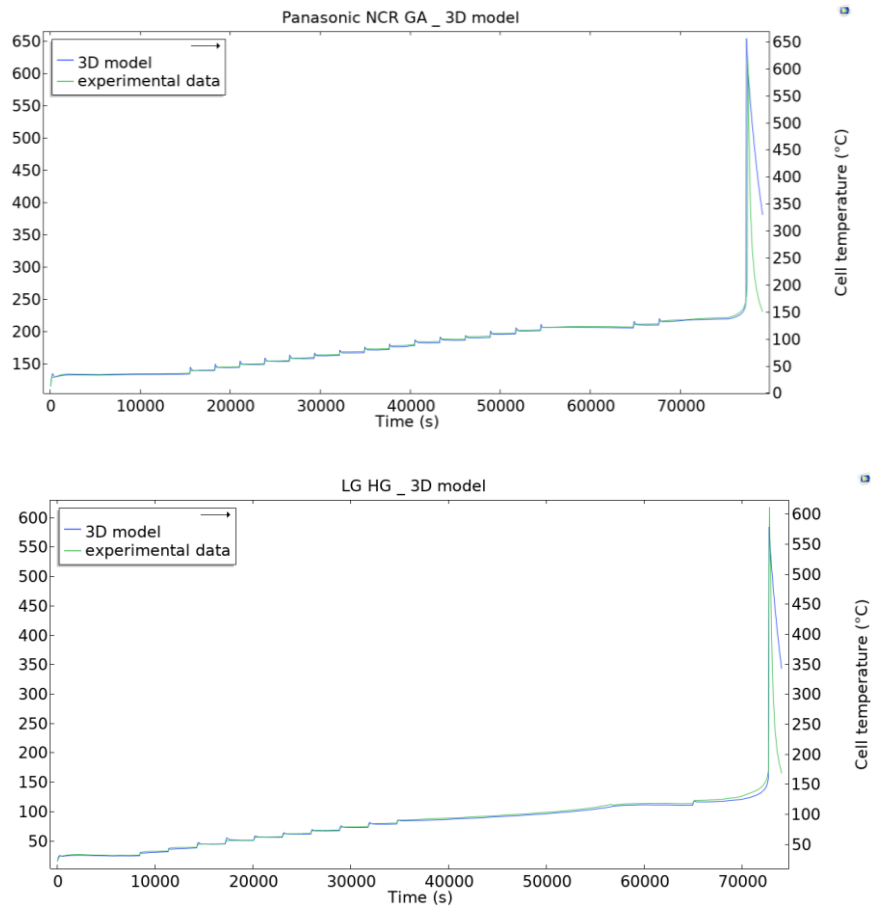


Figure 10 : Calibration des cellules Panasonic NCR GA (au-dessus) and LG HG2 (en dessous)

Démarches de validation du modèle et utilisation prospective

Tout d'abord, nous nous sommes concentrés sur la validation du modèle d'emballage thermique développé à l'échelle de la cellule, tel que calibré avec des paramètres impliquant les caractéristiques spécifiques des chimies riches en Ni des deux technologies sélectionnées, sur la base de la comparaison avec les données expérimentales des tests en étuve.

La figure 11 montre l'évolution temporelle de la température moyenne de peau lors de l'essai en étuve, évaluée pour la cellule P1706 Panasonic NCR GA neuve à partir des réponses individuelles des 4 TC positionnés en surface de la cellule à cet effet et pour comparaison l'évolution temporelle de la température moyenne de peau obtenue à partir du modèle 3D. La température critique T_3 , la température maximale atteinte T_{max} et les temps correspondant à ces températures critiques ont été identifiés. Le modèle donne des résultats satisfaisants en termes de température critique T_3 et de température cutanée moyenne maximale atteinte, au regard des faibles différences de $3,7\text{ °C}$ (-1,9%) et $4,8\text{ °C}$ (-0,9%), respectivement pour T_3 et T_{max} . Cependant, le modèle prédit trop précocement le moment de l'emballage thermique accéléré (135 s à l'avance) par rapport au temps de déclenchement réel de ce processus d'emballage thermique accélérée tel que constaté dans l'essai en étuve. Ce décalage est attribué aux paramètres cinétiques de la réaction de décomposition d'électrode positive et de la réaction d'électrolyte intégrés actuellement dans le modèle.

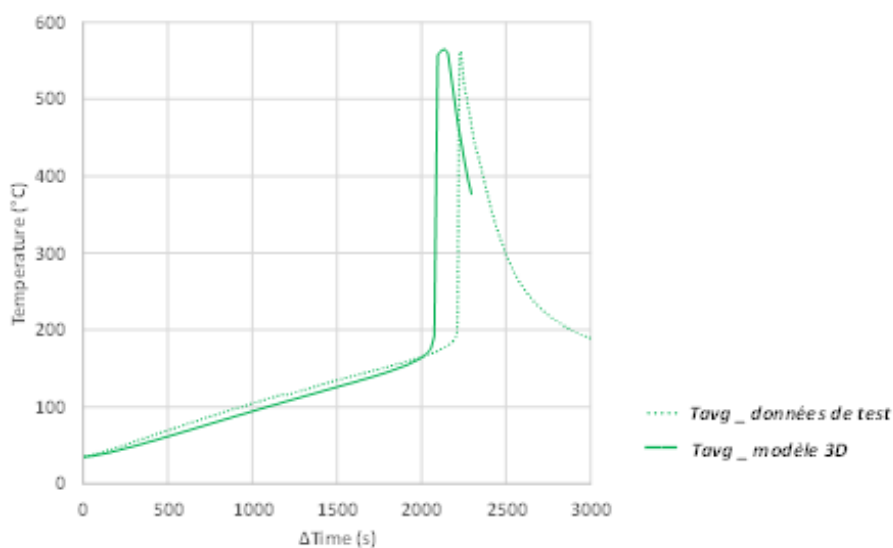


Figure 11 : Evolution de la température moyenne de peau lors du test en étuve comparée aux résultats de simulation.

Après validation, grâce à cet outil de simulation de l'essai en étuve, Une étude paramétrique a permis d'étudier l'impact du niveau de SOC sur l'emballage thermique. Les résultats obtenus avec le modèle sont sur ce plan cohérents avec les résultats des tests HWS ainsi qu'avec les résultats publiés dans la littérature : ils ont confirmé que la sécurité des LIBs augmente avec la

diminution de l'état de charge (%SOC). Le moment d'emballage thermique accéléré s'est produit à une température plus élevée dans le cas des cellules à SOC réduits.

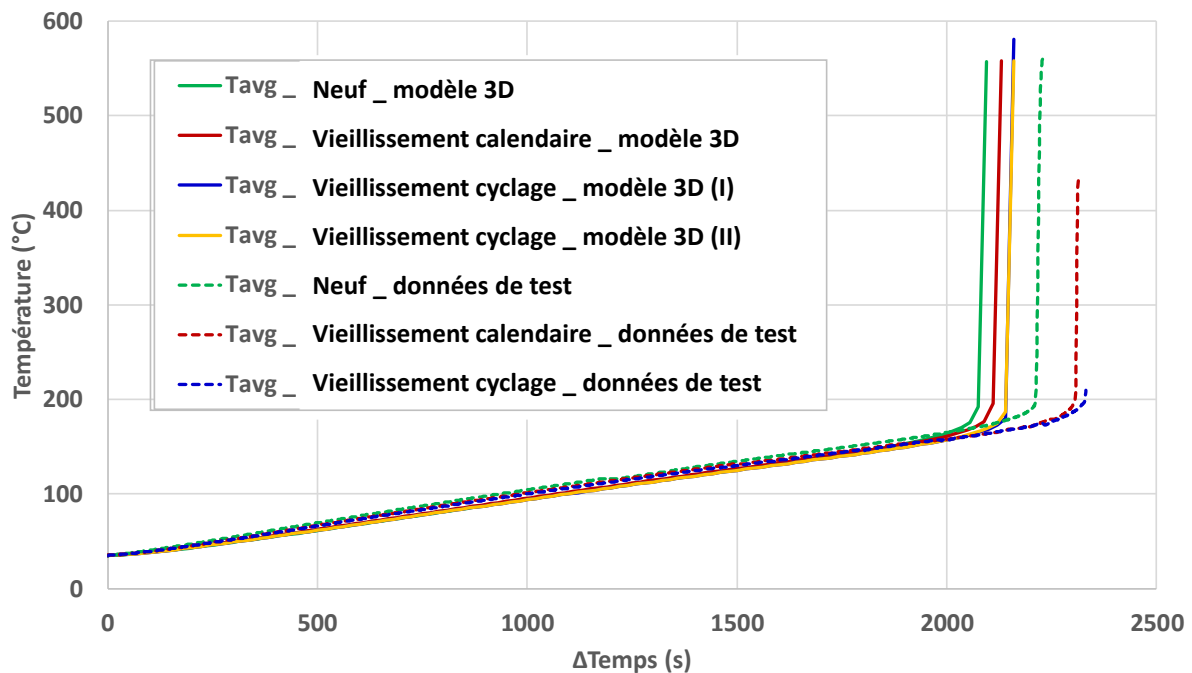


Figure 12 : Evolutions comparées (tests en étuve/simulations numériques) de la température moyenne de peau de cellules Panasonic a) neuve 100% SOC, b) après vieillissement calendaire 100% SOC et c) après vieillissement par cyclage 100% SOC

Par ailleurs, moyennant des hypothèses fortes conditionnant la possibilité d'études paramétriques intéressantes, nous avons pu étudier l'impact de l'épaisseur de la SEI dû au vieillissement calendaire, ainsi que ceux de différents scénarios de vieillissement cyclique correspondant impactant la qualité du SEI. La figure 12 montre quelques résultats de ces dernière études paramétriques comparant tests et simulations numériques

Le modèle 3D a prédit le moment de l'emballage thermique accéléré ($t_{(T_3)}$) de manière relativement trop précoce par rapports aux données d'essais en étuve dans les trois cas (135s trop tôt (soit un écart relatif de -6,1%) pour la cellule neuve, 197s trop tôt (soit un écart relatif de (8,5%) pour la cellule ayant subi un vieillissement calendaire et 188s trop précocement (soit - 8%) pour le cas de la cellule vieillie par cyclage). Ces décalages observés sont vraisemblablement liés aux valeurs attribuées aux paramètres cinétiques du modèle de la réaction de décomposition d'électrode positive et de la réaction électrolytique, lesquelles sont déclenchées à des températures trop basses (120 - 123 ° C et 139 ° C, respectivement) pour toutes les cellules indépendamment de leur état de vieillissement par rapport à la réalité observées dans les tests en étuve. Un dernier résultat observé lors de nos simulations est qu'à vieillissement donné, le vieillissement de type calendaire est plus préjudiciable que le vieillissement par cyclage, en termes de robustesse par rapport au risque d'emballage thermique.

Conclusion et perspectives

Les résultats expérimentaux et de simulation contribuent à la compréhension et à la découverte des facteurs clés qui peuvent améliorer la sécurité de ces batteries Li-ion hautement réactives et à l'étalonnage et la validation du modèle.

Ce modèle développé est capable de prédire le évolution de température, le court-circuit franc (ISC) et enfin le venting pendant l'emballement thermique de batteries Li-ion. Il améliore et étend le modèle initial d'emballement thermique précédemment construit à IFPEN en intégrant l'impact du vieillissement cyclique lié au SOC et à la SEI. Le modèle développé peut être mis en œuvre pour comprendre l'amorçage électrique ou thermique du phénomène d'emballement thermique.

Enfin, ce modèle permet d'explorer davantage de scénarios de cellules subissant un processus d'emballement thermique dans des conditions spécifiées pour lesquelles un paramétrage adéquat peut être défini en relation avec la physique sous-jacente.

Ce travail de thèse a in fine constitué une nouvelle étape dans le développement de modèles adaptés à la réflexion « sécurité », des outils dont le recours devient incontournable dans tout projet innovant de développement de nouveaux systèmes de stockage d'énergie pour lesquels la technologie Li-ion et ses futures variantes restent le choix le plus souvent privilégié.

References

- 1 Myung S.-T., Maglia F., Park K.-J., Yoon C.S., Lamp P., Kim S.-J., Sun Y.-K. (2017) Nickel-Rich Layered Cathode Materials for Automotive Lithium-Ion Batteries: Achievements and Perspectives, *ACS Energy Lett.* **2**, 1, 196–223. DOI: 10.1021/acseenergylett.6b00594.
- 2 Thaler A., Watzenig D. (eds.) (2014) *Automotive battery technology*, Springer, Cham New York. ISBN: 978-3-319-02522-3.
- 3 Feng X., Ouyang M., Liu X., Lu L., Xia Y., He X. (2018) Thermal runaway mechanism of lithium ion battery for electric vehicles: A review, *Energy Storage Materials* **10**, 246–267. DOI: 10.1016/j.ensm.2017.05.013.
- 4 Celina Mikolajczak, Michael Kahn, Kevin White, Richard Thomas Long (2013) *Lithium-Ion Batteries Hazard and Use Assessment: Fire Protection Research Foundation*, Springer.
- 5 Galushkin N.E., Yazvinskaya N.N., Galushkin D.N. (2018) Mechanism of Thermal Runaway in Lithium-Ion Cells, *J. Electrochem. Soc.* **165**, 7, A1303-A1308. DOI: 10.1149/2.0611807jes.
- 6 FAA Office of Security and Hazardous Materials Safety (2017) *Aviation Cargo and Passenger Baggage Events Involving Smoke, Fire, Extreme Heat or Explosion Involving Lithium Batteries or Unknown Battery Types*.
- 7 FAA Office of Security and Hazardous Materials Safety (2020) *Events With Smoke, Fire, Extreme Heat Or Explosion Involving Lithium Batteries*.
- 8 Doughty D.H., Roth E.P. (2012) A General Discussion of Li Ion Battery Safety, *Interface magazine* **21**, 2, 37–44. DOI: 10.1149/2.F03122if.
- 9 Waldmann T., Wohlfahrt-Mehrens M. (2017) Effects of rest time after Li plating on safety behavior—ARC tests with commercial high-energy 18650 Li-ion cells, *Electrochimica Acta* **230**, 454–460. DOI: 10.1016/j.electacta.2017.02.036.
- 10 Waldmann T., Hogg B.-I., Wohlfahrt-Mehrens M. (2018) Li plating as unwanted side reaction in commercial Li-ion cells – A review, *Journal of Power Sources* **384**, 107–124. DOI: 10.1016/j.jpowsour.2018.02.063.
- 11 Xuning Feng, Minggao Ouyang, Xiang Liu, Languang Lu, Yong Xia, Xiangming He (2018) Thermal runaway mechanism of lithium ion battery for electric vehicles_ A review, *Journal of Power Sources* **10**, 246-267. DOI: 10.1016/j.ensm.2017.05.013.
- 12 Doughty D.H., Roth E.P. (2012) A General Discussion of Li Ion Battery Safety, *Interface magazine* **21**, 2, 37–44. DOI: 10.1149/2.F03122if.

- 13 Petit M, Marlair G, Abada S, Wang C-Y (2019) *Safety tests for Li-secondary batteries-Modeling of safety tests and events: Chapter 10B in Electrochemical Power Sources: Fundamentals, Systems and Applications - Li-Battery safety (Eds.: J. Garche & K Brandt)*, Elsevier.
- 14 Jaguemont J., Boulon L., Dubé Y. (2016) A comprehensive review of lithium-ion batteries used in hybrid and electric vehicles at cold temperatures, *Applied Energy* **164**, 99–114. DOI: 10.1016/j.apenergy.2015.11.034.
- 15 M. C. Smart, L. D. Whitcanack (2007) Safe Charge Rates for Lithium ion cells. Effects of Li Plating, *NASA Battery workshop*.
- 16 Abada S., Petit M., Lecocq A., Marlair G., Sauvant-Moynot V., Huet F. (2018) Combined experimental and modeling approaches of the thermal runaway of fresh and aged lithium-ion batteries, *Journal of Power Sources* **399**, 264–273. DOI: 10.1016/j.jpowsour.2018.07.094.
- 17 Abada S., Marlair G., Lecocq A., Petit M., Sauvant-Moynot V., Huet F. (2016) Safety focused modeling of lithium-ion batteries: A review, *Journal of Power Sources* **306**, 178–192. DOI: 10.1016/j.jpowsour.2015.11.100.
- 18 Said M., Tohir M. (2019) Prediction of Lithium-ion Battery Thermal Runaway Propagation for Large Scale Applications Fire Hazard Quantification, *Processes* **7**, 10, 703. DOI: 10.3390/pr7100703.
- 19 Golubkov A.W., Scheikl S., Planteu R., Voitic G., Wiltsche H., Stangl C., Fauler G., Thaler A., Hacker V. (2015) Thermal runaway of commercial 18650 Li-ion batteries with LFP and NCA cathodes – impact of state of charge and overcharge, *RSC Adv.* **5**, 70, 57171–57186. DOI: 10.1039/C5RA05897J.
- 20 Benger R, Wenzl H, Beck H-P, Jiang M, Ohms D, Schaedlich G (2009) Electrochemical and thermal modeling of Lithium-ion cells for use in HEV and EV application, *WEVJ* **3**, 342–351.
- 21 Ouyang D., Chen M., Huang Q., Weng J., Wang Z., Wang J. (2019) A Review on the Thermal Hazards of the Lithium-Ion Battery and the Corresponding Countermeasures, *Applied Sciences* **9**, 12, 2483. DOI: 10.3390/app9122483.
- 22 Liao Z., Zhang S., Li K., Zhang G., Habetler T.G. (2019) A survey of methods for monitoring and detecting thermal runaway of lithium-ion batteries, *Journal of Power Sources* **436**, 226879. DOI: 10.1016/j.jpowsour.2019.226879.
- 23 Placke T., Kloepsch R., Dühnen S., Winter M. (2017) Lithium ion, lithium metal, and alternative rechargeable battery technologies: The odyssey for high energy density, *J Solid State Electrochem* **21**, 7, 1939–1964. DOI: 10.1007/s10008-017-3610-7.
- 24 B. Dandurand, P. Guarneri, G. Fadel, M.M. Wiecek (2013) Equitable multiobjective optimization applied to the design of a hybrid electric vehicle battery, *Journal of Mechanical Design* **135(4)**.
- 25 Forestier C., Lecocq A., Zantman A., Grugeon S., Sannier L., Marlair G., Laruelle S. (2020) Study of the Role of LiNi 1/3 Mn 1/3 Co 1/3 O 2 /Graphite Li-Ion Pouch Cells Confinement, Electrolyte

Composition and Separator Coating on Thermal Runaway and Off-Gas Toxicity, *J. Electrochem. Soc.* **167**, 9, 90513. DOI: 10.1149/1945-7111/ab829e.

- 26 Mario Watchtler (2016) Anode Materials presentation, Zentrum für Sonnenenergie und Wasserstoff-Forschung Baden-Württemberg, Stuttgart, Germany.
- 27 Huang P., Wang Q., Li K., Ping P., Sun J. (2015) The combustion behavior of large scale lithium titanate battery, *Scientific reports* **5**, 7788. DOI: 10.1038/srep07788.
- 28 Ma D., Cao Z., Hu A. (2014) Si-Based Anode Materials for Li-Ion Batteries: A Mini Review, *Nano-micro letters* **6**, 4, 347–358. DOI: 10.1007/s40820-014-0008-2.
- 29 Mou H., Xiao W., Miao C., Li R., Yu L. (2020) Tin and Tin Compound Materials as Anodes in Lithium-Ion and Sodium-Ion Batteries: A Review, *Frontiers in chemistry* **8**, 141. DOI: 10.3389/fchem.2020.00141.
- 30 Nitta N., Wu F., Lee J.T., Yushin G. (2015) Li-ion battery materials: Present and future, *Materials Today* **18**, 5, 252–264. DOI: 10.1016/j.mattod.2014.10.040.
- 31 Goriparti S., Miele E., Angelis F. de, Di Fabrizio E., Proietti Zaccaria R., Capiglia C. (2014) Review on recent progress of nanostructured anode materials for Li-ion batteries, *Journal of Power Sources* **257**, 421–443. DOI: 10.1016/j.jpowsour.2013.11.103.
- 32 Wang R., Feng L., Yang W., Zhang Y., Zhang Y., Bai W., Liu B., Zhang W., Chuan Y., Zheng Z., Guan H. (2017) Effect of Different Binders on the Electrochemical Performance of Metal Oxide Anode for Lithium-Ion Batteries, *Nanoscale research letters* **12**, 1, 575. DOI: 10.1186/s11671-017-2348-6.
- 33 Yen J.-P., Chang C.-C., Lin Y.-R., Shen S.-T., Hong J.-L. (2013) Effects of Styrene-Butadiene Rubber/Carboxymethylcellulose (SBR/CMC) and Polyvinylidene Difluoride (PVDF) Binders on Low Temperature Lithium Ion Batteries, *J. Electrochem. Soc.* **160**, 10, A1811-A1818. DOI: 10.1149/2.083310jes.
- 34 Pritesh Parikh M.S. Role of Polyacrylic Acid (PAA) Binder on the Solid Electrolyte Interphase in Silicon Anodes (2019) *Chem. Mater.* **31**, 7, 2535–2544. DOI: 10.1021/acs.chemmater.8b05020.
- 35 Hein S., Danner T., Westhoff D., Prifling B., Scurtu R., Kremer L., Hoffmann A., Hilger A., Osenberg M., Manke I., Wohlfahrt-Mehrens M., Schmidt V., Latz A. (2020) Influence of Conductive Additives and Binder on the Impedance of Lithium-Ion Battery Electrodes: Effect of Morphology, *J. Electrochem. Soc.* **167**, 1, 13546. DOI: 10.1149/1945-7111/ab6b1d.
- 36 Kim U.-H., Kim J.-H., Hwang J.-Y., Ryu H.-H., Yoon C.S., Sun Y.-K. (2019) Compositionally and structurally redesigned high-energy Ni-rich layered cathode for next-generation lithium batteries, *Materials Today* **23**, 26–36. DOI: 10.1016/j.mattod.2018.12.004.
- 37 Kim U.-H., Kuo L.-Y., Kaghazchi P., Yoon C.S., Sun Y.-K. (2019) Quaternary Layered Ni-Rich NCMA Cathode for Lithium-Ion Batteries, *ACS Energy Lett.* **4**, 2, 576–582. DOI: 10.1021/acsenergylett.8b02499.

- 38 van Nguyen A., Kuss C. (2020) Review—Conducting Polymer-Based Binders for Lithium-Ion Batteries and Beyond, *J. Electrochem. Soc.* **167**, 6, 65501. DOI: 10.1149/1945-7111/ab856b.
- 39 Eshetu G.G., Grugeon S., Laruelle S., Boyanov S., Lecocq A., Bertrand J.-P., Marlair G. (2013) In-depth safety-focused analysis of solvents used in electrolytes for large scale lithium ion batteries, *Physical chemistry chemical physics : PCCP* **15**, 23, 9145–9155. DOI: 10.1039/c3cp51315g.
- 40 Eshetu G.G., Bertrand J.-P., Lecocq A., Grugeon S., Laruelle S., Armand M., Marlair G. (2014) Fire behavior of carbonates-based electrolytes used in Li-ion rechargeable batteries with a focus on the role of the LiPF₆ and LiFSI salts, *Journal of Power Sources* **269**, 804–811. DOI: 10.1016/j.jpowsour.2014.07.065.
- 41 Kalhoff J., Eshetu G.G., Bresser D., Passerini S. (2015) Safer Electrolytes for Lithium-Ion Batteries: State of the Art and Perspectives, *ChemSusChem* **8**, 13, 2154–2175. DOI: 10.1002/cssc.201500284.
- 42 Ghiji M., Novozhilov V., Moinuddin K., Joseph P., Burch I., Suendermann B., Gamble G. (2020) A Review of Lithium-Ion Battery Fire Suppression, *Energies* **13**, 19, 5117. DOI: 10.3390/en13195117.
- 43 Ouyang D., Chen M., Huang Q., Weng J., Wang Z., Wang J. (2019) A Review on the Thermal Hazards of the Lithium-Ion Battery and the Corresponding Countermeasures, *Applied Sciences* **9**, 12, 2483. DOI: 10.3390/app9122483.
- 44 Wang J., Yamada Y., Sodeyama K., Watanabe E., Takada K., Tateyama Y., Yamada A. (2018) Fire-extinguishing organic electrolytes for safe batteries, *Nat Energy* **3**, 1, 22–29. DOI: 10.1038/s41560-017-0033-8.
- 45 Zeng G., An Y., Xiong S., Feng J. (2019) Nonflammable Fluorinated Carbonate Electrolyte with High Salt-to-Solvent Ratios Enables Stable Silicon-Based Anode for Next-Generation Lithium-Ion Batteries, *ACS applied materials & interfaces* **11**, 26, 23229–23235. DOI: 10.1021/acsami.9b05570.
- 46 Zhang Z., Hu L., Wu H., Weng W., Koh M., Redfern P.C., Curtiss L.A., Amine K. (2013) Fluorinated electrolytes for 5 V lithium-ion battery chemistry, *Energy Environ. Sci.* **6**, 6, 1806. DOI: 10.1039/C3EE24414H.
- 47 Jankowski P., Wieczorek W., Johansson P. (2017) SEI-forming electrolyte additives for lithium-ion batteries: Development and benchmarking of computational approaches, *Journal of molecular modeling* **23**, 1, 6. DOI: 10.1007/s00894-016-3180-0.
- 48 Hyung Y.E., Vissers D.R., Amine K. (2003) Flame-retardant additives for lithium-ion batteries, *Journal of Power Sources* **119-121**, 383–387. DOI: 10.1016/S0378-7753(03)00225-8.
- 49 Xia L., Wang D., Yang H., Cao Y., Ai X. (2012) An electrolyte additive for thermal shutdown protection of Li-ion batteries, *Electrochemistry Communications* **25**, 98–100. DOI: 10.1016/j.elecom.2012.09.038.

- 50 Arora P., Zhang Z. (2004) Battery Separators, *Chem. Rev.* **104**, 10, 4419–4462. DOI: 10.1021/cr020738u.
- 51 Feng X., Fang M., He X., Ouyang M., Lu L., Wang H., Zhang M. (2014) Thermal runaway features of large format prismatic lithium ion battery using extended volume accelerating rate calorimetry, *Journal of Power Sources* **255**, 294–301. DOI: 10.1016/j.jpowsour.2014.01.005.
- 52 Jeong H.-S., Kim D.-W., Jeong Y.U., Lee S.-Y. (2010) Effect of phase inversion on microporous structure development of Al₂O₃/poly(vinylidene fluoride-hexafluoropropylene)-based ceramic composite separators for lithium-ion batteries, *Journal of Power Sources* **195**, 18, 6116–6121. DOI: 10.1016/j.jpowsour.2009.10.085.
- 53 Peled E., Menkin S. (2017) Review—SEI: Past, Present and Future, *J. Electrochem. Soc.* **164**, 7, A1703-A1719. DOI: 10.1149/2.1441707jes.
- 54 An S.J., Li J., Du Z., Daniel C., Wood D.L. (2017) Fast formation cycling for lithium ion batteries, *Journal of Power Sources* **342**, 846–852. DOI: 10.1016/j.jpowsour.2017.01.011.
- 55 Kai Liu, Yayuan Liu, Dingchang Lin, Allen Pei, Yi Cui (2019) Materials for lithium-ion battery safety, *Sci Adv* **4** (6), eaas9820. DOI: 10.1126/sciadv.aas9820.
- 56 An S.J., Li J., Daniel C., Mohanty D., Nagpure S., Wood D.L. (2016) The state of understanding of the lithium-ion-battery graphite solid electrolyte interphase (SEI) and its relationship to formation cycling, *Carbon* **105**, 52–76. DOI: 10.1016/j.carbon.2016.04.008.
- 57 Zhang H.-L., Li F., Liu C., Tan J., Cheng H.-M. (2005) New insight into the solid electrolyte interphase with use of a focused ion beam, *The journal of physical chemistry. B* **109**, 47, 22205–22211. DOI: 10.1021/jp053311a.
- 58 Aurbach D. (2000) Review of selected electrode–solution interactions which determine the performance of Li and Li ion batteries, *Journal of Power Sources* **89**, 2, 206–218. DOI: 10.1016/S0378-7753(00)00431-6.
- 59 Kominato A., Yasukawa E., Sato N., Ijuuin T., Asahina H., Mori S. (1997) Analysis of surface films on lithium in various organic electrolytes, *Journal of Power Sources* **68**, 2, 471–475. DOI: 10.1016/S0378-7753(97)02592-5.
- 60 Augustsson A., Herstedt M., Guo J.-H., Edström K., Zhuang G.V., Ross J.P.N., Rubensson J.-E., Nordgren J. (2004) Solid electrolyte interphase on graphite Li-ion battery anodes studied by soft X-ray spectroscopy, *Phys. Chem. Chem. Phys.* **6**, 16, 4185–4189. DOI: 10.1039/B313434B.
- 61 Stocker Richard, Asim Mumtaz, Neophytos Lophitis (2016) Understanding Ageing in Li-ion Cells: An Enabler for Effective Grid Interaction Strategies: Poster, Conference: Manchester Electrical Energy and Power Systems (MEEPS), Manchester.
- 62 Liao Z., Zhang S., Li K., Zhang G., Habetler T.G. (2019) A survey of methods for monitoring and detecting thermal runaway of lithium-ion batteries, *Journal of Power Sources* **436**, 226879. DOI: 10.1016/j.jpowsour.2019.226879.

- 63 Kimberly Berman, Colin Hamilton, Joel Jackson, Richard Carlson (2018) Next Generation Cathode Technologies: Engineering Out Cobalt Is Easier Said Than Done.
- 64 Zhang S.S. (2020) Understanding of performance degradation of LiNi_{0.80}Co_{0.10}Mn_{0.10}O₂ cathode material operating at high potentials, *Journal of Energy Chemistry* **41**, 135–141. DOI: 10.1016/j.jechem.2019.05.013.
- 65 Bak S.-M., Hu E., Zhou Y., Yu X., Senanayake S.D., Cho S.-J., Kim K.-B., Chung K.Y., Yang X.-Q., Nam K.-W. (2014) Structural changes and thermal stability of charged LiNi_xMn_yCo_zO₂ cathode materials studied by combined in situ time-resolved XRD and mass spectroscopy, *ACS applied materials & interfaces* **6**, 24, 22594–22601. DOI: 10.1021/am506712c.
- 66 Noh H.-J., Youn S., Yoon C.S., Sun Y.-K. (2013) Comparison of the structural and electrochemical properties of layered Li[Ni_xCo_yMn_z]O₂ ($x = 1/3, 0.5, 0.6, 0.7, 0.8$ and 0.85) cathode material for lithium-ion batteries, *Journal of Power Sources* **233**, 121–130. DOI: 10.1016/j.jpowsour.2013.01.063.
- 67 Märker K., Reeves P.J., Xu C., Griffith K.J., Grey C.P. (2019) Evolution of Structure and Lithium Dynamics in LiNi_{0.8}Mn_{0.1}Co_{0.1}O₂ (NMC811) Cathodes during Electrochemical Cycling, *Chem. Mater.* **31**, 7, 2545–2554. DOI: 10.1021/acs.chemmater.9b00140.
- 68 Matilda Klett, James A. Gilbert, Krzysztof Z. Pupek, Stephen E. Trask, and Daniel P. Abraham (2016) Layered Oxide, Graphite and Silicon-Graphite Electrodes for Lithium-Ion Cells: Effect of Electrolyte Composition and Cycling Windows, *Journal of The Electrochemical Society* **164**(1), A6095-A6102. DOI: 10.1149/2.0131701jes.
- 69 Birkel C.R., Roberts M.R., McTurk E., Bruce P.G., Howey D.A. (2017) Degradation diagnostics for lithium-ion cells, *Journal of Power Sources* **341**, 373–386. DOI: 10.1016/j.jpowsour.2016.12.011.
- 70 Keil P., Schuster S.F., Wilhelm J., Travi J., Hauser A., Karl R.C., Jossen A. (2016) Calendar Aging of Lithium-Ion Batteries, *J. Electrochem. Soc.* **163**, 9, A1872-A1880. DOI: 10.1149/2.0411609jes.
- 71 Schmitt J., Maheshwari A., Heck M., Lux S., Vetter M. (2017) Impedance change and capacity fade of lithium nickel manganese cobalt oxide-based batteries during calendar aging, *Journal of Power Sources* **353**, 183–194. DOI: 10.1016/j.jpowsour.2017.03.090.
- 72 Broussely M., Biensan P., Bonhomme F., Blanchard P., Herreyre S., Nechev K., Staniewicz R.J. (2005) Main aging mechanisms in Li ion batteries, *Journal of Power Sources* **146**, 1-2, 90–96. DOI: 10.1016/j.jpowsour.2005.03.172.
- 73 Schmitt J., Maheshwari A., Heck M., Lux S., Vetter M. (2017) Impedance change and capacity fade of lithium nickel manganese cobalt oxide-based batteries during calendar aging, *Journal of Power Sources* **353**, 183–194. DOI: 10.1016/j.jpowsour.2017.03.090.
- 74 Gao T., Wang Z., Chen S., Guo L. (2019) Hazardous characteristics of charge and discharge of lithium-ion batteries under adiabatic environment and hot environment, *International Journal of Heat and Mass Transfer* **141**, 419–431. DOI: 10.1016/j.ijheatmasstransfer.2019.06.075.

- 75 Li X., Colclasure A.M., Finegan D.P., Ren D., Shi Y., Feng X., Cao L., Yang Y., Smith K. (2019) Degradation mechanisms of high capacity 18650 cells containing Si-graphite anode and nickel-rich NMC cathode, *Electrochimica Acta* **297**, 1109–1120. DOI: 10.1016/j.electacta.2018.11.194.
- 76 Tian C., Lin F., Doeff M.M. (2018) Electrochemical Characteristics of Layered Transition Metal Oxide Cathode Materials for Lithium Ion Batteries: Surface, Bulk Behavior, and Thermal Properties, *Accounts of chemical research* **51**, 1, 89–96. DOI: 10.1021/acs.accounts.7b00520.
- 77 Zhang S.S. (2020) Problems and their origins of Ni-rich layered oxide cathode materials, *Energy Storage Materials* **24**, 247–254. DOI: 10.1016/j.ensm.2019.08.013.
- 78 Lim J.-M., Hwang T., Kim D., Park M.-S., Cho K., Cho M. (2017) Intrinsic Origins of Crack Generation in Ni-rich LiNi_{0.8}Co_{0.1}Mn_{0.1}O₂ Layered Oxide Cathode Material, *Scientific reports* **7**, 39669. DOI: 10.1038/srep39669.
- 79 Persson K., Sethuraman V.A., Hardwick L.J., Hinuma Y., Meng Y.S., van der Ven A., Srinivasan V., Kostecki R., Ceder G. (2010) Lithium Diffusion in Graphitic Carbon, *J. Phys. Chem. Lett.* **1**, 8, 1176–1180. DOI: 10.1021/jz100188d.
- 80 Petzl M., Danzer M.A. (2014) Nondestructive detection, characterization, and quantification of lithium plating in commercial lithium-ion batteries, *Journal of Power Sources* **254**, 80–87. DOI: 10.1016/j.jpowsour.2013.12.060.
- 81 Uhlmann C., Illig J., Ender M., Schuster R., Ivers-Tiffée E. (2015) In situ detection of lithium metal plating on graphite in experimental cells, *Journal of Power Sources* **279**, 428–438. DOI: 10.1016/j.jpowsour.2015.01.046.
- 82 Jalkanen K., Karppinen J., Skogström L., Laurila T., Nisula M., Vuorilehto K. (2015) Cycle aging of commercial NMC/graphite pouch cells at different temperatures, *Applied Energy* **154**, 160–172. DOI: 10.1016/j.apenergy.2015.04.110.
- 83 Matadi B.P., Geniès S., Delaille A., Waldmann T., Kasper M., Wohlfahrt-Mehrens M., Aguesse F., Bekaert E., Jiménez-Gordon I., Daniel L., Fleury X., Bardet M., Martin J.-F., Bultel Y. (2017) Effects of Biphenyl Polymerization on Lithium Deposition in Commercial Graphite/NMC Lithium-Ion Pouch-Cells during Calendar Aging at High Temperature, *J. Electrochem. Soc.* **164**, 6, A1089–A1097. DOI: 10.1149/2.0631706jes.
- 84 Ghanbari N., Waldmann T., Kasper M., Axmann P., Wohlfahrt-Mehrens M. (2016) Inhomogeneous Degradation of Graphite Anodes in Li-Ion Cells: A Postmortem Study Using Glow Discharge Optical Emission Spectroscopy (GD-OES), *J. Phys. Chem. C* **120**, 39, 22225–22234. DOI: 10.1021/acs.jpcc.6b07117.
- 85 Iturrondobeitia A., Aguesse F., Genies S., Waldmann T., Kasper M., Ghanbari N., Wohlfahrt-Mehrens M., Bekaert E. (2017) Post-Mortem Analysis of Calendar-Aged 16 Ah NMC/Graphite Pouch Cells for EV Application, *J. Phys. Chem. C* **121**, 40, 21865–21876. DOI: 10.1021/acs.jpcc.7b05416.

- 86 Bach T.C., Schuster S.F., Fleder E., Müller J., Brand M.J., Lormann H., Jossen A., Sxetl G. (2016) Nonlinear aging of cylindrical lithium-ion cells linked to heterogeneous compression, *Journal of Energy Storage* **5**, 212–223. DOI: 10.1016/j.est.2016.01.003.
- 87 Osswald P.J., Erhard S.V., Rheinfeld A., Rieger B., Hoster H.E., Jossen A. (2016) Temperature dependency of state of charge inhomogeneities and their equalization in cylindrical lithium-ion cells, *Journal of Power Sources* **329**, 546–552. DOI: 10.1016/j.jpowsour.2016.08.120.
- 88 Pastor-Fernández C., Uddin K., Chouchelamane G.H., Widanage W.D., Marco J. (2017) A Comparison between Electrochemical Impedance Spectroscopy and Incremental Capacity-Differential Voltage as Li-ion Diagnostic Techniques to Identify and Quantify the Effects of Degradation Modes within Battery Management Systems, *Journal of Power Sources* **360**, 301–318. DOI: 10.1016/j.jpowsour.2017.03.042.
- 89 L.E. Downiea, V.L. Chevrierb, J.R. Dahna, and L.J. Krauseb (2013) In Situ Detection of Lithium Plating on Graphite Electrodes by Electrochemical Calorimetry, *Journal of The Electrochemical Society* **160** (4), A588-A594. DOI: 10.1149/2.049304jes.
- 90 Petzl M., Kasper M., Danzer M.A. (2015) Lithium plating in a commercial lithium-ion battery – A low-temperature aging study, *Journal of Power Sources* **275**, 799–807. DOI: 10.1016/j.jpowsour.2014.11.065.
- 91 Anseán D., Dubarry M., Devie A., Liaw B.Y., García V.M., Viera J.C., González M. (2017) Operando lithium plating quantification and early detection of a commercial LiFePO₄ cell cycled under dynamic driving schedule, *Journal of Power Sources* **356**, 36–46. DOI: 10.1016/j.jpowsour.2017.04.072.
- 92 Schindler S., Bauer M., Petzl M., Danzer M.A. (2016) Voltage relaxation and impedance spectroscopy as in-operando methods for the detection of lithium plating on graphitic anodes in commercial lithium-ion cells, *Journal of Power Sources* **304**, 170–180. DOI: 10.1016/j.jpowsour.2015.11.044.
- 93 Lüders C. von, Zinth V., Erhard S.V., Osswald P.J., Hofmann M., Gilles R., Jossen A. (2017) Lithium plating in lithium-ion batteries investigated by voltage relaxation and in situ neutron diffraction, *Journal of Power Sources* **342**, 17–23. DOI: 10.1016/j.jpowsour.2016.12.032.
- 94 Waldmann T., Quinn J.B., Richter K., Kasper M., Tost A., Klein A., Wohlfahrt-Mehrens M. (2017) Electrochemical, Post-Mortem, and ARC Analysis of Li-Ion Cell Safety in Second-Life Applications, *J. Electrochem. Soc.* **164**, 13, A3154-A3162. DOI: 10.1149/2.0961713jes.
- 95 Zhao C., Sun J., Wang Q. (2020) Thermal runaway hazards investigation on 18650 lithium-ion battery using extended volume accelerating rate calorimeter, *Journal of Energy Storage* **28**, 101232. DOI: 10.1016/j.est.2020.101232.
- 96 Inoue T., Mukai K. (2017) Roles of positive or negative electrodes in the thermal runaway of lithium-ion batteries: Accelerating rate calorimetry analyses with an all-inclusive microcell, *Electrochemistry Communications* **77**, 28–31. DOI: 10.1016/j.elecom.2017.02.008.

- 97 Patel D., Robinson J.B., Ball S., Brett D.J.L., Shearing P.R. (2020) Thermal Runaway of a Li-Ion Battery Studied by Combined ARC and Multi-Length Scale X-ray CT, *J. Electrochem. Soc.* **167**, 9, 90511. DOI: 10.1149/1945-7111/ab7fb6.
- 98 Fleischhammer M., Waldmann T., Bisle G., Hogg B.-I., Wohlfahrt-Mehrens M. (2015) Interaction of cyclic ageing at high-rate and low temperatures and safety in lithium-ion batteries, *Journal of Power Sources* **274**, 432–439. DOI: 10.1016/j.jpowsour.2014.08.135.
- 99 Friesen A., Horsthemke F., Mönnighoff X., Brunklaus G., Krafft R., Börner M., Risthaus T., Winter M., Schappacher F.M. (2016) Impact of cycling at low temperatures on the safety behavior of 18650-type lithium ion cells: Combined study of mechanical and thermal abuse testing accompanied by post-mortem analysis, *Journal of Power Sources* **334**, 1–11. DOI: 10.1016/j.jpowsour.2016.09.120.
- 100 Honbo H., Takei K., Ishii Y., Nishida T. (2009) Electrochemical properties and Li deposition morphologies of surface modified graphite after grinding, *Journal of Power Sources* **189**, 1, 337–343. DOI: 10.1016/j.jpowsour.2008.08.048.
- 101 Chang H.J., Trease N.M., Ilott A.J., Zeng D., Du L.-S., Jerschow A., Grey C.P. (2015) Investigating Li Microstructure Formation on Li Anodes for Lithium Batteries by in Situ ⁶Li/ ⁷Li NMR and SEM, *J. Phys. Chem. C* **119**, 29, 16443–16451. DOI: 10.1021/acs.jpcc.5b03396.
- 102 Lewerenz M., Münnix J., Schmalstieg J., Käbitz S., Knips M., Sauer D.U. (2017) Systematic aging of commercial LiFePO₄ | Graphite cylindrical cells including a theory explaining rise of capacity during aging, *Journal of Power Sources* **345**, 254–263. DOI: 10.1016/j.jpowsour.2017.01.133.
- 103 Battery University website Safety concerns with Li-ion battery. Available at: https://batteryuniversity.com/learn/article/safety_concerns_with_li_ion.
- 104 Golubkov A.W., Fuchs D. (2014) Thermal Runaway: Causes and Consequences on Cell Level, in *Automotive battery technology*, Thaler A., Watzenig D. (eds.), Springer, Cham New York, pp. 37–51.
- 105 E.P. Roth, C. Crafts, D. Doughty, J. McBreen (2004) *Advanced Technology Development Program for Lithium-Ion Batteries: Thermal Abuse Performance of 18650 Li-Ion Cells*. DOI: 10.2172/918751.
- 106 Nguyen T.T.D., Abada S., Lecocq A., Bernard J., Petit M., Marlair G., Grugeon S., Laruelle S. (2019) Understanding the Thermal Runaway of Ni-Rich Lithium-Ion Batteries, *WEVJ* **10**, 4, 79. DOI: 10.3390/wevj10040079.
- 107 Chen Z., Qin Y., Ren Y., Lu W., Orendorff C., Roth E.P., Amine K. (2011) Multi-scale study of thermal stability of lithiated graphite, *Energy Environ. Sci.* **4**, 10, 4023. DOI: 10.1039/C1EE01786A.
- 108 Zheng S., Wang L., Feng X., He X. (2018) Probing the heat sources during thermal runaway process by thermal analysis of different battery chemistries, *Journal of Power Sources* **378**, 527–536. DOI: 10.1016/j.jpowsour.2017.12.050.

- 109 Liu X., Ren D., Hsu H., Feng X., Xu G.-L., Zhuang M., Gao H., Lu L., Han X., Chu Z., Li J., He X., Amine K., Ouyang M. (2018) Thermal Runaway of Lithium-Ion Batteries without Internal Short Circuit, *Joule* **2**, 10, 2047–2064. DOI: 10.1016/j.joule.2018.06.015.
- 110 Wang H., Du Z., Rui X., Wang S., Jin C., He L., Zhang F., Wang Q., Feng X. (2020) A comparative analysis on thermal runaway behavior of Li (NixCoyMnz) O2 battery with different nickel contents at cell and module level, *Journal of hazardous materials* **393**, 122361. DOI: 10.1016/j.jhazmat.2020.122361.
- 111 Wang Q., Mao B., Stolarov S.I., Sun J. (2019) A review of lithium ion battery failure mechanisms and fire prevention strategies, *Progress in Energy and Combustion Science* **73**, 95–131. DOI: 10.1016/j.pecs.2019.03.002.
- 112 Wu X., Song K., Zhang X., Hu N., Li L., Li W., Zhang L., Zhang H. (2019) Safety Issues in Lithium Ion Batteries: Materials and Cell Design, *Front. Energy Res.* **7**, 96. DOI: 10.3389/fenrg.2019.00065.
- 113 Escobar-Hernandez H.U., Gustafson R.M., Papadaki M.I., Sachdeva S., Mannan M.S. (2016) Thermal Runaway in Lithium-Ion Batteries: Incidents, Kinetics of the Runaway and Assessment of Factors Affecting Its Initiation, *J. Electrochem. Soc.* **163**, 13, A2691-A2701. DOI: 10.1149/2.0921613jes.
- 114 Harris S.J., Timmons A., Pitz W.J. (2009) A combustion chemistry analysis of carbonate solvents used in Li-ion batteries, *Journal of Power Sources* **193**, 2, 855–858. DOI: 10.1016/j.jpowsour.2009.04.030.
- 115 Christopher J. Orendorff (2012) The Role of Separators in Lithium-Ion Cell Safety, *Electrochem. Soc. Interface* **21** 61. Available at: <https://iopscience.iop.org/article/10.1149/2.F07122if/pdf>.
- 116 Xu J., Wu Y., Yin S. (2017) Investigation of effects of design parameters on the internal short-circuit in cylindrical lithium-ion batteries, *RSC Adv.* **7**, 24, 14360–14371. DOI: 10.1039/C6RA27892B.
- 117 Biensan P., Simon B., Pérès J.P., Guibert A. de, Broussely M., Bodet J.M., Pertion F. (1999) On safety of lithium-ion cells, *Journal of Power Sources* **81-82**, 906–912. DOI: 10.1016/S0378-7753(99)00135-4.
- 118 Chen C.-H., Brosa Planella F., O'Regan K., Gastol D., Widanage W.D., Kendrick E. (2020) Development of Experimental Techniques for Parameterization of Multi-scale Lithium-ion Battery Models, *J. Electrochem. Soc.* **167**, 8, 80534. DOI: 10.1149/1945-7111/ab9050.
- 119 Mayur M., Yagci M.C., Carelli S., Margulies P., Velten D., Bessler W.G. (2019) Identification of stoichiometric and microstructural parameters of a lithium-ion cell with blend electrode, *Physical chemistry chemical physics : PCCP* **21**, 42, 23672–23684. DOI: 10.1039/c9cp04262h.
- 120 Svenningsen G.S., Williams B.R., Blayney M.B., Czornyj E., Schröder I., Merlic C.A. (2020) Lessons Learned—Fluoride Exposure, *ACS Chem. Health Saf.* **27**, 1, 40–42. DOI: 10.1021/acs.chas.9b00015.

- 121 Mei W., Chen H., Sun J., Wang Q. (2019) The effect of electrode design parameters on battery performance and optimization of electrode thickness based on the electrochemical–thermal coupling model, *Sustainable Energy Fuels* **3**, 1, 148–165. DOI: 10.1039/C8SE00503F.
- 122 Sturk D., Rosell L., Blomqvist P., Ahlberg Tidblad A. (2019) Analysis of Li-Ion Battery Gases Vented in an Inert Atmosphere Thermal Test Chamber, *Batteries* **5**, 3, 61. DOI: 10.3390/batteries5030061.
- 123 Baird A.R., Archibald E.J., Marr K.C., Ezekoye O.A. (2020) Explosion hazards from lithium-ion battery vent gas, *Journal of Power Sources* **446**, 227257. DOI: 10.1016/j.jpowsour.2019.227257.
- 124 Barkholtz H.M., Preger Y., Ivanov S., Langendorf J., Torres-Castro L., Lamb J., Chalamala B., Ferreira S.R. (2019) Multi-scale thermal stability study of commercial lithium-ion batteries as a function of cathode chemistry and state-of-charge, *Journal of Power Sources* **435**, 226777. DOI: 10.1016/j.jpowsour.2019.226777.
- 125 Liao Z., Zhang S., Li K., Zhao M., Qiu Z., Han D., Zhang G., Habetler T.G. (2020) Hazard analysis of thermally abused lithium-ion batteries at different state of charges, *Journal of Energy Storage* **27**, 101065. DOI: 10.1016/j.est.2019.101065.
- 126 Perea A., Paoletta A., Dubé J., Champagne D., Mauger A., Zaghbi K. (2018) State of charge influence on thermal reactions and abuse tests in commercial lithium-ion cells, *Journal of Power Sources* **399**, 392–397. DOI: 10.1016/j.jpowsour.2018.07.112.
- 127 Mao B., Huang P., Chen H., Wang Q., Sun J. (2020) Self-heating reaction and thermal runaway criticality of the lithium ion battery, *International Journal of Heat and Mass Transfer* **149**, 119178. DOI: 10.1016/j.ijheatmasstransfer.2019.119178.
- 128 Kvasha A., Gutiérrez C., Osa U., Meatza I. de, Blazquez J.A., Macicior H., Urdampilleta I. (2018) A comparative study of thermal runaway of commercial lithium ion cells, *Energy* **159**, 547–557. DOI: 10.1016/j.energy.2018.06.173.
- 129 Spray R., Barry M., Vickery J. (2019) (Invited) Understanding Downstream Risk from Lithium-Ion Battery Thermal Runaway & Designing for Safety, *ECS Trans.* **89**, 1, 65–71. DOI: 10.1149/08901.0065ecst.
- 130 Peng Y., Zhou X., Hu Y., Ju X., Liao B., Yang L. (2020) A new exploration of the fire behaviors of large format lithium ion battery, *J Therm Anal Calorim* **139**, 2, 1243–1254. DOI: 10.1007/s10973-019-08459-3.
- 131 Carter R., Klein E.J., Atkinson R.W., Love C.T. (2019) Mechanical collapse as primary degradation mode in mandrel-free 18650 Li-ion cells operated at 0 °C, *Journal of Power Sources* **437**, 226820. DOI: 10.1016/j.jpowsour.2019.226820.
- 132 Lammer M., Königseder A., Gluschitz P., Hacker V. (2015) Influence of aging on the heat and gas emissions from commercial lithium ion cells in case of thermal failure, *J. Electrochem. Sci. Eng.* DOI: 10.5599/jese.476.

- 133 Lammer M., Königseder A., Hacker V. (2017) Characterisation of Heat and Gas Emissions in Thermally Induced Battery Failure on Commercially Available 18650 Li-Ion Cells, *ECS Trans.* **80**, 10, 135–143. DOI: 10.1149/08010.0135ecst.
- 134 Lammer M., Königseder A., Hacker V. (2017) Holistic methodology for characterisation of the thermally induced failure of commercially available 18650 lithium ion cells, *RSC Adv.* **7**, 39, 24425–24429. DOI: 10.1039/C7RA02635H.
- 135 Lian T., Vie P.J.S., Gilljam M., Forseth S. (2019) (Invited) Changes in Thermal Stability of Cyclic Aged Commercial Lithium-Ion Cells, *ECS Trans.* **89**, 1, 73–81. DOI: 10.1149/08901.0073ecst.
- 136 Hatchard T.D., MacNeil D.D., Basu A., Dahn J.R. (2001) Thermal Model of Cylindrical and Prismatic Lithium-Ion Cells, *J. Electrochem. Soc.* **148**, 7, A755. DOI: 10.1149/1.1377592.
- 137 Kim G.-H., Pesaran A., Spotnitz R. (2007) A three-dimensional thermal abuse model for lithium-ion cells, *Journal of Power Sources* **170**, 2, 476–489. DOI: 10.1016/j.jpowsour.2007.04.018.
- 138 Petit M., Abada S., Mingant R., Bernard J., Desprez P., Perlo P., Biasotto M., Introzzi R., Lecocq A., Marlair G. (2019) Demobase project: Numerical simulation for seamless integration of battery pack in light electric vehicle, in *32nd Electric Vehicle Symposium (EVS32)*. Available at: <https://doi.org/10.5281/zenodo.3368893>.
- 139 Coman P.T., Rayman S., White R.E. (2016) A lumped model of venting during thermal runaway in a cylindrical Lithium Cobalt Oxide lithium-ion cell, *Journal of Power Sources* **307**, 56–62. DOI: 10.1016/j.jpowsour.2015.12.088.
- 140 Coman P.T., Mátéfi-Tempfli S., Veje C.T., White R.E. (2017) Modeling Vaporization, Gas Generation and Venting in Li-Ion Battery Cells with a Dimethyl Carbonate Electrolyte, *J. Electrochem. Soc.* **164**, 9, A1858-A1865. DOI: 10.1149/2.0631709jes.
- 141 Martin Petit (2019) *Thermal runaway of high power LFP-C Li-ion battery - experimental and model comparison*, rapport IFPEN.
- 142 Cai T., Stefanopoulou A.G., Siegel J.B. (2019) Early Detection for Li-Ion Batteries Thermal Runaway Based on Gas Sensing, *ECS Trans.* **89**, 1, 85–97. DOI: 10.1149/08901.0085ecst.
- 143 Zhang J., Zhang L., Sun F., Wang Z. (2018) An Overview on Thermal Safety Issues of Lithium-ion Batteries for Electric Vehicle Application, *IEEE Access*, 1. DOI: 10.1109/ACCESS.2018.2824838.
- 144 Lei B., Zhao W., Ziebert C., Uhlmann N., Rohde M., Seifert H. (2017) Experimental Analysis of Thermal Runaway in 18650 Cylindrical Li-Ion Cells Using an Accelerating Rate Calorimeter, *Batteries* **3**, 4, 14. DOI: 10.3390/batteries3020014.
- 145 Börner M., Friesen A., Grützke M., Stenzel Y.P., Brunklaus G., Haetge J., Nowak S., Schappacher F.M., Winter M. (2017) Correlation of aging and thermal stability of commercial 18650-type lithium ion batteries, *Journal of Power Sources* **342**, 382–392. DOI: 10.1016/j.jpowsour.2016.12.041.

- 146 Lammer M., Königseder A., Hacker V. (2017) Characterisation of Heat and Gas Emissions in Thermally Induced Battery Failure on Commercially Available 18650 Li-Ion Cells, *ECS Trans.* **80**, 10, 135–143. DOI: 10.1149/08010.0135ecst.
- 147 Murashko K.A., Mityakov A.V., Mityakov V.Y., Sapozhnikov S.Z., Jokiniemi J., Pyrhönen J. (2016) Determination of the entropy change profile of a cylindrical lithium-ion battery by heat flux measurements, *Journal of Power Sources* **330**, 61–69. DOI: 10.1016/j.jpowsour.2016.08.130.
- 148 Jung R., Metzger M., Maglia F., Stinner C., Gasteiger H.A. (2017) Chemical versus Electrochemical Electrolyte Oxidation on NMC111, NMC622, NMC811, LNMO, and Conductive Carbon, *The journal of physical chemistry letters* **8**, 19, 4820–4825. DOI: 10.1021/acs.jpcllett.7b01927.
- 149 Rapport IFPEN 62842 (ed.) *Rapport final du projet ANR VTT 2009 - SIMCAL, mai 2013.*
- 150 Edouard C., Petit M., Forgez C., Bernard J., Revel R. (2016) Parameter sensitivity analysis of a simplified electrochemical and thermal model for Li-ion batteries aging, *Journal of Power Sources*, 325, 482-494. DOI: 10.1016/j.jpowsour.2016.06.030.
- 151 Kassem M., Bernard J., Revel R., Pélissier S., Duclaud F., Delacourt C. (2012) Calendar aging of a graphite/LiFePO₄ cell, *Journal of Power Sources* **208**, 296–305. DOI: 10.1016/j.jpowsour.2012.02.068.
- 152 Mier F.A. (2018) Measurement of 18650 format Lithium-Ion Battery vent mechanism flow parameters, *Master Thesis*, New Mexico Institute of Mining and Technology Socorro, New Mexico.
- 153 Maleki H., Hallaj S.A., Selman J.R., Dinwiddie R.B., Wang H. (1999) Thermal Properties of Lithium-Ion Battery and Components, *J. Electrochem. Soc.* **146**, 3, 947–954. DOI: 10.1149/1.1391704.
- 154 C. Edouard Vieillissement des batteries Li-ion de traction : de mécanismes vers le vieillissement accéléré, Rapport de Thèse de doctorat, octobre 2015 - rapport IFPEN 66165.
- 155 Saleem K., Mehran K., Ali Z. (2020) Online reduced complexity parameter estimation technique for equivalent circuit model of lithium-ion battery, *Electric Power Systems Research* **185**, 106356. DOI: 10.1016/j.epsr.2020.106356.
- 156 Zhang L., Peng H., Ning Z., Mu Z., Sun C. (2017) Comparative Research on RC Equivalent Circuit Models for Lithium-Ion Batteries of Electric Vehicles, *Applied Sciences* **7**, 10, 1002. DOI: 10.3390/app7101002.
- 157 Feng X., Ouyang M., Liu X., Lu L., Xia Y., He X. (2018) Thermal runaway mechanism of lithium ion battery for electric vehicles: A review, *Energy Storage Materials* **10**, 246–267. DOI: 10.1016/j.ensm.2017.05.013.
- 158 Worwood D., Kellner Q., Wojtala M., Widanage W.D., McGlen R., Greenwood D., Marco J. (2017) A new approach to the internal thermal management of cylindrical battery cells for

- automotive applications, *Journal of Power Sources* **346**, 151–166. DOI: 10.1016/j.jpowsour.2017.02.023.
- 159 Shah K., McKee C., Chalise D., Jain A. (2016) Experimental and numerical investigation of core cooling of Li-ion cells using heat pipes, *Energy* **113**, 852–860. DOI: 10.1016/j.energy.2016.07.076.
- 160 Drake S.J., Wetz D.A., Ostanek J.K., Miller S.P., Heinzl J.M., Jain A. (2014) Measurement of anisotropic thermophysical properties of cylindrical Li-ion cells, *Journal of Power Sources* **252**, 298–304. DOI: 10.1016/j.jpowsour.2013.11.107.
- 161 Peng P., Jiang F. (2016) Thermal safety of lithium-ion batteries with various cathode materials: A numerical study, *International Journal of Heat and Mass Transfer* **103**, 1008–1016. DOI: 10.1016/j.ijheatmasstransfer.2016.07.088.
- 162 F.Mier, M.Hargather, S.Ferreira (2018) Experimental quantification of vent mechanism flow parameters in 18650 format lithium ion batteries, SAND2018-9403J. Available at: <https://www.osti.gov/servlets/purl/1498760>.
- 163 Sturm J., Rheinfeld A., Zilberman I., Spingler F.B., Kosch S., Frie F., Jossen A. (2019) Modeling and simulation of inhomogeneities in a 18650 nickel-rich, silicon-graphite lithium-ion cell during fast charging, *Journal of Power Sources* **412**, 204–223. DOI: 10.1016/j.jpowsour.2018.11.043.

Résumé

Au regard du problème de sécurité récurrent constaté depuis la commercialisation des batteries au lithium-ion (LIBs), associé à un manque de maîtrise du risque d'emballement thermique qui les caractérise, cette thèse vise à approfondir la compréhension et la modélisation de ce phénomène complexe à l'échelle cellulaire, en prenant en compte l'influence des nouvelles technologies hautement réactives (dopage en Ni) ainsi que les influences de l'état de charge (SOC) et du vieillissement, afin de comprendre le rôle de ces facteurs clés pour une conception et un fonctionnement intrinsèquement plus sûr de telles batteries au lithium-ion. Grâce à la synergie offerte par les études expérimentales et de modélisation combinées de cette thèse, les connaissances en termes d'initiation et d'évolution de l'emballement thermique des batteries Li-ion riches en Ni se sont enrichies. L'étude de modélisation conduit au développement d'un modèle 3D d'emballement thermique étendu pour prédire les comportements de différentes batteries Li-ion en champ temporel proche et pendant le processus d'emballement thermique. L'étude expérimentale examine l'emballement thermique des LIBs et fournit des bases de données suffisantes pour la calibration et la validation du modèle prédictif. Le modèle développé peut être utilisé comme outil de simulation pour explorer plus de scénarios de cellules subissant un emballement thermique dans des conditions spécifiées pour lesquelles un paramétrage adéquat peut être défini en relation avec la physique sous-jacente. Ce travail ouvre de nouvelles perspectives en matière de stratégie de gestion de la sécurité des batteries Li-ion.

Mots clés: batteries au Lithium-ion (LIB), modélisation 0D/3D multi-physique de l'emballement thermiques, COMSOL, calibration et validation sur 18650 NCA/graphite-SiO_x et NMC811/graphite-SiO_x; essais/simulations : épreuves BTC (ARC) et test en étuves.

Abstract:

Since the commercialization of Lithium-Ion Battery (LIB) by Sony Inc. in 1991 until today, recurrent incidents involving LIBs have been reported worldwide. During these incidents, the most energetic catastrophic failure of a LIB system is the thermal runaway event. With the emergence of highly reactive Ni-rich LIBs in the market, battery safety is becoming even more critical because these newly introduced LIBs present such high energy density which could lead to more catastrophic events subsequent to the thermal runaway. Therefore, this thesis aims to go deeper into the understanding and modelling of this complex phenomenon at cell scale, taking into account the influence of novel highly reactive technologies and the influence of state of charge (SOC) and aging, in order to understand what the key factors are towards inherently safer design and operation of LIBs. Thanks to the synergism offered by combined experimental and modelling studies of this thesis, knowledge in terms of initiation and evolution of the thermal runaway of Ni-rich Li-ion batteries has been enriched. The modelling study leads to the development of a 3D extended thermal runaway model to predict the behaviours of different Li-ion batteries nearby and during thermal runaway. The experimental study investigates the thermal runaway of LIBs and provides suitable databases for the predictive model calibration and validation. The developed model can be used as a simulation tool to explore more scenarios of cells undergoing thermal runaway in specified conditions for which adequate parameterization can be defined in relation with underpinning physics. This contributes to the future Li-ion battery safety management system in depth.

Keywords: Lithium-ion batteries (LIB), 0D/3D multi-physics modelling of thermal runaway, COMSOL, calibration and validation on 18650 NCA / graphite-SiO_x and NMC811 / graphite-SiO_x; tests / simulations: BTC tests (ARC) and oven test.